universität
wien

MASTERARBEIT / MASTER'S THESIS

Titel der Masterarbeit / Title of the Master's Thesis

„Simulation of Quantum Confinement and Plasmonic Response in Geometrically Designed Silicon Structures within Graphene Lattice"

verfasst von / submitted by

Daryoush Nosraty Alamdary, BSc

angestrebter akademischer Grad / in partial fulfilment of the requirements for the degree of

Master of Science (MSc)

Vienna, 2017

Studienkennzahl lt. Studienblatt / degree programme code as it appears on the student record sheet:	A 066 876
Studienrichtung lt. Studienblatt / degree programme as it appears on the student record sheet:	Masterstudium Physik/Master's Degree Physics
Betreut von / Supervisor:	Assoc. Prof. Dr. Jani Kotakoski
Mitbetreut von / Co-Supervisor:	Dr. Toma Susi

Contents

Acknowledgement

Preface

1 Introduction
- 1.1 Tight Binding description of Graphene w/ Impurities . . . 3
- 1.2 Plasmonics of Graphene . . . 8
- 1.3 Quantum Confinement in Graphene . . . 12

2 Theory & Methods
- 2.1 Structural Optimizations & Basic DFT . . . 15
  - 2.1.1 Analytical Tersoff 1989 (T89) Potential . . . 15
  - 2.1.2 Analytical Erhard Albe Potential . . . 16
  - 2.1.3 Kohn-Sham Equations, PW's, FD, PAW, LCAO . . . 17
  - 2.1.4 Forces and Stress . . . 26
- 2.2 Density Functional Theory of Electronic Properties . . . 28
  - 2.2.1 Exchange-Correlation Functionals . . . 28
  - 2.2.2 STM Theory & Simulation . . . 32
- 2.3 Time-Dependent Density Functional Theory . . . 37
  - 2.3.1 Linear Density Dielectric Response . . . 37
  - 2.3.2 Linear Response: Casida's Method & Time Propagation . . . 39
  - 2.3.3 Localized Surface Plasmon Resonances . . . 43

3 Analytical Potential Simulations Results
- 3.1 Evaluating the Analytical Potentials . . . 45
  - 3.1.1 Tersoff Potential in LAMMPS . . . 45
  - 3.1.2 Tersoff & EA in LAMMPS . . . 48
  - 3.1.3 EA Potential in Atomistica & ASE . . . 51
- 3.2 Geometries, & Energetics of the Structures . . . 54
  - 3.2.1 Zigzag- & Armchair Lines: Dense, Dashed & Double-Dashed . . . 54
  - 3.2.2 Hexagons and Triangles . . . 58
  - 3.2.3 Squares, Circles, and Mixed Structures . . . 61

4 DFT Simulation Results
- 4.1 DFT Relaxation Results of Selected Structures . . . 66
  - 4.1.1 ZZ-Lines, ABZZ-Line & ACh-Line . . . 66
  - 4.1.2 Hexagons and Triangles . . . 68
  - 4.1.3 Squares, Circles, and Mixed Structures . . . 70
- 4.2 Quantum Confinement . . . 73
  - 4.2.1 Initial STM/STS of Structures w/ Fermi Level Convergence . . . 73
  - 4.2.2 STM/STS of Select Structures w/ Converged Unoccupied Bands . . . 82

4.3 Linear Plasmonic Response 89
    4.3.1 TDDFT Linear Dielectric Response & EELS 89
    4.3.2 FD LrTDDFT & Time-Propagation TDDFT, Induced Fields 97
    4.3.3 LCAO Time-Propagation TDDFT & LSPR's 112

5 Discussions & Conclusions

Appendices

A Optimization Algorithms

A.1 FIRE 132
A.2 Conjugate Gradient 133
A.3 BFGS 134

B Scripts

B.1 GPAW-code Modifications 135

Glossary

Bibliography

Acknowledgement

I would like to take this opportunity to thank my supervisor Prof. Jani Kotakoski, who trusted me to carry out this work and supported me throughout the difficulties and challenges, both scientific and organizational, for this thesis to be completed at this level, and who provided me with the tools necessary to learn and carry out the research necessary for this work, beyond any regular and normal level of any master's thesis. I would also like to thank Dr. Toma Susi for helping me get started with GPAW and ASE, to the level of independence, and guiding this work with respect to the content of the goals of his project, and for many discussions we had with regards to the physics of this thesis and his project, which in the end has brought my knowledge and skill sets to a whole new level. I hope the results from this work, however small, have had a role in pushing forward the very challenging tasks of his interesting project.

Daryoush Nosraty Alamdary Vienna, the 25th of July, 2017

Zusammenfassung

Heutige Materialwissenschaft, insbesondere die Physik kondensierter Materie, würde unvorstellbar sein ohne die Vielfalt von Kohlenstoff Allotropen. Unter ihnen, dem Einatom-dicken Graphene, ist besonders interessant, wegen seines einzigartigen elektronischen und mechanischen Eingenschaften. Dieser Nulllückenhalbleiter ist vielen modernen wissenschaftlichen Erforschungen unterworfen. Getrieben durch solche modernen Techniken und experimentelle Methoden, wie ultraniedrige Temperaturabtastung der Rastertunnelmikrokopie (RTM), oder hoch Auflösungabtastung der Rastertransmissionselektronenmikroskopie (RTEM), die Wissenschaft von Graphene verspricht, potenziell einer am meisten Wirkungsvolle Bereiche der Forschung in der modernen Physik zu sein. Folgend in dieser Linie der Forschung, basiert auf die Forschungsergebnisse von *Crommie, Lutz & Eigler* in 1993, welche die Erzeugung von Quanten-Corral auf einer Metalloberfläche durch Eisen-Adatomen bewiesen haben, es vorgeschlagen wurde, innerhalb des Forschungsprojektes *Heteratom Quantum Corrals and Nanoplasmonics in Graphene* (HeQuCoG), dass derselbe Affekt, in Graphene beobachtet werden könnte, diesmal mittels eingebetteter Silikonatomen. Das Thema dieser Arbeit ist, die erweiterten Si-Strukturen, die wie Verschmutzung in Graphene eingebettet sind, die lokal die Entbindung der elektronischen Wellenfunktionen in die Form von Quanten-Corrals abändern können, und auch unterschiedliche optische und plasmonische Antwortfunktionen vom System in linearem Limes erzeugen können, zu erforschen.

Der entscheidende Vorteil von diesen Graphene-basierten Strukturen gegenüber den Adatomen auf den Metalloberflächen ist, dass sie Kovalent gebunden sind, welche sie, bis zu dem Raumtemperatur und viel darüber, stabil macht. Deshalb in dieser Arbeit, eine theoretische Studie, durch computergestützte Methoden, durchgeführt wird, in eine systematische Art und Weise, anfangend damit, die Geometrie der Strukturen zu entspannen, und die Energetik der Strukturen pro Größe zu konvergieren. Weitere Simulationen der Strukturen (Geometrie Relaxation) sind dann mit dem *Dichtefunktionaltheorie*-Code (DFT), GPAW (*Grid-bas Projector Augmented Wave*), der besonders dafür bekannt ist, fähig dazu zu sein, große Strukturen zu behandeln, durchgeführt. Die entspannten Strukturen, sind dann mittels des RTM-Simulationspakets analysiert, für die Erfassung der eingeschlossenen elektronischen Zuständen. Zusätzlich zu der Ebene-welle basierten Methode der linearen dielektrischen Antwortfunktion, welche auch das Elektronenenergieverlustspektroskopie- (EELS) Spektrum von periodischen Systemen berechnen würde, dieses Programm auch die zeitabhängige-DFT-Paket (TDDFT) anbietet, welches das optischen Photoabsorptionsspektrum von den großen Strukturen ausrechnen, und auch deren lokalisierte Oberflächenplasmonenresonanzen (LSPR) visualisieren kann. Die experimentelle Bestätigung der Ergebnissen dieser Arbeit bleibt das Ziel des oben-genannten Forschungsprojektes HeQuCoG, welche von Bedeutung für die Physik der elektronischen Eigenschaften der Materie, und deren relevante Industrie, sein könnte.

Abstract

Today's materials science, especially condensed matter physics, would be unimaginable without the variety of carbon allotropes. Among them, the one-atom thick graphene, is of special interest, due to its unique electronic and mechanical properties. This zero gap semiconductor, is subject to many modern scientific explorations. Driven by such modern techniques and experimental methods, like ultra-low temperature *scanning tunnelling microscopy* (STM), or high resolution *scanning transmission electron microscopy* (STEM), the science of graphene promises to be one of most potentially impactful areas of research in modern science and modern physics. Following in this line of research, based on the research findings of *Crommie, Lutz* & *Eigler* in 1993, which demonstrated the creation of a quantum corral on the surface of a metal using iron ad-atoms, it was proposed, within the research-project *Heteroatom quantum corrals and nanoplasmonics in graphene* (HeQuCoG), that the same effect could be observed in graphene, using embedded silicon atoms. The topic of this thesis-research is to explore extended Si-structures, embedded in graphene like impurities, that could locally alter the confinement of the electronic wavefunctions into the form of quantum corrals, and also cause different optical and plasmonic response of the system in the linear limit.

The crucial advantage of these graphene-based structures over the adatoms on metal surfaces is that they are covalently bond, which makes them stable up to room temperature and above. Therefore, in this thesis, a theoretical study of such structures are carried out using computer-based techniques, in a systematic way, starting by relaxing the geometries and converging the energetics per size of the structures. Further relaxations of the select structures, are then done using a *density functional theory* (DFT) code, known as (*Grid-based projector augmented wave* (GPAW) which is particularly known for being capable of handling large structures. The relaxed structures are then analysed using the STM simulation package of the software for capturing the confined electronic states, and their shapes and sizes. For the linear response measurements, in addition to the plane-wave based linear dielectric response method, which would also calculate the *electron energy loss spectroscopy* (EELS) spectrum of periodic systems, this code offers *time-dependent DFT* (TDDFT) implementation, which can calculate the optical photo-absorption spectrum, and also visualize the *localized surface plasmonic resonance* of large systems. The experimental verification of the results obtained in this work remain the objective of the research project HeQuCoG, which may have implications for the physics of electronic properties of materials, and its related industries.

Preface

The science of carbon is one of most fascinating sciences that man has discovered in the modern era. The physics of carbon based materials, is amongst most modern and most complicated areas of the solid-states physics, due to the fact, that these materials have demonstrated significant number of special properties, which can only be explained by the modern quantum science. Especially, the low dimensional materials such as *single walled nano-tubes* (SWNT) or graphene are the jewels of the modern materials sciences. The reason for that is the combination of the electronic (including optical) as well as mechanical properties, the existence of which in materials such as graphene simultaneously, make it extremely fascinating to study for the physicists of the modern era.

More specifically, the semiconductor physics, which has emerged within the last decades, is today one of the most important branches of physics, which studies the very electronic properties, that within carbon materials have fascinated the physicists in the recent decades. The science of the electronic properties of carbon-based sciences belong to the most modern and the most sophisticated areas of physics and mathematics. As a widely known example of such, the Prof. Mildred Dresselhaus, who is known as the "queen of carbon sciences", is among those scientists, who have significantly made use of the mathematical theories, such as group theory, in order to explain the electronic and optical properties of solid-state materials, specially carbon-based molecules. As a student of physics, one of my most favorite subjects is the study of semiconductors and their electronic properties within solid-states physics. Specifically, the spectroscopy and doping of semiconductors, plus the fabrication technologies, which are connected with the study of such properties and materials, not only are the cutting edge of the current technologies, they also have direct relevance and application for the industry, for which I have developed a deep passion.

Within the Austrian Science Funds (FWF), individual project: "Heteroatom quantum corrals and nanoplasmonics in graphene", (HeQuCoG) I found the very interesting subject that I had been looking for, for my masters-thesis, as this project is the exact application of the kind of science that I described above. Despite it being all simulation-based however, my master-thesis serves as the basis for the production of the graphene based semiconductor materials, which can have very interesting electronic properties worthy of research for many many years and application in the semiconductor industries. As the title of the project suggest, the goal of the project is that to produce such structures within the graphene lattice, using mostly silicon, which would enhance the plasmonic response of the graphene material within the linear regime, however in massive structures with more that 400 atoms, the simulation of which requires special techniques, unique to the code that was used for these sets of simulations. Furthermore, due to the possibility of creating closed structures, based on lattice symmetry, it could be expected that some of the created structure induce an strong quantum confinement upon lattice, confining the surface electronic states to form quantum corrals and quantum mirages. However, the actual creation of such structures using STEM, and STM microscopy and Ion implantation requires first the theoretical study of such materials, using computer-simulation software, for which my thesis-work is designated.

However, the STM (and STS) simulations done in this thesis on the selected structures are done using a specific limit of STM imaging, reducing the STM-tip into a virtual point. This theoretical description, while being only one of the models (much earlier models) of STM, has the disadvantage of not being able to reproduce the interference, and multi-scattering effects, observed in actual STM experiments and rather described by other STM simulation packages. Therefore, there is the possibility of theoretical expansion of this work by such means as to observe local quantum fluctuations in the local density of states (LDOS), which has been proposed to a theoretical physics group at the TU Vienna for collaboration on a publication. In addition to this, there is much possibility of experimental verification of the results of this thesis, and/or the expansions thereof. One of the current topics of research is using the quantum corrals for quantum computation purposes, while another topic, also beyond the scope of this project, would be band-gap engineering, using controlled patterns and large structures in super-cells. However, direct attempts to verify or reproduce the results of this work experimentally remains first and foremost, within the tasks of the aforementioned FWF individual project HeQuCoG.

Chapter 1

Introduction

1.1 Tight Binding description of Graphene w/ Impurities

Graphene is a allotrope of carbon, which as stated before belongs in the group of low dimensional quantum solids, which in the latest decade have dominated the field of condensed matter physics. The shape of graphene is a sheet of single atomic honeycomb-lattice, normally obtained from graphite. In graphite itself, the graphene layers are only held by *Van der Waals* (VdW) forces, which are very week, and which can be explained using quantum mechanics. The science of graphene is extremely vast, from manipulation of its mechanical properties, to engineering its band gap and manipulating its optical properties. There are many interesting properties, which fall under the electronic properties, currently being subject of many research projects. Some mechanical properties of graphene are also of interest usually within other allotrope, such as SWNT's, but the electronic properties are particularly interesting, because of the potential in graphene to be of use in semiconductor devices.

There are many ways to describe the graphene lattice in crystallography, but the simplest way is to describe a graphene lattice using rhombus with periodic boundary conditions having only two atoms in the cell [1], as shown in (1.1), which is also called the primitive unit cell, with:

$$a_1 = \frac{a}{2}(3, \sqrt{3})$$

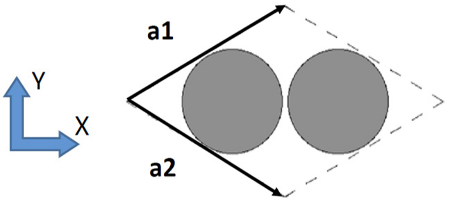

$$a_1 = \frac{a}{2}(3, -\sqrt{3}) \qquad (1.1)$$

as the lattice vectors, and $\mathrm{C}_1 = (a_1 + a_2)/3$, $\mathrm{C}_2 = 2(a_1 + a_2)/3$, as the atomic positions, where $a \approx 1.42$ Å is the C-C bond length (BL) . However, we have in most of our simulations used a rectangular cell containing 4 atoms. The unit cell has the advantage, that it can be arranged in two different ways, *zigzag* and *armchair*, from which the nanoribons and the nanotubes of the same name are built. The lattices built by these unit cells are however only 90 rotated with respect to each other. Fig. 1.1, demonstrate the rhombus unit cell's position within the graphene lattice, and fig. 1.2 illustrates the two rectangular cells which were used in different sets of calculations:

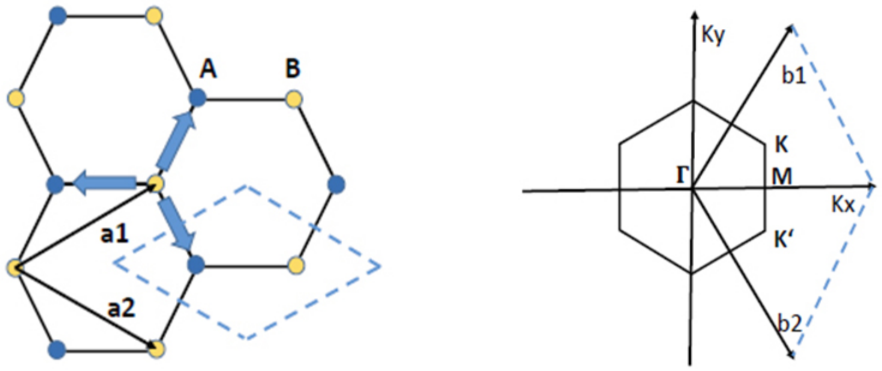

Figure 1.1: Left: Rhombus unit cell vectors and the atomic positions of graphene A-B sublattices. Right: Reciprocal lattice vectors $b_{1/2}$ and the Brillouin zone (Γ, **M**, **K** and **K'** points).

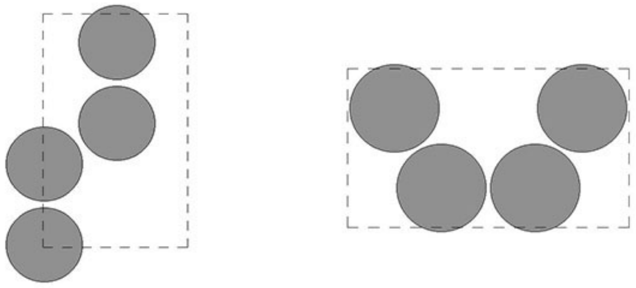

Figure 1.2: Left: The zigzag unit cell, appropriate for making zigzag lines. Right: Armchair unit-cell appropriate for making armchair lines

As the choices of unit-cells imply, crystallographic symmetry is a very important concept in the physics of solid states, and here is it no different. We are looking to create the most symmetric structures possible, using the proper unit-cell and the size of the super-cell since, these symmetries play important role in vibrational and dielectric properties of the materials. Therefore, even when the super-cell of a structure has to very large the orientation (and the position) of the embedded structures with respect to the honeycomb lattice of graphene is important, due to their affect on the aforementioned properties. In order to pave the way into the theories of linear response, dielectric properties, and plasmonic response of graphene-based materials, we should first briefly review the electronic structure of graphene.

The traditional description for the electronic properties, band structure calculations of graphene is using the *Tight Binding Approximation*. This model, despite being quiet old (*first discussed by P. R. Wallace in 1946*), produces very good results in comparison to experimental results. Of course in the latest decades, using the formalism of density functional theory, and its implementations in computer software on supercomputers, delivers more precise results regarding the electronic structure and properties of graphene. One of the reasons for that is for example the existence of *Dirac points*, *K* and *K'*, [1] defined by the following coordinates (a is the same C-C BL):

$$K = (\frac{2\pi}{3a}, \frac{2\pi}{3\sqrt{3}a}) \qquad K = (\frac{2\pi}{3a}, -\frac{2\pi}{3\sqrt{3}a}) \tag{1.2}$$

where (a is the same C-C BL) the electrons, which move at speeds of $v_F = (1/300)c$ (where c is the speed of light), resemble fermions that are described using the formalism of *Quantum*

Electrodynamics (QED). The existence of such fermions (*Dirac Fermions)* then transform the old and traditional tight-binding Hamiltonian defined as [1]:

$$H = -t \sum_{\langle i,j \rangle, \sigma} \left(a^{\dagger}_{\sigma,i} b_{\sigma,j} + h.c. \right) - t' \sum_{\langle i,j \rangle, \sigma} \left(a^{\dagger}_{\sigma,i} a_{\sigma,j} + b^{\dagger}_{\sigma,i} b_{\sigma,j} + h.c. \right) \tag{1.3}$$

into

$$H \sim -iv_F t \int dxdy \left(\hat{\Psi}^{\dagger}_1(r) \sigma \cdot \nabla \hat{\Psi}_1(r) + \hat{\Psi}^{\dagger}_2(r) \sigma \cdot \nabla \hat{\Psi}_2(r) \right) \tag{1.4}$$

while t' is set to zero, and the vectors $\boldsymbol{\sigma} = (\sigma_x, \sigma_y), \boldsymbol{\sigma}^* = (\sigma^*_x, \sigma^*_y)$. The a_σ, b_σ in eq. 1.3 are the A/B sublattice annihilation operators of spin-σ electrons, and t, t' are the nearest-neighbour/next-nearest neighbour transfer-integrals. The previous creation and annihilation operators are then replaced with the two component electron wave-functions, $\Psi^{\dagger}_i = (a^{\dagger}_i, b^{\dagger}_i)_{i=1,2}$ in real space, which near the Dirac points obey the 2D Dirac equation (having the energy eigenvalue E):

$$-iv_F \boldsymbol{\sigma} \cdot \nabla \psi(\boldsymbol{r}) = E\psi(\boldsymbol{r}) \tag{1.5}$$

Since the honeycomb lattice is made up of six covalent σ bonds (not to be mistaken with the Pauli spin operator $\overrightarrow{\sigma} = \boldsymbol{\sigma}$, which has components), the $2p_z$ orbital which is perpendicular to the $x - y$ plane forms the half-filled π-bond.

From the Hamiltonian in eq. 1.3 however, the energy bands for π and π^* ($+$ and -) can be derived as follows:

$$E_{\pm}(\boldsymbol{k}) = \pm t\sqrt{3 + f(\boldsymbol{k})} - t' f(\boldsymbol{k}) \tag{1.6}$$

with:

$$f(\boldsymbol{k}) = 2\text{cos}\left(\sqrt{3}k_y a\right) + 4\text{cos}\left(\frac{\sqrt{3}}{2}k_y a\right)\cos\left(\frac{3}{2}k_x a\right) \tag{1.7}$$

which is visualized in 3D in fig. 1.3 for $t = 2.8$ eV and $t' = 0.2t$, also showing the concept of Dirac fermions in Dirac cone described by eq. 1.5.

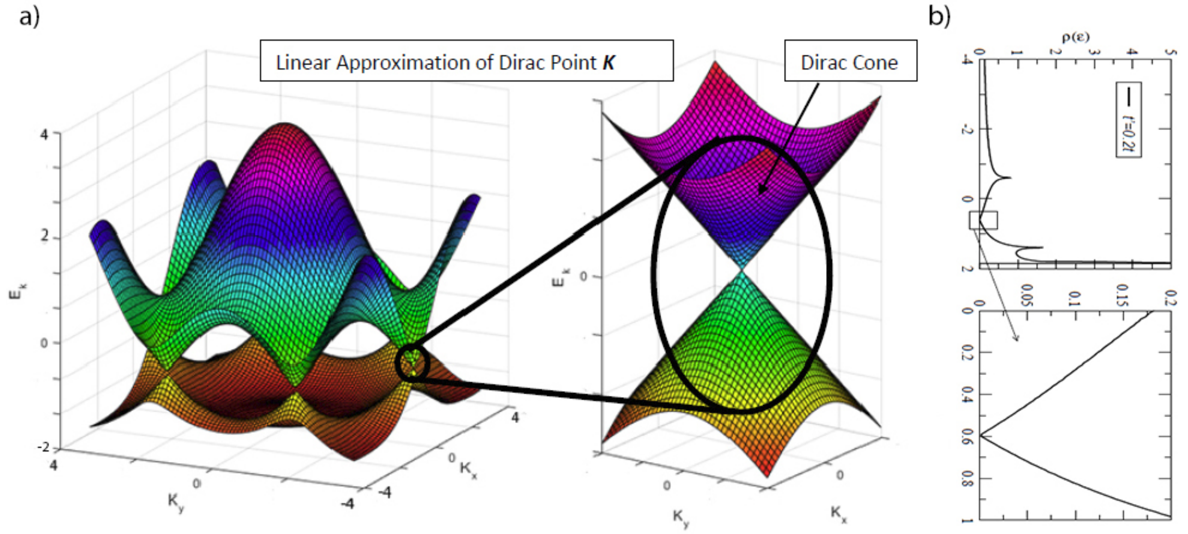

Figure 1.3: a) The 3D plot of π and π^* bands for $t' = 0.2t$ described by TB equation in eq. 1.6 and 1.7. b) The TB *Density of States* (DOS) around the Dirac point in graphene for $t' = 0.2t$, reprinted with permission from [1], Copyright (2009) by American Physical Society.

while fig. 1.4 illustrate the complete 2D band structure and the DOS of graphene, showing all 4 bands σ, σ^*, π, and π^*, calculated in DFT (using the Purdew Burke Erzerhof (PBE) XC-functional):

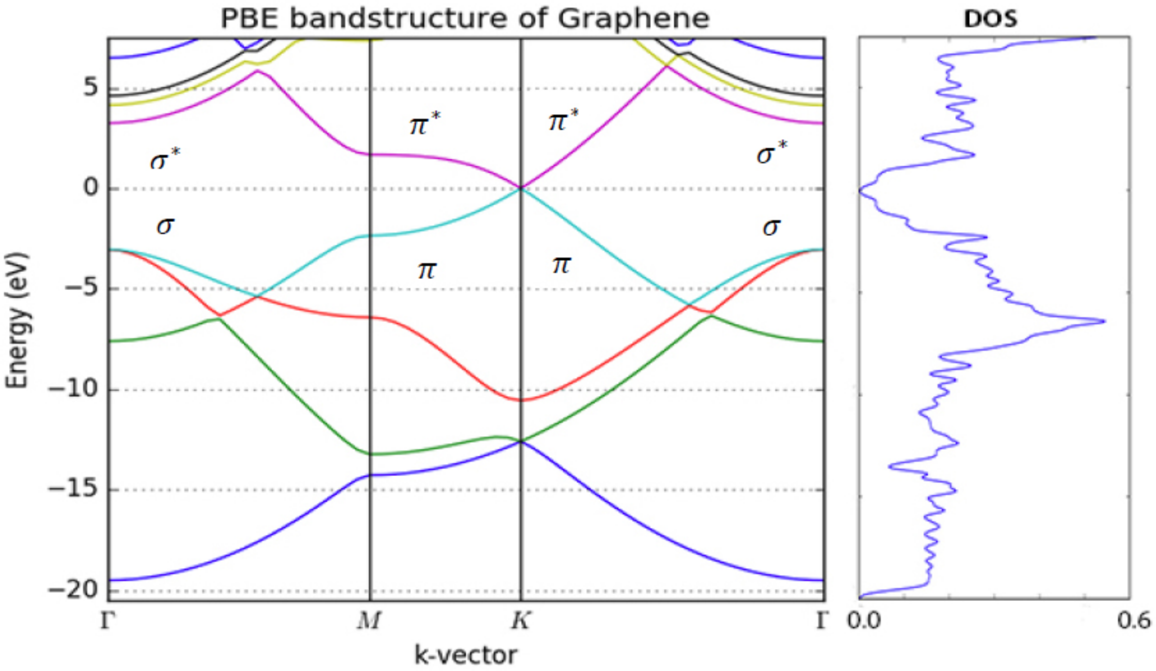

Figure 1.4: Left(c): The dispersion direction (band structure) in the graphene lattice including the Dirac point ($\boldsymbol{K}$). Right(d): The corresponding DOS in graphene.

At this point it is important that we discuss the effects of disorder and impurity on the electronic properties of graphene. These defects could be intrinsic like ripples and topological defects, or extrinsic like ad-atoms, vacancies, charges on top, and crack and edges. One type of disorder is the one that couples to single site energy, acting as a chemical potential shift for the fermions, causing a local shift in the Dirac point. The additional term to the Dirac Hamiltonian in eq. 1.3, resulting from this coupling, which is diagonal in sub-lattice indices could be written as:

$$H_{dd} = \sum_i V_i \left(a_i^\dagger a_i + b_i^\dagger b_i \right) \Rightarrow H_{dd} = \int d^2 r \sum_{a=1,2} V_a(\boldsymbol{r}) \hat{\Psi}_a^\dagger(\boldsymbol{r}) \hat{\Psi}_a(\boldsymbol{r}) \tag{1.8}$$

Where V_i is the strength of the impurity potential at site i (which could be a point impurity at some position within the lattice like a singe trivalent silicon within the graphene lattice). Note that this is not an interaction potential between the graphene sublattices (A/B sublattices), as this is already included in the nearest-neighbour transfer integral t. The charge potentials are also important for determining the transport and spectroscopic properties.

Especially the Coulomb impurity potential (and the 2D problem arising from it), and the coupling constant:

$$V_a(r) = \frac{e^2}{\epsilon_0} \frac{1}{r} \qquad\qquad g = \frac{Ze^2}{\epsilon_0 v_F} \tag{1.9}$$

where ϵ_0 is the dielectric constant of the medium, and Z is the charge impurity, can be studied analytically, and it resembles the case of the 3D relativistic Hydrogen problem. However, the form of the eigenfunctions are determined by graphene's dimensionless coupling constant. The significance of this constant is in the fact, that for $g > g_c = 1/2$, just like the 3D QED problem, the 2D problem of Coulomb impurity becomes unstable, leading to a super-critical behaviour, effecting the LDOS in such a way that bound states appear outside the band, while scattering resonance appear within the band. In the case of our research topic, we stury a kind of impurity that locally very much resembles a charge potential, inducing a Coulomb potential and charge density, consequently effecting the LDOS in a significant way as seeb in the STM images. However, due to the impurity/dopant atom (silicon) having the same number of valance electrons as the carbon, the analytical case of Coulomb impurity cannot be fully applicable to our case.

The second type of disorder, which changes the distance and angle between the p_z-orbitals, modifies the hopping energies leading to the following addition to the Hamiltonian, instead of eq. 1.8):

$$H_{od} = \sum_{i,j} \left\{ \delta_{ij}^{(ab)} \left(a_i^\dagger b_j + h.c. \right) + \delta_{ij}^{(aa)} \left(a_i^\dagger a_j + b_i^\dagger b_j \right) \right\} \tag{1.10}$$

where the deltas, $\delta t_{ij}^{(ab)}$ ($\delta t_{ij}^{(aa)}$), are the change of hopping energy between the orbitals on lattice sites R_i and R_j, while the indices a and b indicate different sub-lattices. If there is no Fourier component $K - K'$ in the Fourier representation of Hamiltonian, meaning that the Dirac cones are not coupled by disorder, then we can write the above Hamiltonian in real space as:

$$H_{od} = \int d^2r \left[\mathcal{A}(\boldsymbol{r}) a_1^\dagger(\boldsymbol{r}) b_1(\boldsymbol{r}) + h.c. + \phi(\boldsymbol{r}) \left(a_1^\dagger(\boldsymbol{r}) a_1(\boldsymbol{r}) + b_1^\dagger(\boldsymbol{r}) b_1(\boldsymbol{r}) \right) \right] \tag{1.11}$$

with:

$$\mathcal{A}(\boldsymbol{r}) = \sum_{\overrightarrow{\delta}_{ab}} \delta t^{(ab)}(\boldsymbol{r}) e^{-i \overrightarrow{\delta}_{ab}} \cdot \mathrm{K} \quad , \quad \phi(\boldsymbol{r}) = \sum_{\overrightarrow{\delta}_{ab}} \delta t^{(ab)}(\boldsymbol{r}) e^{-i \overrightarrow{\delta}_{ab}} \cdot \mathrm{K} \tag{1.12}$$

while for the other cone instead of $\mathcal{A}(\boldsymbol{r})$, $\mathcal{A}^*(\boldsymbol{r})$ is used ($\phi(\boldsymbol{r}) = \phi^*(\boldsymbol{r})$). Writing $\mathcal{A}(\boldsymbol{r})$ as a vector, due to lack of inversion symmetry for nearest neighbour hopping:

$$\overrightarrow{\mathcal{A}}(\boldsymbol{r}) = \mathcal{A}_x(\boldsymbol{r}) + i\mathcal{A}_y(\boldsymbol{r}) = (\mathcal{A}_x(\boldsymbol{r}), \mathcal{A}_y(\boldsymbol{r})) \tag{1.13}$$

Therefore we can rewrite the Dirac Hamiltonian in one cone as:

$$H_{od} = \int d^2r \left[\hat{\Psi}_1^\dagger(\boldsymbol{r}) \boldsymbol{\sigma} \cdot \overrightarrow{\mathcal{A}}(\boldsymbol{r}) \hat{\Psi}_1(\boldsymbol{r}) + \phi(\boldsymbol{r}) \hat{\Psi}_1^\dagger(\boldsymbol{r}) \hat{\Psi}_1(\boldsymbol{r}) \right] \tag{1.14}$$

The existence of the vector potential implies the presence of an effective magnetic field $\overrightarrow{B} = c/(ev_F)\nabla \times \overrightarrow{\mathcal{A}}$. The other Dirac cone is related to the first one by time reversal, as well as the effective magnetic field, which in the second cone is reversed.

The impurities within the lattice of graphene also have an effect on the electronic states within their vicinities. The Fermi energy due to the concentration n_i of impurities, is shifted $\simeq v_F \sqrt{n_i}$. The Dirac equation also has localized solutions satisfying man boundary condition, which if solved for circular defects, results in localized and semi-localized states. These states decay with $1/r$ as distance from the center of the defects. The Dirac equation of the two-component wave-function $\psi(\boldsymbol{r}) = (\phi_1(\boldsymbol{r}), \phi_2(\boldsymbol{r}))$ accordingly becomes:

$$\partial_w \phi_1(w, w^*) = 0 \quad , \quad \partial_{w^*} \phi_2(w, w^*) = 0 \tag{1.15}$$

with $w = x + iy$. The corresponding wave-functions for the given boundary condition have the following form:

$$\Psi_K(\tilde{\boldsymbol{r}}) \propto (1/(x+iy)^n, 0) \quad , \quad \Psi_{K'}(\tilde{\boldsymbol{r}}) \propto (0, 1/(x-iy)^n) \tag{1.16}$$

In addition to its electronic structure as described above, also the conductance and the transport properties of graphene are affected by disorder, especially doping and impurity, which as mentioned before, can result in localized and semi-localized states. At room temperatures, the conductivity of graphene can be explained in terms of the classical formalism. However, for lower temperatures as well as in the case of impurities and doping quantum corrections become important and interference effects also become visible, though many calculations demonstrate a conductivity of the order of $e^2/\hbar$, which is the universal value of conductivity when the Fermi energy is at the Dirac point. The lowest order perturbation theory in 2D graphene becomes the diffusion of electrons in a scattering medium given by the *Einstein relation* $\sigma_0 = e^2 D(E_F)\mathcal{D} = e^2/4\hbar$ (with diffusion coefficient $\mathcal{D} = v_F^2\tau/2$), where the impurities play the role of the scattering potentials.

The quantum corrections $\sigma = \sigma_0 + \delta\sigma$ are the results of Born approximation calculations of the impurity potentials. Since the interference effects are responsible for *Anderson* metal-insulator transitions, the main quantum mechanical correction term to the conductivity is believed to be due to weak localization. However currently in addition to the semi-classical *Kubo* formulation of the conductivity (beyond the *Drude* model), the *random phase approximation* (RPA) formulation of the self-consistent field-theoretic conductivity within linear response regime, plays an important role for determining the transport and electronic properties of graphene in presence of a disorder.

1.2 Plasmonics of Graphene

Plasmons are the quanta of the plasmonic oscillations; A quasi-particle of the normal mode oscillations resulting from long range Coulomb interaction within the lattice. Plasmons are also the zeros of the dynamical dielectric function [19]. The long-wavelength plasmon dispersion for mono-layer graphene (MLG) and (BLG) can be written as:

$$MLG : \omega_p(q \longrightarrow 0) = \left(\frac{e^2 v_F q}{\kappa\hbar}\sqrt{\pi n g_s g_v}\right)^{1/2} \qquad BLG : \omega_p(q \longrightarrow 0) = \left(\frac{2\pi n e^2}{\kappa m} q\right)^{1/2} \tag{1.17}$$

where $g_s g_v$ are the degeneracy factors and κ the dielectric constant. This is an example of a classical (BLG) vs. non-classical (MLG) dispersion relations, which in the case of MLG (which is the same as 2D pristine graphene), is a direct indication of the linear Dirac like energy momentum dispersion [19].

For pristine graphene, for which the Fermi energy is at the Dirac point, based on tight-binding approximation, there is only one excitation, namely the intraband transition from the completely filled π band to the completely empty π^* (conduction) band. The excitations can form a single particle excitations (SPE) region in (q, ω) space for wave-vectors of $q = k - K$ (with K as Dirac point) in the momentum space, where the spectral weights of the allowed excitations are given by $S(q,\omega) = -\frac{1}{\pi}\mathrm{Im}\left[\Pi(q,\omega)\right]$, with $\Pi(q,\omega)$ as the polarization function. In RPA this function is given by [20]:

$$\Pi(q,\omega) = -\frac{g_s g_v}{L^2}\sum_{kss'} \frac{f(\epsilon_{s\mathbf{k}}) - f(\epsilon_{s'\mathbf{k}'})}{\omega + \epsilon_{s\mathbf{k}} - \epsilon_{s'\mathbf{k}'} + i\eta} F_{ss'}(\mathbf{k}, \mathbf{k}') \tag{1.18}$$

where $\mathbf{k}' = \mathbf{k} + \mathbf{q}$, and $s, s' = \pm 1$ denote the band indices. Furthermore [58],

$$F_{ss'}(\mathbf{k}', \mathbf{k}) = (1 + ss'\cos\theta)/2 = |\langle \epsilon_{s\mathbf{k}}, \mathbf{k}| \mathrm{e}^{-i\mathbf{q}\cdot\mathbf{r}} |\epsilon_{s'\mathbf{k}'}, \mathbf{k}'\rangle|^2 \tag{1.19}$$

is the overlap of states, and $f(\epsilon_{s\mathbf{k}}) = [\exp\{\beta(\epsilon_{s\mathbf{k}} - \mu)\} + 1]^{-1}$ the Fermi-Dirac distribution. The effects of many-body interactions in graphene make the plasmonics very complicated and fascinating, since the plasmons in graphene can interact with many quasi-particle such as photons, phonons, and electrons.

Due to the fact that graphene is a 2D material, the theory and the dispersion of surface plasmons (SP's) are very important for graphene plasmonics. Here we discuss two models to describe the graphene plasmons, namely the semi-classical model and the RPA (*Random Phase Approximation*). Considering the fact that the dispersion relation of electrons in graphene are mostly linear, the charge carriers seem more like massless relativistic Dirac fermions, as expected. Therefore, the low energy conductivity of graphene consists of both intraband and interband contributions. Without considering the *Hall conductivity* ($\pm 2(2N+1)e^2/h$ [1]) the Kubo formulation for conductivity $\sigma(\omega, \mu, \Gamma, T)$ can be written as [10]:

$$-\frac{ie^2(\omega + i2\Gamma)}{\pi\hbar^2}\left[\frac{1}{(\omega + i2\Gamma)}\int_0^\infty E\left(\frac{\partial f(E)}{\partial E} - \frac{\partial f(-E)}{\partial E}\right)dE - \int_0^\infty \frac{f(-E) - f(E)}{(\omega + i2\Gamma)^2 - 4(E/\hbar)^2}dE\right] \tag{1.20}$$

with $f(E) = \{1 + \exp\left[(E - \mu)/k_B T\right]\}^{-1}$ as the same Dirac-Fermi distribution, and $2\Gamma = \tau^{-1}$ the electron relaxation time in graphene. As mentioned previously, the above expression can be split into two parts $\sigma = \sigma_{intra} + \sigma_{inter}$, where the two integrals are the contributions of the respective parts. The intraband part is given by [10]:

$$\sigma_{intra} = i\frac{e^2 k_B T}{\pi\hbar^2(\omega + i\tau^{-1})}\left[\frac{\mu}{k_B T} + 2\ln\left(e^{-\mu/k_B T} + 1\right)\right] \tag{1.21}$$

The chemical potential of pristine graphene, which is generally known to be $\mu \leq E_F$, is obtained from the carrier density:

$$n = \frac{2}{\pi\hbar^2 v_F^2}\int_0^\infty [f(E) - f(E + 2\mu)] \Rightarrow \mu \approx E_F\left[1 - \pi^2(k_B T/\mu)^2/12\right] \tag{1.22}$$

while for heavily doped or gated graphene $|\mu| \gg k_B T$, $\mu \approx E_F \approx \sqrt{\pi\hbar^2 v_F^2 n}$. In a gated graphene system, where n can be controlled by the gate voltage, for $T\mu \to 0$ we get the Drude form of the intra-band conductivity [65]:

$$\sigma_{intra} = \frac{in_s e^2 V^2}{(\omega + i0)\mu} = \frac{e^2 g_s g_v}{16\hbar}\frac{4i}{\pi\Omega} \tag{1.23}$$

where $\Omega = \hbar\omega/\mu$, and $n_s = g_s g_v \mu^2/4\pi\hbar^2 V^2$ is the carrier charge density at $T = 0$. For the same condition $|\mu| \gg k_B T$, the interband contribution is given by [10]:

$$\sigma_{inter} = \frac{e^2}{4\hbar}\left[\theta(\hbar\omega - 2|\mu|) + \frac{i}{\hbar}\ln|\frac{\hbar\omega - 2|\mu|}{\hbar\omega - 2|\mu|}|\right] \tag{1.24}$$

with $\theta(\hbar\omega - 2|\mu|)$ as the *Heaviside* step-function. Fig. 1.5, illustrates the separate contributions to the conductivity at zero-, and non-zero temperatures:

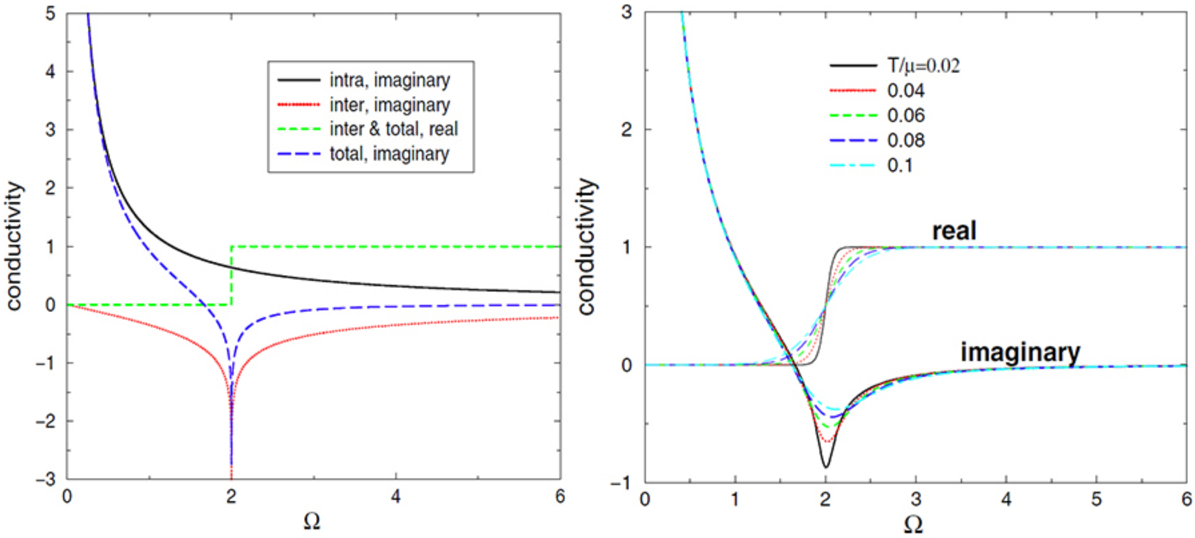

Figure 1.5: Imaginary and the real parts of the inra-, inter-band contributions to the conductivity at zero temperature (left), and at non-zero temperatures (right) as a function of $\Omega = \hbar\omega/\mu$. Reprinted with permission from [65], Copyright (2007) American Physical Society.

The total conductivity is therefore made up of two parts, the real and the imaginary, $\sigma = \sigma' + i\sigma''$, which determine which kind of (electromagnetic) EM surface waves that would be supported, since the two modes that can propagate in graphene are found to be TM (transverse electric, s-polarized) and TE (transverse magnetic, p-polarized). For $\sigma'' > 0$ ($\sigma'' < 0$), the TM (TE) are supported. Also for the same values the main contributions would result from intraband (interband) parts, while the frequency regions would be THz, far-infrared (far- and near-field). Using the Maxwell's equations and the *Dyadic Green's function*, and for the given medium-interface with the permeability and dielectric constants (μ_r, ε_r), and (μ_r', ε_r') (it is assumed that the graphene is trapped between two medium along the z-axis), the dispersion relations of these modes can be calculated . For the TM modes therefore we have [10]:

$$\frac{\varepsilon_r}{\sqrt{k_{TM}^2-(\varepsilon_r\omega^2/c^2)}}+\frac{\varepsilon_r'}{\sqrt{k_{TM}^2-(\varepsilon_r'\omega^2/c^2)}}+\frac{i\sigma}{\omega\varepsilon_0}=0 \tag{1.25}$$

with $\varepsilon_r' = \varepsilon_r' = 1$ for a isolated graphene, resulting in the dispersion relation for the TM mode: $k_{TM} = k_0\sqrt{1-(2/\sigma\eta_0)^2}$, with $\eta_0 = \sqrt{\mu_0/\varepsilon_0} \approx 377\Omega$.

For a highly doped graphene of thickness Δ, the effective dielectric constant would be $\varepsilon = \varepsilon_0 + i\sigma/\omega\Delta$. Furthermore, for the same highly doped graphene on substrate, $(\varepsilon_r' = 1, \varepsilon_r \neq 1)$, the TM mode dominates, as well as the intraband contribution in the conductivity. Having the following limits for the chemical potential $\mu \approx E_F$ and $|\mu| \gg k_BT$, the following expression are the approximate dispersion relations for the surface plasmons [10]:

$$k_{SP} \approx \frac{\pi\hbar^2}{e^2E_F}\varepsilon_0(\varepsilon_r+1)\omega\left(\omega+\frac{i}{\tau}\right) \quad , \quad \lambda_{SP} \approx \lambda_0\alpha\frac{4E_F}{\varepsilon_r+1}\frac{1}{\hbar(\omega+i\tau^{-1})} \tag{1.26}$$

with $\alpha = e^2/4\pi\varepsilon_0\hbar c$ is the fine-structure constant.

The RPA model of the dispersion is more complicated, due to the fact that that the electrons at the Dirac points interact heavily with the plasmons, making their experimental spectrum different that the theoretical predictions of the RPA model. However, at zero temperature, in the limit of $q \to 0$ (and for $\varepsilon(\omega, q) = 0$), under the assumption of infinite relaxation time of the electrons, this model can predict well the dispersion and the spectrum of the graphene plasmons within the self-consistent field linear response theory formalism. In this model the electrons move in the self-consistent field composed of an external field and the induced field of all of the electrons.

Even though the approximate relation for the RPA dispersion could be given without the definition of the RPA conductivity, it is important to mention the path to the derivation of the approximate relation (eq. 1.17) starting from the RPA conductivity. Recalling the RPA polarization function $\Pi(q, \omega)$ (eq. 1.18), by defining the electron scattering rate at the Fermi energy $\tau(E_F)^{-1}$ and $\omega_\gamma = \omega + i\tau(E_F)^{-1}$, in order to account for the electron conservation [21], taking into account the scattering, we can redefine the polarization function as:

$$\Pi_\gamma(q, \omega) = \frac{\omega_\gamma}{\omega \Pi(q, \omega)^{-1} + i\tau^{-1}(E_F)\Pi(q, 0)^{-1}} \tag{1.27}$$

which is called the RPA relaxation time approximation taking into account the finite scattering rate, while the $\Pi(q, 0)$ is obtained by setting $\tau(E_F)^{-1}$ and ω to zero. Then the RPA-RT (RPA relaxation time) conductivity is given by [21]:

$$\sigma_{\mathrm{RPA}}(q, \omega) = -i\omega \frac{e^2}{q^2} \Pi_\gamma(q, \omega) \tag{1.28}$$

If we then consider a graphene sample placed between the air and a substrate of constant permittivity ε_{sub}, the dispersion relation is the solution of the following equation:

$$\varepsilon_{ave} + i\frac{q}{2\omega}\sigma_{RPA}(q, \omega) = 0 \quad , \quad \varepsilon_{ave} = (\varepsilon_{sub} + \varepsilon_0)/2 \tag{1.29}$$

re-arranging the above equation in this form $\varepsilon(q, \omega) = 1 - v(q)\Pi_\gamma(q, \omega)$, we can then use the following approximation for the polarization function [20]:

$$\Pi(q, \omega) \approx \left\{ \begin{array}{l} \dfrac{D_0 \gamma^2 q^2}{2\omega^2} \left[1 - \dfrac{\omega^2}{4E_F^2} \right], \gamma q < \omega < 2E_F \\ D_0 \left[1 + i\dfrac{\omega}{\gamma q} \right], \omega < \gamma q \end{array} \right\} \tag{1.30}$$

Using these approximations, for the single layer graphene the dispersion relation could be written as:

$$\omega_{SP}(q \to 0) = \omega_0 \sqrt{q} \quad , \quad \omega_0 = (g_s g_v e^2 E_F / 2\kappa)^{1/2} \tag{1.31}$$

with κ as the background lattice dielectric constant, and $g_s = 2$, $g_v = 2$ the spin and the valley degeneracy. One can see that the density dependence of the plasmon in monolayer graphene $\omega_0 \propto n^{1/4}$ shows a different behaviour than the classical 2D plasmons $\omega_0 \propto n^{1/2}$.

Since there are two kinds of electrons in graphene, namely the σ, and the π, there are two other kinds of plasmons, in addition to the low energy (≤ 3 eV) 2D plasmons, namely the π and the $\sigma + \pi$, which appear in pristine graphene at energies of ~ 4.7 eV , and 14.6 eV. The 2D plasmons on the other hand appear in doped graphene. The best way to probe the plasmons in graphene experimentally is by EELS. Fig. 1.6 shows the EELS spectrum of pristine graphene for different q-limits against that of multi-layer stacked graphene (graphite), illustrating the difference between the plasmons in graphite, and the non-classical surface plasmons of graphene, which rapidly disappear for large momenta.

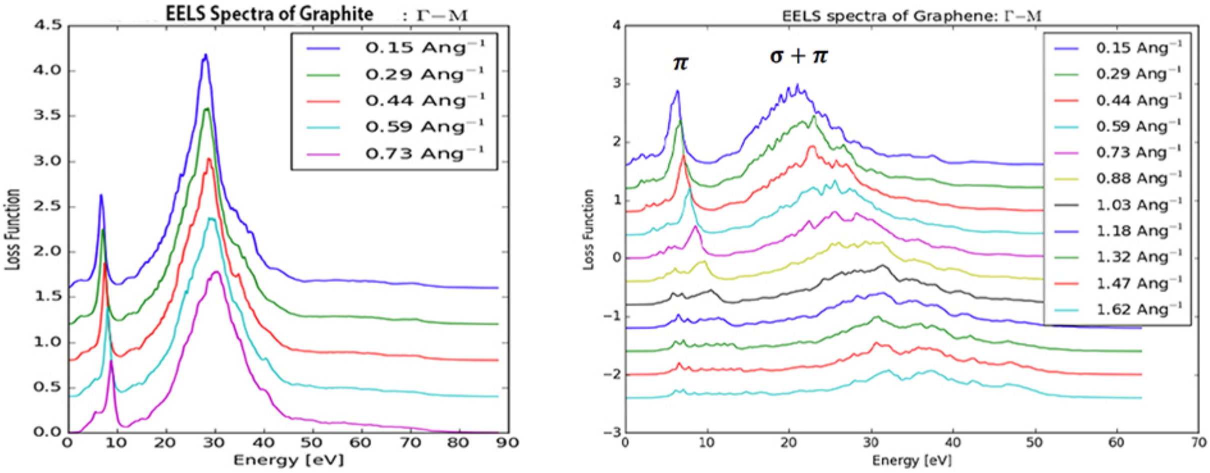

Figure 1.6: Left: The graphite (multi-layer graphene stacking) EELS spectrum for different (increasing) momentum vectors (q's). Right: The EELS spectrum of graphene for different Increasing) q's, showing the π and $\sigma + \pi$ plasmons.

1.3 Quantum Confinement in Graphene

Finally it is important, to talk about the theoretical concepts and the experiments of quantum confinement in graphene or graphene based materials, because one of the goals in this thesis is a direct simulation of quantum confinement and possibly creating the quantum corrals on the graphene lattice, while using silicon atoms only as the static potential. Even though the concept of quantum corrals have been almost exclusively limited to the case of ad-atoms on the metallic surfaces, there have been experiments arising from the principles of localization of the Dirac Fermions in graphene, which are more in line with general cases of quantum confinement in semiconductors.

The charge carriers in graphene, as are the surface charge carries of topological insulators, are 2D relativistic Dirac fermions. Using these carries, it is possible to show the formation of the confined states and corrals due to the presence of the impurity-potential. Starting from the massless Dirac Hamiltonian [15]:

$$H = v_F(\boldsymbol{k} \times \boldsymbol{\sigma}) \cdot \hat{z} + \sum_{i=1}^{N} V_i(\boldsymbol{r}) \tag{1.32}$$

with $\boldsymbol{k} = (k_x, k_y)$ as the planar momentum, $\boldsymbol{\sigma} = (\sigma_x, \sigma_y, \sigma_z)$ as the Pauli matrices, and i the index-number of the impurities. If we set the Fermi velocity and lattice constant to unity $v_F = a_a = 1$, then we can write the impurity potential as:

$$V_i(\boldsymbol{r}) = (U_i\sigma_0 + \frac{1}{2}\boldsymbol{J}_i\boldsymbol{S} \cdot \boldsymbol{\sigma})\delta(\boldsymbol{r} - \boldsymbol{r}_i) \tag{1.33}$$

where U_i is the potential (magnetic) scattering strength, with the following definition that $U_i(J_i = 0)/J_i(U_i = 0)$ would denote the scalar/magnetic impurities, and S the spin of the impurity. Then a quantum interference effects will take place which is the result of the interaction between the STM tip and the sample surface, which would be observed in the measurement of the LDOS. In the next section we will talk about the theory of quantum corrals in relation to the STM application theory, but for now we mention the formalism in a non-rigorous way.

In the STM measurement of such systems as described above, The LDOS would be proportional by the imaginary part of the trace of the electron Green function:

$$\mathrm{LDOS}(r,E) \equiv -\frac{1}{\pi}\mathrm{Im}\left\{\mathrm{Tr}\left[G(r,r,E)\right]\right\} \tag{1.34}$$

while the Green function is defined as:

$$G(r,r',E) = G_0(r,r',E) + \sum_{i,j=1}^{N} G_0(r,r_i,E)\cdot T(r_i,r_j,E)G_0(r_j,r',E) \tag{1.35}$$

The form of the $T(r_i,r_j,E)$ matrix ($\mathcal{T}$) is a bit strange, as it is defined for numerical calculations. Starting from the expression:

$$T(r_i,r_j,E) = V_i\delta_{i,j} + V_i\sum_{l=1}^{N} G_0(r_i,r_l,E)T(r_l,r_j,E) \tag{1.36}$$

The final expression for the T matrix would be:

$$\mathcal{T} = \frac{\mathcal{H}_{imp}}{\mathcal{I} - \mathcal{H}_{imp}G_0} = \mathcal{H}_{imp} + \mathcal{H}_{imp}G_0\mathcal{T} \tag{1.37}$$

where $\mathcal{H}_{imp}$, $\mathcal{G}_0$, and G_0 are each separate matrices, in addition to $\mathcal{I}$, which is the identity. The impurity Hamiltonian is a diagonal matrix given by $\mathcal{H}_{imp} = diag(V_1, V_2, ..., V_N)$, and the unperturbed Green's function is given by the Fourier transformation of the following:

$$G_0(\boldsymbol{k},i,E) = \left[i\boldsymbol{E} - v_F(\boldsymbol{k}\times\boldsymbol{\sigma})\cdot\hat{z}\right]^{-1} \tag{1.38}$$

or for numerical calculations as:

$$G(r,r',E) = G_0(r,r',E) + \mathcal{G}_0\mathcal{T}\mathcal{G}_0' \tag{1.39}$$

The $\mathcal{G}_0'$, and $\mathcal{G}_0$ are single column and single row matrices, each with $2\times 2N$ entries, where the elements are arranged in the following way:

$$\begin{aligned}\mathcal{G}_0 &= \left(G(r,r_1,E)......G(r,r_N,E)\right)\\ \mathcal{G}_0' &= \left(G(r_1,r',E)......G(r_N,r',E)\right)^T\end{aligned} \tag{1.40}$$

These matrices, which together could be compacted into the G_0 matrix, denote the propagation of the electrons to the impurities from the STM tip and vice versa. Fig. 1.7 shows the LDOS measurements in a non-magnetic corral of 80 ad-atoms with a radius of $R_0 = 50\text{Å}$, at different positions showing a resonance at the Dirac level for large enough potential. For a barrier potential of small value the LDOS (in red dots) doesn't show any fluctionations, which are the result of confinement, but once the barrier potential is big enough, both at the center and $r = (25,0)$ we see resonances (as seen in the fig. 1.7).

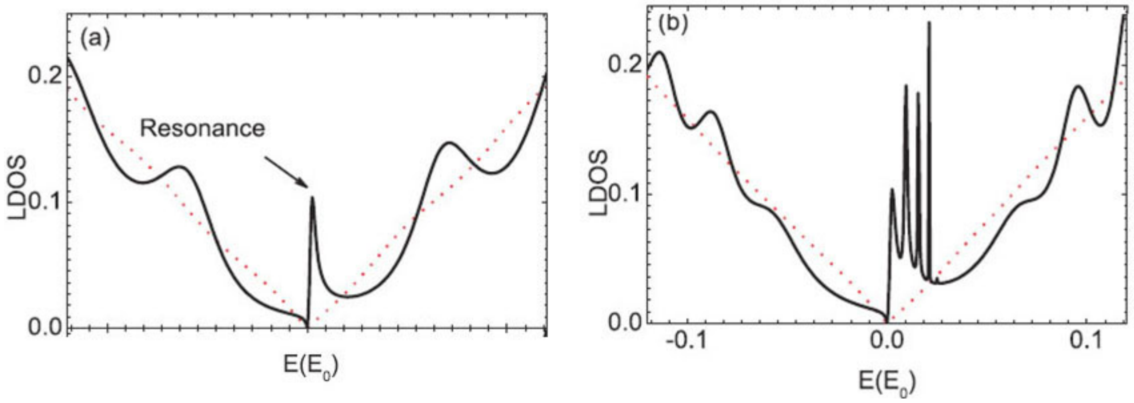

Figure 1.7: The resonance at the Dirac level in the center (left) of the 80 ad-atom corral, and at position $r = (25, 0)$ (right) in a STM experiment for a small (red dots) and large enough potentials. Reprinted with permission from [15], Copyright (2011) American Physical Society.

Chapter 2

Theory & Methods

2.1 Structural Optimizations & Basic DFT

2.1.1 Analytical Tersoff 1989 (T89) Potential

One of the most important analytical inter-atomic potentials used in different classical MD codes is the empirical inter-atomic bond-order potential created by *J.Tersoff*. This potential applied to three-body systems of silicon and carbon, in codes such as LAMMPS and Atomistica, is one of the potentials that we originally used for the calculations of Si-C systems, in the form of silicon doping of graphene. Many physical and chemical problem require the calculation of the total energy as the function of the atomic coordinates. The problem is constructing a potential beyond quantum mechanics, that is computationally not too expensive, and that can give the total energy of the system as the function of the atomic coordinates $E(\{r\})$.

Among other approaches, the approach of *Biswas and Hamann* [35] opened a new door for describing covalent semiconductors like silicon. They argued that [35] the ″...cohesive energies of many real and the hypothetical arrangement of silicon is known from reliable quantum mechanical calculations.″ Therefore, such information may be used as database for an initial attempt of constructing an interatomic potential which correctly describes the cohesive energy over a wide range of atomic coordinates and bondings geometry. In particular this argument was the foundation for the construction of the new model known as the *bond order potential*. The approach of Biswas and Hamann implies that a 3-body potential does not adequately describe the cohesive bonds of silicon over a long range, and many-body potentials like 4-body and 5-body would have too many free parameters. Therefore this N-body potential approach has to be abandoned altogether.

The trend that emerges for the bond-order potential, is that of a monotonically decreasing function of coordination. The balancing factors are the trade off between bond-order and number of bonds, which together determine the equilibrium coordination. For many elements of periodic table, one of above factors would dominate, and only a few elements would have an intermediate coordination. A suitable inter-atomic potential can be constructed with the following form:

$$E = \sum_i E_i = \frac{1}{2}\sum_{i \neq j} V_{ij} \qquad , \qquad V_{ij} = f_C(r_{ij})\left[a_{ij} f_R(r_{ij}) + b_{ij} f_A(r_{ij})\right] \tag{2.1}$$

where E is the total energy, E_i the site energy and V_{ij} the bond energy. The functions f_R and f_A represent repulsive and attractive part potentials as the functions of r_{ij} the atomic distance between the atoms i and j, while f_C is the cut-off function, limiting the range of the potential, in order to reduce the computational burden. The most important parts of the above potential, is the b_{ij} function, which represents the bond-order measure. The determination of these functions are not trivial, but it is in general assumed that b_{ij} is a monotonically decreasing function of coordination of atoms i and j. However, a_{ij} is merely a range limiting function.

In determining the exact form of the above functions, the choice of exponential functions for f_R and f_A has a very desirable feature [35]:

$$f_R(r) = A \cdot \exp(-\lambda_1 r) \quad , \quad f_R(r) = -B \cdot \exp(-\lambda_2 r) \tag{2.2}$$

and for the cut-off function:

$$f_C(r) = \begin{Bmatrix} 1 & , r < R - D \\ \frac{1}{2} - \frac{1}{2}\sin\left[\frac{\pi}{2}(r-R)/D\right] & , R - D < r < R + D \\ 0 & , r > R + D \end{Bmatrix} \tag{2.3}$$

which is a short range, continuous and differentiable function for all r, going from 1 to 0, covering the first-neighbour shell in most structures. And finally the bond-order function b_{ij} as described above is given by:

$$\begin{aligned} b_{ij} &= (1 + \beta^n \xi_{ij}^n)^{-1/2n} \\ \xi_{ij} &= \sum_{k \neq i,j} f_C(r_{ik}) g(\theta_{ijk}) \exp[\lambda_3^3 (r_{ij} - r_{ik})^3], \\ g(\theta) &= 1 + c^2/d^2 - c^2/[d^2 + (h - \cos\theta)^2], \end{aligned} \tag{2.4}$$

with θ_{ijk} as the angle between the bonds ij and ik, $c/d/h$ as the normal constants, and $\lambda_{1/2/3}$ as the Morse-type potential constants. Additionally the form for a_{ij}:

$$a_{ij} = (1 + \alpha^n \eta_{ij})^{-1/2n} \quad , \quad \eta_{ij} = \sum_{k \neq i,j} f_C(r_{ik}) \exp[\lambda_3^3 (r_{ij} - r_{ik})^3], \tag{2.5}$$

where α is chosen so small so that $a_{ij} \simeq 1$, for atoms outside the first-neighbour shell. The a_{ij} is used for completeness, for improvement of the potential, but it is mostly set equal to 1.

This set of suggested potential form can be used for a variety of elements. The free parameters can be set to reproduce a large database of known properties of materials.

2.1.2 Analytical Erhard Albe Potential

As we saw in the previous section, the importance of the bond-order potential, which in general form was applicable to a variety of elements, was due to the fact that the previous models could not describe the cohesive energy of the semiconductors accurately enough, in particular silicon and hybrid compounds of silicon. However, this effort seems to be an understatement, if we are to, by having used such extra-accurate potentials, make a statement about the importance of the semiconductor materials and the simulations of their properties. Among them silicon-carbide holds a special place due to the combination of the its mechanical and electronic properties.

As stated, the bond-order potential by Tersoff is widely known as one of the most accurate and effective potentials for describing systems of moderate size. However, this potential along with its modified versions are not so useful, if the simulation requires a more extensive smapling of the configuration space [34]. Therefore, a more robust and accurate model based on the previous Tersoff potential is proposed, where a new set of parameters for interactions $Si - Si$, $C - C$, and $Si - C$ are proposed. This new potential, which fall within the *Brenner*-class potentials (due to their use of the Brenner-functional), is known as the *Erhard-Albe* silicon-carbide analytical potential [34].

The functional that is introduced has been applied to metals and metal-carbides successfully, in addition to having used for the description of semiconductors. The cohesive energy as a sum over the bond energies is given by:

$$E = \sum_{i>j} f_C(r_{ij}) \left[V_R(r_{ij}) - \underbrace{\frac{b_{ij} + b_{ji}}{2}}_{\overline{b_{ij}}} V_A(r_{ij}) \right] \tag{2.6}$$

where $V_R(r)$ and $V_A(r)$ are the repulsive and the attractive pair-wise potentials defined as below:

$$V_R(r) = \frac{D_0}{S-1} \exp\left[-\beta\sqrt{2S}(r - r_0)\right] \quad , \quad V_A(r) = \frac{SD_0}{S-1} \exp\left[-\beta\sqrt{2/S}(r - r_0)\right] \tag{2.7}$$

with D_0 and β as the dimer energy and parameter of the dimer ground state oscillation, and r_0 the bond length. The S is obtained from the slope of the *Pauling plot*, and the cut-off function $f_C(r)$ is exactly as defined in eq. 2.4. The fit known as the Pauling plot is the fit used to approximate the results obtained from the quantum mechanical or first principles calculations.

The bond-order function b_{ij} which we introduces in the previous section also takes a similar form as in the Tersoff potential:

$$b_{ij} = (1 + \chi_{ij})^{-1/2} \quad , \quad \chi_{ij} = \sum_{k \neq i,j} f_C(r_{ik}) g(\theta_{ijk}) \exp[2\mu(r_{ij} - r_{ik})] \tag{2.8}$$

only with the function χ_{ij} slightly different, while the angular function $g(\theta)$ is also exactly the same. The nine parameters 2μ, γ, c, d and h determine the three-body interaction, based on atom types i and j. The parameter adjustment which leads to the optimization of the potential is done in the following way, first the dimer pair-parameter are adjusted (D_0, r_0, β), and then from the Pauling slope the S. Then the three-body interaction parameters are adjusted by fitting to the cohesive energies and bond lengths of highly symmetric structures, and to the elastic constants of ground structures. For silicon dimer some of the above parameters, such as (D_0, r_0, β) are known experimentally, where D_0 is the dimer binding energy, r_0 the equilibrium bonding distance, and β the potential parameter related to the ground-state oscillation wave number k.

2.1.3 Kohn-Sham Equations, PW's, FD, PAW, LCAO

Density functional theory, which is basically the theory of the electronic structure of solids based on *first principles* (many-body quantum mechanics), as it had originally been developed in 60's and the 70's, has evolved much in the recent decades and recent years. If we start from the foundation of the DFT and *Hohenberg-Kohn* (HK) theorems, it will be a long path before we reach the theory of the variation of the DFT-code which we have used in this work, known as GPAW. Therefore we start from the basic core of the DFT, the eigenvalue *Kohn-Sham* equation, the Kohn-Sham variational method to the self consistence loop, and then we develop the theory into the *projector augmented-wave* method (PAW), grid-decomposition of the PAW method (FD, for finite difference), and the *linear combination of the atomic orbitals* (LCAO) method. The original Kohn-Sham scheme, was rewriting the previous many-body problem in terms of an auxiliary system of an independent particles and interacting density, which proved to be very successful approximation.

Two assumptions are made in the Kohn-Sham scheme, which we need to mention before illustrating the scheme [13]:1- The ground state density can be represented by the ground state density of the non-interacting auxiliary system. 2- The Hamiltonian of the auxiliary system has a usual kinetic operator and a much simplified effective local potential acting on the electron of spin σ and coordinates $\mathbf{r}$, $V^{\sigma}_{eff}(\mathbf{r})$. This potential which is usually the characteristic of the Kohn-Sham scheme, has to be spin-dependent, except in the case of spin-symmetry. Based on these assumptions The schematic Kohn-Sham *Ansatz*, which is the relationship between the independent particle Kohn-Sham system and the full many-body problem, is as follows [13]:

$$\begin{tikzcd}
V_{ext} \arrow[d] & n_0(\mathbf{r}) \arrow[l, "\text{HK}"'] \arrow[r, leftrightarrow, "\text{KS}"] & n_0(\mathbf{r}) \arrow[r, "\text{HK}_0"] & V_{KS}(\mathbf{r}) \arrow[d] \\
\Psi_i(\{\mathbf{r}\}) & \Psi_i(\{\mathbf{r}\}) \arrow[l] \arrow[u] & \psi_{i=1,N_e}(\mathbf{r}) \arrow[u] & \psi_i(\mathbf{r}) \arrow[l]
\end{tikzcd} \tag{2.9}$$

where HK_0 denotes the Hohenberg-Kohn theorem of non-interacting problem. Using the *Hartee* atomic unites $\hbar = m_e = e = 4\pi/\epsilon_0$, the auxiliary Hamiltonian is defined as:

$$H^{\sigma}_{aux} = -\frac{1}{2}\nabla^2 + V^{\sigma}(\mathbf{r}) \tag{2.10}$$

The Kohn-Sham energy functional of the ground state density is given by:

$$E_{KS} = T_s[n] + \int \mathrm{d}\mathbf{r} V_{ext}(\mathbf{r}) n(\mathbf{r}) + E_{Hartree}[n] + E_{II} + E_{xc}[n] \tag{2.11}$$

where the kinetic energy $T_s[n]$ is defined as:

$$T_s = -\frac{1}{2}\sum_{\sigma}\sum_{i=1}^{N^{\sigma}} \langle \psi^{\sigma}_i | \nabla^2 | \psi^{\sigma}_i \rangle = \frac{1}{2}\sum_{\sigma}\sum_{i=1}^{N^{\sigma}} \int \mathrm{d}^3 r |\nabla \psi^{\sigma}_i(\mathbf{r})|^2 \tag{2.12}$$

and the density of the auxiliary system:

$$n(\mathbf{r}) = \sum_{\sigma} s(\mathbf{r}, \sigma) = \sum_{\sigma}\sum_{i=1}^{N^{\sigma}} |\psi^{\sigma}_i(\mathbf{r})|^2 \tag{2.13}$$

As for the potentials, the $V_{ext}(\mathbf{r})$ is the spin-independent potential due to external fields and the nuclei, and E_{II} the nuclei-interaction term. The remaining terms have to include the classical Coulomb term, and the many-body *exchange-correlation* terms (XC). The Hartee term $E_{Hartree}[n]$:

$$E_{Hartree}[n] = \frac{1}{2}\int \mathrm{d}^3 r \mathrm{d}^3 r' \frac{n(\mathbf{r}) n(\mathbf{r}')}{|\mathbf{r} - \mathbf{r}'|} \tag{2.14}$$

replaces the Coulomb potential with interacting electron-density potential, and the XC-term:

$$E_{xc}[n] = F_{HK}[n] - (T_s[n] + E_{Hartree}[n]) = \langle \hat{T} \rangle - T_s[n] + \langle \hat{V}_{int} \rangle - E_{Hartree}[n] \tag{2.15}$$

However, the XC-term, under the consideration of the *exchange-correlation hole* concept, which states, that the XC-term keeps electrons apart and therefore gives rise to encountering a hole at $\mathbf{r'}$, can be written like the Hartree term:

$$E_{xc}[n] = \frac{e^2}{2} \int d^3r \int d^3r' \frac{n(\mathbf{r}) n_{xc}(\mathbf{r}, \mathbf{r'})}{|\mathbf{r} - \mathbf{r'}|} \tag{2.16}$$

In order to solve the above energy functional for the ground state density and then the energy eigenvalues, the Kohn-Sham variational must be applied:

$$\frac{\delta E_{KS}}{\delta \psi_i^{\sigma *}(\mathbf{r})} = \frac{\delta T_s}{\delta \psi_i^{\sigma *}(\mathbf{r})} + \left[\frac{\delta E_{ext}}{\delta n(\mathbf{r}, \sigma)} + \frac{\delta E_{Hartree}}{\delta n(\mathbf{r}, \sigma)} + \frac{\delta E_{xc}}{\delta n(\mathbf{r}, \sigma)} \right] \frac{\delta n(\mathbf{r}}{\delta \psi_i^{\sigma *}(\mathbf{r})} = 0 \tag{2.17}$$

with the orthogonalization condition of $\langle \psi_i^{\sigma} | \psi_j^{\sigma'} \rangle = \delta_{i,j} \delta_{\sigma, \sigma'}$. Reforming the above equation and using the definition of the effective potential V_{eff}^{σ} from (2.32) of the auxiliary Hamiltonian, we can write:

$$\frac{\delta E_{KS}[n]}{\delta n(\mathbf{r}, \sigma)} = \frac{\delta T_s[n]}{\delta n(\mathbf{r}, \sigma)} + \frac{\delta V_{eff}[n]}{\delta n(\mathbf{r}, \sigma)} \tag{2.18}$$

Therefore:

$$\frac{\delta V_{eff}[n]}{\delta n(\mathbf{r}, \sigma)} = \left[\frac{\delta E_{ext}}{\delta n(\mathbf{r}, \sigma)} + \frac{\delta E_{Hartree}}{\delta n(\mathbf{r}, \sigma)} + \frac{\delta E_{xc}}{\delta n(\mathbf{r}, \sigma)} \right] \tag{2.19}$$

and:

$$V_{eff}^{\sigma}(\mathbf{r})|_{min} = V_{KS}^{\sigma}(\mathbf{r}) = V_{ext}(\mathbf{r}) + V_{Hartree}(\mathbf{r}) + V_{xc}^{\sigma}(\mathbf{r}) \tag{2.20}$$

With the the auxiliary Hamiltonian and the Kohn-Sham Hamiltonian become fully identical under the above definition for the effective potential:

$$H_{aux}^{\sigma} = H_{KS}^{\sigma} = -\frac{1}{2} \nabla^2 + V_{KS}^{\sigma}(\mathbf{r}) \tag{2.21}$$

And so having clearly defined the Kohn-Sham Hamiltonian, we can now set out to solve the Kohn-Sham eigenvalue problem:

$$\left(H_{KS}^{\sigma} - \varepsilon_i^{\sigma} \right) \psi_i^{\sigma}(\mathbf{r}) = 0 \tag{2.22}$$

This is a fundamental stage from which all the new procedures and variations of this basic theory branch out. There are multiple different strategies to solve the above eigenvalue problem, as there a varieties of definitions for the given potentials. For example the used wave-functions could be a grid (mesh) or plane-wave, or *linearised augmented plane wave* (LAPW), and XC-term could be GGA, or LDA or LSDA (see the abbreviations list). The kinetic operator could be relativistic or non-relativistic, and there is even the possibility of inclusion of time variable, which would eventually bring us to one of the most important variations of the DFT, that we have also extensively used in this thesis, namely the time-dependant DFT (TDDFT). The below figure lists some of these variations. However, regardless of the all these options for solving and modifying the Kohn-Sham equation, one mathematical principle remains at the heart, and that is the self-consistence. No matter what definitions are used for any of the terms in eq. 2.15, the resulting density must be self-consistent. The flow chart in fig. 2.1 illustrates this principle (i.e. the SCF loop) [13]:

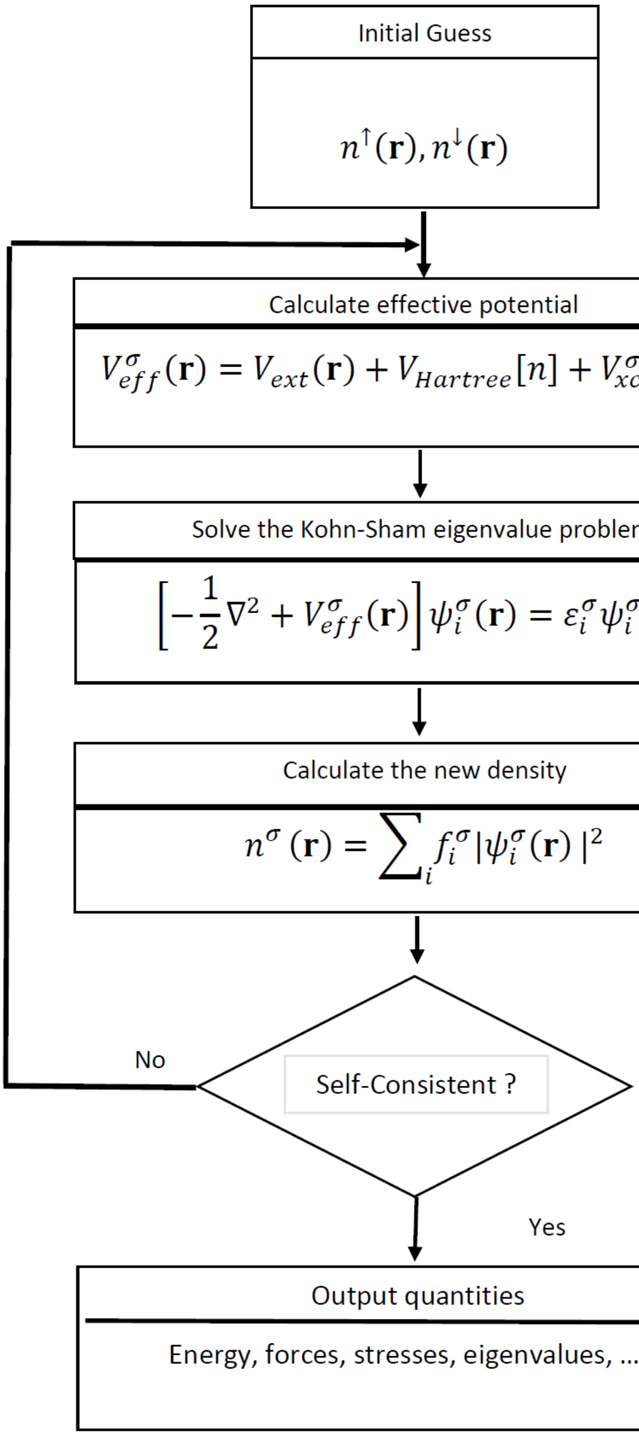

Figure 2.1: The chart of the *self consistence field* (SCF) loop of the Kohn-Sham equation, represented in a step by step form, which in case of consistency results in all the desired output quantities [13].

Having introduced the set of strategies for solving the Kohn-Sham equations, the actual solutions, as mentioned previously, depends on a set of definitions used for each component of the equations. For example, we start with defining an expression for the wavefuctions from which the densities are calculated. Starting from the Kohn-Sham eigenvalue equation:

$$\hat{H}_{eff}(\mathbf{r})\psi_i(\mathbf{r}) = \left[-\frac{1}{2}\nabla^2 + V_{eff}(\mathbf{r})\right]\psi_i(\mathbf{r}) = \varepsilon_i\psi_i(\mathbf{r}) \tag{2.23}$$

we then expand the wave-functions into a set of orthonormal plane-waves :

$$\psi_i(\mathbf{r}) = \sum_q c_{i,\mathbf{q}} \times \frac{1}{\sqrt{\omega}} \exp(i\mathbf{q}\cdot\mathbf{r}) \equiv \sum_{\mathbf{q}} c_{i,\mathbf{q}} \times |\mathbf{q}\rangle \tag{2.24}$$

with the sets satisfying the ortho-normalization condition:

$$\langle\mathbf{q}'|\mathbf{q}\rangle \equiv \frac{1}{\Omega}\int_\Omega \mathrm{d}\mathbf{r} \;\; \exp(-i\mathbf{q}'\cdot\mathbf{r})\exp(-i\mathbf{q}\cdot\mathbf{r}) = \delta_{\mathbf{q},\mathbf{q}'} \tag{2.25}$$

Using this plane-wave ansatz results in a new set of expressions by applying the Hamiltonian of the system. For example the kinetic energy term becomes: $\langle\mathbf{q}'| - \nabla^2|\mathbf{q}\rangle = \frac{1}{2}|q|^2\delta_{\mathbf{q},\mathbf{q}'}$ while the effective potential can be Fourier decomposed in the following way:

$$V_{eff}(\mathbf{r}) = \sum_m V_{eff}(\mathbf{G}_m)\exp(i\mathbf{G}_m\cdot\mathbf{r}) \;\; , \;\; V_{eff}(\mathbf{G}) = \frac{1}{\Omega_{cell}}\int_{\Omega_{cell}} V_{eff}(\mathbf{r})\exp(-i\mathbf{G}\cdot\mathbf{r})\mathrm{d}\mathbf{r} \tag{2.26}$$

so that it could be written as: $\langle\mathbf{q}'|V_{eff}|\mathbf{q}\rangle = \sum_m V_{eff}(\mathbf{G}_m)\delta_{\mathbf{q}'-\mathbf{q},\mathbf{G}_m}$. If we define $\mathbf{q} = \mathbf{k} + \mathbf{G}_m$, and $\mathbf{q}' = \mathbf{k} + \mathbf{G}_{m'}$, the expectation value of the Hamiltonian can be written as the following diagonal matrix:

$$\sum_{m'} H_{m,m'}(\mathbf{k})c_{i,m'}(\mathbf{k}) = \varepsilon_i(\mathbf{k})c_{i,m}(\mathbf{k}) \tag{2.27}$$

with $H_{m,m'}(\mathbf{k})$ is defined as:

$$H_{m,m'}(\mathbf{k}) = \langle\mathbf{k}+\mathbf{G}_m|\hat{H}_{eff}|\mathbf{k}+\mathbf{G}_{m'}\rangle = \frac{\hbar^2}{2m_e}|\mathbf{k}+\mathbf{G}_m|^2\delta_{m,m'} + V_{eff}(\mathbf{G}_m - \mathbf{G}_{m'}) \tag{2.28}$$

At this point it is relevant to introduce the theorem, which is of significant importance for the calculations of the band structure, as it makes use of one important lattice-symmetry, thereby reformulating the Fourier decomposition of the wave-function in eq. 2.24, namely the *Bloch theorem*. The theorem is the basis for formulation of the lattice-periodicity, which together with formalism of the Fourier-space (k-space and the *Brillioun zone*) construct the foundation of the plane-wave expansion in DFT. According to the theorem, each wavefunction that is the eigenfunction of the Schrödinger equation (2.49) for a given $\mathbf{k}$ can be written be expanded:

$$\psi_{i,\mathbf{k}} = \sum_m c_{i,m}(\mathbf{k}) \times \frac{1}{\sqrt{\Omega}}\exp(i(\mathbf{k}+\mathbf{G}_m)\cdot\mathbf{r}) = \exp(i\mathbf{k}\cdot\mathbf{r})\frac{1}{\sqrt{N_{cell}}}u_{i,\mathbf{k}}(\mathbf{r}) \tag{2.29}$$

where the summation over $\mathbf{q}$ is limited $\mathbf{q} = \mathbf{k} + \mathbf{G}_m$, and $\Omega = N_{cell}\Omega_{cell}$, while:

$$u_{i,\mathbf{k}}(\mathbf{r}) = \frac{1}{\sqrt{\Omega_{cell}}} = \sum_m c_{i,m}(\mathbf{k})\exp(i\mathbf{G}_m\cdot\mathbf{r}) \tag{2.30}$$

The above expression shows the periodicity of the crystal-lattice, which is the main part of the Bloch theorem. Being the Fourier coefficients of the decomposition $u_{i,\mathbf{k}}(\mathbf{r})$ also build an orthonormal set:

$$\frac{1}{\Omega_{cell}}\int_{cell} \mathrm{d}\mathbf{r}u^*_{i,\mathbf{k}}(\mathbf{r})u_{i',\mathbf{k}}(\mathbf{r}) = \sum_m c^*_{i,m}(\mathbf{k})c_{i',m}(\mathbf{k}) = \delta_{i,i'} \tag{2.31}$$

Furthermore, in limits of large Ω where the k points become a dense continuum, and the energy-bands become continuous, the set of eigenstates and the eigenvalues $i = 1, 2, ...$ for each k

point may be found by diagonalizing the Hamiltonian in the basis $\mathbf{k}+\mathbf{G}_m, m = 1, 2, ...$

Next we need to talk about one of the most significant variations of DFT from the plane-wave formalism, which find many applications in simulation of large systems. In our simulations, as mentioned before, we have implemented the real-space implementation of the PAW formulations of the DFT. Therefore, we approach the real-space implementation and formalism alongside introducing the PAW formalism which is, mathematically speaking, a transformation formalism of the PW-formulation, in order to carry out the simulations with more computational efficiency. In real-space implementation, which is called the *finite differences* (FD) method, the real space of the system, is turned into a grid. The total wavefunction is then evaluated at each of the grid points, which are separated by a designated parameter(s) h_x, h_y, h_z called the grid-spacing. This formalism however is not an alternative to the k-point decomposition, as the periodic systems still would have a k-point expansion of the wave-function, in addition to real space grid-decomposition. going in between the spaces, namely the Fourier-space, and the real-space is realized by using *fast Fourier transform* algorithm (FFT) on the variables. However, in the calculation of the ground state density of the Kohn-Sham equations, in the second derivative has the following form in the DF method [13]:

$$\left[\frac{\partial^2\psi}{\partial x^2}\right]_{x_i,y_j,z_k} = \sum_{-m}^{m} C_m\psi(x_i+mh_x, y_j, z_k) + O(h^{2m+2}) \tag{2.32}$$

resulting in the Laplacian in a uniform 3D-grid being [39]:

$$\left[\nabla^2\psi\right]_{x_i,y_j,z_k} = \sum_{n=-N}^{N}\sum_{m=-N}^{N}\sum_{l=-N}^{N} C_{lmn}\psi(x_i+lh_x, y_j+mh_y, z_k+nh_z) \tag{2.33}$$

In order to move on to the real-space grid implementation, we define the following notations, and call the smooth partial wave functions $\tilde{\phi}_i^a(\mathbf{r})$, where the core state $\tilde{\phi}_i^{a,core}(\mathbf{r})$ are frozen, and the index a denotes atom-centred [38]. Using these states and their projection operators the transformation $\mathcal{T}$ can be written as [38]:

$$\mathcal{T} = \mathbf{1} + \sum_i\sum_a(|\phi_i^a\rangle - |\tilde{\phi}_i^a\rangle)\langle\tilde{p}_i^a| \tag{2.34}$$

where the atom-centered all-electron wavefunctions are defined as (n, l, m are the quantum numbers used in Hydrogen-atom wave-functions):

$$\phi_i^a(\mathbf{r}) = \phi_{nl}^a(r)Y_L(\mathbf{r}) \quad , \quad \tilde{\phi}_i^a(\mathbf{r}) = \tilde{\phi}_{nl}^a(r)Y_L(\mathbf{r}) \tag{2.35}$$

with $Y_L(\mathbf{r})$ as the real-valued spherical harmonics (L is the combined index of l, m). The atomic augmentation sphere has the distance r_c^a, as the cut-off radius, which sets the above functions equal resulting in the linear transformation being $\mathcal{T} = \mathbf{1}$ for $r > r_c^a$. Therefore the projection operators which we define for the smooth partial wavefunctions $\tilde{p}_i^a = \tilde{p}_{nl}^a(r)Y_L(\mathbf{r})$, would fulfill the following relation:

$$\int_0^{r_c^a} r^2 dr\tilde{p}_{nl}^a(r)\tilde{\phi}_{nl}^a(r) = \delta_{nn'} \quad , \quad \langle\tilde{p}_{i_1}^a|\tilde{\phi}_{i_2}^a\rangle = \delta_{i_1i_2} \tag{2.36}$$

If we set the atomic position at $\mathbf{R}^a$ (*Bravais lattice vector*), the above condition becomes effective for $|\mathbf{r}-\mathbf{R}^a| > r_c^a$

Now we can expand the total atom-centered wavefunction Ψ (and its smooth pseudo version $\tilde{\Psi}$) in terms of the all-electron (AE) and smooth pseudo (PS) partial waves $\phi_i^a(\mathbf{r}), \tilde{\phi}_i^a(\mathbf{r})$:

$$\Psi_n^a(\mathbf{r}) = \sum_i P_{in}^a \phi_i^a(\mathbf{r}) \qquad , \qquad \tilde{\Psi}_n^a(\mathbf{r}) = \sum_i P_{in}^a \tilde{\phi}_i^a(\mathbf{r}) \tag{2.37}$$

where the coefficient are given by $P_{in}^a = \langle \tilde{p}_i^a | \tilde{\Psi}_n \rangle$. Note that for $|\mathbf{r} - \mathbf{R}^a| < r_c^a$, $\Psi_n = \Psi_n^a$ and $\tilde{\Psi}_n = \tilde{\Psi}_n^a$ with $\Psi_n(\mathbf{r}) = \mathcal{T}\tilde{\Psi}_n(\mathbf{r})$. Therefore, the total wavefunction takes the following form:

$$\Psi_n = \tilde{\Psi}_n + \sum_a (\Psi_n^a - \tilde{\Psi}_n^a) \tag{2.38}$$

Also the PAW formalism gives the smooth-core PS electron densities, which has also contributions from the atom-centred PS-density, as follows:

$$\tilde{n}(\mathbf{r}) = \sum_n f_n |\tilde{\Psi}_n(\mathbf{r})|^2 + \sum_a \tilde{n}_c^a(|\mathbf{r} - \mathbf{R}^a|) \tag{2.39}$$

which is equal to the all-electron (AE) density $n(\mathbf{r})$ outside the r_c^a, where f_n's are the occupation numbers according to the Fermi-Dirac distribution of electronic orbitals $(0-2)$, and $\tilde{n}_c^a(\mathbf{r})$ the smooth version of the frozen core electron density $n_c^a(\mathbf{r})$. If we define the atomic density matrix $D_{i_1 i_2}^a$:

$$D_{i_1 i_2}^a = \sum_n \langle \tilde{\Psi}_n | \tilde{p}_{i_1}^a \rangle f_n \langle \tilde{p}_{i_2}^a | \tilde{\Psi}_n \rangle \tag{2.40}$$

using that, the atom-centered AE and PS densities could be written as:

$$n^a(\mathbf{r}) = \sum_{i_1, i_2} D_{i_1 i_2}^a \phi_{i_1}^a(\mathbf{r}) \phi_{i_2}^a(\mathbf{r}) + n_c^a(\mathbf{r}) \qquad , \qquad \tilde{n}^a(\mathbf{r}) = \sum_{i_1, i_2} D_{i_1 i_2}^a \tilde{\phi}_{i_1}^a(\mathbf{r}) \tilde{\phi}_{i_2}^a(\mathbf{r}) + \tilde{n}_c^a(\mathbf{r}) \tag{2.41}$$

from which the full AE density could be written as (also using the Bravais lattice vector R^a of atom a):

$$n(\mathbf{r}) = \tilde{n}(\mathbf{r}) + \sum_a (n^a(\mathbf{r}) - \tilde{n}^a(\mathbf{r})) = \tilde{n}(\mathbf{r}) + \sum_a [n^a(\mathbf{r} - \mathbf{R}^a) - \tilde{n}^a(\mathbf{r} - \mathbf{R}^a)] \tag{2.42}$$

The form of the above total smooth PS wavefunction in eq. 2.38 could be further illustrated using the fact that in the case of Brilloun zone sampling of the period structures, the same Bloch theorem applies and that the only difference is that the wavefunction is in the real space, whore periodicity is expressed in terms of the Bravais lattice vector $\mathbf{r}$:

$$\tilde{\Psi}_{n\mathbf{k}}(\mathbf{r} + \mathbf{R}) = \mathrm{e}^{i\mathbf{k}\cdot\mathbf{R}} \tilde{\Psi}_{n\mathbf{k}}(\mathbf{r}) \tag{2.43}$$

Having introduced the most important parameters in the grid-implementation of PAW formalism, in addition to the kinetic energy that we previously introduced, every other variable gets defined in terms of these parameters, such as the electrostatic multipole moments and compensation charges. However, here we define only the neutral charge density $\tilde{\rho}(\mathbf{r})$, and it's Poisson equation, so that we can define the PAW energy functional. For a given compensation charge $\tilde{Z}^a(\mathbf{r})$ we have for the neutral charge density [38]:

$$\tilde{\rho}(\mathbf{r}) = \tilde{n}(\mathbf{r}) + \sum_a \tilde{Z}^a(\mathbf{r} - \mathbf{R}^a) \qquad , \qquad \nabla^2 \tilde{v}^H = -4\pi\tilde{\rho} \tag{2.44}$$

with $\tilde{v}^H(\mathbf{r})$ as the pseudo-Hartree potential. Now we can introduce the PAW total energy, which has a contribution from the "soft" energy (which in turn is a function of the smooth PS wavefunction):

$$E = \tilde{E} + \sum_a (E^a - \tilde{E}^a) \tag{2.45}$$

which has three separate energy terms, from which the two within the sum is called the atomic corrections:

$$\begin{aligned} \tilde{E} = \sum_n f_n \int d\mathbf{r} \tilde{\Psi}_n^*(\mathbf{r}) \left(-\frac{1}{2}\nabla^2\right) \tilde{\Psi}_n(\mathbf{r}) + \frac{1}{2}\int d\mathbf{r} \tilde{v}^H(\mathbf{r})\tilde{\rho}(\mathbf{r}) \\ + E_{xc}\left[\tilde{n}(\mathbf{r})\right] + \int d\mathbf{r} \tilde{n}(\mathbf{r}) \sum_a \overline{v^a}(|\mathbf{r} - \mathbf{R}^a|) \end{aligned} \tag{2.46}$$

where $\overline{v^a}$ is an arbitrary localized potential which equal to zero for $r > r_c^a$. For E^a we have:

$$\begin{aligned} E^a = \sum_i^{core} \int d\mathbf{r} \phi_i^{a,core}(\mathbf{r}) \left(-\frac{1}{2}\nabla^2\right) \phi_i^{a,core}(\mathbf{r}) + \sum_{i_1 i_2} D_{i_1 i_2}^a \int d\mathbf{r} \phi_i^a(\mathbf{r}) \left(-\frac{1}{2}\nabla^2\right) \phi_i^a(\mathbf{r}) \\ + \frac{1}{2}\int d\mathbf{r} \int d\mathbf{r}' \frac{[n^a(\mathbf{r}) + Z^a(\mathbf{r})][n^a(\mathbf{r}') + Z^a(\mathbf{r}')]}{|\mathbf{r} - \mathbf{r}'|} + E_{xc}[n^a(\mathbf{r}] \end{aligned} \tag{2.47}$$

and for $\tilde{E}^a$:

$$\begin{aligned} \tilde{E}^a = \sum_{i_1 i_2} D_{i_1 i_2}^a \int d\mathbf{r} \tilde{\phi}_{i_1}^a(\mathbf{r}) \left(-\frac{1}{2}\nabla^2\right) \tilde{\phi}_{i_2}^a(\mathbf{r}) \\ + \frac{1}{2}\int d\mathbf{r} \int d\mathbf{r}' \frac{[\tilde{n}^a(\mathbf{r}) + \tilde{Z}^a(\mathbf{r})][\tilde{n}^a(\mathbf{r}') + \tilde{Z}^a(\mathbf{r}')]}{|\mathbf{r} - \mathbf{r}'|} + E_{xc}[\tilde{n}^a(\mathbf{r})] + \int d\mathbf{r} \tilde{n}^a(\mathbf{r}) \overline{v^a}(r) \end{aligned} \tag{2.48}$$

The grid for the E^a and $\tilde{E}^a$ is a radial one inside the augmentation sphere.

With this level of details in the PAW formalism in the real-space grid implementation, we can now expand our formalism to localized atomic basis sets, which are the building block of PAW-LCAO implementation. It should be said that the method discussed here is different than the LCAO pseudo-potential method used in codes such as *Siesta*. In this formalism, we define the PS wavefunction again as an expansion, however in terms of localized atomic orbital-like functions $|\Phi_\mu\rangle$ [41]:

$$|\tilde{\Psi}_n\rangle = \sum_\mu c_{\mu n} |\Phi_\mu\rangle \quad , \quad \rho_{\mu\nu} = \sum_n c_{\mu n} f_n c_{\nu n}^* \tag{2.49}$$

where $c_{\mu n}$ are variational parameters for the expansion and the f_n again the occupation number. Ans so with that PS density is given by:

$$\tilde{n}(\mathbf{r}) = \sum_{\mu\nu} \Phi_\mu^*(\mathbf{r}) \Phi_\nu(\mathbf{r}) \rho_{\nu\mu} + \sum_a \tilde{n}_c^a(\mathbf{r}) \tag{2.50}$$

In order to express the energy and the other quantities in LCAO we first express the following three matrices in terms of basis functions:

$$T_{\mu\nu} = \langle \Phi_\mu | -\frac{1}{2}\nabla^2 | \Phi_\nu \rangle \quad , \quad P_{i\mu}^a = \langle \tilde{p}_i^a | \Phi_\mu \rangle \quad , \quad \Theta_{\mu\nu} = \langle \Phi_\mu | \Phi_\nu \rangle \tag{2.51}$$

using which the atomic density matrices, and the kinetic energy could be expressed as:

$$D_{ij}^a = \sum_{\mu\nu} P_{i\mu}^a \rho_{\mu\nu} P_{j\nu}^{a*} \quad , \quad \sum_n f_n \langle \tilde{\Psi}_n | -\frac{1}{2}\nabla^2 | \tilde{\Psi}_n \rangle = \sum_{\mu\nu} T_{\mu\nu}\rho_{\nu\mu} \tag{2.52}$$

and the potential term:

$$V_{\mu\nu} = \int \Phi_\mu^*(\mathbf{r})\tilde{v}(\mathbf{r})\Phi_\mu(\mathbf{r})d\mathbf{r} \tag{2.53}$$

where $\tilde{v} = \tilde{v}_{\mathrm{Ha}}[\tilde{\rho}] + \overline{v} + v_{\mathrm{xc}}[\tilde{n}]$. Having defined the individual terms, now we can move on to define the Hamiltonian, the eigenvalue and the Kohn-Sham equation.

Starting from the equivalent of the Kohn-Sham equation in the PAW-LCAO formalism for the PS wavefunction $\tilde{H}|\tilde{\Psi}_n\rangle = S|\tilde{\Psi}_n\rangle\epsilon_n$, with $S = \mathcal{T}^\dagger\mathcal{T}$ as the overlap operator, we can define the discretized Hamiltonian [41]:

$$H_{\mu\nu} = \frac{\partial E}{\partial \rho_{\nu\mu}} = T_{\mu\nu} + V_{\mu\nu} + \sum_{aij} P_{i\mu}^{a*}\Delta H_{ij}^a P_{j\nu}^a \quad , \quad \Delta H_{ij}^a = \frac{\partial E}{\partial D_{ji}^a} \tag{2.54}$$

where the matrix representation of the overlap operator would be given by:

$$S_{\mu\nu} = \langle \Phi_\mu | S | \Phi_\nu \rangle = \Theta_{\mu\nu} + \sum_{aij} P_{i\mu}^{a*}\Delta S_{ij}^a P_{j\nu}^a \tag{2.55}$$

using the parameters in eq. 2.51, the following orthogonality condition is expressed using:

$$\sum_{\mu\nu} c_{\mu m}^* S_{\mu\nu} c_{\nu n} = \delta_{mn} \tag{2.56}$$

and the generalized eigenvalue problem take the following form:

$$\sum_\nu H_{\mu\nu} c_{\nu n} = \sum_\nu S_{\mu\nu} c_{\nu n}\epsilon_n \tag{2.57}$$

where the Hamiltonian and the overlap matrix are the knowns, while $c_{\mu n}$ and the eigenvalues ϵ_n the unknowns.

In contrast to the FD and the PW mode, the LCAO formalisn depends heavily on the basis functions for the SCF loops, since there are no actual wavefunctions involved, other than densities. As in the GPAW, the first initial guess for any SCF loop is done based on the LCAO atomic basis-sets. These functions are atom-centred orbitals, composed of a radial part and the spherical harmonics part. Given the quantum numbers n, l, m, $\Phi_{nlm}(\mathbf{r}) = \varphi_{nl}(r)Y_{lm}(\mathbf{r})$. The strictly localized radial functions, which are all zero beyond the cut-off radius, are used to make the Hamiltonian and the overlap matrix narrow in their representation. These basis functions are categorizes and named as: single-zeta (SZ), single-zeta polarized (SZP), double-zeta (DZ), double-zeta polarized (DZP), etc. The SZ refers the the first basis orbitals $\varphi_{nl}^{AE}(r)$, which are obtained for each valance state by solving the Kohn-Sham equations for an isolated atom in a coulomb potential with a certain cut-off radius $\varphi_{nl}^{AE}(r)$. The extra basis functions, (multiple zeta) with the same angular momentum are constructed with the split-valance technique, which are to improve the radial flexibility.

2.1.4 Forces and Stress

Structural optimization (relaxation), is one of the most important and most popular simulations that are done in the field of computer-based materials and solid state physics. The two major methods are the DFT and analytical potential-based MD (*molecular dynamics*) codes. The DFT codes are mostly written for the calculations of the electronic structure, and not atomic/ionic relaxations, due to the fact that applying the DFT method to large structures would become extremely expensive, to the point that not even the current supercomputers would be able to properly execute the codes. That is why we turn to alternative methods as starting point, some of which are directly based on DFT, such as the LCAO (*local combination of the atomic orbitals*), or rely on analytical potentials, such *LAMMPS*, *Atomistica*, etc.

The most important factors for the structural optimization in both methods, are the calculations of the forces that act between the ions, and the stress between the atoms. In analytical potentials, the motion and the forces obey the laws of classical Newtonian mechanics. While the force is the time derivative of the classical momentum, $\mathrm{P_i} = \frac{d}{dt}(m_i v_i) = \mathrm{F}_i$, it is also the gradient of the total analytical (classical) potential, $F = -\frac{d}{dr}U_{tot}(r)$, which is defined in the specific code. In [29] there are quite a few of the analytical potentials listed. Accordingly the total energy, which would need to be minimized as the forces are minimized between the atoms, has a typical form of [29]:

$$E_{system} = \underbrace{E_{bond} + E_{vdW} + E_{Coul}}_{2-body} + \underbrace{E_{val,angle}}_{3-body} + \underbrace{E_{tors}}_{4-body} + \underbrace{E_{over}}_{multi-body} + ... \tag{2.58}$$

where $E_{val,angle}$ is the angle strain term, E_{tors} the torsional energy, and E_{over} the over-coordination energy. As an example, in LAMMPS these terms translate into the following energy sums [64]:

$$E(r_1, ..., r_N) = \sum_{i,j} E_{pair}(r_i, r_j) + \sum_{ij} E_{bond}(r_i, r_j) + \sum_{ijk} E_{angle}(r_i, r_j, r_k) + E_{4-body} + ... \tag{2.59}$$

However the expression for the computation of the stress tensor using the classical potentials is a bit more complicated, even though the stress in the classical continuum mechanics can simply be written as [28]:

$$div\boldsymbol{\sigma} + \rho\boldsymbol{b} = \rho\ddot{\boldsymbol{r}} \tag{2.60}$$

where the $\boldsymbol{\sigma}$ is the stress, ρ the mass density, and $\boldsymbol{b}$ the body force density. The second derivative denotes the derivative of the displacement with respect to the origin. The expression for the computational stress tensor is basically derived from the following equation of pressure [27]:

$$P = \frac{Nk_BT}{V} + \frac{\langle W \rangle}{3V} \tag{2.61}$$

where $\langle W \rangle$ is the ensemble average of the internal virial, and it represents the contribution of the total virial due to forces acting between the atoms:

$$W(\boldsymbol{r}^N) = -3V\frac{dU}{dV} \quad , \quad \boldsymbol{r}^N = \boldsymbol{r}_1, ..., \boldsymbol{r}_N \tag{2.62}$$

This scalar virial which is related to the global virial tenor $\mathbf{W}$ by $W = Tr\mathbf{W}$, depends like the potential on the atomic positions $\boldsymbol{r}_i$.

Due to the fact that the forces are defined as, $\boldsymbol{F}_i = -\frac{d}{d\boldsymbol{r}_i}U(\boldsymbol{r}^N)$ the correct form of the virial under periodic boundary conditions have been shown to be:

$$W(\boldsymbol{r}^N) = \sum_{i=1}^{N} \boldsymbol{r}_i \cdot \boldsymbol{F}_i - 3V \left(\frac{\partial U}{\partial V}\right)_{\boldsymbol{r}^N} \tag{2.63}$$

Even though the above expression represents a standard expression for the virial derived from the continuum and classical mechanics, a more general expression involving also the statistical mechanics is given by:

$$W(\boldsymbol{r}^N) = \sum_{i=1}^{N} \boldsymbol{r}_i \cdot \boldsymbol{F}_i + \sum_{\boldsymbol{n}\in Z^3} \mathbf{Hn} \cdot \sum_{j=1}^{N} \boldsymbol{F}'_{i\boldsymbol{n}} \tag{2.64}$$

where $\boldsymbol{F}'_{i\boldsymbol{n}}$ is not the total force on an atoms, but the partial force on the atom located at $\boldsymbol{r}_i + \mathbf{Hn}$. Finally, using this and a few relations to reform the expression, for the total virial tensor we get:

$$\mathbf{W}(\boldsymbol{r}^N) = \sum_{\boldsymbol{n}\in Z^3} \sum_{i=1}^{N} \sum_{j>i}^{N} \boldsymbol{F}_{ij\boldsymbol{n}} \otimes \boldsymbol{r}_{ij\boldsymbol{n}} + \sum_{\boldsymbol{n}\in Z^3}{}' \sum_{i=1}^{N} \boldsymbol{F}_{ii\boldsymbol{n}} \otimes \boldsymbol{r}_{ii\boldsymbol{n}} \tag{2.65}$$

And with that we write the total stress tensor $\mathbf{P}$ as [27]:

$$\mathbf{P} = \frac{1}{V}\langle \sum_{i=1}^{N} m_i v_i \otimes v_i + \mathbf{W}(\boldsymbol{r}^{\boldsymbol{N}}) \rangle \tag{2.66}$$

Now we compare these expression with their equivalents in the DFT formalism. Obviously in DFT, the total energy functional of the ground state is obtained using a variational principle, which is known as the *Hohenberg-Kohn* theorem [30]:

$$E = E[n_0(\overrightarrow{r})] = min\,\{E[(\overrightarrow{r})]\} \qquad , \qquad \frac{\delta E[n(\overrightarrow{r})]}{\delta(\overrightarrow{r})} \tag{2.67}$$

At this point, directly relevant for the calculation of the forces, it is not the Kohn-Sham equations, but a theorem known as the *Hellmann-Feynman* theorem. Using this theorem the following expression results in the calculation of the forces acting on a given atom located at the ionic coordinates $\overrightarrow{R} = (\overrightarrow{R}_I)$ [30]:

$$-\overrightarrow{F}_I = \nabla_I E_0(\overrightarrow{R}) = \frac{\partial}{\partial \overrightarrow{R}} \langle \Psi_0(\overrightarrow{R}) | H(\overrightarrow{R}) | \langle \Psi_0(\overrightarrow{R}) \rangle = \langle \Psi_0(\overrightarrow{R}) | \nabla_I H(\overrightarrow{R}) | \langle \Psi_0(\overrightarrow{R}) \rangle \tag{2.68}$$

namely the expectation of the gradient of the electronic Hamiltonian. Note that the terms such as $\langle \nabla_I \Psi_0 | H | \Psi_0 \rangle = \langle \Psi_0 | H | \Psi_0 \nabla_I \rangle = 0$ vanish due to the variational principle.

Similarly the stress tensor σ_{ij}, which defines the variation of the energy functional with respect to the infinitesimal distortion [30], is also given by the above theorem. Namely for distortion of the basis vector $a'_{(k),i} = \sum_j (\delta_{ij} + t_{ij}) a_{(k),i}$, we have for the stress tensor:

$$\sigma_{ij} = -\frac{\partial E(\overrightarrow{a}'_{(k)})}{\partial t_{ij}} = -\langle \Psi_0 | \frac{\partial}{\partial t_{ij}} H(\overrightarrow{a}'_{(k)}) | \Psi_0 \rangle \tag{2.69}$$

where t_{ij} is the directional strain.

2.2 Density Functional Theory of Electronic Properties

2.2.1 Exchange-Correlation Functionals

The core of the DFT calculations lies in the form and the choice of the exchange-correlation potential (functional), as this is the differentiating part, which separates DFT from the its predecessors such the *Hartee Fock*, or *Thomas-Fermi* theory. One of the earliest types of XC-functional that was proposed (by Kohn and Sham) was the type which would characterize the electronic structure of solids as a homogeneous Fermi gas, and therefore the interactions as local. This model, known as the *local densities approximations* (LDA) which was extended to local spin densities approximation (LSDA) was proposed to be an integral over all space, while being local in terms of exchange and correlation energy density [13]

$$
\begin{aligned}
E_{xc}^{LSDA}[n^{\uparrow}, n_{\downarrow}] &= \int \mathrm{d}^3 r n(\mathbf{r}) \epsilon_{xc}^{hom}(n^{\uparrow}(\mathbf{r}, n^{\downarrow}(\mathbf{r})) \\
&= \int \mathrm{d}^3 r n(\mathbf{r}) [\epsilon_{x}^{hom}(n^{\uparrow}(\mathbf{r}), n^{\downarrow}(\mathbf{r})) + \epsilon_{c}^{hom}(n^{\uparrow}(\mathbf{r}), n^{\downarrow}(\mathbf{r}))]
\end{aligned}
\tag{2.70}
$$

The logic behind the LDA is that the effect of exchange and correlation is short. while this might be a good approximation for homogeneous free electron gas (as in the metals), for solids with covalant bonds, this local approximation are not so accurate. To go beyond the local approximations, one can first include the magnitude of the gradient of the density $|\nabla n^{\sigma}|$. With that the *generalized-gradient approximations* (GGA) expansion of the XC-functional is given by the following expression [13]

$$
\begin{aligned}
E_{xc}^{GGA}[n^{\uparrow}, n_{\downarrow}] &= \int \mathrm{d}^3 r n(\mathbf{r}) \epsilon_{xc}(n^{\uparrow}, n_{\downarrow}, |\nabla n^{\uparrow}|, |\nabla n^{\downarrow}|, ...) \\
&\equiv \int \mathrm{d}^3 r n(\mathbf{r}) \epsilon_{x}^{hom}(\mathbf{r}) F_{xc}(n^{\uparrow}, n_{\downarrow}, |n^{\uparrow}|, |n^{\downarrow}|, ...),
\end{aligned}
\tag{2.71}
$$

where $\epsilon_x^{hom}(n)$ is the exchange energy of the unpolarized electron gas, and F_{xc} a dimensionless function.

For the exchange functional of the same unpolarized system of density $n(\mathbf{r})$, the following relation (spin scaling) holds:

$$
E_x[n^{\uparrow}, n_{\downarrow}] = \frac{1}{2}[E_x[2n^{\uparrow}] + E_x[2n^{\downarrow}]
\tag{2.72}
$$

For exchange we need to consider the expansion of the spin-unpolarized $F_x(n, |\nabla n|)$

$$
F_x = 1 + \frac{10}{81} s_1^2 + \frac{146}{2025} s_2^2 + ...
\tag{2.73}
$$

where:

$$
s_m = \frac{|\nabla^m n|}{(2k_F)^m n} = \frac{|\nabla^m n|}{2^m (3\pi^2)^{m/3} (n)^{(1+m/3)}}
\tag{2.74}
$$

with the $k_F = 3(2\pi/3)^{1/2} r_s^{-1}$, and r_s the average distance between the atoms. The factor F_x has different shape for different derivations of the GGA-potential, such as the *PBE*, *PW91*, and *B88*. These variations differ significantly, where s is large ($s \geq 3$). Finally, we have the gradient expansion of the correlation in the lowest order as follows:

$$
F_c = \frac{\epsilon_c^{LDA}(n)}{\epsilon_x^{LDA}(n)} (1 - 0.219, 51 s_1^2 + ...),
\tag{2.75}
$$

Having defined the functionals for the LDA and GGA potentials, it is possible to derive the explicit form of the XC-potentials for these functionals. The functionals are functions of local densities $n(\sigma, \mathbf{r})$ and their gradients at $\mathbf{r}$, and so for LDA we have:

$$\delta E_{xc}[n] = \sum_{\sigma} \int \mathrm{d}\mathbf{r} \left[\epsilon_{xc}^{hom} + n \frac{\partial \epsilon_{xc}^{hom}}{\partial n^{\sigma}} \right]_{\mathbf{r},\sigma} \delta n(\mathbf{r}, \sigma) \tag{2.76}$$

Therefore the XC-potential:

$$V_{xc}^{\sigma}(\mathbf{r}) = \left[\epsilon_{xc}^{hom} + n \frac{\partial \epsilon_{xc}^{hom}}{\partial n^{\sigma}} \right]_{\mathbf{r},\sigma} \tag{2.77}$$

Taking the simple derivatives the following are the separate terms of the exchange and correlation for LDA:

$$V_{x}^{\sigma}(\mathbf{r}) = \frac{4}{3} \epsilon_{x}^{hom}(n(\mathbf{r}, \sigma)) \qquad , \qquad V_{c}(r_s) = \epsilon_{c}(r_s) - \frac{r_s}{3} \frac{\mathrm{d}\epsilon_{c}(r_s)}{\mathrm{d}r_s} \tag{2.78}$$

There are a variety of expressions, such as *Hedin-Lundqvist* (HL), and *Perdew-Zunger* (PZ), which give explicit forms for the correlation energy.

For GGA we proceed up to the linear order variation of the functional with $\delta \nabla n = \nabla \delta n$:

$$\delta E_{xc}[n] = \sum_{\sigma} \int \mathrm{d}\mathbf{r} \left[\epsilon_{xc} + n \frac{\partial \epsilon_{xc}}{\partial n^{\sigma}} + n \frac{\partial \epsilon_{xc}}{\partial \nabla n^{\sigma}} \nabla \right]_{\mathbf{r},\sigma} \tag{2.79}$$

therefore by partial integration of the last differential operator we get for the XC-potential:

$$V_{xc}^{\sigma}(\mathbf{r}) = \left[\epsilon_{xc} + n \frac{\partial \epsilon_{xc}}{\partial n^{\sigma}} - \nabla \left(n \frac{\partial \epsilon_{xc}}{\partial \nabla n^{\sigma}} \right) \right]_{\mathbf{r},\sigma} \tag{2.80}$$

Here we further discuss the explicit *Perdew-Burke-Ernzerdorf* (PBE) form of the GGA correlation potential, in which the dimensionless $F_x(0) = 1$ for the recovery of the local approximations, and:

$$F_x(s) = 1 + \kappa - \kappa/(1 + \mu s^2/\kappa) \tag{2.81}$$

with the value of $\kappa = 0.0804$ chosen to satisfy the Lieb-Oxford inequality lower bound, and $\mu = 0.21951$ to cancel the correlation term. For the correlation functional we have:

$$E_{c}^{GGA-PBE}[n^{\uparrow}, n_{\downarrow}] = \int \mathrm{d}^3 r n \left[\epsilon_{c}^{hom}(r_s, \zeta) + H(r_s, \zeta, t) \right] \tag{2.82}$$

where t is a dimensionless gradient $t = |\nabla n|/(2\phi k_{TF} n)$ and r_s the local value of the density parameter, with $\phi = ((1+\zeta)^{2/3} + (1-\zeta)^{2/3})/2$. The expression for H is given by:

$$H = \frac{e^2}{a_0} \gamma \phi^3 \log \left(1 + \frac{\beta}{\gamma} t^2 \frac{1 + At^2}{1 + At^2 + A^2 t^4} \right) \tag{2.83}$$

with $e^2/a_0 = 1$, $a_0 =$ Bohr radius, and A:

$$A = \frac{\beta}{\gamma} \left[\exp \left(\frac{-\epsilon_{c}^{hom}}{\gamma \phi^3 \frac{e^2}{a_0}} \right) - 1 \right]^{-1} \tag{2.84}$$

Having introduced the two most common forms of XC-potential, we can now briefly mention some more advanced XC-potentials specifically available in GPAW. Even though the extent of these advanced and hybrid functionals requires an entire chapter to describe, here we suffice to describing one special functional GLLB-SC, namely the *Gauss-Lobatto-Legendre-Birkhoff solids corrected* approximation of the exact exchange E_{XX} [43]. For this purpose we start from the exact exchange functional defined in GPAW, which is claimed to be the first real-space PAW implementation of the functional. The Fock exact exchange is given by [40]:

$$E_{XX} = -\frac{1}{2}\sum_{ij\sigma} f_{i\sigma} f_{j\sigma} K^C_{ij\sigma,ij\sigma} \tag{2.85}$$

with i, j as the indices of states and Σ as the spin. The Coulomb matrix is therefore given by:

$$K^C_{ij\sigma_1,kl\sigma_2} = (n_{ij\sigma_1}|n_{kl\sigma_2}) = \int \frac{\mathrm{d}\mathbf{r}\mathrm{d}\mathbf{r}'}{|\mathbf{r}-\mathbf{r}'|} n^*_{ij\sigma_1}(\mathbf{r}) n_{kl\sigma_2}(\mathbf{r}') \tag{2.86}$$

with $n_{ij\sigma}(\mathbf{r}) = \psi^*_{i\sigma}\psi_{j\sigma}(\mathbf{r})$ as the density-matrix element of spin σ. The PAW partitioning of the AE and PS with the atom-centred corrections naturally apply to this density-matrix elements:

$$n_{ij\sigma} = \tilde{n}_{ij\sigma} + \sum_a (n_{ij\sigma} - \tilde{n}^a_{ij\sigma}) \tag{2.87}$$

here once again we make use of the compensation charge in order to eliminate the cross terms between different augmentation spheres, as in the PAW formalism:

$$\tilde{\rho}_{ij} = \tilde{n}_{ij} + \sum_a \tilde{Z}^a_{ij} \quad , \quad \tilde{Z}^a_{ij}(\mathbf{r}) = \sum_{lm} Q^1_{lm,ij}\hat{g}^a_{lm}(\mathbf{r}) \tag{2.88}$$

with $\tilde{\rho}_{ij}$ as the smooth compensated pair density. This in turn results in the Coulomb matrix partitioning into smooth part and the local corrections:

$$K^C_{ij,kl} = (\tilde{\rho}_{ij}|\tilde{\rho}_{kl}) + \sum_a \Delta K^{C,a}_{ij,kl} \tag{2.89}$$

The local corrections term, which is a limit of difference of two Coulomb matrices $K^{C,a}_{ij,kl}$, is an import term in linear response TDDFT formalism, and therefore we will elaborate later on its exact form.

For solving the Coulomb integral over the kernel $1/|\mathbf{r}-\mathbf{r}'|$, the Poisson equation is solved $\nabla^2\tilde{v}_{ij} = -4\pi\tilde{\rho}_{ij}$. The Coulomb matrix in eq. 2.86, which could be written as the expansion coefficient, also includes the core-core interaction, which are calculated once for all the atoms with frozen core orbitals. Now we can further explain the Fock operator, corresponding the exact exchange energy functional. The operator itself does not have an explicit form in real-space grid, as it is a non-local operator, however it's action is very similar to a projector operator acting on a PS wavefunction:

$$f_n\hat{\tilde{v}}^F|\tilde{\psi}_n\rangle = \partial E_{XX}/\partial\langle\tilde{\psi}_n| = -\sum_m f_m\tilde{v}_{nm}(\mathbf{r})|\tilde{\psi}_m\rangle + \sum_a\sum_i |\tilde{p}^a_i\rangle\Delta v^{Fa}[\tilde{v}_{nm},\{P^a_{jm}\}] \tag{2.90}$$

The first part of the above equation $-\sum_m f_m\tilde{v}_{nm}(\mathbf{r})|\tilde{\psi}_m\rangle$, which deals with the pseudo-quantities, can be accurately solved on the coarse real-space grid, making a converged E_{XX} SCF loops possible at moderately high computational cost. However the solution of applying the Fock operator requires solving the Poisson equation for all the pairs of orbitals, making it in general computationally expensive. The comparison of the implementation in PBE and PBE0 however, with the plane-wave PAW implemented in codes such as VASP, and the experimental values, indicate good agreement [40], despite heavy computational costs.

For that reason there exist the GLLB approximation of the exact exchange E_{xx}, which is later one modified into GLLB-SC. In GLLB the exchange potential is separated into [43]:

$$v_x(\mathbf{r}) = v_S(\mathbf{r}) + v_{resp}(\mathbf{r}) \tag{2.91}$$

where the v_S is approximated using the GGA exchange energy density ϵ_x^{GGA}, $v_S(\mathbf{r}) = \frac{2\epsilon_x^{GGA}(\mathbf{r};n)}{n(\mathbf{r})}$. The response part can be approximated using the common denominator approximation, and exchange scaling relations:

$$v_{resp}(\mathbf{r}) = \sum_i^{occ} K[n]\sqrt{\varepsilon_r - \varepsilon_i}\frac{|\psi_i(\mathbf{r})|^2}{n(\mathbf{r})} \quad , \quad K = \frac{8\sqrt{2}}{3\pi^2} \approx 0.382 \tag{2.92}$$

Based on this scheme we will extend this approximation into GLLB-SC, in which the whole exchange-correlation is separated into two parts, both of which also contain additionally, a contribution from PBEsol [43]. In the quasi-particle band gap there are two terms, one of which leads to the necessity of using the GLLB-SC for a more correct calculation of the band gap of an N-electron system (with I as the ionization potential and A the electron affinity) [43]:

$$E_{gap}^{QP} = I - A = E[n_{N-1}] - 2E[n_N] + E[n_{N+1}] = E_{gap}^{KS} + \Delta_{xc} \tag{2.93}$$

The first term $E_{gap}^{KS} = \varepsilon_{N+1} - \varepsilon_N$ is the Kohn-Sham band gap, and the second term is, which is called the derivative discontinuity, is a bang gap discontinuity which emerges at integer occupations J as the function $\mathbf{r}$:

$$\Delta^{xc} = \Delta_{xc}(\mathbf{r}) = \lim_{\delta \to 0}[v_{xc}(\mathbf{r}; J + \delta) - v_{xc}(\mathbf{r}; J - \delta)] \tag{2.94}$$

The exchange correlation potential v_{xc} can be approximated similar to GLLB by spliting into two parts:

$$v_{xc}(\mathbf{r}) = v_S(\mathbf{r}) + v_{resp}(\mathbf{r}) \tag{2.95}$$

which are in turn approximated using the PBEsol as follows:

$$v_S(\mathbf{r}) = 2\epsilon_{xc}^{(PBEsol)}(\mathbf{r}) \quad , \quad v_{resp}(\mathbf{r}) = \sum_i^{occ} w_i \frac{|\psi_i(\mathbf{r})|^2}{n(\mathbf{r})} \tag{2.96}$$

where the coefficient w_i are calculated using the computationally heavy Fock operator $w_i = \langle i | v_x(\mathbf{r}) - \hat{v}_x^F | i \rangle$. The exchange potential in the previous equation was first approximated using the GLLB approximation [44], in which exchange scaling and asymptotic behaviour in addition to fitting to the homogeneous electron gas (HEG) was used. If we shift the potential w_i by a constant, it should have not any physical meaning. If we further take the highest occupied eigenvalue ε_H as reference and we set $w_i = f(\varepsilon_r - \varepsilon_i)$, with $f(0) = 0 = w_H$, we realise that:

$$w^i = K_x\sqrt{\varepsilon_r - \varepsilon_i} \tag{2.97}$$

due to the scaling properties of f, ε_i, and v_x as follows:

$$v_x[n_\lambda](\mathbf{r}) = \lambda v_x[n](\lambda\mathbf{r}) \quad , \quad n_\lambda = \lambda^3 n(\lambda\mathbf{r}) \quad , \quad \varepsilon_i[n_\lambda] = \lambda^2\varepsilon_i[n(\mathbf{r})] \tag{2.98}$$

so that for $f(\lambda^2(\varepsilon_r - \varepsilon_i)) = \lambda f(\varepsilon_r - \varepsilon_i)$ taking the response potential of HEG to be $v_{resp} = k_F/2\pi$, with $k_F = (3\pi^2 n)^{1/3}$ the approximated response potential becomes:

$$v_{resp}^{HEG} = \frac{V}{8\pi^3}\int_{|\mathbf{k}|<k_f} d\mathbf{k} K_x\sqrt{\varepsilon_r - \varepsilon_{\mathbf{k}}} \quad , \quad \varepsilon_r - \varepsilon_k = (k_F^2/2 + v_{KS}) - (k^2/2 + v_{KS}) \tag{2.99}$$

by setting $v_{resp}^{HEG} = k_F/2\pi$ the prefactor which is obtained by electron gas fit is calculated to be, $K_x = 8\sqrt{2}/3\pi^2 \approx 0.382$. In GLLB approximation, this same fitting scheme is used for the correlation part of the response to get a prefactor K_c, but in GLLB-SC, PBEsol, and GGA-functionals are used for v_c, scr and $v_{c,reps}$ so that:

$$v_{c,reps}^{PBEsol} = v_c^{PBEsol}(\mathbf{r}) - 2\epsilon_c^{PBEsol}(\mathbf{r}) \tag{2.100}$$

with the full GLLB-SC potential is given by [43]:

$$v_{GLLB-SC}(\mathbf{r}) = 2\epsilon_{xc}^{PBEsol}(\mathbf{r}) + \sum_i^{occ} K_x\sqrt{\varepsilon_r - \varepsilon_i}\frac{|\psi_i(\mathbf{r})|^2}{n(\mathbf{r})} + v_{c,resp}^{PBEsol}(\mathbf{r}) \tag{2.101}$$

Now returning to the gap in the spectrum of the quasi-particle, the discontinuity in GLLB-SC is similar to GLLB, with the difference that in GLLB the discontinuity comes with the coefficients w_i. As we said the discontinuity happens for integer occupations j of the N-electron system, and so the reference energy ϵ_r splits into two values for particle number N when it is close to the integers J: ϵ_J, for $N \leq J$, and ϵ_{J+1} for $N > J$. What happens here is that for $N > J$ the *lowest unoccupied molecular orbital* (LUMO) becomes the *highest occupied molecular orbital* (HUMO), and so in this limit, is where the discontinuity happens:

$$\Delta_{x,reps}(\mathbf{r}) = \sum_i^N K_x(\sqrt{\varepsilon_{N+1} - \varepsilon_i} - \sqrt{\varepsilon_N - \varepsilon_i})\frac{|\psi_i(\mathbf{r})|^2}{n(\mathbf{r})} \tag{2.102}$$

The above approximation is not a constant, and it would affect the wavefunction. That is why it should be compared with first order perturbation theory expansion:

$$\Delta_{x,resp} = \langle \Psi_{N+1}|\Delta_{x,resp}^{GLLB}|\Psi_{N+1}\rangle \tag{2.103}$$

The first approximation to the derivative discontinuity was derived by solving the v_{xc} from the Sham-Schlüter equation [43]. However, a better approximation of v_{xc} was obtained my *Mark Casida* in terms of the self-energy:

$$v_{xc}(\mathbf{r}) = \sum_i^N \frac{\mathrm{Re}\left\{\psi_i(\mathbf{r})\hat{\Sigma}^{xc}(\epsilon_i)\psi_i(\mathbf{r})\right\}}{n(\mathbf{r})} + \sum_i^N \frac{\left\langle \psi_i|v_{xc} - \hat{\Sigma}^{xc}(\epsilon_i)|\psi_i\right\rangle |\psi_i(\mathbf{r})|^2}{n(\mathbf{r})} \tag{2.104}$$

With that taking into account the equivalence between eq. 2.97 and $\langle i|v_x(\mathbf{r}) - \hat{v}_x^F|i\rangle$, the GLLB, and GLLB-SC can be thought of the following matrix element approximation:

$$\left\langle \psi_i|v_x - \hat{\Sigma}^x(\epsilon_i)|\psi_i\right\rangle \approx K_x\sqrt{\varepsilon_r - \varepsilon_i} \tag{2.105}$$

2.2.2 STM Theory & Simulation

During the work of this thesis, half of the effort has been concentrated on coming up with geometrical structures, that would first successfully simulate the confinement of quantum surface states of graphene, and further possibly resemble and encourage the creation of quantum corrals on graphene, as originally done on the surface of a metal by adatoms [6]. However, there are two constrains that need to be mentioned here in order to clarify the goals and achievements. First is that the creation of actual quantum corrals, as were done on a metal surface using a STM, requires geometrical closed structures that have a couple of hundred Ångström (100-200 Å) in diameter. These structures are created using at least 60 Si-atoms adatoms on the surface of the metal, and there is in principle no constrains as to where these atoms could be positioned. Secondly, as the formalism of the creation of quantum corrals indicate [6], in order for a successful creation of the wave-like fluctuations in the LDOS, a material STM-tip needs to be inserted onto the surface of the probe, at which point the electronic states emanate from the tip all the way onto the barriers (the Si-lines) and bounce back towards the tip, which then results in an interference pattern on the surface, and creates a position dependent fluctuations in the LDOS. This process is best described by the *Bardeen's approach* and *NEGF* formalism [6], [42]

Taking these two actual constrains into account, one must consider the fact that in our simulations, we are dealing with structures, that are only about 20-40 Å in diameter, due to the limitations of relaxing the structures even in LCAO mode in DFT. Namely, any structures of 100 Å across cannot be relaxed in DFT-LCAO. Secondly, in regard to the latter constrain, in our simulations we used a STM package which was formulated based on the *Tersoff-Hamman* (TH) approximation. In this formalism, the STM tip is reduced to a s orbital, and there is no interference between the tip-states and the surface states [5]. Therefore, this model cannot fully simulate the quantum corrals. However, as the results will show, the observation of confined surface quantum states were successful using the TH approximation STM simulations, due to the fact that the closed Si-structures had induced enough large electric dipole moment, so that a standalone states were created without any external interference of an external potential (namely the STM tip).

The TH theory is based on the Bardeen's theory of tunnelling. As mentioned before, the particular characteristic of the TH model, is that the tip-states are factorized out of the problem by representing the tip by a potential and an arbitrarily localized wave-function. Geometrically, it resembles a point and as later on we shall see, it is represented by a s orbital. Therefore, in this model the STM image can only be attributed to the properties of the surface states alone. The tunnelling current, based on the Bardeen model, summing the currents from tip to surface and from surface to tip is given by [6]:

$$I = \frac{4\pi e}{\hbar}\sum_{\nu\mu}\left[f(E^S_\mu - E^S_F) - f(E^T_\nu - E^T_F)\right]|M_{\mu\nu}|^2\delta(E^T_\nu - E^S_\mu - eV) \tag{2.106}$$

where f the is the Fermi-Dirac distribution, $M_{\mu\nu}$ the tunnelling matrix and V the bias voltage, and $E^{S,T}_F$ the Fermi energy of the surface/tip ($E^{S,T}_{\mu,\nu}$ are the energies eigenvalues of $\psi^{S,T}_{\mu,\nu}$). Replacing the the sum with an integral and using a smaller measurement resolution than k_BT, we can rewrite the above equation in terms of densities, and use a step function instead of the Fermi-Dirac distribution:

$$I = \frac{4\pi e}{\hbar}\int_0^{eV} d\epsilon n^T(E^T_F - eV + \epsilon)n^S(E^S_F + \epsilon)|M|^2 \tag{2.107}$$

where n^T and n^S are the tip and the substrate DOS's. Both of the surface and tip states contribute to the tunnelling current and it would be impossible to omit one from the above equation, rather one could approximate one in an arbitrary fashion. Taking a small bias voltage we can evaluate the above integral with:

$$I = \frac{4\pi e}{\hbar}Vn^T(E^T_F)n^S(E^S_F)|M|^2 \tag{2.108}$$

The corresponding differential conductivity is given by:

$$\frac{dI}{dV} = \frac{4\pi e}{\hbar}n^T(E^T_F)n^S(E^S_F + eV)|M(E^S_F + eV, E^T_F)|^2 \tag{2.109}$$

Which illustrates the ability of the STM to access the occupied and unoccupied states of the substrate by changing the sign of the bias voltage.

Now we turn to describing the tunnelling matrix $M_{\mu\nu} = \langle \psi_\nu^T | U_T | \psi_\mu^S \rangle$ by surface integral:

$$M_{\mu\nu} = \int_{z>z_0} \psi_\mu^S \underbrace{\left(E_\nu^T + \frac{\hbar^2}{2m} \frac{\partial^2}{\partial z^2} \right)}_{U^T} \psi_\nu^{T*} d^3r \tag{2.110}$$

where U^T is the tip potential. Taking $E_\mu^S = E_\nu^T$ due to the elastic tunnelling, and realising that the sample potential is zero, we get:

$$M_{\mu\nu} = -\frac{\hbar}{2m} \int_{z>z_0} \left(\psi_\nu^{T*} \frac{\partial^2 \psi_\mu^T}{\partial z^2} - \psi_\mu^{*S} \frac{\partial^2 \psi_\nu^T}{\partial z^2} \right) d^3r \tag{2.111}$$

Taking into account the following identity:

$$\psi_\nu^{T*} \frac{\partial^2 \psi_\mu^S}{\partial z^2} - \psi_\mu^S \frac{\partial^2 \psi_\nu^{T*}}{\partial z^2} = \frac{\partial}{\partial z} \left[\psi_\mu^{T*} \frac{\partial \psi_\nu^S}{\partial z} - \psi_\nu^S \frac{\partial \psi_\mu^S}{\partial z} \right] dxdy \tag{2.112}$$

The above one dimensional equation, which is the surface integral of two electrodes, contains only information about the wavefunctions over the surface between the two electrodes, and it can be extended to three dimensions:

$$M_{\mu\nu} = \frac{\hbar}{2m} \int_{\Omega^T} \left[\psi_\mu^S \Delta \psi_\nu^{T*} - \psi_\nu^{T*} \Delta \psi_\mu^S \right] \cdot d\overrightarrow{r} = \frac{\hbar}{2m} \int_\Sigma \left[\psi_\mu^S \overrightarrow{\nabla} \psi_\nu^{T*} - \psi_\nu^{T*} \overrightarrow{\nabla} \psi_\mu^S \right] \cdot d\overrightarrow{S} \tag{2.113}$$

The energy dependence of the tunnelling matrix must not be overlooked, as the energy scale in STS experiments easily exceeds ±2 eV. Therefore, we no turn to define M in terms of the eigenvalues of the tip and substrate wavefunctions. In the region between the tip and the substrate we have:

$$\psi_\mu^S(z) = \psi_\mu^S(0) \mathrm{e}^{-\chi_\mu^S z} \quad , \quad \psi_\mu^S(z) = \psi_\mu^S(s) \mathrm{e}^{\chi_\nu^T z - s} \tag{2.114}$$

where $\chi_\mu^S = \sqrt{2m|E_\mu^S|}/\hbar = \chi_\nu^T$ due to $E_\mu^S = E_\nu^T$, which is the result of elastic tunnelling. Using these relations the tunnelling matrix can be written as:

$$M_{\mu\nu} = \frac{\hbar^2}{2m} \mathrm{e}^{-\chi_\mu^S s} \int_{z=z_0} 2\chi_\mu^S \psi_\mu^S(0) \psi_\nu^T(s) dxdy \tag{2.115}$$

As we can see the argument in the integral is a constant, due to the fact that the $\psi_\nu^T(s)$ is the value of the tip-wavefunction at its surface. The above matrix element corresponds to constant height STM imaging since $z = z_0$ the integral is position independent, and the energy dependence comes from the decay constant χ_μ^S. The main contributions to the energy spectrum, as integrated in eq. 2.107, come from the energy spectrum of the tip near the Fermi level, and the substrate's empty states, $\sim$ eV above the Fermi level.

Now we are in the position to derive the final TH approximation, which is an approximation of the tunnelling matrix based on the used atomic orbital for the tip, which we here take it to be an s-orbital. The mentioned functions above, the tip and the surface near the Fermi obey the following Schrödinger equation:

$$-\frac{\hbar^2}{2m} \Delta \psi = -\Phi \psi \quad , \quad \Delta \psi = \chi^2 \psi \tag{2.116}$$

the s-orbital approximation of the tip delivers two solutions for the above equation, regular and irregular, from which we are interested in the regular one, namely the following modified Bessel function:

$$\psi_\nu^T(\overrightarrow{r} - \overrightarrow{R}_T) = Ck_0^{(1)}(\chi|\overrightarrow{r} - \overrightarrow{R}_T|) = C\frac{e^{-\chi|\overrightarrow{r} - \overrightarrow{R}_T|}}{\chi|\overrightarrow{r} - \overrightarrow{R}_T|} \tag{2.117}$$

where C is a normalization constant. Using this description for the tip wavefunction, results in the following expression for the tunnelling matrix:

$$M_{\mu\nu}(\overrightarrow{R}_T) = \frac{C\hbar^2}{2m}\int_{\Omega_T} \left[k_0^{(1)}(\chi|\overrightarrow{r} - \overrightarrow{R}_T|)\Delta\psi_\mu^S(\overrightarrow{r} - \overrightarrow{R}_T) - \psi_\mu^S(\overrightarrow{r} - \overrightarrow{R}_T)\Delta k_0^{(1)}(\chi|\overrightarrow{r} - \overrightarrow{R}_T|)\right] d\overrightarrow{r} \tag{2.118}$$

Noticing the singularity of the second part if the integral ar $\overrightarrow{r} = \overrightarrow{R}$ and the relationship between the Green function and the modified Bessel function $G(\overrightarrow{r} - \overrightarrow{r}') = \chi k_0^{(1)}(\chi|\overrightarrow{r} - \overrightarrow{r}'|)$, where $\Delta G(\overrightarrow{r} - \overrightarrow{r}') = -4\pi\delta(\overrightarrow{r} - \overrightarrow{r}')$, we rewrite the Δk_0 in the above integral as $(\chi^2 k_0^{(1)} - 4\pi\delta/\chi)$, which would reduce the tunnelling matrix, approximated with an s-orbital wavefunction into the following expression:

$$M_{\mu\nu}(\overrightarrow{R}_T) = -\frac{2\pi C\hbar^2}{\chi m}\psi_\mu^S(\overrightarrow{R}_T) \tag{2.119}$$

The above result is an approximation of an spherical tip around the point R_T with a point, so that the tunnelling matrix is only proportional to the sample wavefunction at the highest point of the surface. Fig. 2.2 illustrates the original Bardeen model of the spherical tip:

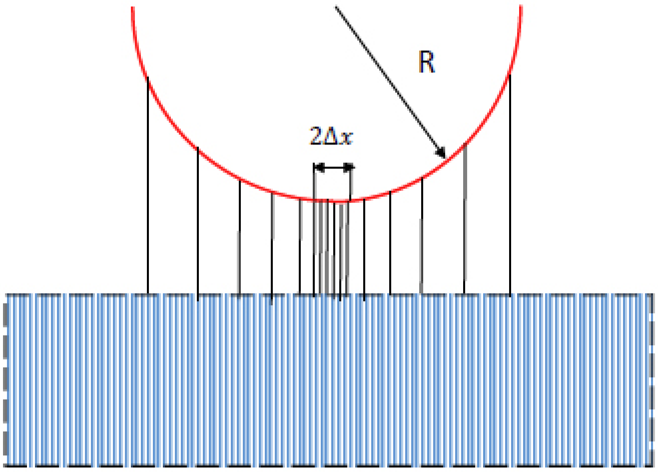

Figure 2.2: Estimation of the tip current by using the closest point to the surface where the current density is the highest. [6]

from which, it could be seen that in order to approximate the entire sphere, only the closest point to the surface could be taken into consideration and replaced with an atomic orbital, which in our case is an s-orbital. From the above expression we can now calculate the tunnelling current:

$$I(\overrightarrow{R}_T, V) = \frac{16\pi^3 C^2\hbar^3 e}{\chi^2 m^2} n^T \int_0^{eV} d\epsilon n^S(\overrightarrow{R}_T, E_F^S + \epsilon) \tag{2.120}$$

where n^T is a constant, and $n^S(\overrightarrow{R}_T, \epsilon) = \sum_\mu \delta(E^S_\mu - \epsilon)|\psi^S_\mu(\overrightarrow{R}_T)|^2$. Using these the final form of the tunnelling current would be:

$$I(\overrightarrow{R}_T, V) = \frac{16\pi^3 C^2 \hbar^3 e}{\chi^2 m^2} n^T \int_{E^S_F}^{E^S_F + eV} d\epsilon \sum_\mu \delta(E^S_\mu - \epsilon)|\psi^S_\mu(\overrightarrow{R}_T)|^2 \tag{2.121}$$

from which and the differential conductivity is:

$$\frac{dI(\overrightarrow{R}_T, V)}{dV} = \frac{16\pi^3 C^2 \hbar^3 e}{\chi^2 m^2} n^T \sum_\mu \delta(E^S_\mu - \epsilon)|\psi^S_\mu(\overrightarrow{R}_T)|^2 \tag{2.122}$$

Turning to our theory of quantum corrals in the multi-scattering formalism, which we introduced in section 1.3, we note that the tunnelling current is proportional to the integral of LDOS [15]

$$I \propto \int_{E_F}^{E_F + eV} n^T(\epsilon) \mathrm{LDOS}(R_T, \epsilon) d\epsilon \tag{2.123}$$

Therefore, we have for the LDOS and the differential conductivity:

$$\frac{dI}{dV}(\overrightarrow{R}_T, V) \propto \mathrm{LDOS}(\overrightarrow{R}_T, \epsilon) \propto \sum_\mu \delta(E^S_\mu - \epsilon)|\psi^S_\mu(\overrightarrow{R}_T)|^2 \tag{2.124}$$

from eq. 1.34 we know that $\mathrm{LDOS}(\mathrm{r}, \epsilon) \propto -(1/\pi)\mathrm{Im}[\mathrm{G}^{ret}(\mathrm{r}, \mathrm{r}, \epsilon)]$, and setting $\overrightarrow{R}_T = \mathrm{r}$ as free position, we get:

$$-\frac{1}{\pi}\mathrm{Im}[\mathrm{G}^{ret}(\mathrm{r}, \mathrm{r}, \epsilon)] = \sum_\mu \delta(E^S_\mu - \epsilon)|\psi^S_\mu(\mathrm{r})|^2 \tag{2.125}$$

where the retarded Green's function may be written in time domain as [6]:

$$\mathrm{G}^{ret}(\mathrm{r}', \mathrm{r}, t) = -i\theta(t) \sum_\mu \langle \mathrm{r}'|e^{-iE^S_\mu t/\hbar}|\psi^S_\mu\rangle\langle\psi^S_\mu|\mathrm{r}\rangle \tag{2.126}$$

and in the energy domain by taking the Fourier transform:

$$\mathrm{G}^{ret}(\mathrm{r}', \mathrm{r}, \epsilon) = \sum_\mu \frac{\psi^{S*}_\mu(\mathrm{r})\psi^S_\mu(\mathrm{r}')}{\epsilon - E^S_\mu + i\delta} \tag{2.127}$$

meaning that the surface states and their eigenvalues have to be the eigenvalues and the eigenfunctions of the scattering Hamiltonian, and it's relation to the Green's function. In conclusion, we see that the scattering theory using the Green's function, that we have already talked about in section 1.3 must be related to the surface states in the way that we described here, in order for a quantum corral to be observed using a TH-STM model. Even if the scattering is of the lowest order, some sort of confined state may still be observable in this formalism, which is the basis of our STM simulations. However, a complete quantum corral image can only be produced when a full multi-scattering takes place, and the tip states are there to interfere with the backscattered surface states constructively. And this is only possible in the non-equilibrium Green function formalism of STM, and STM simulations that are based on NEGF.

2.3 Time-Dependent Density Functional Theory

2.3.1 Linear Density Dielectric Response

In this section we discuss the theory of optical excitations and the dielectric as well as the EELS spectra of period systems in time-dependent DFT. All of these spectra are obtained from a frequency-dependent linear density-response function evaluated at real-space positions r, which has been subject to a time-dependent perturbation of frequency ω from position r'. It must be mentioned here, that there are a varieties of formalism regarding the linear response in *density functional perturbation theory* (DFPT), such as the Green's function approach (and other methods) by *S. Baroni & R. Resta*, or the *Sternheimer* linear response [51]. But the formalism that we introduce here are exclusively subject of TD-DFT, despite some similarities, which by extension into frequency independent exchange-correlation kernels, results in *Casida's equation*. As we shall see later, linear response from Casida's equation is a powerful method of calculating optical spectra for large molecules in a real-grid based formalism. Therefore, we are here in principle discussing the plane-wave version of the Casida's equation which is known as the linear response TDDFT (LrTDDFT).

The induced density from the linear density response function $\chi(\mathrm{r}', \mathrm{r}, \omega)$ is given by the following equation:

$$\delta n(\mathrm{r}, \omega) = \int d\mathrm{r} \chi(\mathrm{r}', \mathrm{r}, \omega) \delta V_{ext}(\mathrm{r}', \omega) \tag{2.128}$$

which leads to the central concept in TDDFT:

$$\chi(\mathrm{r}', \mathrm{r}, \omega) = \frac{\delta n(\mathrm{r}, \omega)}{\delta V_{ext}(\mathrm{r}', \omega)} \tag{2.129}$$

For periodic systems, where the sampling of the first Brilloun zone is required, the response function can be written in terms of it generic form $\chi_{\mathrm{GG}'}(\mathrm{q}, \omega)$:

$$\chi(\mathrm{r}', \mathrm{r}, \omega) = \frac{1}{N_q \Omega} \sum_{\mathrm{q}}^{\mathrm{BZ}} \sum_{\mathrm{GG}'} e^{i(\mathrm{q}+\mathrm{G})\cdot\mathrm{r}} \chi_{\mathrm{GG}'}(\mathrm{q}, \omega) e^{-i(\mathrm{q}+\mathrm{G})\cdot\mathrm{r}} \tag{2.130}$$

where G, and G' are the reciprocal lattice vectors, q is the wave-vector in the first Brilloun zone, and Ω the volume of the real-space primitive-cell. The evaluation of the optical properties using the above response function are done in RPA and ALDA (adiabatic LDA) level in GPAW, but this method is not quiet accurate for the optical excitations, since the electron-hole attraction are not properly taken into consideration. However, for the dielectric properties of the extended systems, this method has produced very accurate results which have been reported to be in good agreement with EELS experiments for bulk-metal surface, graphene-based systems, semiconductors, and superconductors.

Recalling the PAW formalism, we first note that all-electron expectation value of a semi-local operator is given by:

$$\langle \psi_{n\mathrm{k}} | A | \psi_{n\mathrm{k}} \rangle = \langle \tilde{\psi}_{n\mathrm{k}} | A | \tilde{\psi}_{n\mathrm{k}} \rangle + \sum_{a,ij} \langle \tilde{\psi}_{n\mathrm{k}} | \tilde{p}_i^a \rangle \langle \tilde{p}_i^a | \tilde{\psi}_{n\mathrm{k}} \rangle \times \left[\langle \phi_i^a | A | \phi_j^a \rangle - \langle \tilde{\phi}_i^a | A | \tilde{\phi}_j^a \rangle \right] \tag{2.131}$$

The point that the above expression makes clear regarding the expectation values, is that there is always the atomic PAW corrections to any expectation values, given by the second term in the sum. This is due to the fact that one has access to the frozen core states in PAW formalism, and for systems of localized d and f electrons the PAW formalism offers a distinct advantage in calculation the linear response. Having said that, which is the relevant concept for the calculation of the Kohn-Sham response function, one can obtain the interacting density function $\chi_{\mathrm{GG'}}(\mathrm{q},\omega)$ from the non-interaction Kohn-Sham density response function $\chi^0_{\mathrm{GG'}}(\mathrm{q},\omega)$, and an electron-electron interaction kernel, which in our case can either be evaluated in ALDA, or RPA level:

$$\chi_{\mathrm{GG'}}(\mathrm{q},\omega) = \chi^0_{\mathrm{GG'}}(\mathrm{q},\omega) + \sum_{\mathrm{G_1G_2}} \chi^0_{\mathrm{GG'}}(\mathrm{q},\omega) K_{\mathrm{G_1G_2}} \chi_{\mathrm{G_2G'}}(\mathrm{q},\omega) \tag{2.132}$$

The above equation is Dyson-like equation, which if reformed would be:

$$\chi = (1 - \chi^0 K)^{-1} \chi^0 \tag{2.133}$$

which maybe solved by gaining the right-hand side from the ground state. Furthermore, the two terms that are introduced in the above equation, namely the Kohn-Sham density response function $\chi^0_{\mathrm{GG'}}(\mathrm{q},\omega)$, and the interaction kernel $K_{\mathrm{G_1G_2}}$ have an extensive definition, which will briefly illustrate here.

First the non-interaction Kohn-Sham response function in it's Bloch representation is given by:

$$\chi^0_{\mathrm{GG'}}(\mathrm{q},\omega) = \frac{2}{\Omega} \sum_{\mathrm{k},nn'} (f_{n\mathrm{k}} - f_{n'\mathrm{k+q}}) \frac{n_{n\mathrm{k},n'\mathrm{k+q}}(\mathrm{G}) n^*_{n\mathrm{k},n'\mathrm{k+q}}(\mathrm{G'})}{\omega + \epsilon_{n\mathrm{k}} - \epsilon_{n'\mathrm{k+q}} + i\eta} \tag{2.134}$$

where the PAW term:

$$n_{n\mathrm{k},n'\mathrm{k+q}}(\mathrm{G}) = \langle \psi_{n\mathrm{k}} | e^{-i(\mathrm{q+G})\cdot\mathrm{r}} | \psi_{n\mathrm{k+q}} \rangle \tag{2.135}$$

which is known as the charge-density matrix, while the plane-wave term $e^{-i\mathrm{k}\cdot\mathrm{r}}$, $\mathrm{k} = \mathrm{q} + \mathrm{G}$ are expanded as follows:

$$e^{-i\mathrm{k}\cdot\mathrm{r}} = 4\pi \sum_{lm} i^l j_l(kr) Y_{lm}(\hat{\mathrm{r}}) Y_{lm}(\hat{\mathrm{k}}) \tag{2.136}$$

$\epsilon_{n\mathrm{k}}$ are the energy eigenvalues of the all-electron wave-function $\psi_{n\mathrm{k}}$, and $f_{n\mathrm{k}}$ are the (Fermi-Dirac) occupation numbers. The other representation of the Kohn-Sham response function, which is in real-space like the response function in eq. 2.129, can be obtained from the first order perturbation theory [51]

$$\chi^0(\mathrm{r'},\mathrm{r},\omega) = \lim_{\kappa\to 0^+} \sum_{a,i} (n_i - n_a) \left[\frac{\phi_i^*(\mathrm{r})\phi_a(\mathrm{r})\phi_i(\mathrm{r'})\phi_a^*(\mathrm{r'})}{\omega - (\varepsilon_a - \varepsilon_i) + i\eta} - \frac{\phi_i(\mathrm{r})\phi_a^*(\mathrm{r})\phi_a(\mathrm{r'})\phi_i^*(\mathrm{r'})}{\omega - (\varepsilon_a - \varepsilon_i) + i\eta} \right] \tag{2.137}$$

where i's are the occupied and a's the unoccupied Kohn-Sham orbitals, with n's as their respective occupation number. Therefore, as we can see the Kohn-Sham response function as given in the perturbation theory and in TDDFT are very close to each other. As we shall see, the main difference in calculation of the total density response function lies in the form of the eigenvalue problem (the Hamiltonian), that is set to be solved as a result of the external perturbation or field (V_{ext}).

Secondly, the interaction kernel $K^{\mathrm{G_1G_2}}(\mathrm{q})$, which has a Coulomb part and an XC-part, has different form in ALDA compared to RPA. Given the diagonal Coulomb kernel in Bloch representation [48]:

$$K^C_{\mathrm{G_1G_2}}(\mathrm{q}) = \frac{4\pi}{|\mathrm{q} + \mathrm{G_1}|^2} \delta_{\mathrm{G_1G_2}} \tag{2.138}$$

the XC-kernel in ALDA is given by [48]:

$$K^{xc-ALDA}_{\mathrm{G}_1\mathrm{G}_2}(\mathrm{q}) = \frac{1}{\Omega}\int d\mathrm{r} f_{xc}\left[n(\mathrm{r})\right] e^{-i(\mathrm{G}_1-\mathrm{G}_2)\cdot\mathrm{r}} \tag{2.139}$$

where f [52]

$$f^{ALDA}_{xc}[n(\mathrm{r})] = \frac{\partial^2 E_{xc}[n]}{\partial n^2}|_{n_0(\mathrm{r})} = \frac{dv^{LDA}_{xc}}{dn}|_{n_0(\mathrm{r})} \tag{2.140}$$

while the RPA interaction kernel, as it is used also in Casida's equation in real-space, is given by [49]

$$K^{RPA}_{ij\sigma,kq\tau} = \int d\mathrm{r}_1 d\mathrm{r}_2 \frac{n^*_{ij\sigma}(\mathrm{r}_1)n_{kq\tau}(\mathrm{r}_2)}{|\mathrm{r}_1-\mathrm{r}_2|} = (n_{ij\sigma}|n_{kq\tau}) \tag{2.141}$$

With that we can now introduce the relevant quantities in dielectric calculations, which starts with the dielectric function itself in reciprocal space defined as:

$$\epsilon^{-1}_{\mathrm{GG'}}(\mathrm{q},\omega) = \delta_{\mathrm{GG'}} + \frac{4\pi}{|\mathrm{q}+\mathrm{G}|^2}\chi_{\mathrm{GG'}}(\mathrm{q},\omega) \tag{2.142}$$

The frequency-dependent dielectric function in real-space is then obtained using the FFT algorithm, given in general as $\epsilon^{-1}(\mathrm{r},\mathrm{r}',\omega) = \delta V_{tot}(\mathrm{r},\omega)/\delta V_{ext}(\mathrm{r}',\omega)$. The macroscopic dielectric function, which can be calculated with local field effects or without it is given:

$$\mathrm{W-LFC} \quad \epsilon_M(\mathrm{q},\omega) = \frac{1}{\epsilon^{-1}_{00}(\mathrm{q},\omega)} \quad , \quad \mathrm{Wo-LFC} \quad \epsilon_M(\mathrm{q},\omega) = \epsilon_{00}(\mathrm{q},\omega) \tag{2.143}$$

Furthermore, the optical-absorption spectrum ABS the EELS spectrum are given by:

$$\mathrm{EELS} = -\mathrm{Im}\frac{1}{\epsilon_{\mathrm{M}}(\mathrm{q},\omega)} \quad , \quad \mathrm{ABS} = \mathrm{Im}\epsilon_M(\mathrm{q}\to 0,\omega) \tag{2.144}$$

while the macroscopic dielectric function itself can be calculated from the polarizability, $\mathrm{Im}\epsilon_M(\mathrm{q},\omega) = 4\pi\mathrm{Im}\alpha_M(\mathrm{q},\omega)$.

2.3.2 Linear Response: Casida's Method & Time Propagation

With the formalism of the linear density response formalism in TDDFT at hand, we now move to another set of implementations of linear response within the TDDFT framework, which have more to do with the time-dependency of the Kohn-Sham formalism, as the evolution of the dipole-moment with time becomes the central issue. However, a method named after Mark Casida, has proven to be an equivalent to the observation of the changes in dipole moment in time, even though it originates from solving the time-dependent Kohn-Sham equation [49]

$$i\frac{\partial}{\partial t}\psi_n(\mathbf{r},t) = \left[-\frac{\nabla^2}{2} + v_s(\mathbf{r},t)\right]\psi_n(\mathbf{r},t) \equiv F_s\psi_n(\mathbf{r},t) \tag{2.145}$$

where $v_s(\mathbf{r},t)$ the time-dependent Kohn-Sham effective potential:

$$v_s(\mathbf{r},t) = v_{ext}(\mathbf{r},t) + v_H(\mathbf{r},t) + v_{xc}(\mathbf{r},t) \tag{2.146}$$

and the all electron KS wavefunction $\psi_n(\mathrm{r},t)$:

$$\psi_n(\mathbf{r}) = \tilde{\psi}_n(\mathbf{r}) + \sum_a(\psi^a_n(\mathbf{r}-\mathbf{R}_a) - \tilde{\psi}^a_n(\mathbf{r}-\mathbf{R}_a)) \tag{2.147}$$

with the atom-centred AE and smooth wavefunctions ψ_n^a, $\tilde{\psi}_n^a$ expandable in terms of the atom-centred partial waves ϕ_j^a, and $\tilde{\phi}_j^a$ as described in eq. **??**. where the Hartree time-dependent potential is defined as a function of the time-dependent density $n(\mathbf{r}, t)$:

$$v_H(\mathbf{r}, t) = \int d\mathbf{r}' \frac{n(\mathbf{r}', t)}{|\mathbf{r} - \mathbf{r}'|} \quad , \quad n(\mathbf{r}, t) = \sum_n^{occ} f_n |\psi_n(\mathbf{r}, t)|^2 + \sum_a n_c^a(|\mathbf{r} - \mathbf{R}_a|) \tag{2.148}$$

where f_n is the occupation number of each orbital and $n_c^a(|\mathbf{r} - \mathbf{R}_a|$ the atom-centred frozen core electron density contribution.

Now here comes the crucial part in understanding the TDDFT formalism of linear response. In the previous formalism we obtained the response function perturbatively. while being the in the reciprocal space, we stated that the central concept in TDDFT is given by the eq. 2.129, while solving a Dyson-like equation for calculating the response function from the KS non-interacting response function and the interaction kernel. In real-space linear response TDDFT (LrTDDFT), almost the exact same formalism is applied although in real-space, with the main mathematical difference being that fact that the Dyson-like equation is replaced by a set of linear equations. There are a few more differences between the formalism however, the most notable of them being fact that linear density response (LDR) is applicable to extended systems since it is in reciprocal space and the Brilloun-zone is sampled by acquiring the KS response function in the reciprocal space. But LrTDDFT is done in real space for the given system without any extension to periodic boundary conditions (PBC). Therefore, in LrTDDFT it is the dipole oscillator strengths and the excitation energies that are important, while in the LDR the dipole transition matrix is part of the KS response function which gets extended into the entire space by the virtue of Bloch theorem, and Fourier transformed into the real-space response function.

Therefore, as we said in LrTDDFT in order to calculate the perturbation to the time-dependent density, it is expanded up to first order and set in a couple of linear equations against the external perturbative equation. However, without going into all that detail we start from the main equation for finding the dipole oscillator strength and the excitation energies namely the Casida equation [49]

$$\Omega F_I = \omega_I^2 F_I \tag{2.149}$$

with the transition energy to the excitation state s being $\hbar\omega_s$, while Ω is expanded in terms of KS particle-hole excitations, included in which is the interaction kernel similar to eq. {151}:

$$\Omega_{ij\sigma,kq\tau} = \delta_{ik}\delta_{jq}\delta_{\sigma\tau}\varepsilon_{ij\sigma}^2 + 2\sqrt{f_{ij\sigma}\varepsilon_{ij\sigma}f_{kq\tau}\varepsilon_{kq\tau}} K_{ij\sigma,kq\tau} \tag{2.150}$$

where $\varepsilon_{ij\sigma} = \varepsilon_{j\sigma} - \varepsilon_{i\sigma}$ and $f_{ij\sigma} = f_{j\sigma} - f_{i\sigma}$ are the energy and occupation number differences, with i, j, k, q as band indices and σ, τ as spin projection indices. The K interaction kernel, which is also the coupling matrix has two parts, $K_{ij\sigma,kq\tau} = K_{ij\sigma,kq\tau}^{RPA} + K_{ij\sigma,kq\tau}^{xc}$. The $K_{ij\sigma,kq\tau}^{RPA}$ is defined in eq {2.160}, and $K_{ij\sigma,kq\tau}^{xc}$ is defined as:

$$K_{ij\sigma,kq\tau}^{xc} = \int d\mathrm{r}_1 d\mathrm{r}_2 n_{ij\sigma}^*(\mathrm{r}_1) \frac{\delta^2 E_{xc}}{\delta\rho_\sigma(\mathrm{r}_1)\rho_\tau(\mathrm{r}_2)} n_{kq\tau}^*(\mathrm{r}_2) \tag{2.151}$$

with ρ_σ as the spin densities, and $n_{ij}(\mathrm{r})$ as pair density:

$$n_{ij}(\mathrm{r}) = \psi_i^*(\mathrm{r})\psi_j(\mathrm{r}) = \tilde{n}_{ij} + \sum_a (n_{ij}^a - \tilde{n}_{ij}^a) \tag{2.152}$$

We can now expand upon our formalism and arrive at the desired dipole oscillator strength and its eigenvalues, by introducing the set of quantities which we have previously mentioned in describing the PAW formalism in real-space, such as the compensation charge density $\tilde{Z}^a_{ij}$:

$$\int d\mathbf{r}_2 \frac{n^a_{ij}(\mathbf{r}_2) - \tilde{n}^a_{ij}(\mathbf{r}_2) - \tilde{Z}^a_{ij}(\mathbf{r}_2)}{|\mathbf{r}_1 - \mathbf{r}_2|} = 0 \quad , \quad \tilde{Z}^a_{ij}(\mathbf{r}_2) = \sum_L Q^a_{L,ij} g^a_l(\tilde{Z}^a_{ij}(r)) \tag{2.153}$$

with $L = l + m$ and $g^a_l(r)$ as an arbitrary function, $\int drr^{l+2} g^a_l(r) = 1$. The coefficients are further defined as follows:

$$Q_{L,ij} = \sum_{i_1 i_2} \Delta_{L,ij} P^a_{ii_1} P^a_{ji_2} \quad , \quad \Delta_{L,ij} = \int d\mathbf{r} r^l Y_L(\hat{\mathbf{r}})[\phi^a_{i_1}(\mathbf{r})\phi^a_{i_2}(\mathbf{r}) - \tilde{\phi}^a_{i_1}(\mathbf{r})\tilde{\phi}^a_{i_2}(\mathbf{r})] \tag{2.154}$$

where the expansion coefficients P^a_{ii} are defined in eq. 2.51. Using the following notation, $\tilde{\rho_{ij}}(\mathbf{r}) = \tilde{n_{ij}}(\mathbf{r}) + \sum_a \tilde{Z}^a_{ij}(\mathbf{r} - \mathbf{R}_a)$ we can rewrite the RPA kernel as:

$$K^{RPA}_{ij\sigma,kq\tau} = (\tilde{\rho}_{ij}|\tilde{\rho}_{kq}) + \sum_a \Delta K^{RPA,a}_{ij\sigma,kq\tau} \quad , \quad \Delta K^{RPA}_{ij\sigma,kq\tau} = (n^a_{ij}|n^a_{kq})_a - (\tilde{n}^a_{ij} + \tilde{Z}^a_{ij}|\tilde{n}^a_{kq} + \tilde{Z}^a_{kq})_a \tag{2.155}$$

And for the definition of $(*|*)$ we refer to the eq. 2.141. Furthermore, using the following notation:

$$K^{xc}_{ij\sigma,kq\tau}[n_\sigma, n_\tau] = \lim_{\varepsilon \to 0} \int d\mathbf{r} n^*_{ij\sigma}(\mathbf{r}) \frac{v^\sigma_{xc}[n_\sigma, n_\tau + \varepsilon n_{kq\tau}](\mathbf{r}) - v^\sigma_{xc}[n_\sigma, n_\tau - \varepsilon n_{kq\tau}](\mathbf{r})}{2\varepsilon} \tag{2.156}$$

we can write the XC-kernel similar to the RPA-kernel in the following way:

$$\begin{aligned} K^{xc}_{ij\sigma,kq\tau}[n_\sigma, n_\tau] &= \tilde{K}^{xc}_{ij\sigma,kq\tau}[\tilde{n}_\sigma, \tilde{n}_\tau] + \Delta K^{xc,a}_{ij\sigma,kq\tau} \\ \Delta K^{xc,a,\pm}_{ij\sigma,kq\tau} &= \lim_{\varepsilon \to 0} \frac{K^{xc,a,+}_{ij\sigma,kq\tau} - K^{xc,a,-}_{ij\sigma,kq\tau}}{2\varepsilon} \end{aligned} \tag{2.157}$$

where:

$$K^{xc,a,\pm}_{ij\sigma,kq\tau} = \langle \psi^a_{i\sigma}|v_{xc}[n^a_\sigma, n^a_\tau \pm \varepsilon n^a_{kq\tau}]|\psi^a_{j\tau}\rangle - \langle \tilde{\psi}^a_{i\sigma}|v_{xc}[\tilde{n}^a_\sigma, \tilde{n}^a_\tau \pm \varepsilon \tilde{n}^a_{kq\tau}]|\tilde{\psi}^a_{j\tau}\rangle \tag{2.158}$$

Now we can introduce the dipole oscillator strength, which is dimensionless, and is related to the eigenvectors F_I of the omega matrix Ω:

$$f_{I\alpha} = \frac{2m_e}{\hbar e^2} \omega_I \mu^2_{I\alpha} = \frac{2m_e}{\hbar e^2} \left| \sum_{ij\sigma}^{f_{i\sigma} > f_{j\sigma}} (\boldsymbol{\mu}_{ij\sigma})_\alpha \sqrt{f_{ij\sigma}\varepsilon_{ij\sigma}} (F_I)_{ij\sigma} \right|^2 \qquad \alpha = x, y, z \tag{2.159}$$

where the dipole transition moment of the ground $|0\rangle$ and the excited state $|I\rangle$ and the KS transition dipoles are given by:

$$\boldsymbol{\mu}_I = -e\langle 0| \sum_{k=1}^N \mathbf{r}_k |I\rangle \quad , \quad \boldsymbol{\mu}_{ij\sigma} = -e\langle \psi_{i\sigma}|\mathbf{r}|\psi_{j\sigma}\rangle \tag{2.160}$$

where N is the number of the electrons. And as usual the KS dipole transition can be partitioned in PAW, into smooth part and atom-centred part:

$$\begin{aligned} \boldsymbol{\mu}_{ij\sigma} &= -e\langle \tilde{\psi}_{i\sigma}|\mathbf{r}|\tilde{\psi}_{j\sigma}\rangle + \sum_a \sum_{pq} P^*_{i\sigma p} P_{j\sigma q} \boldsymbol{\mu}^a_{pq} \\ (\boldsymbol{\mu}^a_{pq})_m &= -e\sqrt{4\pi} \left[\frac{\Delta^a_{1m,pq}}{\sqrt{3}} + \Delta^a_{L=0,pq} (\mathbf{R}_a)_m \right] \end{aligned} \tag{2.161}$$

where the constants $\Delta^a_{L,pq}$ are as defined in eq. 2.154.

The continuation of this formalism, which similarly to the calculation of the optical excitation spectrum would lead, is known as the time-propagation TDDFT. This formalism however, is not exclusive to the calculation of the optical spectra, but also other dynamical effects, though the time-evolution of the dipole moment remains one of the most important applications. Returning to our time-dependent Schrödinger equation $i\hbar\partial_t\psi_n(t) = \hat{H}(t)\psi_n(t)$, where it undergoes the PAW transformation as follows [51]

$$i\hbar\hat{\mathcal{T}}^\dagger\partial_t\hat{\mathcal{T}}\tilde{\psi}_n(t) = \hat{\mathcal{T}}^\dagger\hat{H}(t)\hat{\mathcal{T}}\tilde{\psi}_n(t) \quad , \quad i\hbar\hat{S}\partial_t\tilde{\psi}_n(t) = \tilde{H}(t)\tilde{\psi}_n(t) \tag{2.162}$$

where $\tilde{S} = \hat{\mathcal{T}}^\dagger\hat{\mathcal{T}}$ is the PAW overlap operator. Now in contrast to the previous formalism, where the spectrum is simply calculated by the excitation energies, the evolution of the dipole moment requires the application of a delta pulse of a dipole field $\mathbf{E}(t) = \epsilon\mathbf{k^0}\delta(t)\hbar/a_0e$, a.k.a "the kick", which would instantaneously change the KS wavefunctions:

$$\psi(t=0^+) = \exp\left(i\frac{\epsilon}{a_0}\mathbf{k^0}\cdot\mathbf{r}\right)\psi(t=0^-) \tag{2.163}$$

where ϵ is the unitless perturbation parameter, $\mathbf{k^0}$ the polarization vector of the field, and a_0 the Bohr radius. Having applied the kick observe than the time-dependent many body wavefunction in its linear order expansion expansion:

$$|\Psi(t=0^+)\rangle = \left(1 - i\frac{\epsilon}{ea_0}\mathbf{k^0}\cdot\hat{\boldsymbol{\mu}}\right)|0\rangle + O(\epsilon^2) \tag{2.164}$$

where the $\hat{\boldsymbol{\mu}} = -e\sum_{k=1}^N \mathrm{r}_k$ is the dipole operator, using which one can extend the expansion to excited states as well:

$$|\Psi(t)\rangle = c_0|0\rangle + \sum_I e^{-i\omega_I t}c_I|I\rangle \tag{2.165}$$

with the coefficients given by:

$$c_0 = 1 - i\frac{\epsilon}{ea_0}\mathbf{k^0}\cdot\langle 0|\hat{\boldsymbol{\mu}}|0\rangle \quad , \quad c_I = 1 - i\frac{\epsilon}{ea_0}\mathbf{k^0}\cdot\langle I|\hat{\boldsymbol{\mu}}|0\rangle \tag{2.166}$$

which would allow the expansion of the time-dependent density as well:

$$n(\mathbf{r},t) = n_0(\mathbf{r}) + \sum_I(e^{-i\omega_I t}c_I\langle 0|\hat{n}(\mathbf{r})|I\rangle + c.c.) \tag{2.167}$$

with $\hat{n} = \sum_{k=1}^N \delta(\mathbf{r}-\mathbf{r}_k)$ as the density operator. Due to the absence of the magnetic fields we can therefore write:

$$\boldsymbol{\mu}(t) = -e\int d\mathbf{r}n(\mathbf{r},t)\mathbf{r} = \boldsymbol{\mu}(0) - \frac{2\epsilon}{ea_0}\sum_I \sin(\omega_I t)(\mathbf{k^0}\cdot\boldsymbol{\mu}_I)\boldsymbol{\mu}_I \tag{2.168}$$

from which the dipole oscillator strength can be obtained vie Fourier transform. However, more generally one calculates:

$$\boldsymbol{S}(\omega)\mathbf{k^0} = \frac{2m_e a_0}{e\hbar\pi}\omega\frac{1}{\epsilon}\int_0^T dt\sin(\omega t)g(t)[\boldsymbol{\mu}(0) - \boldsymbol{\mu}(t)] \tag{2.169}$$

which is the oscillator strength in terms of polarization direction $\mathbf{k^0}$, with T as the simulation-time and $g(t)$ as the envelope of the spectrum (Gaussian or Lorentzian). From the above result the following important relation between the dipole strength tensor, and the folded oscillator strength:

$$\mathbf{k^0}_\alpha\cdot\boldsymbol{S}(\omega)\mathbf{k^0}_\alpha = \sum_I f_{I\alpha}\tilde{g}(\omega-\omega_I) \tag{2.170}$$

with $\tilde{g}(\omega)$ as the folded Fourier transform.

2.3.3 Localized Surface Plasmon Resonances

Finally, we need to talk about the concept, which turns out to be useful in visualizing the plasmonics of graphene, due to the fact that the embedded structures, among other effects, do localized the surface plasmons in graphene and the details of such localizations are as important as the plasmonic spectra themselves. One important distinction however needs to be made between the surface plasmons, which are also called the surface plasmon polaritons (SPP), and the localized surface plasmons (LSP) [10]. While on the metallic surfaces, the surface plasmons propagate like an electromagnetic field by coupling to the electron plasma of the conductors, LSP's are non-propagating excitations of the conduction electrons, that are coupled to an electromagnetic field. This helps us distinguish the fact in our simulations, that even though on graphene one might observe propagating surface plasmons, once the silicon impurities are introduced, the plasmons become localized and no-longer take propagating shape. The reason for that is the scattering that takes place by the nanoparticles, which in our case are the Si-atoms within the metallic surface of the graphene. The visualization simulations, will clarify this concept in the coming sections, as does the figure below:

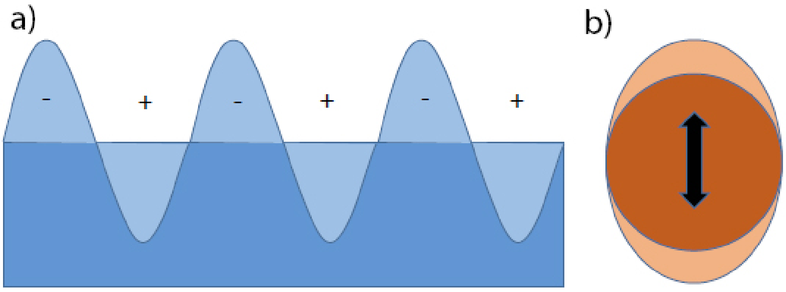

Figure 2.3: The comparison of the surface plasmons (a), with the localized surface plasmons (b) [45].

As stated above, the reason of interest in the LSPR's is the fact that the optical excitations of the nanostructures, that we are studying, have a maxima at the LSPR frequencies, and this is a general fact about the LSPR's [45].

Having calculated the SP frequency and dispersion relation in graphene in 1.2, we need to turn to some classical electromagnetic theory in order to be able to give an approximate theoretical description. The fact about the theories of LSPR, is that it is almost always described as surface plasmons of a spherical nanoparticle, for which $d \ll \lambda$ with the d as the diameter of the particle. If we start with the Mie theory of scattering, with the complex refractive index of metals as $\tilde{n} = n_R + in_I$, and n_m the real refractive index of the medium, we define the following parameters [45] to be used in cross-sections (eq. 2.172).

$$\begin{aligned} a_L &= \frac{m\psi_L(mx)\psi'_L(x) - \psi'_L(mx)\psi_L(x)}{m\psi_L(mx)\chi'_L(x) - \psi'_L(mx)\chi_L(x)} \\ b_L &= \frac{\psi_L(mx)\psi'_L(x) - m\psi'_L(mx)\psi_L(x)}{\psi_L(mx)\chi'_L(x) - m\psi'_L(mx)\chi_L(x)} \end{aligned} \tag{2.171}$$

where $x = k_m r$, and $m = \tilde{n}/n_m$, with k_m the wave-vector of the medium and r the radius of the nanoparticle. The ψ's and χ's are Riccati-Bessel function with $L = 2, 4, ...$ representing dipole, quadrupole, or multipoles of scattering. With that the scattering and extinction cross-sections are defined as:

$$\sigma_{sca} = \frac{2\pi}{|k|^2}\sum_{L=1}^{\infty}(2L+1)(|a_L|^2+|b_L|^2) \quad , \quad \sigma_{ext} = \frac{2\pi}{|k|^2}\sum_{L=1}^{\infty}(2L+1)[Re(a_L+b_L)] \tag{2.172}$$

where the absorption cross-section defined as $\sigma_{abs} = \sigma_{ext} - \sigma_{sca}$. The dielectric function of the medium is given by $\varepsilon_m = n_m^2$, and equivalently the dielectric function of the metal is $\tilde{\varepsilon} = \varepsilon_1 + i\varepsilon_2$ where:

$$\varepsilon_1 = n_R^2 - n_I^2 \qquad , \qquad \varepsilon_2 = 2n_R n_I \tag{2.173}$$

and the above formalism simplifies significantly for small particle ($x \ll 1$), into power series, and the resonance condition becomes $\varepsilon_1 = -2\varepsilon_m$ since this maximizes the extinction cross-section. So we use the expansion up to the order x^3, in which we get:

$$b_1 \approx 0 \quad , \quad a_1 \approx -i\frac{2x^3}{3}\frac{n_R^2 - n_1^2 + i2n_R n_I - n_m^2}{n_R^2 - n_1^2 + i2n_R n_I + 2n_m^2} \tag{2.174}$$

which is equivalent to:

$$a_1 = \frac{2x^3}{3}\frac{-i\varepsilon_1^2 - i\varepsilon_1\varepsilon_m + 3\varepsilon_2\varepsilon_m - i\varepsilon_2^2 + i2\varepsilon_m^2}{(\varepsilon_1 + 2\varepsilon_m)^2 + (\varepsilon_2)^2} \tag{2.175}$$

Using the above relation, and putting it in eq. 2.172, we get for the cross-sections:

$$\begin{aligned} \sigma_{ext} &= \frac{18\pi\varepsilon_m^{3/2}V}{\lambda}\frac{\varepsilon_2(\lambda)}{[\varepsilon_1(\lambda) + 2\varepsilon_m]^2 + \varepsilon_2(\lambda)^2} \\ \sigma_{sca} &= \frac{32\pi^4\varepsilon_m^2 V^2}{\lambda^4}\frac{(\varepsilon_1 - \varepsilon_m)_2}{[\varepsilon_1(\lambda) + 2\varepsilon_m]^2 + \varepsilon_2(\lambda)^2} \end{aligned} \tag{2.176}$$

So far there has been no explicit argument about the dielectric function of the metal itself, other than its role in calculation of the cross-sections. However, in order to calculate the resonance frequency of the LSP's, the explicit from of the dielectric function is necessary. For the sake of simplicity, we do not use the expression that we have derived in , and suffice to the simplest model, namely the Drude-model:

$$\varepsilon_1 = 1 - \frac{\omega_p^2}{\omega^2 + \gamma^2} \qquad \gamma \ll \omega_p \quad \Rightarrow \quad \varepsilon_1 = 1 - \frac{\omega_p}{\omega^2} \tag{2.177}$$

using the resonance condition $\varepsilon_1 = -2\varepsilon_m$ we get for the resonance frequency and wavelength:

$$\omega_{max} = \frac{\omega_p}{\sqrt{2\varepsilon_m + 1}} \qquad , \qquad \lambda_{max} = \lambda_p\sqrt{2n_m^2 + 1} \tag{2.178}$$

where λ_p (ω_p) is the plasma wavelength of the material. Therefore, if we wanted to calculate the correct LSPR frequencies for our systems, we would need to use the dielectric function calculated in linear density response TDDFT, and use the SP frequency for graphene in eq. 1.26. Furthermore, for systems that not spherical, a numerical scheme such as the *discrete dipole approximation* (DDA) or the *finite different time domain* (FDTD) has to be used for the calculation of the LSPR frequencies.

Chapter 3

Analytical Potential Simulations Results

3.1 Evaluating the Analytical Potentials

3.1.1 Tersoff Potential in LAMMPS

As the theoretical and the introductory sections have already indicated, in order to find the most efficient path to the correct results, we started by using a few different potentials, within a couple of different codes. However, since the experimental verifications are not part of this thesis, the reference for benchmarking remains first the literature values for the physical quantities, and the DFT calculations for any computational simulations. Therefore, the first task would be finding the most reliable analytical potential, which would produce the closest results to the DFT simulations, which then are compared against the literature values. The first code of choice for simulating large structures, was LAMMPS, due to its vast choice of bond-order potentials, and relative ease of use. The LAMMPS program is a whole package, where the analytical potentials are provided in addition to different optimization and MD-engines. Therefore, LAMMPS could be used without any external interface, just by inputing a set of parameters in a *BASH* (Bourne again shell) format. The disadvantage of using LAMMPS is the fact that there is nor GUI (graphical user interface) which one might use for designing a structure, and so the atomic positions and the primitive unit-cell has to be manually defined in LAMMPS. However, it is always the supercell that undergoes the simulation and not the primitive unit-cell.

After having tested a few structures, and having ruled out certain structures, and lines, the first set of simulations of zigzag-lines produce the following structures using the Tersoff potential, as shown in fig. 3.1.

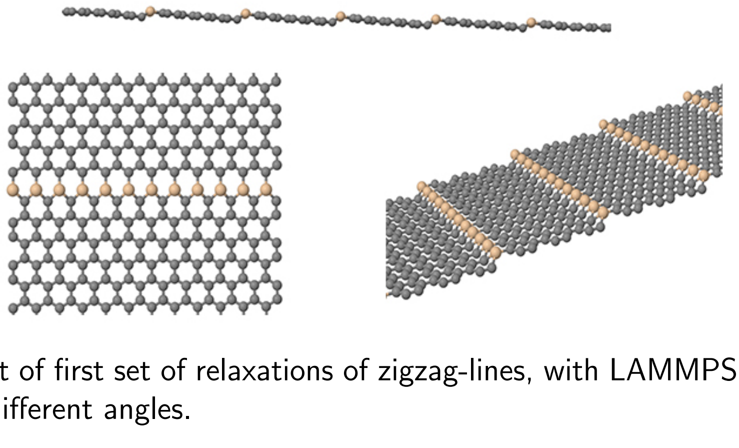

Figure 3.1: The result of first set of relaxations of zigzag-lines, with LAMMPS using the Tersoff Si-C potential from different angles.

The above relaxation, was done with FIRE algorithm since in choosing the right cell-size, this algorithm proved to be the smoothest, namely least prone to be stuck in local extrema. Choosing the right cell-size was done using a BASH script, in which both x, y coordinates were changed in an interval, one by one, which were expected to produce results as seen in fig. 3.2.

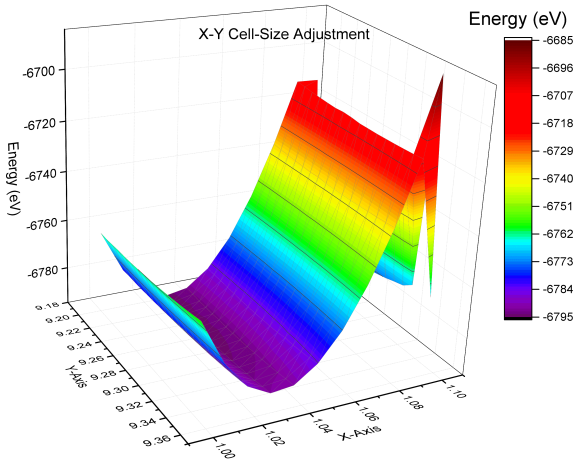

Figure 3.2: The X-Y coordinates cell-adjustment using the FIRE algorithm and the Tersoff potential in LAMMPS, showing the minimum only for X coordinate.

In the above 3D diagram the darkest point on the surface in principle has the lowest energy. However, regarding the above results it must be said that, such structures despite having the lowest energy in one direction, namely the x coordinate, in the y direction do not represent the lowest energy structures, as the diagram also indicates. The y coordinate adjustment, as seen in fig. 3.3, of the absolute lowest energy would result in a wavy structure, which we will present an example of an at the end of this section.

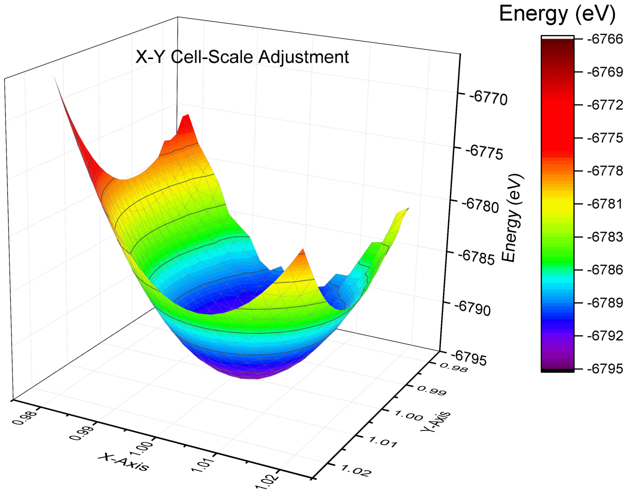

Figure 3.3: The X-Y coordinates cell-scale adjustment, in the interval of $\pm 2\%$, using the FIRE algorithm and the Tersoff potential in LAMMPS.

These structures were considered not realistic, and physically undesirable due to the fact that the flat graphene in between the lines was lost, resulting in an wavy sheet, which could be easily destroyed by the electron beam or the phonon vibrations at room temperatures. For that reason, as the fig. 3.2 shows, the global minimum for the cell-size could not be clearly determined. Therefore, the results were relaxed a second time using a *restart* command in LAMMPS which further relaxes a previously relaxed result with the possibility of rescaling the cell-coordinates. This way of fine-tuning the cell-size was known to find the local minimum on the energy curve. That's why we chose a small $\pm 2\%$ rescaling interval for both x, and y coordinates to find the clear and absolute minimum of the energy in the curve, as shown in 3.3.

However, even despite having found a good candidate for zigzag line structure, and observing a smooth set of relaxation curves (harmonic at the minimum), the relaxed results were no different than those in fig. 3.1. Therefore, in the next set of relaxations we chose to start with strickter relaxation parameters (10000 iterations, 10^{-12} eV threshold). But the change in results were minimal, as seen in fig. 3.4.

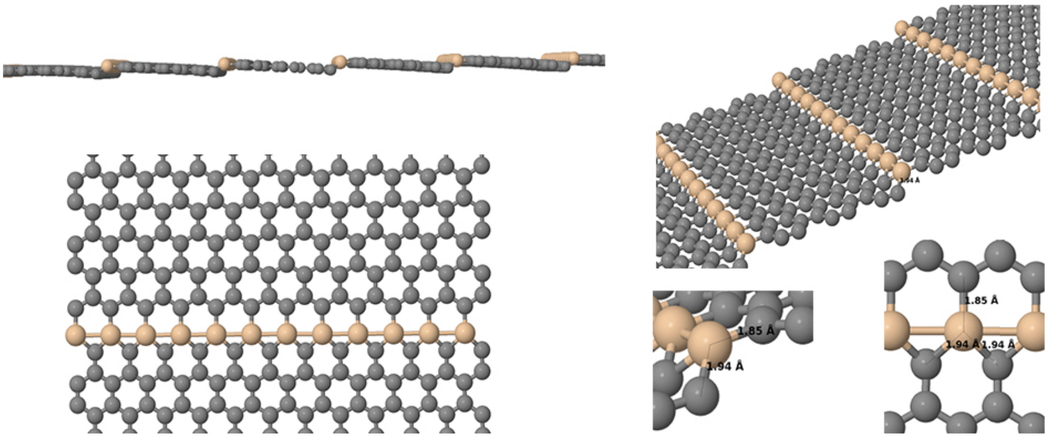

Figure 3.4: The results of simulations with strickter parameters of relaxation using the FIRE algorithm and the Tersoff potential.

The logic behind the above relaxations was to find a physically acceptable structure while approaching the energy minimum, by searching in the x direction and taking a guess by expanding the y coordinate in multiples of graphene cell y-coordinate ($\approx 2.42\text{Å}$), so that our structure would have a flat graphene in between the lines, as seen in fig. 3.5.

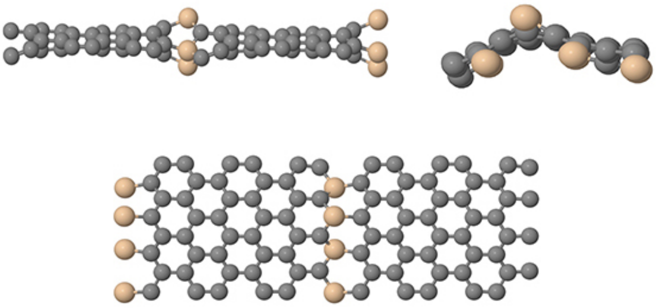

Figure 3.5: An example of a zigzag-line structure with global and local minimum-energy cell-size, using the Tersoff potential

The absolute minima in the global X-Y cell-size search and local fine-tuning would produce structures like the one above in fig. 3.3. Therefore, using the Tersoff potential in LAMMPS for the above zigzag line, we seemed to be unable to achieve this goal, since the flat structures of above were not at the global energy minimum, and also slightly unrealistic. And the structure that were at the global energy minimum were completely distorted, and unphysical.

3.1.2 Tersoff & EA in LAMMPS

After having measured the bond-lengths, and established non-conclusiveness of the results obtained from Tersoff potential in LAMMPS, we decided to benchmark the potential against another analytical potential and then check the results with DFT. The best candidate was the analytical potential of Erhard-Albe, which is based on the Brenner functional. The set of structures that we chose for benchmarking (other than graphene itself), was the 2D Si-C, single trivalent Si in graphene, and a custom zigzag (ZZ) line structure, where the lines are on alternating sublattices, with a distance of three graphene-rows in between. The custom zigzag line structure relaxed using Tersoff potential, and the EA potential, had the best converged form as in fig. 3.6 and 3.7.

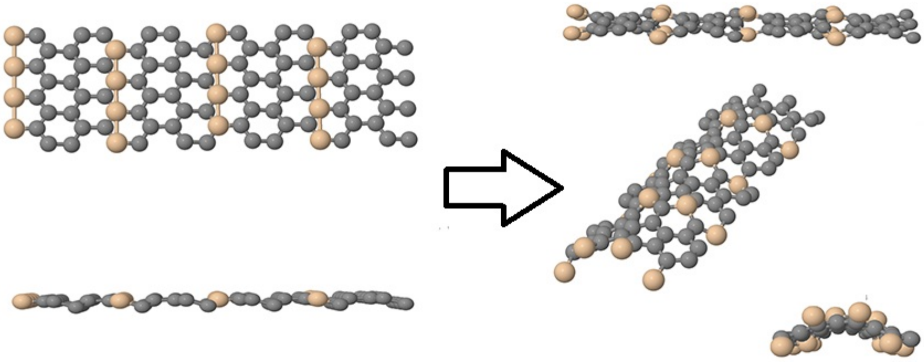

Figure 3.6: Relaxed structure of the custom zigzag line, with the Tersoff potential and starting from a somehow different initial guess.

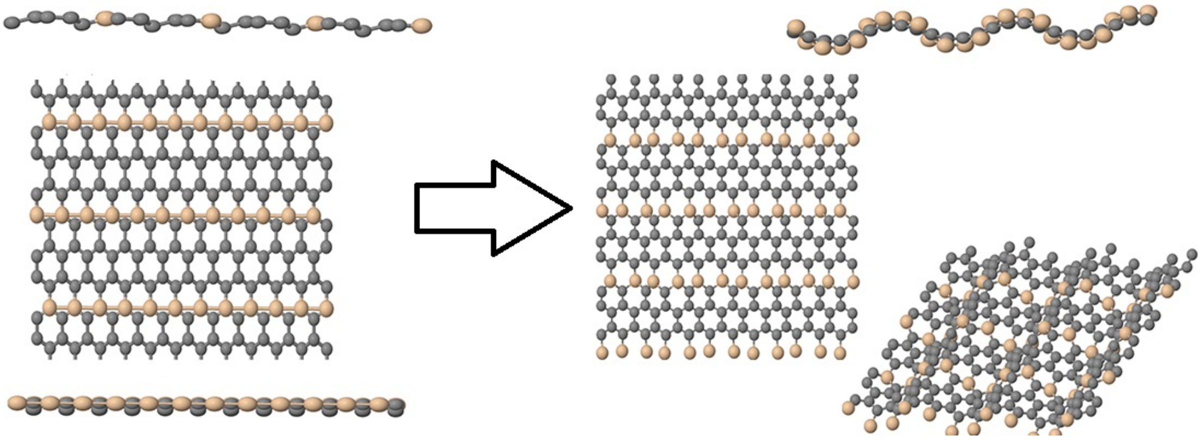

Figure 3.7: Relaxed structure of the custom zigzag line, with the EA potential and starting from a somehow different initial guess.

The above set of results were achieved using the exact same parameters, and initial condition, with the only difference being the analytical potential used. The results, represent the global (and local) minimum on the energy/relaxation curve, which we previously considered unphysical and unrealistic. They indeed look very similar, but the DFT simulations, in a combined method of PW and FD, produced a completely different result, as seen in fig. 3.8

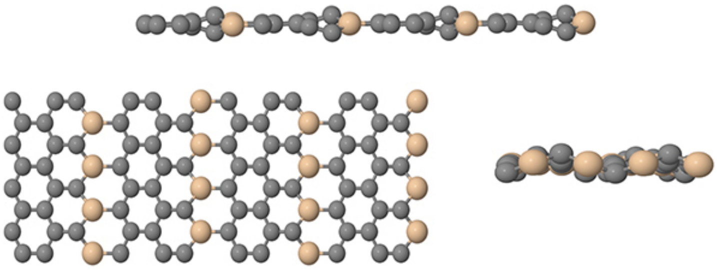

Figure 3.8: The DFT results of zigzag line relaxations using the PBE-GGA XC-functional, in PW and FD mode.

It turns out for this system, namely the custom zigzag line with 3 graphene rows in between, taking the DFT structure (or a similar configuration) as the starting point, using both of the potentials, an acceptable corrugated structure could be produced, as seen in fig. 3.9.

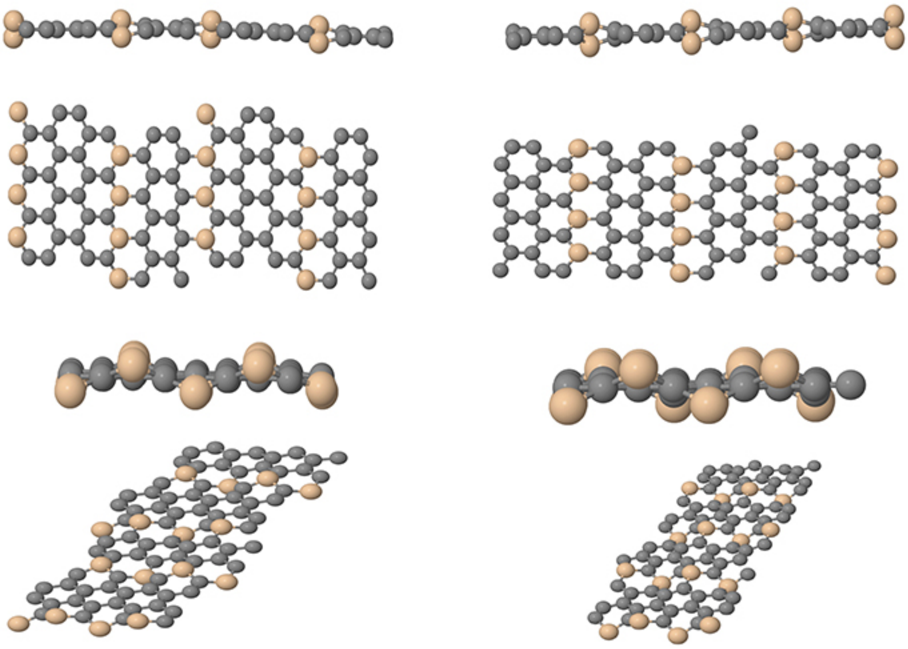

Figure 3.9: The relaxation results of custom zigzag line structure using both Tersoff (left) and EA (right) potentials, starting from the DFT relaxed structure as initial guess.

Therefore, it is clear that having the Si-lines close to each other, the Tersoff potential can produce as reasonable result as the EA potential. However bond-length differences in fig. 3.10 are noticeable.

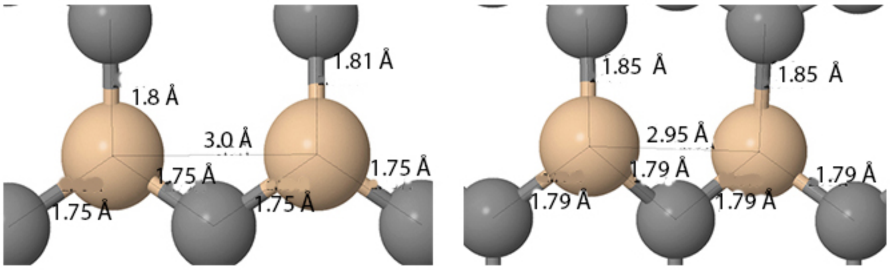

Figure 3.10: The bond lengths differences of custom zigzag line structure using both Tersoff (left) and EA (right) potentials, starting from the DFT relaxed structure as initial guess.

Now we can look at the rest of the structures, that we compared in both of the potentials. Fig. 3.11 shows the single trivalent silicon in a graphene sheet from different angles, and the 2D Si-C sheet.

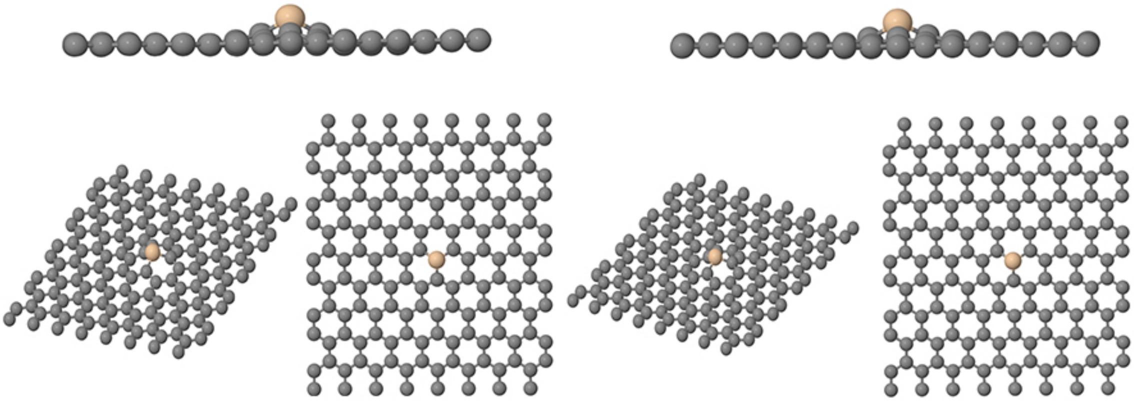

Figure 3.11: The relaxation results of single trivalant silicon in graphene using both Tersoff (left) and EA (right) potentials.

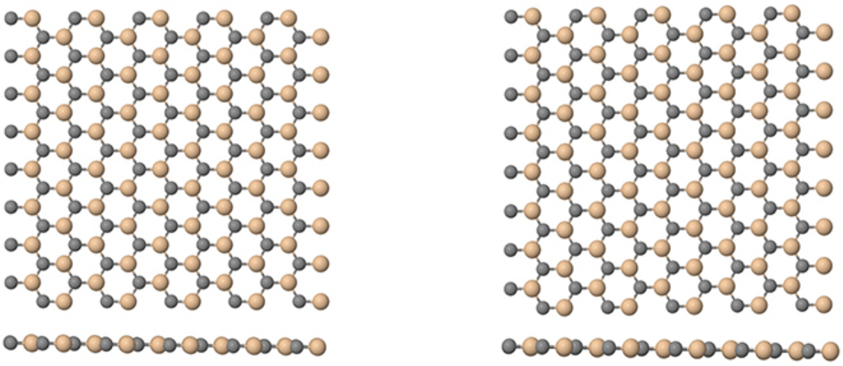

Figure 3.12: The relaxation results of 2D Si-C sheet using both Tersoff (left) and EA (right) potentials.

So far every comparison almost shows the same result for both of the potentials. In order to summarize and gain some more insight however, we can now compare the numbers of bond-lengths and the energies of the above 3 structures with the DFT (in FD mode), in tab. 3.1 (μ_C is the carbon chemical potential calculated from prisitine graphene energy in the given potential).

Table 3.1: The summary of the relaxation data of bond-lengths, and embedding energies per C/Si-atoms in different structures, for Tersoff, EA, and DFT-PBE potentials in FD mode.

Potential Structure	Tersoff T89	Erhard-Albe	DFT-PBE
μ_C in Graphene	1.462 Å -7.392 eV	1.478 Å -7.385 eV	1.426 Å -9.223 eV
Custom ZZ line	1.75 Å -2.324 eV	1.79 Å -3.2651 eV	1.748 Å -2.686 eV
Trivalant Single Si	1.76 Å -2.658 eV	1.75 Å -2.795 eV	1.761 Å -1.582 eV
2D Si-C Sheet	1.81 Å -3.984 eV	1.82 Å -4.661 eV	1.792 Å -4.737 eV

The above energies are per atom energies, and in the case of the 3 structures with silicon, the energies are embedding energies of single Si-atom. For the bond-lengths in the custom ZZ line, the value refers to the shortest two bonds. The comparisons of the values the Tersoff potential might be correct choice compared to the DFT results, other than in the case of 2D Si-C, where the energy per Si-atom is closer to the DFT energy. But the fact is that, as the further simulations demonstrate, for structures where the Si-atoms are close to each other, the Tersoff potentials seems a better choice, however as the Si-structures get further away from each other the interaction range of the Tersoff potential does not resemble that of the DFT, and since the structures do not interact, flat lines like those in fig. 3.1 and 3.2, appear as the minimum energy structures. Fig. 3.13 illustrates this fact.

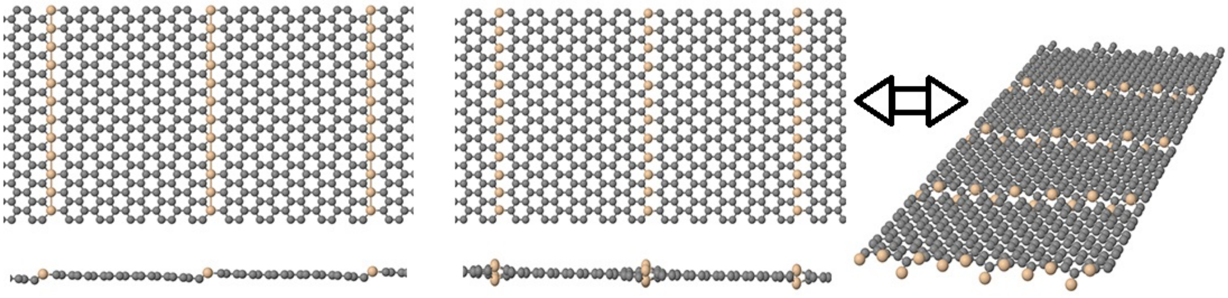

Figure 3.13: The relaxed ZZ-line results with 10 rows of graphene in between, relaxed using the Tersoff (left) and EA (center and right) potentials.

As the figure in the far left above shows, when the distance between the lines increases, the lines in the Tersoff potential no longer interact, and therefore the corrugated line shape disappears. But for the EA potential, even with 10 graphene rows in between the Si-lines, ZZ lines in the above structure still interact, which leads to a corrugated line structure, in between which there is flat pristine graphene. Therefore, the choice for the further simulations was the EA potential.

3.1.3 EA Potential in Atomistica & ASE

Knowing the limitations and the advantages of EA potential and the LAMMPS environment, we decided to continue with the EA potential, however in a different environment, which offered a few advantages over LAMMPS. The *atomic simulations environment* (ASE), which is also the interface to the GPAW code, could be coupled to the EA potential using the Atomistica calculator, which is an analytical MD engine. It has a set of Brenner-functional based potentials, in addition to other inter-atomic potentials. The main advantage of this method is that, while using ASE as the minimizer/optimizer engine, all the optimization algorithms of ASE could be used for energy-minimization, such as SciPyMinCG, or BFGS, and also the size of the supercell could be adjusted using the *Strain-Filter* (SF). The existence of strain-filter significantly increases the optimization efficiency, compared to LAMMPS where only atomic positions are optimized. Therefore, we decided to study the convergence behaviour of one system, and compare it to GPAW.

The optimization is ASE was done in two stages, one using loops adjusting the X-Y coordinate, while optimizing the atomic positions up to 5000 iterations, thereby looking for the global minimum cell-size. Second, taking the absolute lowest X-Y cell-size in energy, and further optimizing the atomic positions and the cell-size using the strain-filter in sequences, while decreasing the force threshold, as shown in fig. 3.14.

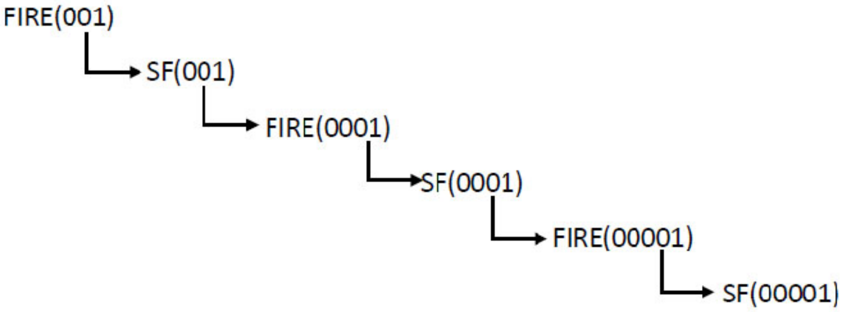

Figure 3.14: The relaxation scheme in ASE with EA potential, using the FIRE algorithm and the Strain-Filter (SF) in sequences while decreasing the threshold.

Enabling the energy function in ASE, the two dimensional X-Y cell adjustment produces curves like these, in fig. 3.15

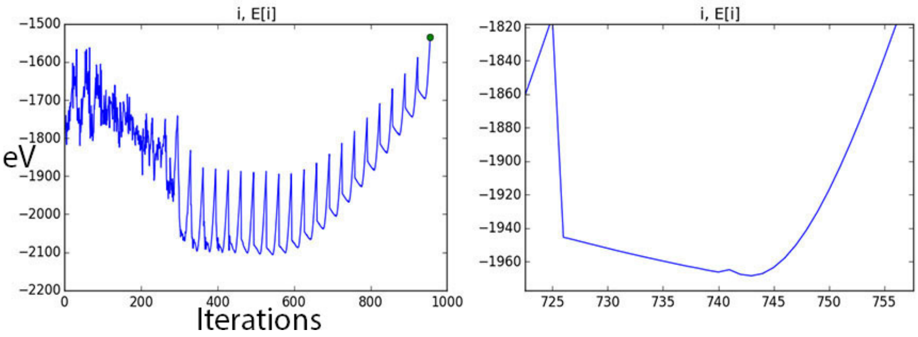

Figure 3.15: The X-Y cell-size adjustment energy curves, showing the global lowest energy X-Y combination for the cell.

From which the best guess for the X-Y coordinates of the cell could be chosen for further optimization using the strain-filter according to the scheme in fig. 3.14.

However, in certain structures, like the single trivalent silicon in graphene, it makes a difference whether or not the silica-patterns are symmetrically embedded onto the graphene or anti-symmetrically. Fig. 3.16 shows the 6x super-cell size relaxed structure, both in symmetric and antisymmetric configurations:

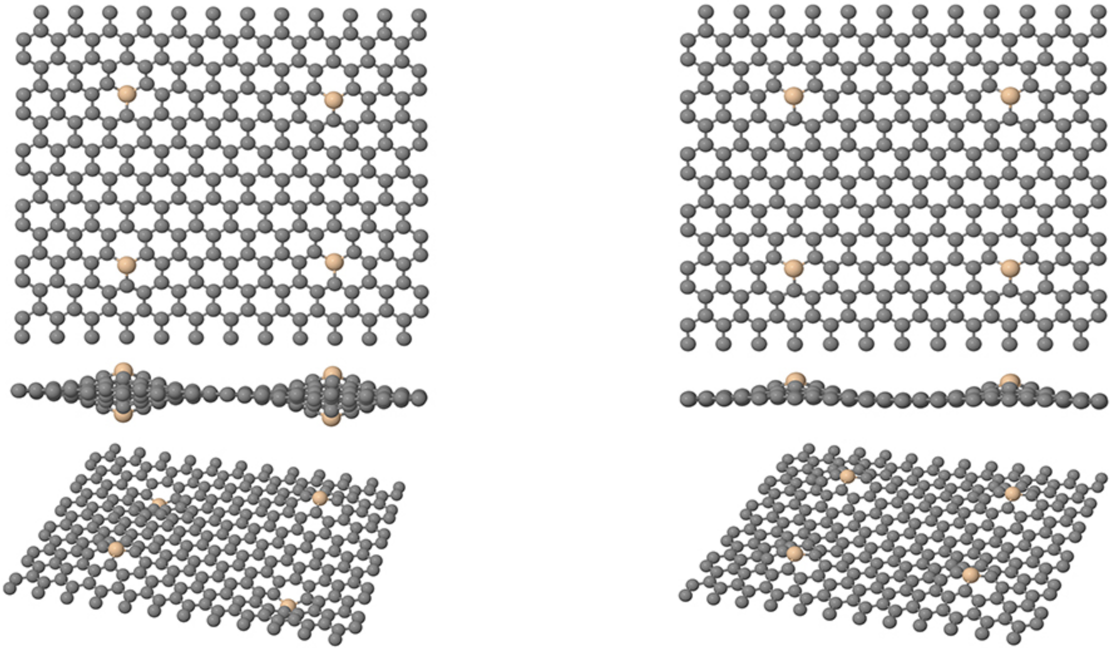

Figure 3.16: The relaxed trivalent single silicon in graphene for 6x supercell in both symmetric and anti-symmetric configuration.

Now we can compare the symmetric case with DFT and compare the convergence curves. For that we relaxed 3 different supercell size in DFT for the symmetric case, with two different chemical potentials. Fig. 3.17 shows the results (note that the Energy / Si is calculated according to $E_{Si} = (E_{Tot} - N_C \cdot \mu_C)/N_{Si}$).

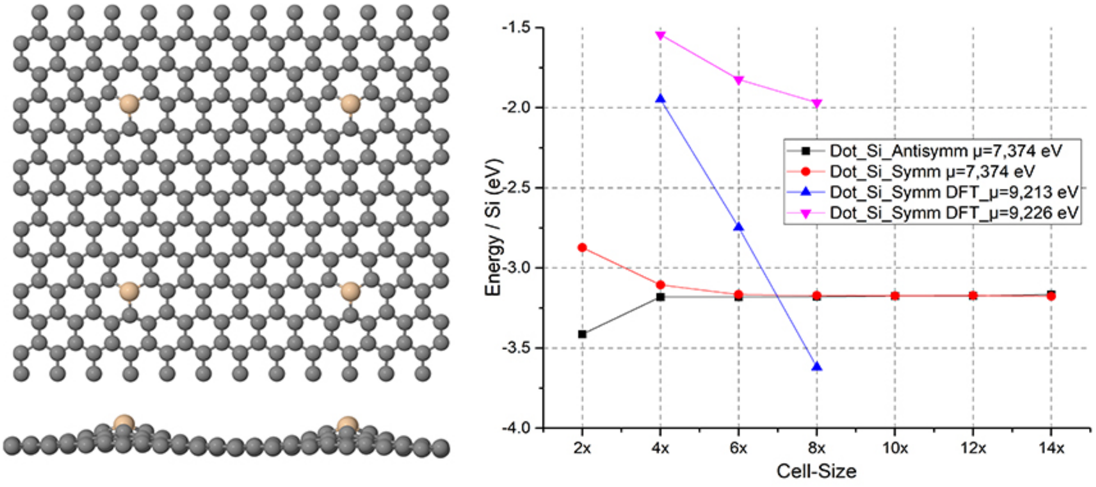

Figure 3.17: Left: The relaxed symmetric trivalent single silicon in graphene for 6x supercell in DFT. Right: the convergence behaviour of the symmetric/antisymmetric single silicon in graphene using EA in ASE and DFT-PBE

Where N_C is the number of C-atoms and μ_C is the carbon chemical potential. The bond-lengths in EA are 1.77Å and in DFT-PBE 1.76Å, and the convergence behavior in the case of a symmetric configuration are similar between EA and the DFT, and therefore the relaxation method in ASE using the EA could be trusted for the rest of the structures.

3.2 Geometries, & Energetics of the Structures

3.2.1 Zigzag- & Armchair Lines: Dense, Dashed & Double-Dashed

The first set of structures that we studied, were the lines, since we had already did the benchmarking using the dense ZZ line. The number of lines, that could be embedded in graphene is quite large taking into account the distance between the Si-atoms along the line as a variety. Specifically the ZZ-line is of particular interest, and so starting with ZZ-line ,we also study the effect of distance between the Si-atom on the convergence and the energetics. Fig. 3.18 shows the converged cell-size for the dense ZZ-line, in both symmetric and anti-symmetric configuration.

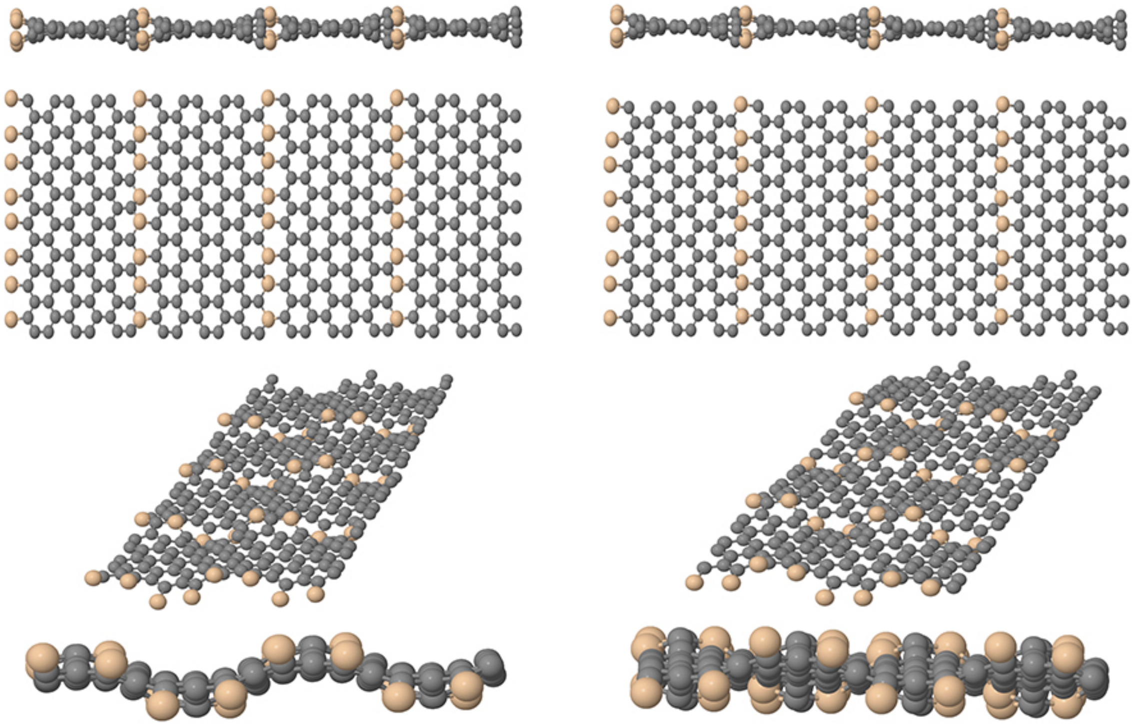

Figure 3.18: Left: The relaxed ZZ line structure for the converged cell-size of 6x in both symmetric (left), and antisymmetric (right) configurations.

In the case of the above structures, similar to the case of the single silicon in graphene as well, there seems to be no difference energetically in arranging the lines symmetrically or antisymmetrically, since the above cell-size is the converged size (namely that there are no interactions between the lines). For the converged cell-size, the energies overlap and remain the same for larger cell-sizes (see fig. 3.17), while for the smaller cells there is energy difference between the symmetric and the antisymmetric case. Looking at the structures from the long-side, it can be seen, that the distortion in graphene remains similar in both cases, and that explains the indifference in embedding energy per silicon. In addition to the energy, the bond-lengths of the above structures are shown in fig. 3.19.

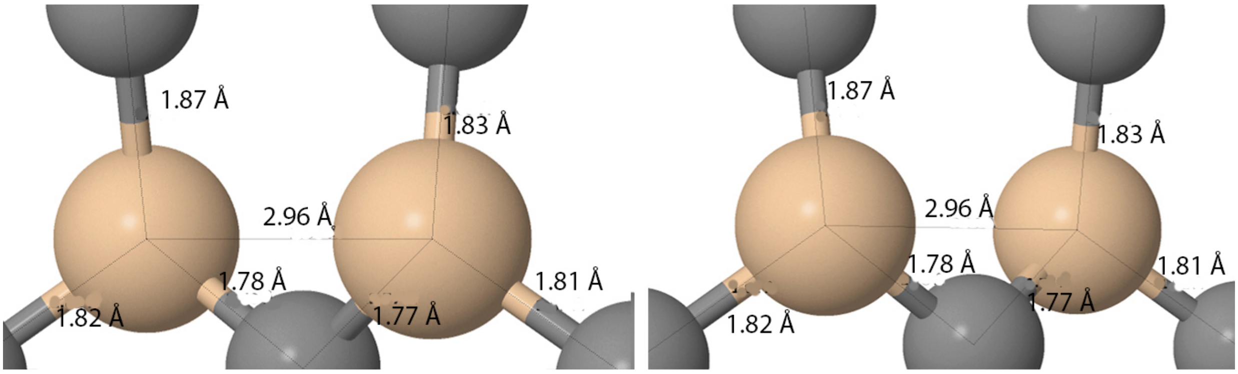

Figure 3.19: The bond lengths of the symmetric ZZ-line in 6x supercell (left) compare to the antisymmetric ZZ-line bond lengths.

Also the bond-lengths in the above variations seem to be exactly the same, proving the equality of the configurations for this cell-size.

The next studied structure was the dashed version of the ZZ-line, shown in fig. 3.20.

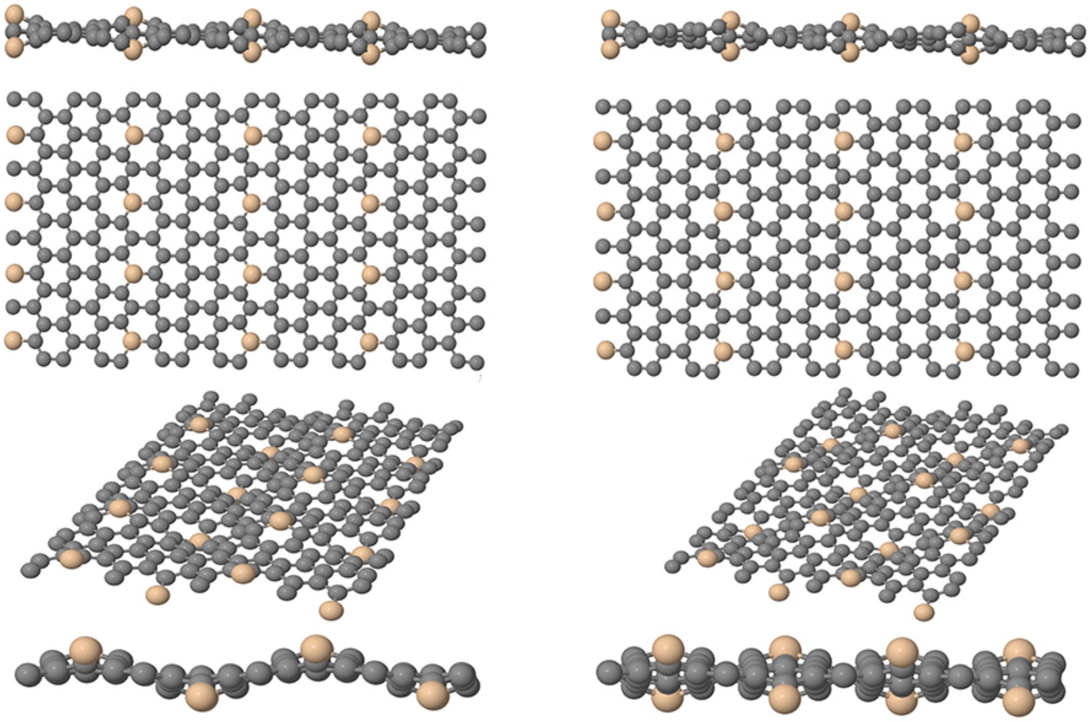

Figure 3.20: The relaxed dashed ZZ-line for the converged 4x cell-size, in symmetric (left) and antisymmetric (right) configurations.

For the above structures in the above supercell of 4x, the total energy difference was ≈ 1 eV in favour of the antisymmetric configuration (1819.5 eV symmetric, and 1820.5 eV antisymmetric) for a total of 1029 atoms. Therefore, even though as we explained before the antisymmetric structure is preferred, for the converged supercell size this preference disappears, with the amount of silicon embedding-energy per atom being almost the same.

In fig. 3.21 present the other two versions of the dashed ZZ-line, namely the double-dashed (DD) ZZ-line, and the quad-dashed (QD) ZZ-line, both only in antisymmetric configurations.

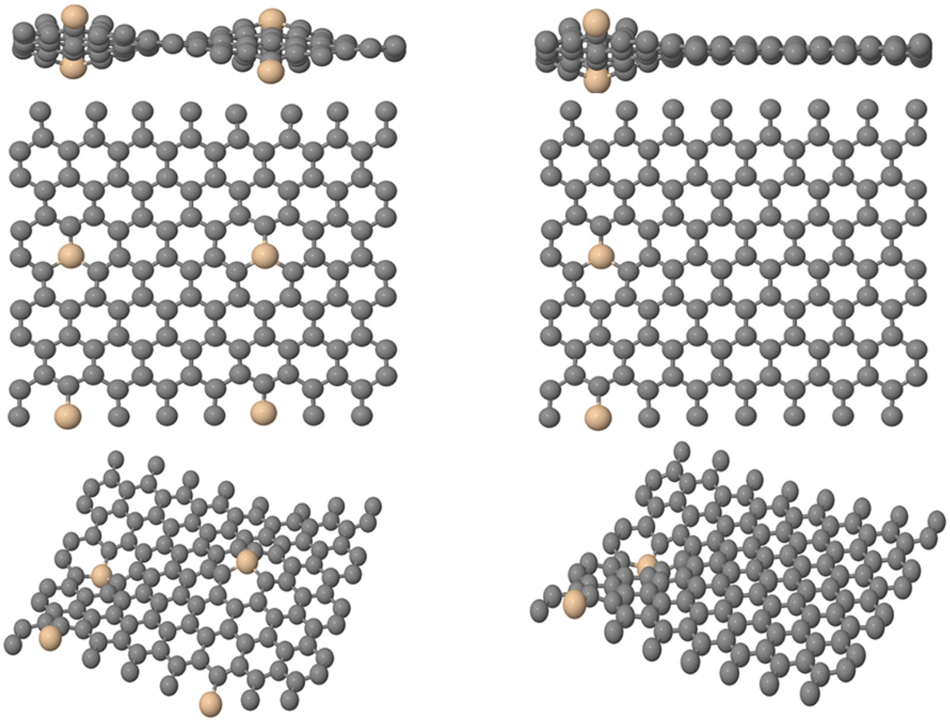

Figure 3.21: The relaxed (left) double dashed- (DD), and (right) quad-dashed (QD) ZZ-line for the converged 4x cell-size, in antisymmetric configurations.

Now we can summarize and compare the convergence behaviours of the ZZ-line for cell-size and the distance between the Si-lines along the line (dashing) in the following common plots (in the left plot 1.0, 2.0, 3.0, 4.0 mean the dense,dashed, DD and QD, ZZ-line), in fig. 3.22.

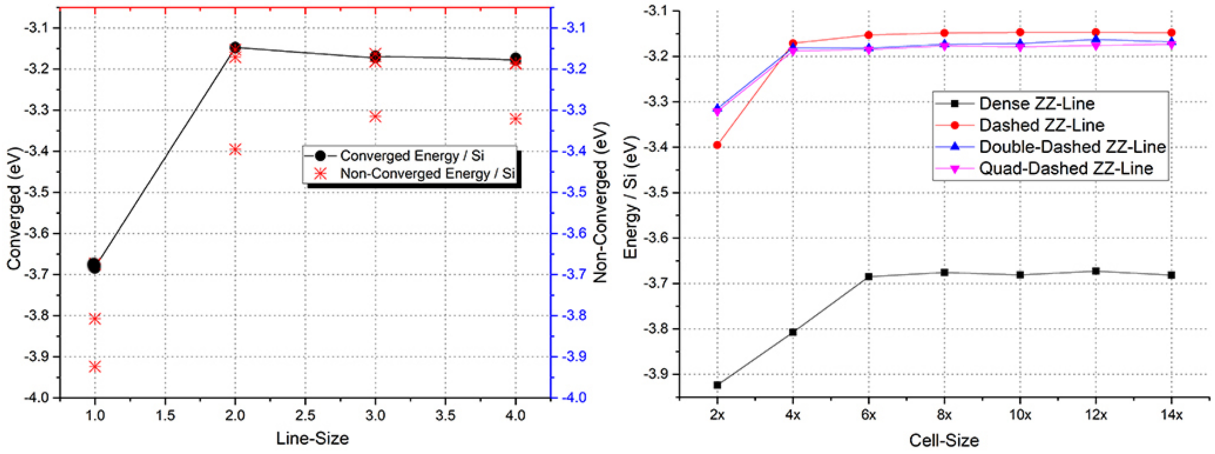

Figure 3.22: The convergence behaviour of the ZZ-line, as the function of the cell-size (right), and the distance between the Si-atoms, or line size (left). Note: The left diagram is the rotated version of the right diagram where the divergent points from the lines are marked with red stars.

According to the above results, the converged cell-size and line-size (distance between the Si-atoms) for the ZZ-line, would be the dashed ZZ-line, as both of the diagrams indicate. As it turns out, the dashed ZZ-line relaxed using EA in ASE, also in full agreement with the equivalent DFT calculations, while the dense ZZ-line shows discrepancies. And as well shall see in the next chapter, this should explain, why we get different results for DFT relaxations of the dense ZZ-line. However, there are still two types of lines left which we want to study, and those are the armchair-line (AC-line) and the alternate sub-lattice ZZ-line (ABZZ-line), which is the ZZ-line, with Si-atoms being put on alternating sub-lattices one at a time, as seen in fig. 3.23

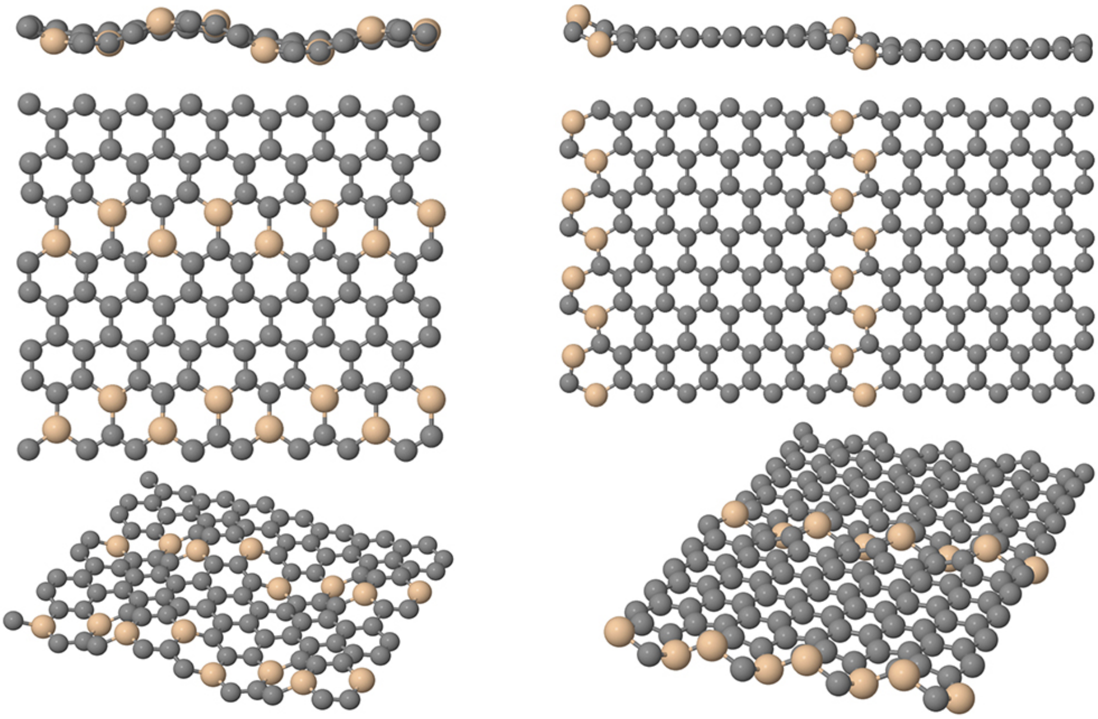

Figure 3.23: The relaxed ABZZ-line (left) and ACh-line (right), in their converged cell-sizes according to the energy/cell-size curve.

Accordingly, we have the convergence behaviour of these two alternative forms of lines, together and with respect to the ZZ-lines, as can be seen in fig. 3.24.

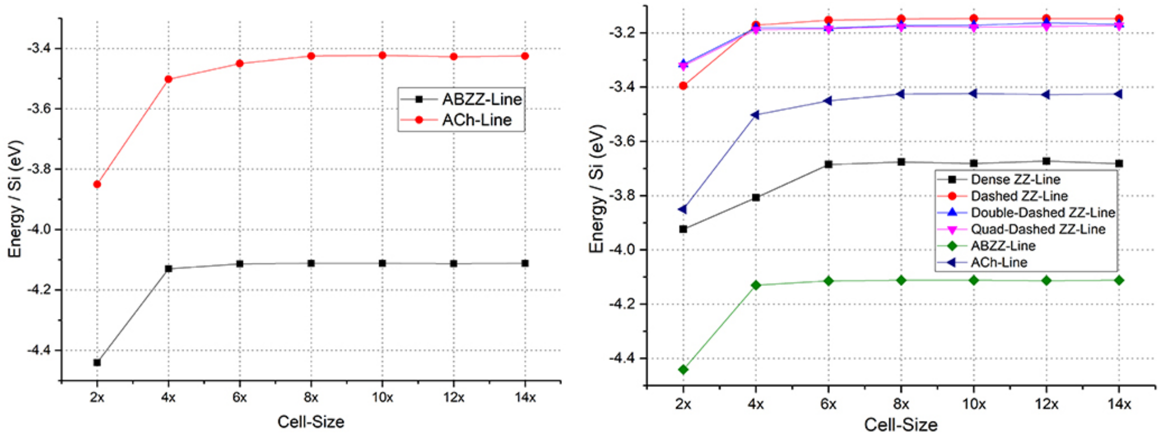

Figure 3.24: The convergence behaviour of ABZZ-line and ACh-line with respect to each other, and the ZZ-lines.

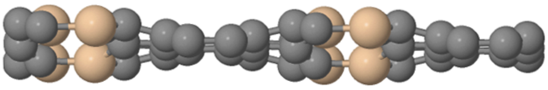

Figure 3.25: The side view of the ABZZ-line in 4x cell, showing the flat graphene in the middle.

The ABZZ-line in 4x structure, despite being seemingly wavy and distorted, is flat in between the silicon lines, as the fig. 3.25 shows. However, in order to have more flat between the silicon-lines, the 6x cell was chosen to be on the safe side.

3.2.2 Hexagons and Triangles

Next in line would be the lattice symmetric structures, namely hexagons and triangles. These structures could be made very easily using the dense ZZ-line, or any other variant of it (dashed-, DD-, etc.). In the case of the closed structures. Hence only the largest ones are presented here, unless we use the smaller sizes for some other purpose, in which case we will present both (all) sizes. For example, the smallest and the largest hexagon (1x, and 16x) are presented in fig. 3.26

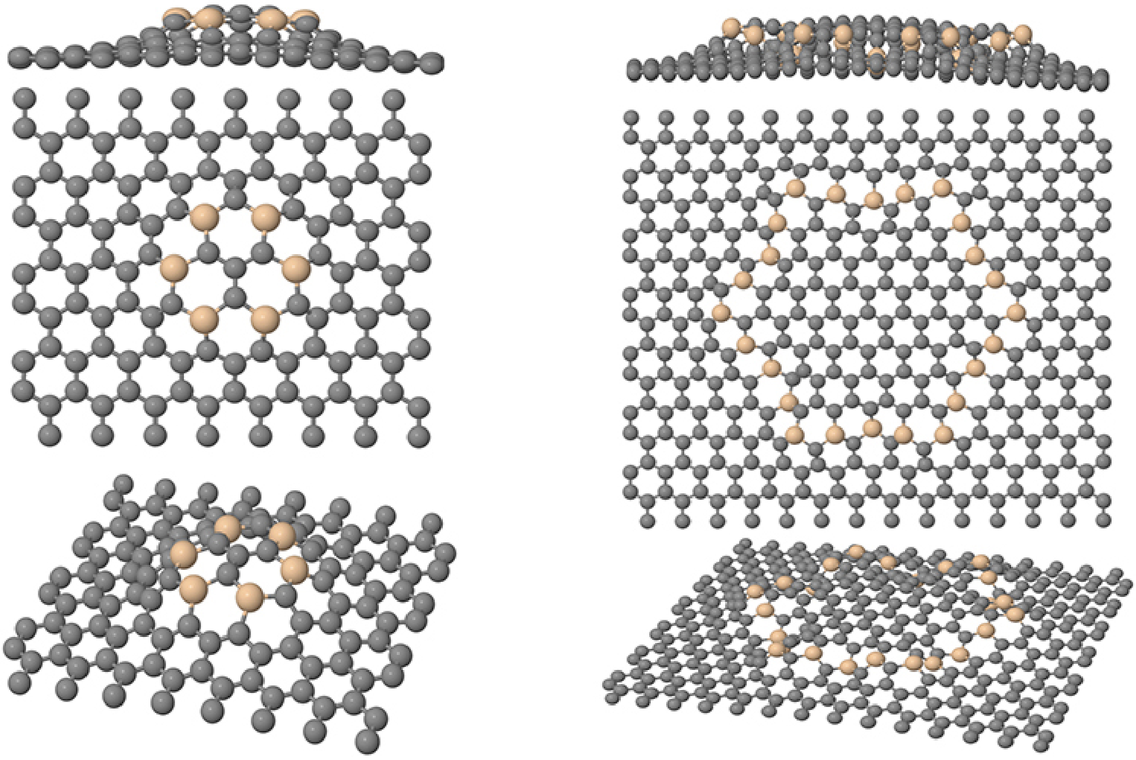

Figure 3.26: The relaxed structures of smallest (left) and the largest (right) hexagons in their converged cell-sizes.

The smallest hexagons were examined up to the convergence cell-size, while the same behaviour is also expected for the larger hexagons as a general rule. The following diagrams show the convergence behaviour of the hexagons similar to the ZZ-lines:

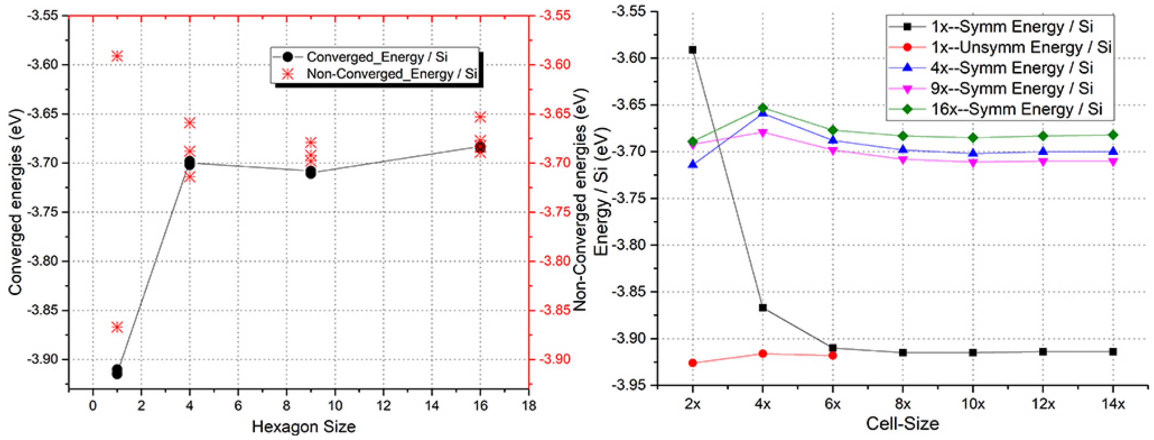

Figure 3.27: The convergence behaviour of the hexagons based on structure-size (left) and based on the cell size (right). Note: The left diagram is the rotated version of the right diagram where the divergent points from the lines are marked with red stars.

As for the triangles, we relaxed 6 different sizes, starting from the smallest triangle, which is made of ZZ line, with only one carbon inside it. The following are the two largest sizes that were relaxed in symmetric form only, even though the smaller sizes, were relaxed both in symmetric and antisymmetric configurations:

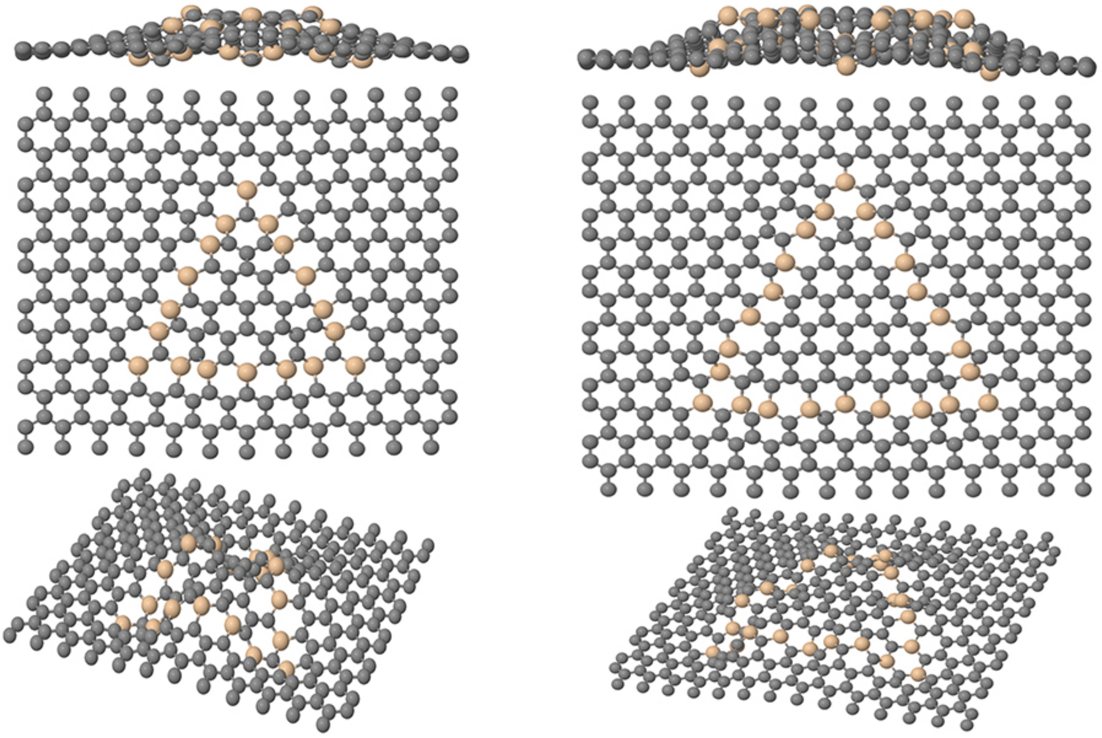

Figure 3.28: The relaxed 21x and 36x triangles in converged cell sizes of 6x respectively.

But fig. 3.29 shows the energy curves of both symmetric and antisymmetric configurations:

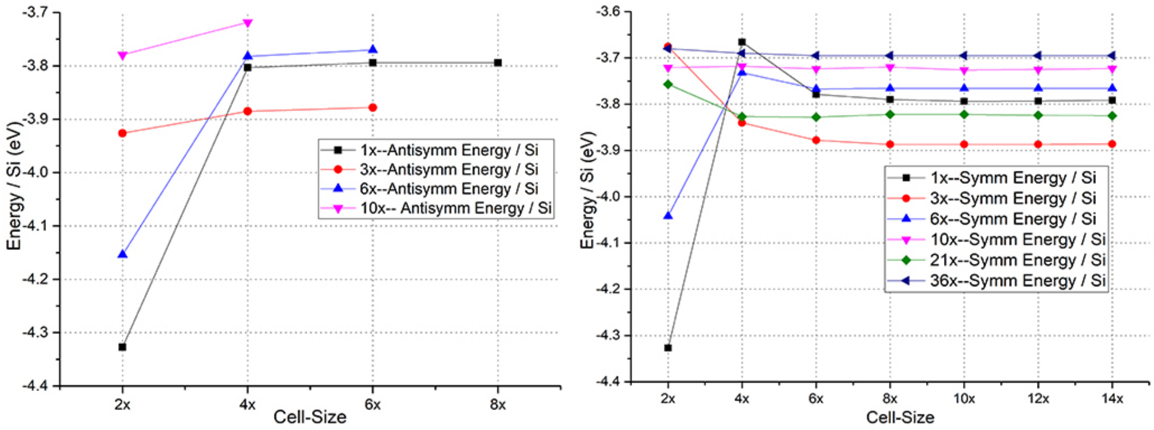

Figure 3.29: The energy curves of the triangles for different triangle sizes in antisymmetric (left) and symmetric configurations (right).

The above triangle names are in terms of their area with respect to the area of the smallest triangle of 3 Si-atoms surrounding a carbon atom. Respectively the size of the cells are named based on the rows of graphene between the successive structures in the periodic boundary conditions, hence the different cell size despite the same name of 6x.

As the above diagrams show, the antisymmetric curves follow the logical pattern of increasing in energy with the cell-size, since as we know, as the density of Si-atoms in graphene increases the embedding energy decreases, and approaches that of 2D SiC. However, in the case of the symmetric structures, some times the decrease in the cell-size causes the structure to change, which explains why in some of the cases smaller cell-sizes have larger embedding-energy. This also applies to the case of hexagons, as seen in fig. 3.27.

In addition to the structures made with the dense ZZ-line in hexagonal and triangular shapes, we made a couple of structures using the dashed ZZ-line, namely the largest hexagon and the triangle, as shown in fig. 3.30.

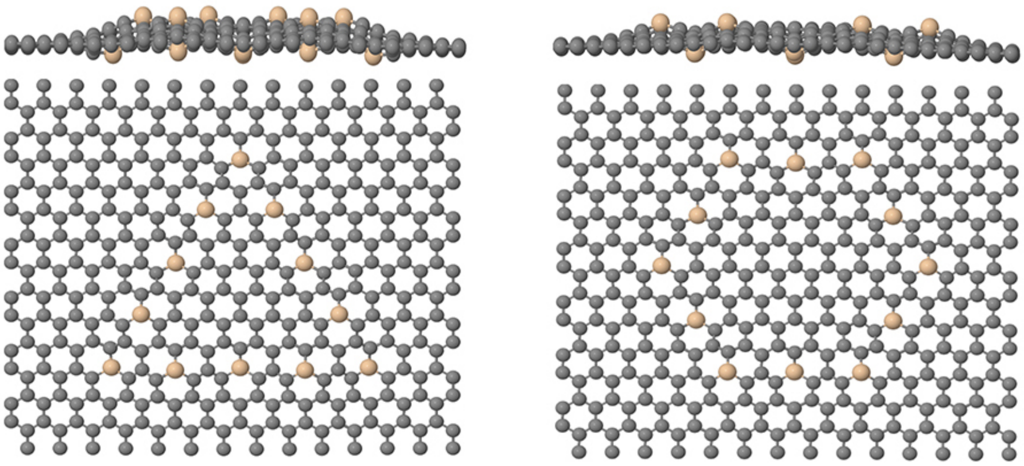

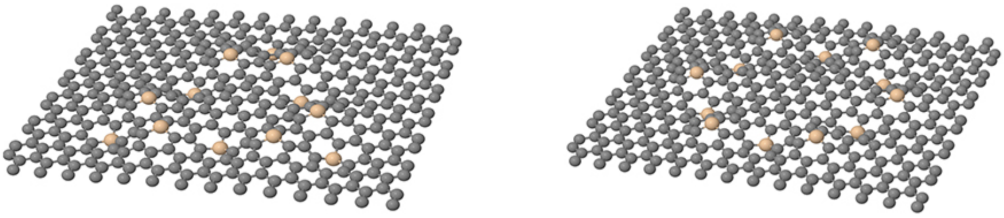

Figure 3.30: The relaxed dashed 36x-triangle, and dashed 16x-hexagon in 6x supercell sizes, which is definitely the converged size.

With regards to the cell-size energy convergence we know from comparison of the dashed ZZ-line to the dense ZZ-line, that the dashed case converges for smaller cell-size than the dense ZZ-line, and since 6x cell is still sufficient for DFT simulations, choosing the 6x cell-size for the dashed versions of the triangle and hexagon relieves us of having to calculate the energy curves.

3.2.3 Squares, Circles, and Mixed Structures

In this section we look at the structures that are not lattice-symmetric like the hexagons and triangles, and are also not always made of the same ZZ-line. For the convergence behaviour of these structure no predictions can be made, other than the fact that if the structures remain the same throughout the cell-size change, at some point one cell-size for that structure should be converged, and that structure should be the dominant one. Starting with the squares, we present the largest square size and its dashed version in fig. 3.31.

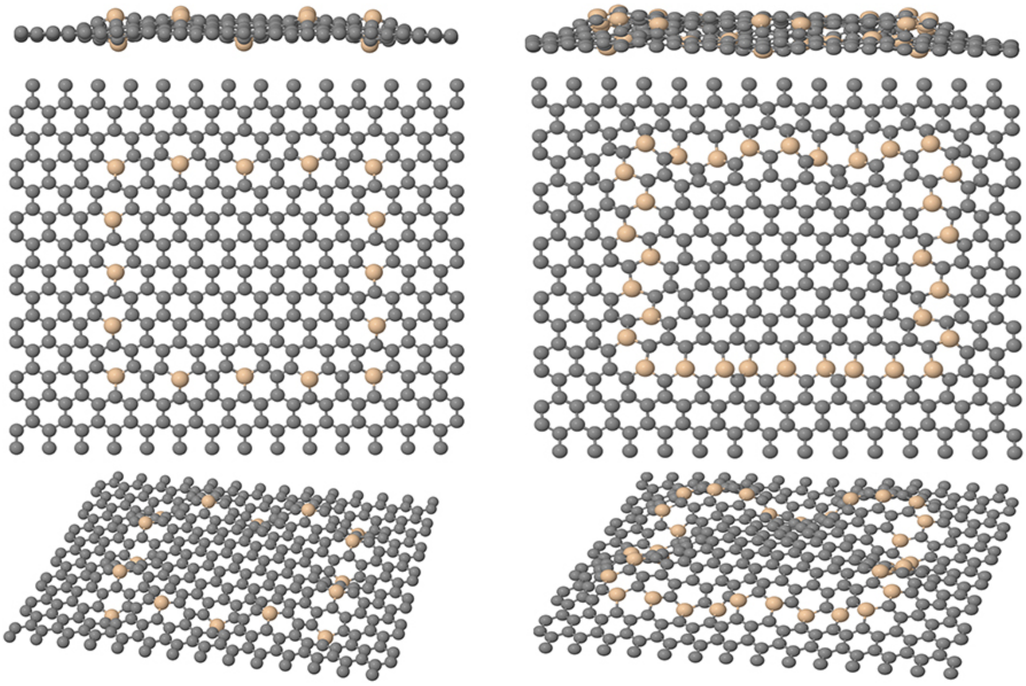

Figure 3.31: The relaxed 8x squares in 6x converged cell-size, in dashed (left) and dense (right) variations.

Accordingly the following are the convergence curves with and without the dashed 8x-square:

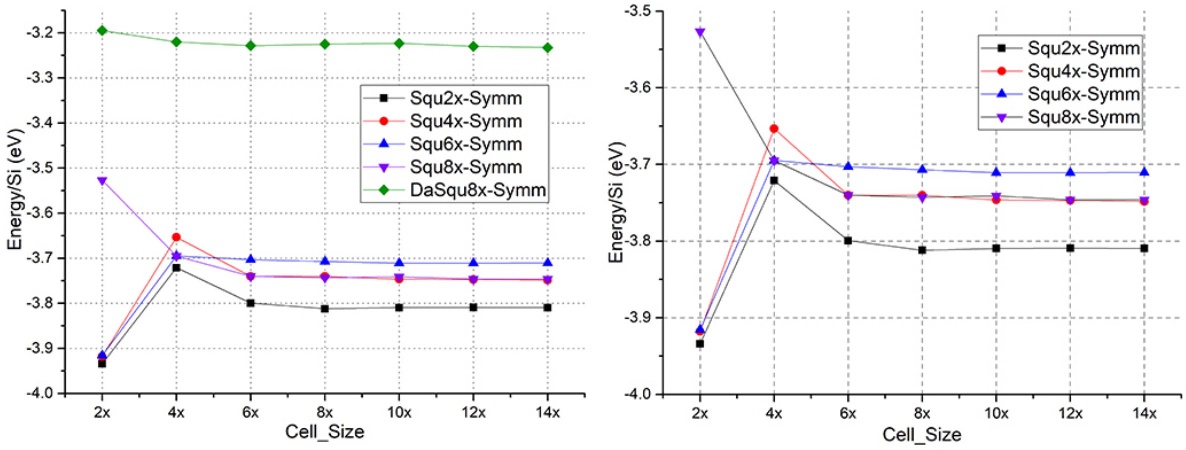

Figure 3.32: The convergence behaviour of the squares, with (left) the dashed 8x-square, and without (right).

Now we move to the circles, which are least lattice symmetric structures. The smallest circle, made with 12 silicon atoms, is a particular symmetrical structure, as it encloses a coronene, and therefore is dodecagon. However, this is the only lattice-symmetrical circle that can be embedded into the graphene lattice. Any other circle of larger size require distorting the lattice symmetry. Therefore, the energy curves in the convergecne diagram can only be interpreted approximately for choosing the converged cell-size only, and not for comparing the convergence behaviour of different circle sizes. In the following however, we present the smallest circle, the dodecagon, and the 4x circle, since the 5x is presented in a modified version as the mixed custom structures:

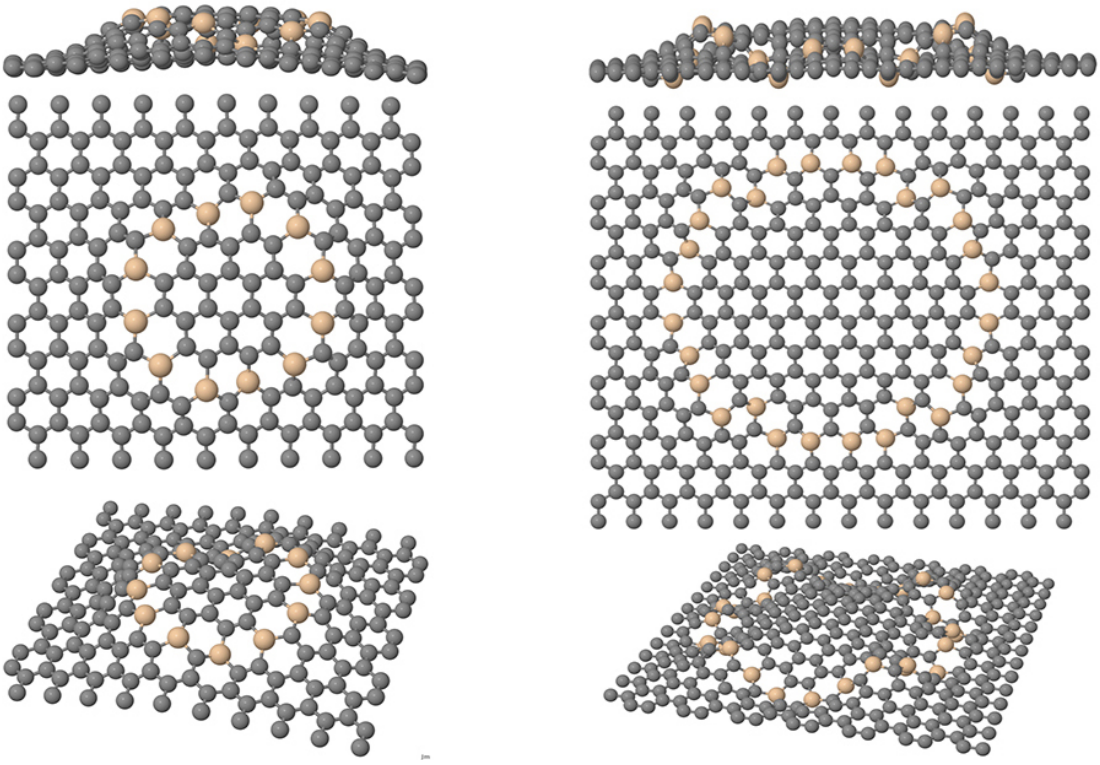

Figure 3.33: Left: The dodecagon circle in the graphene lattice with a cell size of 6x. Right: The 4x circle in a 6x super-cell.

As the above images show the EA potential was not quite capable of reaching the ideal relaxed state for the dodecagon, which would an elevated perfectly symmetric dodecagon, enclosing the coronene according to the DFT calculations. However starting from a DFT relaxed structure, the EA potential also relaxes the structure into a perfectly symmetric and elevated dodecagon, depicted in fig. 3.34, as opposed to the structure in fig {3.33}.

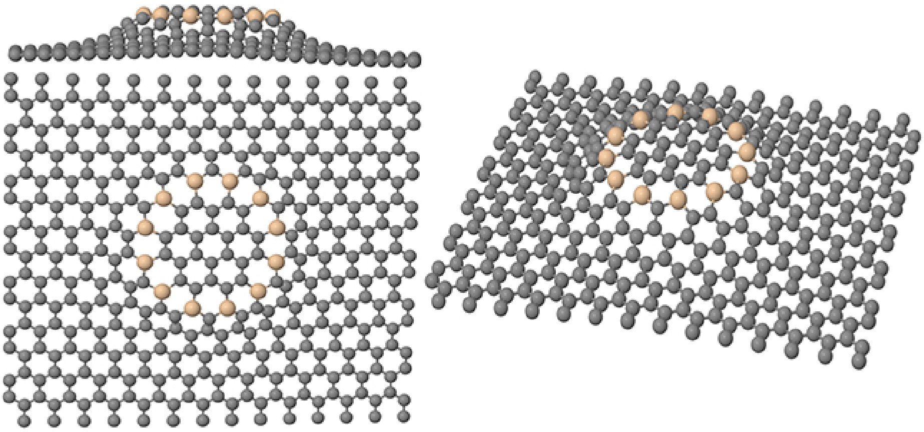

Figure 3.34: The relaxed dodecagon circle using the EA starting from the relaxed state of the DFT.

Also energetically is the structure in fig. 3.34 (slightly) more favourable using the EA potential, however, the potentials has a hard time reaching this state on its own from a purely random corrugated initial state.

We can now look at the convergence behaviour of the circles, keeping in mind the difference between the different sizes of the circles, similar to the structures in fig. 3.33, where the smaller circle is the 1x size, and the larger circle is the 4x size:

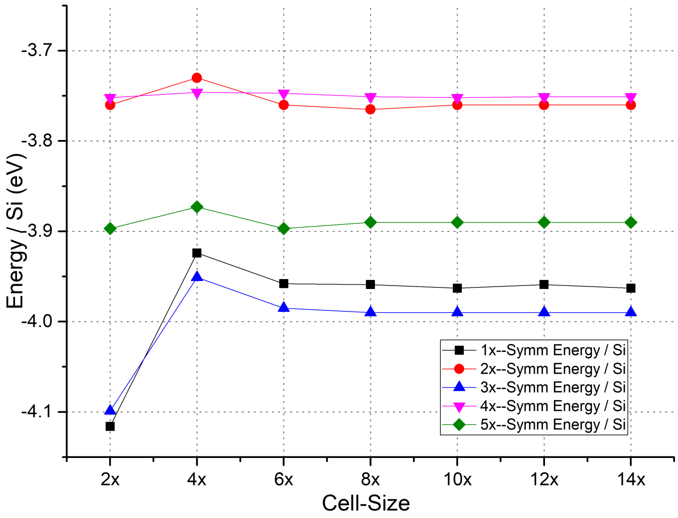

Figure 3.35: The convergence behaviour of different circle sizes, all having a larger degree of symmetry than the hexagons, while being structurally different from each other.

One important fact about the circles, despite their structural differences, is that in order to make them on the graphene lattice, all three kinds of lines that we previously mentioned, namely the ZZ-line, the AC-line, and the ABZZ-line, have to be used in order to make a reasonably circular shape on the graphene lattice. This is even true about the dodecagon circle. Therefore, despite the fact that we regarded the circles as non-symmetrical structures, there is a certain degree of symmetry involved in making the circles in fig. 3.33, which may be lower or higher than the structures in fig. 3.26. Furthermore, as the diagram shows there is similarity between the structures, in that they almost all converge for 6x cell-size.

The last set of structures are "custom" structures, which are not easily categorizable in terms of their size and shape with respect to the previous structures, but still fall within certain larger categories. Even though originally, we had many such custom structures, including ones that had two layers of silicon enclosing, we only decided to 3 large structure to be relaxed and consequently examined using DFT. Here we present these 3 structures, and their convergence behaviour in fig. 3.37. Two of the structures resemble circle and a square in a 650 atom cells, with the name of XXL-Cir/Squ, and the other structure is a large hexagon made with the ABZZ-line as seen in fig. 3.36.

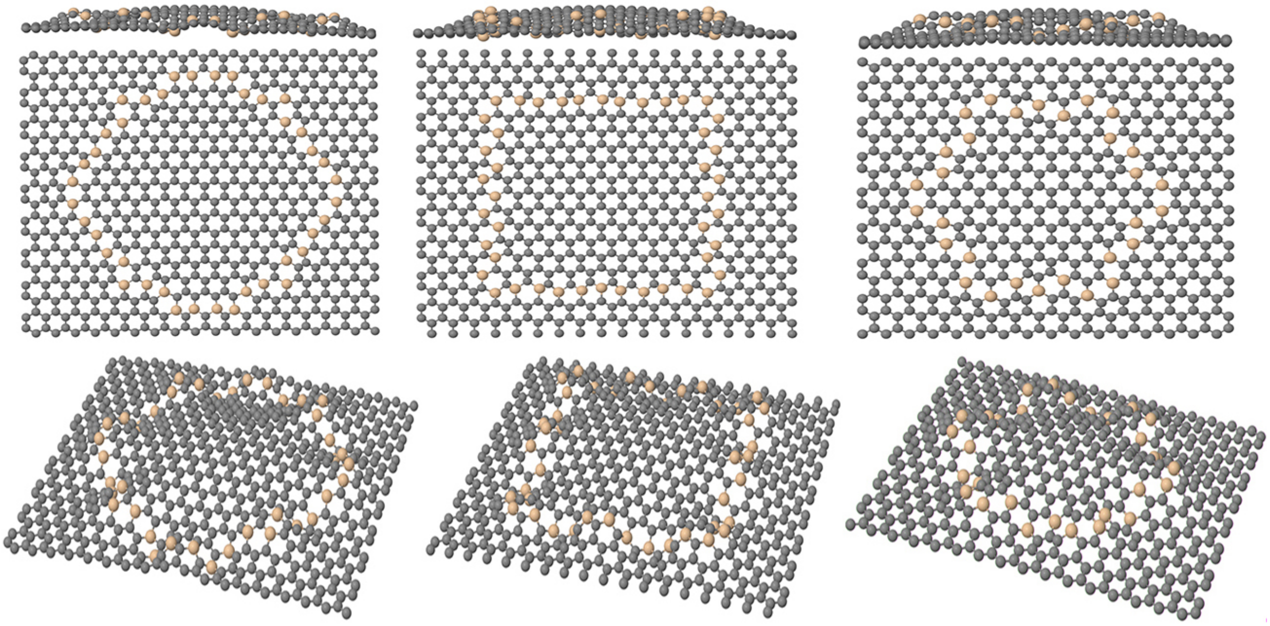

Figure 3.36: The XXL-Circle in its converged cell-size of 4x (left), the XXL-Square in its converged cell-size of 6x (center), and the ABZZ-Hexagon in its converged cell-size of 6x (right).

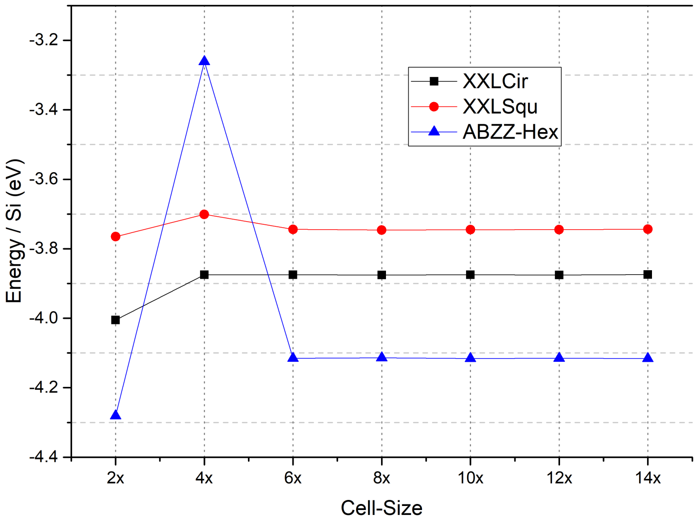

Figure 3.37: The convergence behaviour of the extra large structures.

The above cell-sizes are chosen according to the curves below, while as mentioned before the x part of the cell size indicates the number of the graphene rows between periodic images of the silicon shapes for that particular structure. Therefore as we see the 6x cell of XXL-Square have $\approx$ 650 atoms, while the 6x cell of the ABZZ-Hexagon has $\approx$ 510 atoms.

It should be said that these cell-sizes of roughly 650 atoms, constituted the DFT limit for relaxation, using the LCAO mode of the GPAW. It is said that DFT codes are usually appropriate for up to 350 atoms, which obviously has to be in LCAO mode. Normally for this size of cells, DFTB methods are used. However, we were fortunate to be able to utilize this variations of LCAO formulation in real space, which could handle this number of atoms relatively good, as far as the relaxations with periodic boundary conditions were concerned. With that we have presented and analysed all of our structures in EA potential, and have examined their temperature stability. In the next section we present the relaxation results of the select of the above structures, and move on to present the STM/STS and linear plasmonic response simulations that were done on those structures.

Chapter 4

DFT Simulation Results

4.1 DFT Relaxation Results of Selected Structures

4.1.1 ZZ-Lines, ABZZ-Line & ACh-Line

The first set of the structures from the EA-potential relaxations would be the lines, namely the ZZ-line and the dashed ZZ-line (DaZZ-line), the ABZZ-line, and the ACh-line. Each of these lines have been used for the STM, and plasmonic response simulations as well, A systematic study of these structures is presented in (a). Here we only present the results, for those structures that were used in STM/STS, and plasmonic response simulations in fig. 4.1.

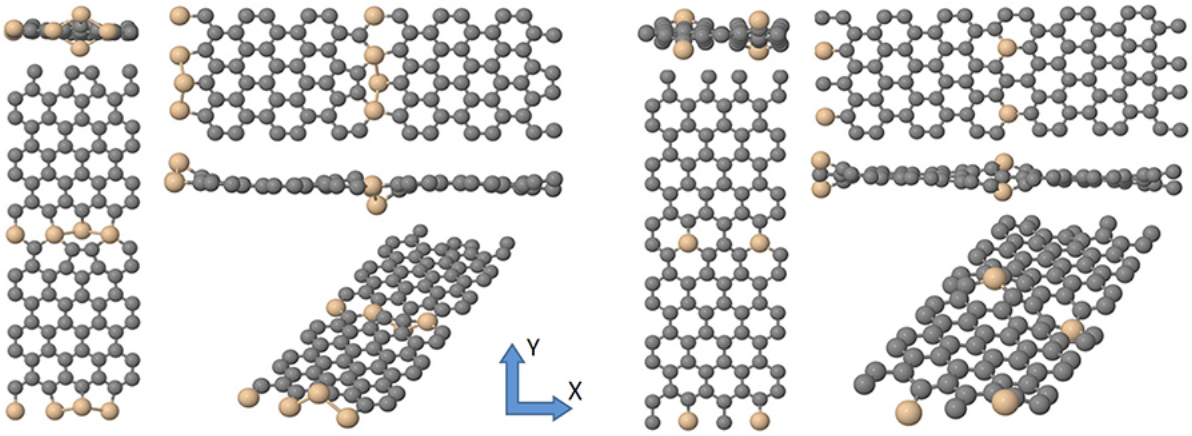

Figure 4.1: The lowest energy relaxed 6x ZZ-line (left) and 6x DaZZ-line (right) in their optimal cell-size in antisymmetric configuration.

The DaZZ-line above was relaxed in 4 different sizes, 4x,6x, and 8x, but since the dense ZZ-line is relaxed in 6x cell, therefore we also used the DaZZ-line in that cell.

The above structures were relaxed in plane-wave mode, due to their small size, using the Unit-Cell filter for the optimization of the cell-size. For the ZZ-line, the pseudo-flat structure, which has one silicon atom sticking out of the plane, proved to have the minimum energy, despite other relaxations similar in shape to the EA results being also possible to achieve with DFT. In (a), the other "corrugated" ZZ-line is also presented. The fact remains, that when used for making round structures on the graphene lattice, similar to the DaZZ-line, the ZZ-line abandons this pseudo-flat formation, and manifests a corrugated/wavy nature. The ABZZ-line, and the ACh-line are shown in fig. 4.2.

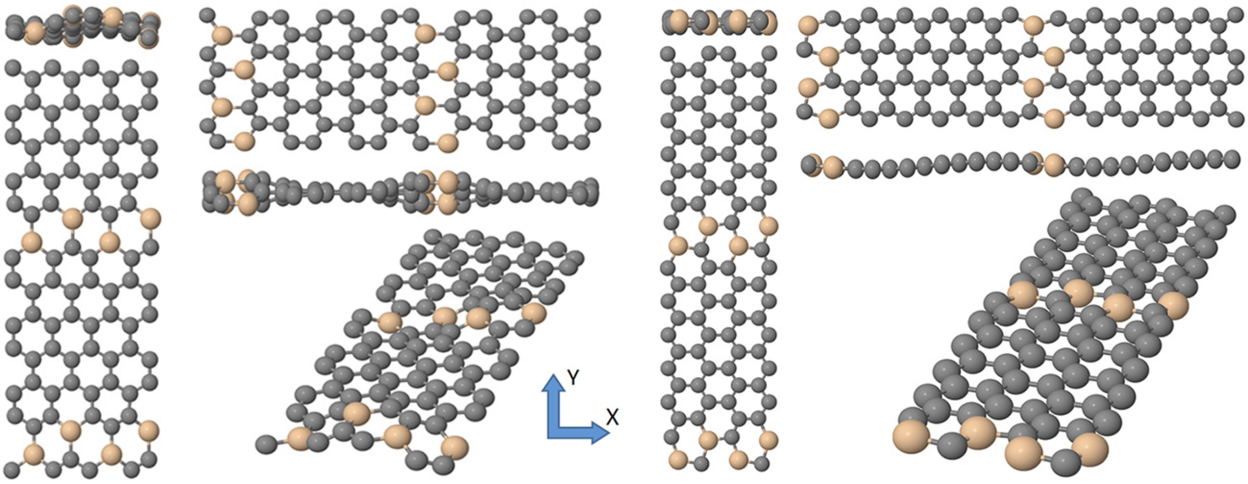

Figure 4.2: The lowest energy relaxed 6x ABZZ-line (left) and 6x ACh-line (right) in their optimal cell-size in antisymmetric configuration.

The bond lengths (BL's) of the silicon-carbon bonds are expected to be within the limits that were discussed in the benchmarking section. Different Si-C bonds lengths for structures relaxed with the PBE XC-potential are shown in fig. 4.3.

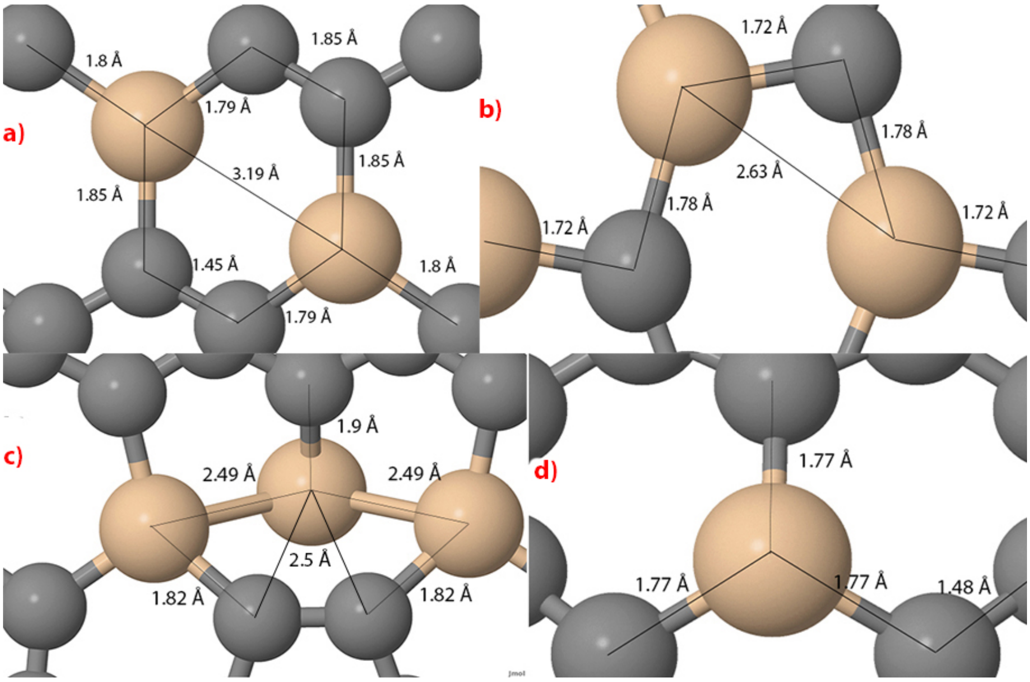

Figure 4.3: Different BL's of ABZZ-line (a), ACh-line (b), ZZ-line (c), and DaZZ-line (d) relaxed with PBE-DFT.

As it could be seen in fig. 4.3, the shortest BL is at 1.72 Å, while the longest BL reaches 1.9 Å with the pseudo-flat ZZ-line. However this structure is a bit atypical in that it is overall flat with the exception of a single "trivalent" silicon, which is closer to the neighbouring silica as to the carbons with which it is supposed to form a bond (BL of 2.49 Å with Si-atoms, compared to 2.5 Å with the carbons), hence not being even trivalent in nature. With that it is expected that for all the rest of structures, the BL's remain between $1.72 - 1.9$ Å. Tab. 4.1 summarizes the embedding energies.

Table 4.1: The comparison of the energetics of the lines in PBE-DFT (FD mode) and EA analytical potential.

Energies Structure	$E_{Embed/Si}(\mathrm{eV})$ PBE-DFT	$E_{Embed/Si}(\mathrm{eV})$ EA
ZZ-line 6x	-3.24	n.a.
DaZZ-line 6x	-1.78	-3.15
ABZZ-line 6x	-2.76	-4.11
ACh-line 6x	-2.92	-3.45

All of the above structures in their chosen 6x cells have the same number of atoms (48 atoms), which makes the comparison possible and meaningful. The flat ZZ-line does not have an equivalent in EA, and therefore the energy of that structure in EA would not be applicable to the comparison with DFT. The embedding energies of the DFT results seem to correlate with the flatness of the structure; the flatter the structure the higher the embedding energy, but this does not seem to be the case with the EA potential

4.1.2 Hexagons and Triangles

The largest hexagon is one of the most important structures in this study, on which both STM simulations and plasmonic repsonse simulations are done. However the smallest hexagon, which we additionally relaxed we used only for comparing and benchmarking the photo-absorption spectra between FD and LCAO modes in time-propagation TDDFT. The structures are shown in fig. 4.4.

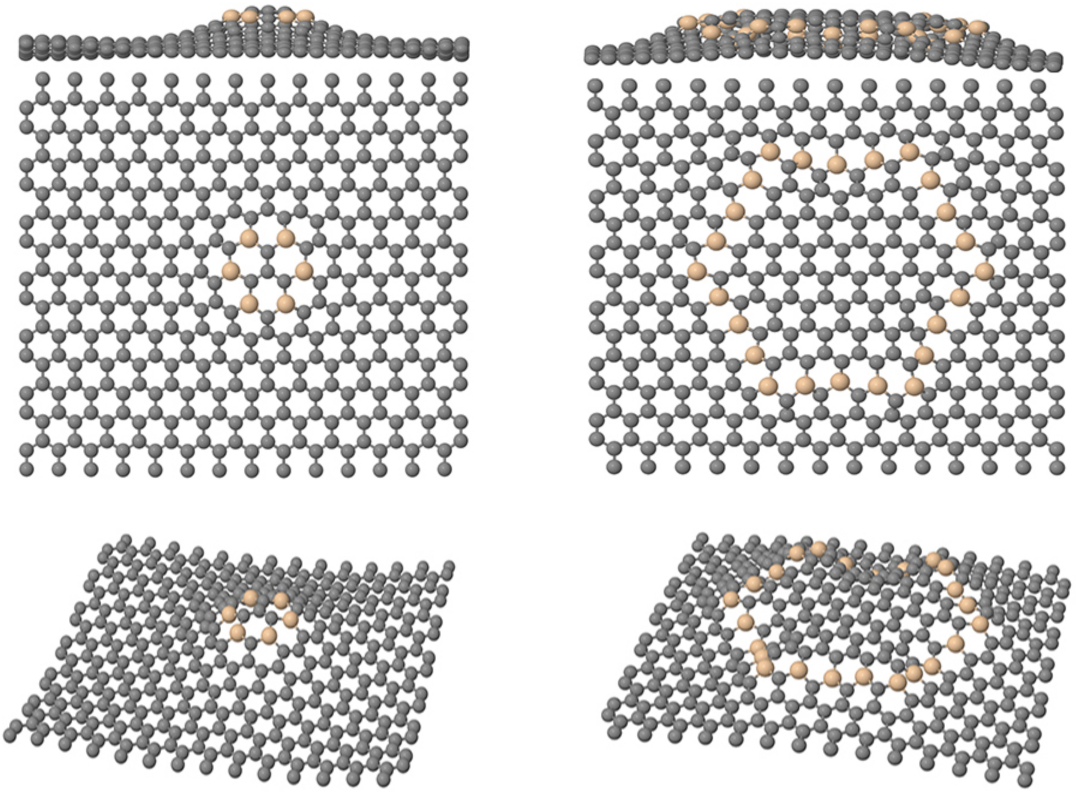

Figure 4.4: The smallest 6-Si hexagon used for benchmarking in spectrum simulations (left) compared to the largest hexagon relaxed in LCAO-mode using PBE.

In fig. 4.5, we show the two largest triangles (21x and the 36x), which were both examined for STM, additionally the 36x triangle (Triangle36x) was used thoroughly for STM/STS and the spectra.

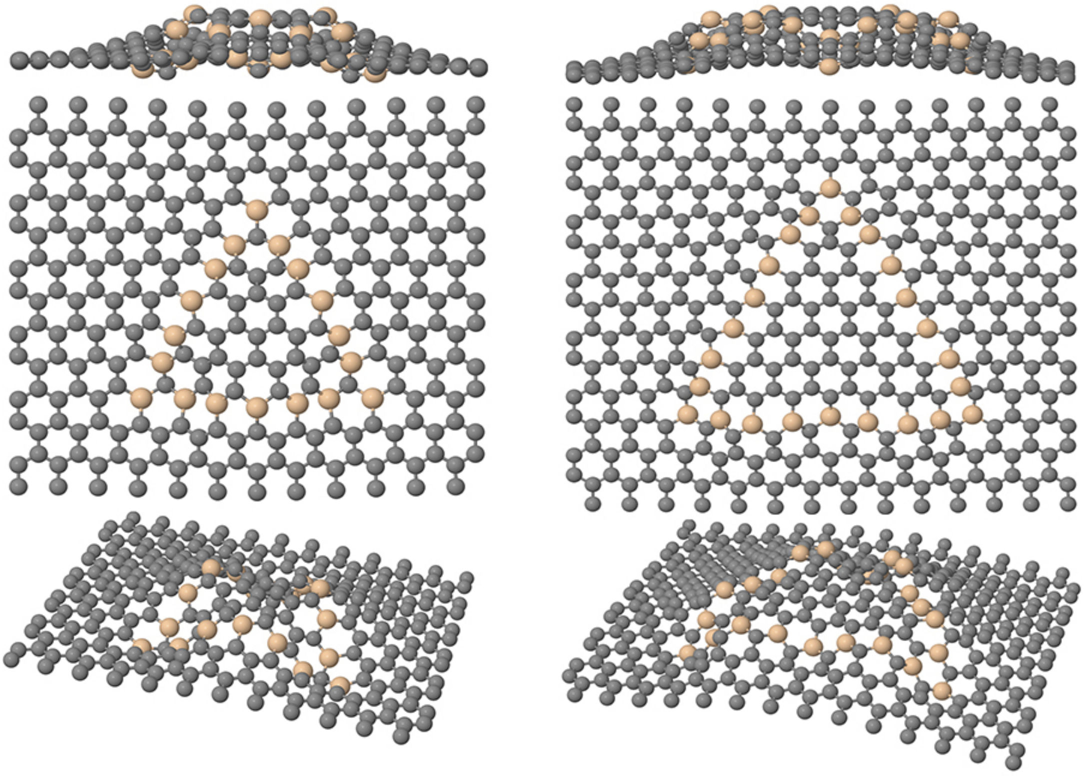

Figure 4.5: The 21x and 36x triangles relaxed in LCAO mode with PBE XC-functional.

The embedding energies are listed in tab. 4.2.

Table 4.2: The comparison of the energetics of the triangles and the hexagons in PBE-DFT and EA analytical potential.

Energies Structure	$E_{Embed/Si}(\mathrm{eV})$ PBE-DFT	$E_{Embed/Si}(\mathrm{eV})$ EA
Hex_1x 6x	-2.03	-3.92
Hex_16x 6x	-2.68	-3.68
Tri_21x 6x	-2.91	-3.83
Tri_36x 6x	-2.44	-3.69

The embedding energies of the hexagons show a different trend in DFT as in EA. The reason for that could be the fact that the small hexagon in DFT distorts the lattice more than the larger 16x hexagon, while in the case of the triangles it is vice versa. Therefore when a particular structure distorts the lattice the Si-embedding energy rises, both in DFT and EA. Having said that, it should be also noted that some structures relax differently in EA as in the DFT, such as the small hexagon, which has a flat lattice in EA but a slightly distorted lattice in DFT.

Finally we look at the dashed version of the largest hexagon and the triangle, in fig. 4.6.

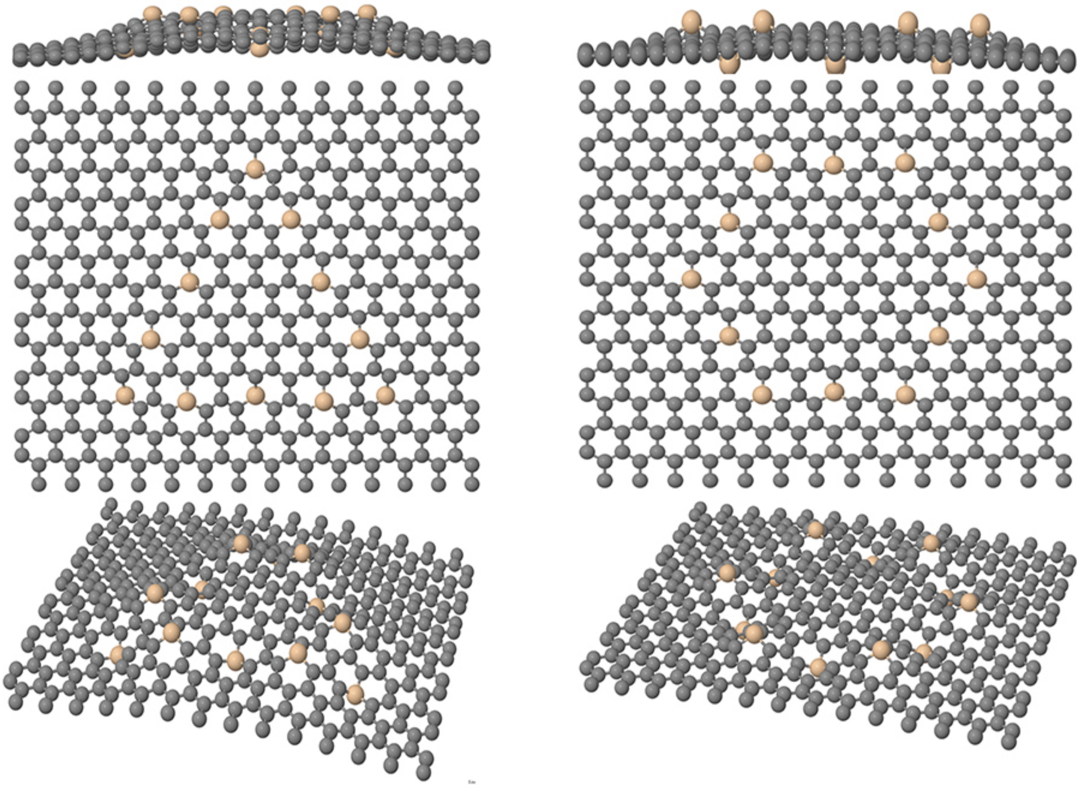

Figure 4.6: The dashed version of the 36x triangle and 16x hexagon in 6x cells with the total of 392 atoms.

Of the two dashed structures above the hexagon is the flatter one. The energetics of the structures have to reflect that in DFT and also EA if the same fact could be said about the EA structures. Tab. 4.3 shows the energetics in DFT and EA.

Table 4.3: The comparison of the energetics of the triangles and the 16x hexagon in PBE-DFT and EA analytical potential.

Energies Structure	$E_{Embed/Si}(\mathrm{eV})$ PBE-DFT	$E_{Embed/Si}(\mathrm{eV})$ EA
DaHex_16x 6x	-1.18	-3.12
Tri_36x 6x	-1.18	-3.11

The two structures are very similar in terms of the energetics, with the minor difference due to the dashed hexagon being slightly flatter. The above structures are therefore different variations of the same symmetric structures (380 C + 12 Si atoms). The only difference is the way these atoms are arranged, and the slight difference in the flatness is accounted for by the slight embedding (total) energy difference in both DFT and EA.

4.1.3 Squares, Circles, and Mixed Structures

As for the circles we present the two structures which were also discussed in the analytical potential section, namely the small dodecagon circle, and the Circle4x in fig. 4.7. And as for the squares we only present the largest one (Square8x) plus the dashed version of it in fig. 4.8

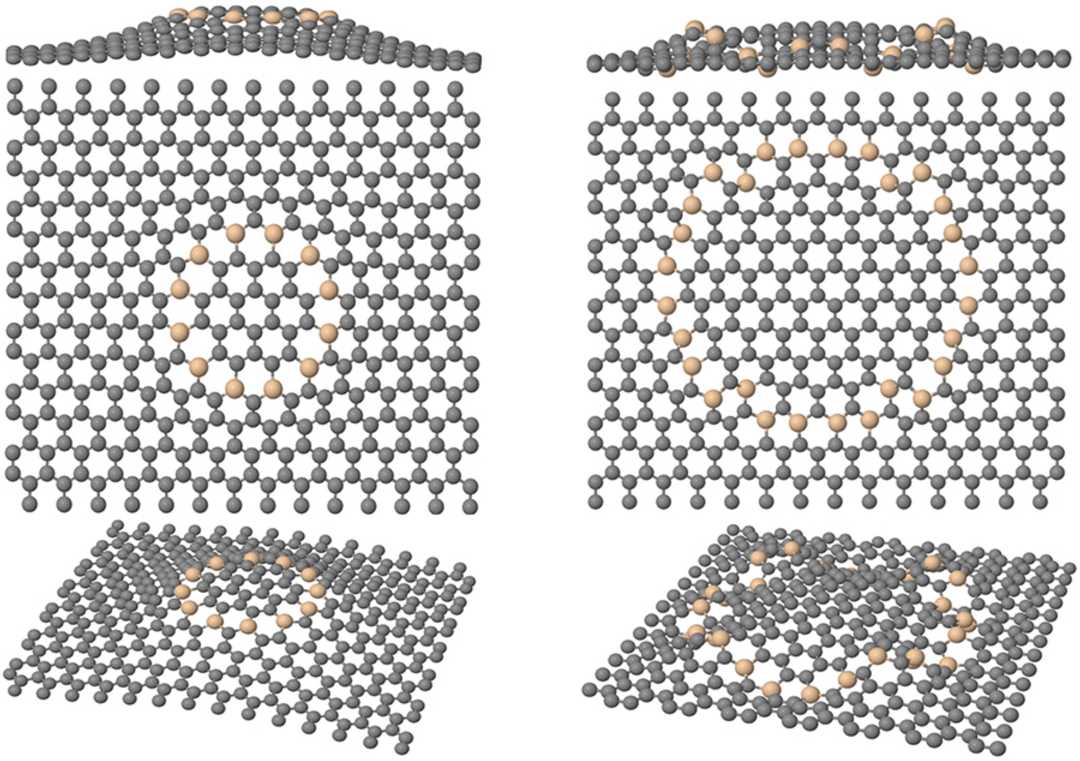

Figure 4.7: The 1x dodecagon circle, and Circle4x in their converged cell sizes of 10x and 4x.

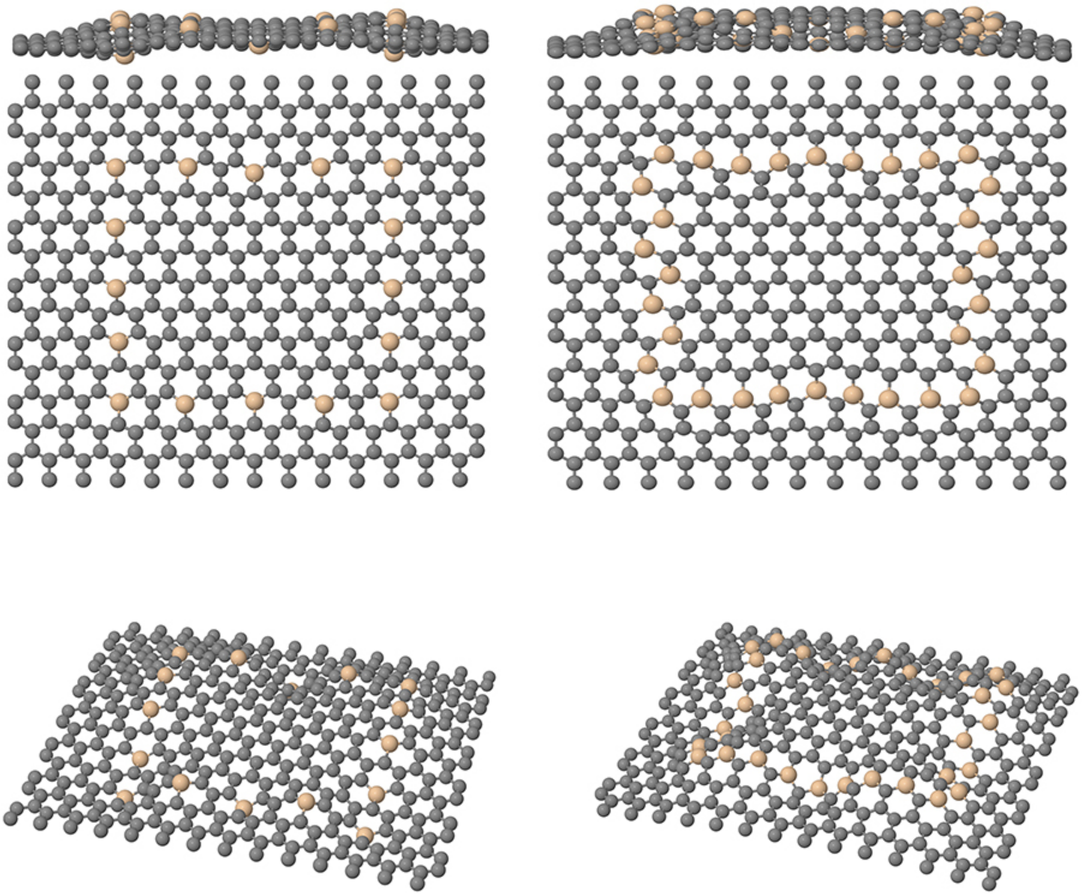

Figure 4.8: The Square8x and its dashed version, in their 6x converged cell size.

The embedding energies are listed in tab. 4.4.

Table 4.4: The comparison of the energetics of the select circles and squares PBE-DFT and EA analytical potential.

Energies Structure	$E_{Embed/Si}(\mathrm{eV})$ PBE-DFT	$E_{Embed/Si}(\mathrm{eV})$ EA
Dodecagon 6x	-2.50	-3.96
Cir_4x 6x	-2.55	-3.75
Squ_8x 6x	-2.29	-3.74
DaSqu_8x 6x	-1.31	-3.22

It is interesting that the DFT energies of the circles are close, while that of the Circle4x and the Square8x in EA are close. One face about the DFT energies are observable, and that is that the dashed structures usually have an embedding energy that is close to the half of the dense version. The EA energies of of the dashed and the dense consistently show that the dashed version have higher energies and are mostly around $\approx 3.1\ \mathrm{eV}$.

Now we can look at the large structures as the last set of the structures that were relaxed in DFT, in fig. 4.9.

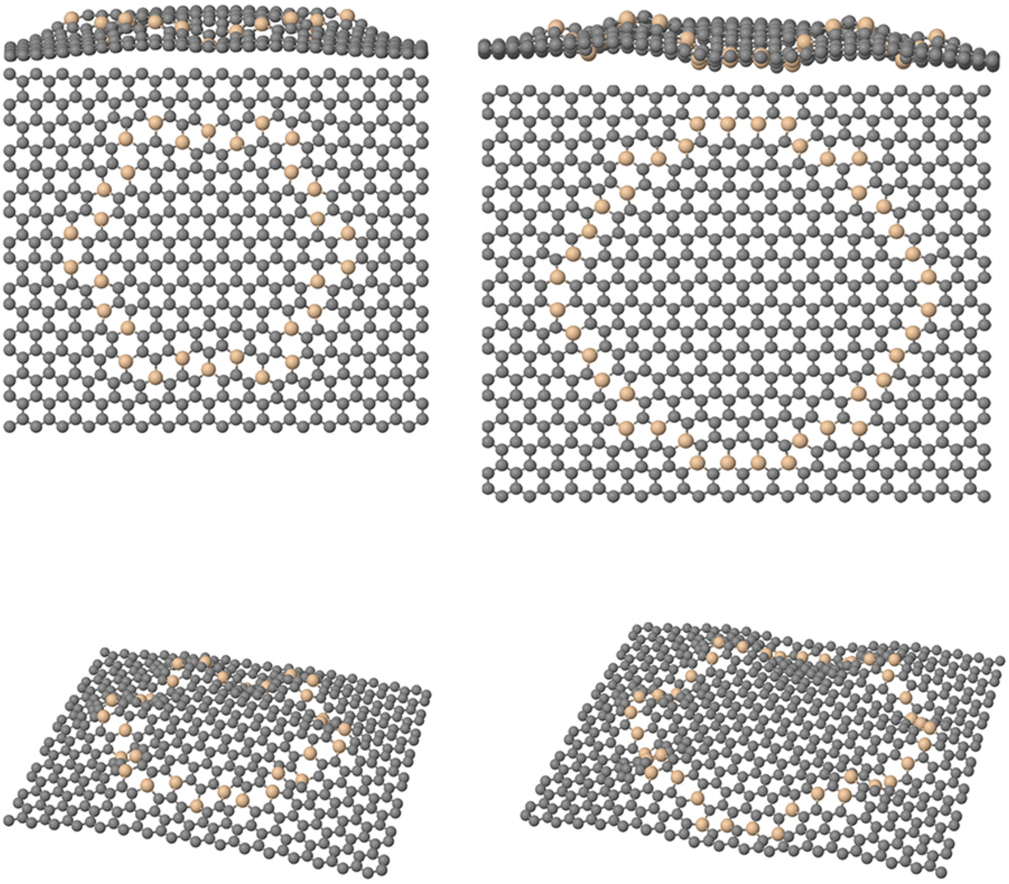

Figure 4.9: The two extra large structures, the XXL-Circle and the large ABZZ-Hexagon in their relaxed cell sizes of 4x and 6x respectively.

And finally we look at the energetics of the above structures in tab. 4.5.

Table 4.5: The comparison of the energetics of the additional large structures in PBE-DFT and EA analytical potential.

Energies Structure	$E_{Tot}(\mathrm{eV})$ PBE-DFT	$E_{Embed/Si}(\mathrm{eV})$ PBE-DFT	$E_{Embed/Si}(\mathrm{eV})$ EA
ZZHex 4x	-2.39	-4.12	
XXLCir 4x	-2.42	-3.88	

The energies are very close both in DFT and EA, although DFT prefers the XXL circle, the EA prefers the ABZZ-hexagon. However due to the small energy differences, it could be said that the structures are equally highly favourable, and that is due to the symmetric corrugation of the graphene lattice in addition to small amounts of lattice distortion, which when combined usually constitute the best form of creating impurity defect.

4.2 Quantum Confinement

4.2.1 Initial STM/STS of Structures w/ Fermi Level Convergence

In the first part of the STS/STM simulations we look at the STM/STS, at constant heights, of the structures whose unoccupied bands have not been additionally converged, in search of confined surface electronic states. The selected structures which showed potential for confining a surface state, were chosen for further convergence of the unoccupied bands, the STM/STS results of which are presented in the next section. For the sake of comparison however, one structure, the ACh-Line, we examine both in this and the next section, consequently with and without the converged unoccupied bands.

However one relevant consideration for STM image simulations is, would be what is the right distance for a constant height STM imaging. Another one, would be the selection of the bias voltages. Furthermore, as we have mentioned in the introductory sections, the Si impurity in graphene cannot be seen as a Coulomb impurity, and it is of central importance in this project to examine and understand the effect of this impurity on the electronic properties of graphene. For this purpose we start by looking at a few plots from the DOS, and STS of pristine graphene and a single trivalent Si in graphene (similar to fig. 3.11) the sheet (Dot_Si_4x, 1 Si in 31 C atoms), while the STS plots are done for different heights. The DOS's of graphene sheet with and without the singe trivalent Si are shown in fig 4.10

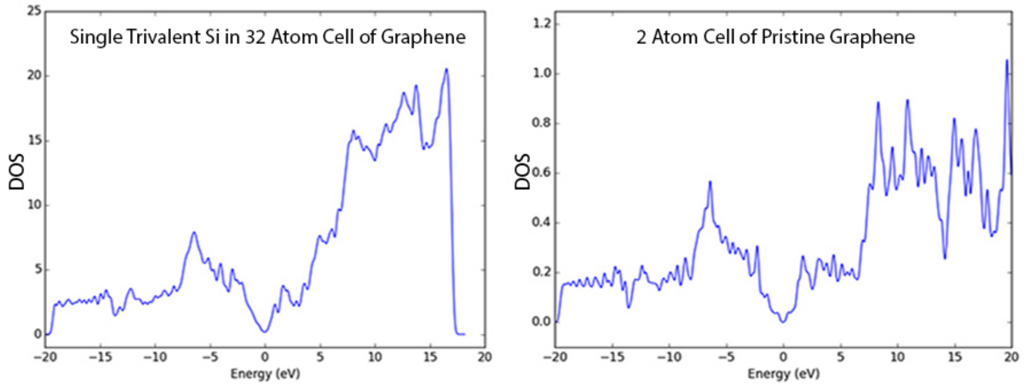

Figure 4.10: The Kohn-Sham DOS of pristine graphene with (left) and without (right) single trivalent Si.

STS simulations carried out at different heights for a C atoms in pristine graphene and for a Si impurity are presented in fig. 4.11. STS of the single Si atom would illustrate the effect of the Si atom impurity on the LDOS of atoms in graphene near a Si atom.

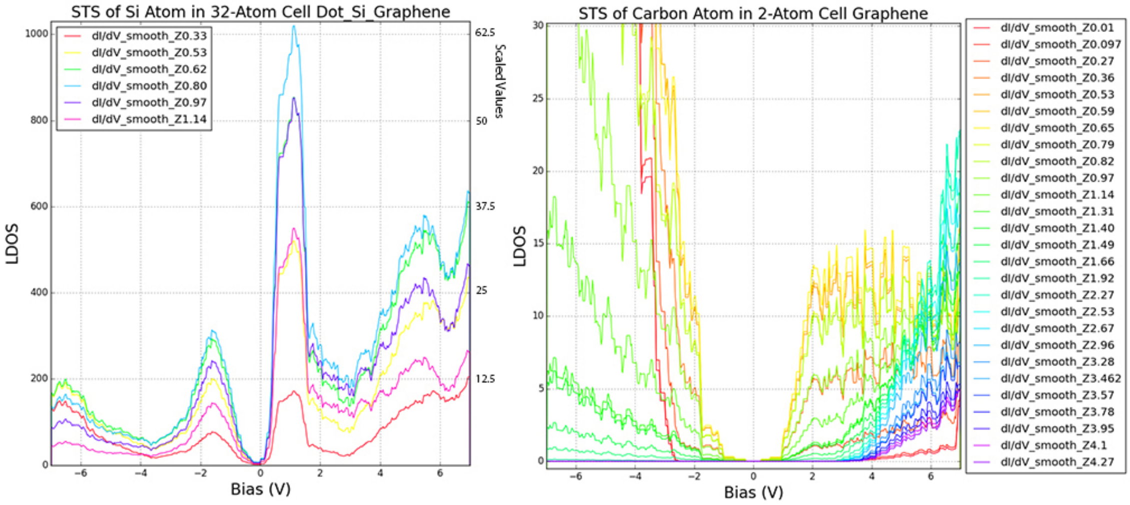

Figure 4.11: The STS of C atom in 2-atom cell pristine graphene (right) and Si atom in 32-atom Dot_Si graphene (left), for different z-heights (right axis of the Si-STS shows the scaled LDOS values based on the cell sizes of $32/2$ atoms.

Clearly one can see completely different spectra, and the fact that the STS of C atoms resembles the DOS of graphene, while the STS of the Si atom is completely different. The significant contributions of the Si-spectra (LDOS) to the LDOS of the neighbouring atoms, and the total DOS could be between $0 - 2 \ \ \mathrm{eV}$ and $4 - 7 \ \ \mathrm{eV}$, as indicated by the two clear peaks. As far as the other two questions are concerned, one can see that for graphene the STS signal is at it's highest at $Z = 0.65 \ \ \text{Å}$, and the negative biases disappear for $Z \geq 2.0$ Å (see fig. 4.13). While this difference between the negative bias and positive bias contributions of the C atom in graphene decreases for heights $> 0.65 \ \ \text{Å}$, for the Si atom the positive bias contribution remain strong beyond the peak value of $Z = 0.80$ Å. Fig. 4.12 shows the STS's of C-atom in graphene separated from the peak intensity height.

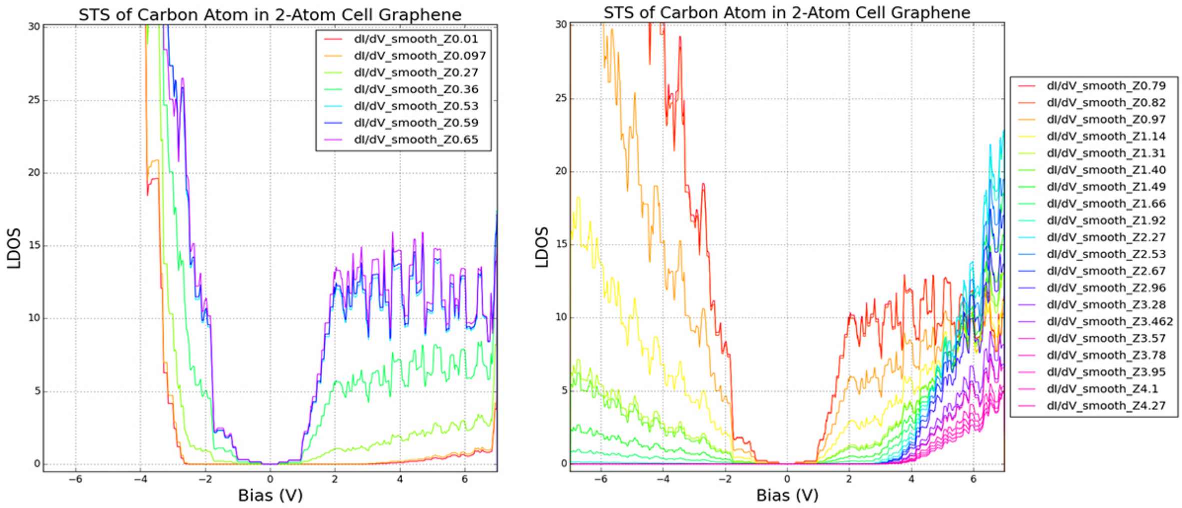

Figure 4.12: The STS of C atom in 2-atom cell pristine graphene up to the peak point (left) and from the peak point to $Z = 4.27$ Å (right).

First we look at the atomic position of each structure, on which STS was performed in fig. 4.13.

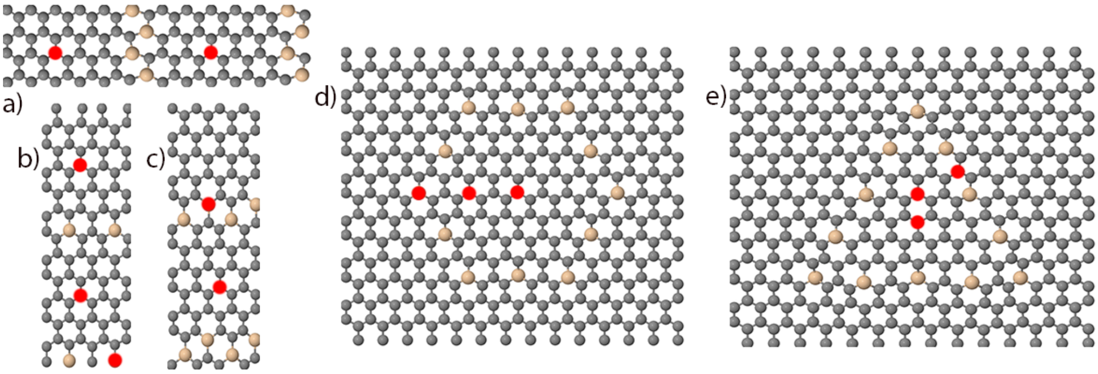

Figure 4.13: The atomic positions of a) ACh-line, b) DaZZ-line, c) ABZZ-line, d) dashed hexagon16x, e) dashed triangle36x, for STS simulations.

Now we look at the line structures, their STS/STM images to gain an idea of the capabilities of different lines in confining electronic states on the surface. The Dense ZZ-line however has been left out due to its peculiar geometry, and therefore we are left with the DaZZ-line, the ABZZ-line, and the ACh-Lin to get started with, in fig. 4.14

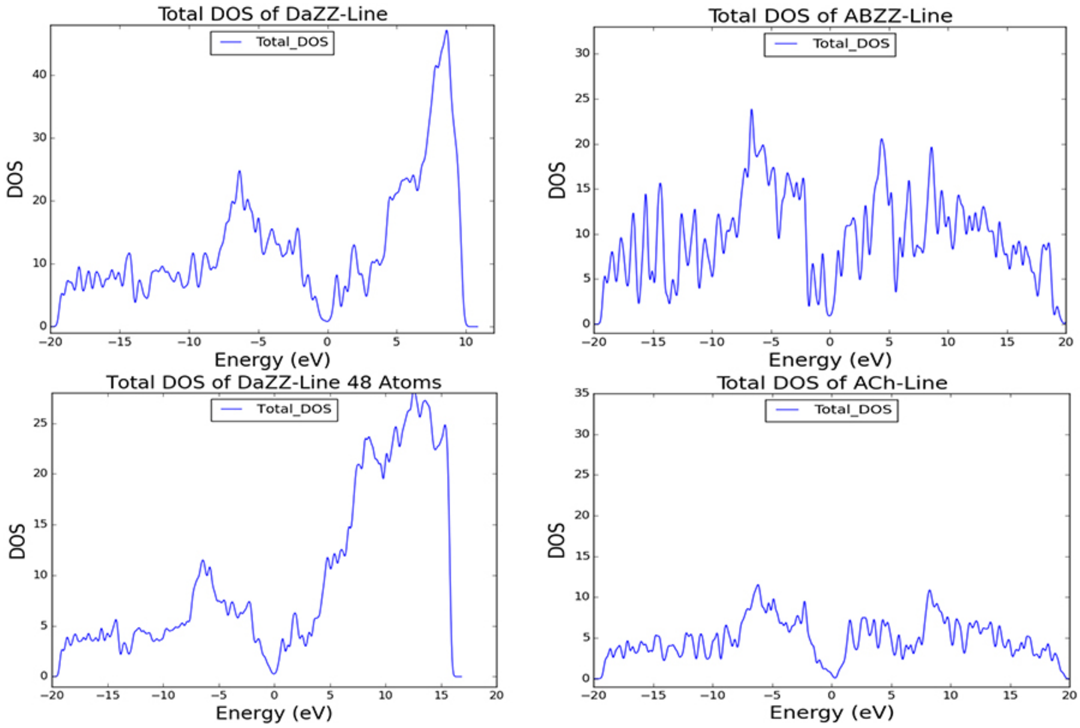

Figure 4.14: The Kohn-Sham total DOS's of DaZZ-line, ABZZ-line, and the ACh-Line, while converged only up to the Fermi level (except the lower left plot).

The above DOS's include only converged occupied bands, and therefore are only valid up to the Fermi level. However looking at the DOS of DaZZ-line and comparing that to the DOS of the half-cell DaZZ-line (48-atom cell), which has converged unoccupied bands, the spectrum above the Fermi level looks very similar to the converged case, and therefore the STS of the single atoms can be expected to give qualitatively correct results. In fig. 4.15 we show the STS's of middle and border Si-atom of the DaZZ-line.

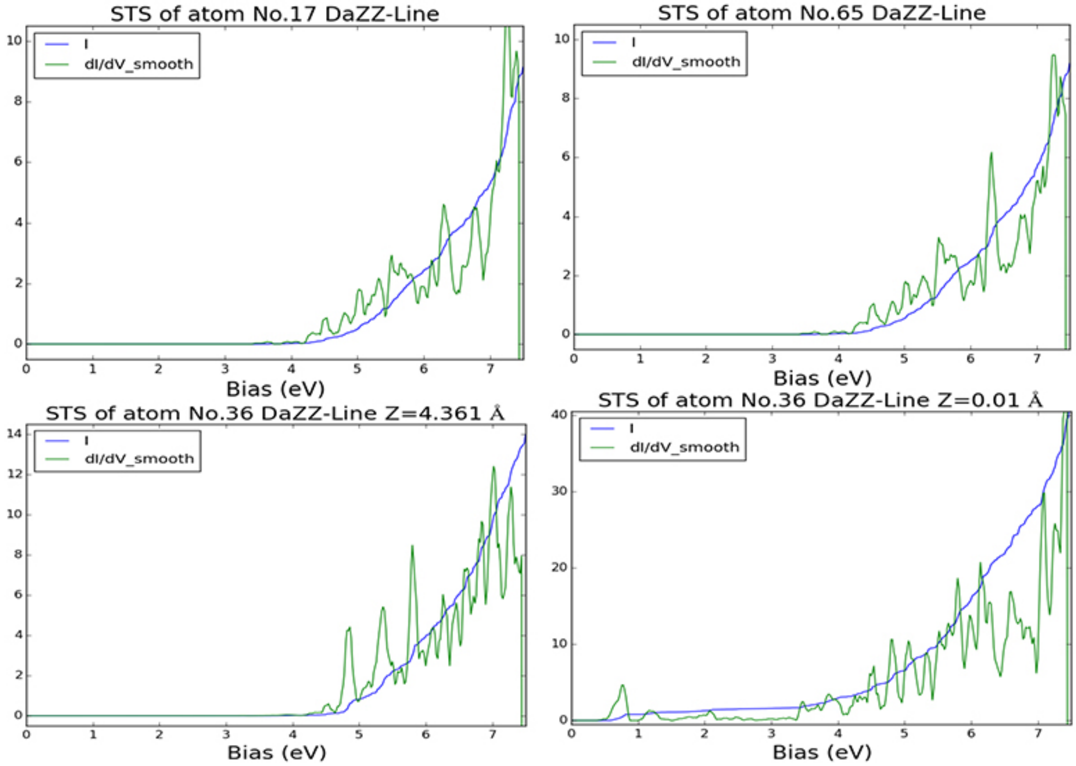

Figure 4.15: Above: The STS of two central atoms at $Z = 4.361$ Å. Below: The STS of the Si atom within the DaZZ-line at two different heights.

Now we present the STM results for the DaZZ-line at two different heights, which showed many peaks in the LDOS of the central atoms, taken at the peak biases according to the STS results:

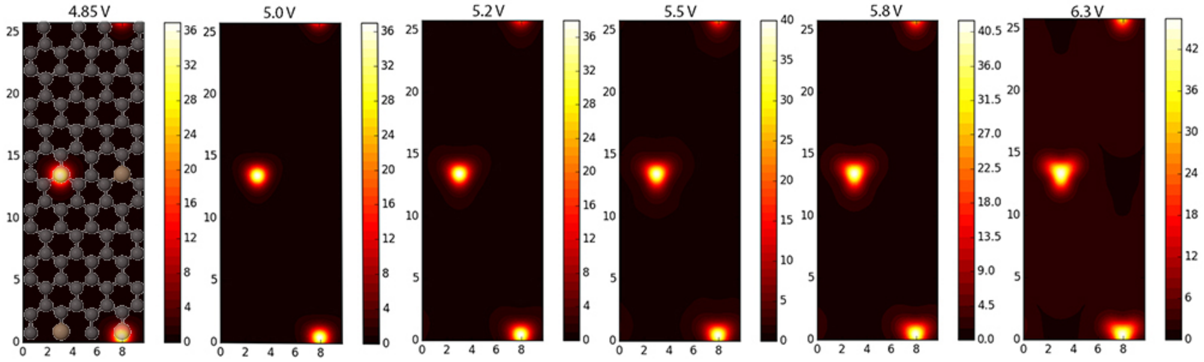

Figure 4.16: STM results of the DaZZ-line at 2.5Å for the bias set of $[4.85, 5.0, 5.2, 5.5, 5.8, 6.3]$ V (left to right) .

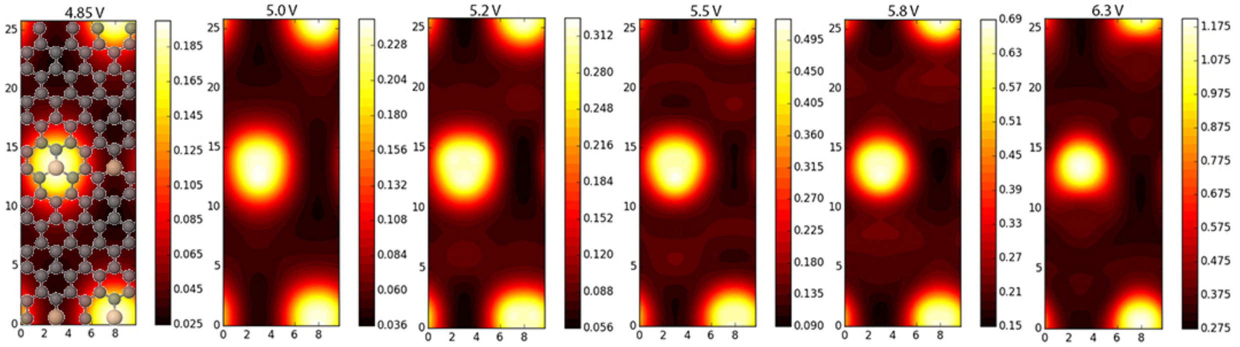

Figure 4.17: STM results of the DaZZ-line at 4.361Å for the bias set of $[4.85, 5.0, 5.2, 5.5, 5.8, 6.3]$ V (left to right) .

At $Z = 2.5$ Å there are no states in between the Si-atoms to be observed, other than the fact that the trivalent nature of the Si-C bonds become clear for the larger biases. However at $Z = 4.361$ Å for bias of 5.5 V there a weak feature appears in between the Si-lines, which we look at more closely (repeated) in fig. 4.18.

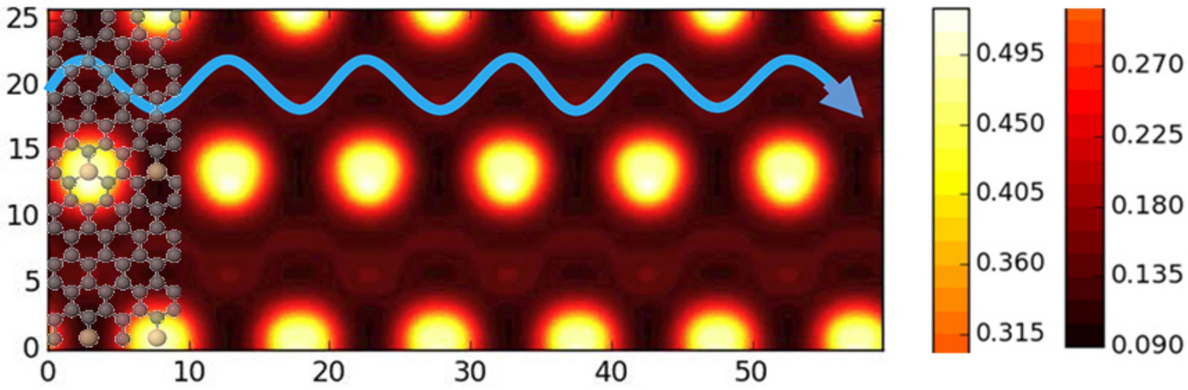

Figure 4.18: The weak confined state in between the Si-lines, in the form of a sinusoidal wave as marked with the blue arrow.

As for the two other structures, it is not expected that any confined states appear in the STM images, however for the sake of comparison and reference we examine them as well, in fig. 4.19.

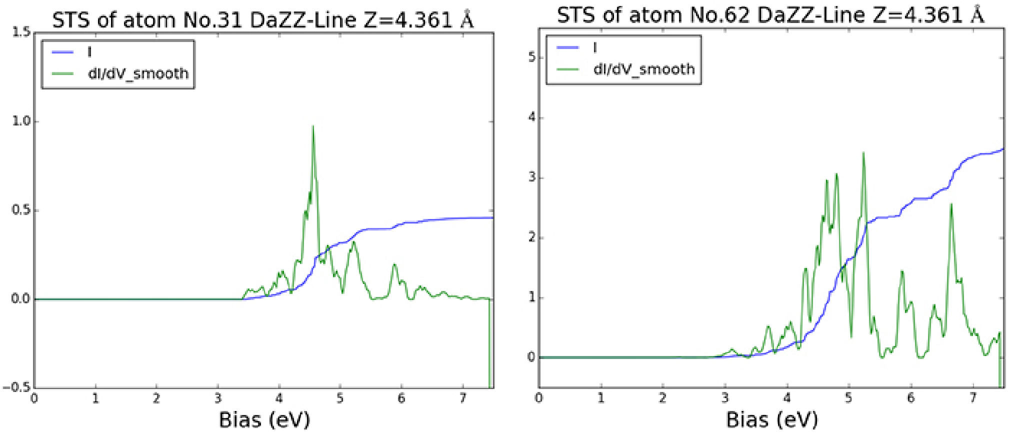

Figure 4.19: The STS of a central atom and a Si in the ABZZ-line at $Z = 4.361$ Å.

The spectra indicate a clear peak in the LDOS at 4.5 V, and so we take a look at the STM images at two different height similar to the DaZZ-line case, in fig. 4.20.

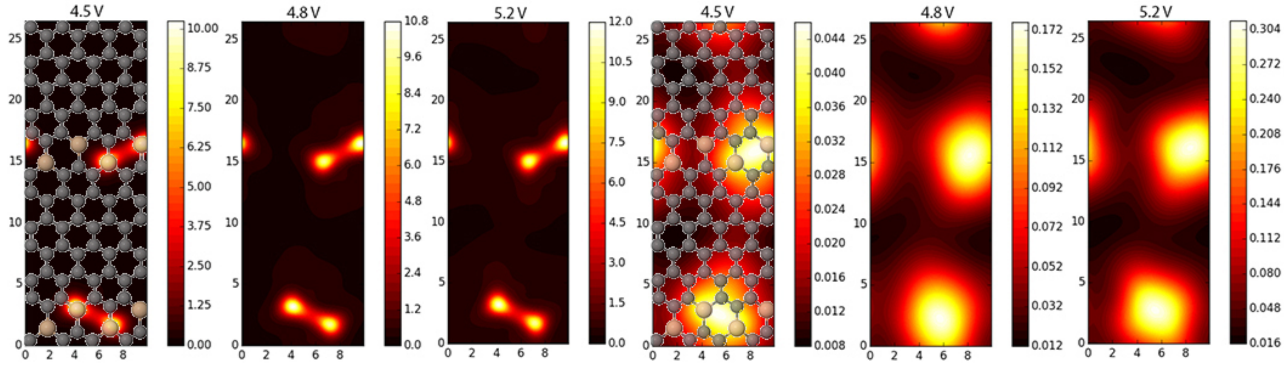
4.5 V
4.8 V
5.2 V
4.5 V
4.8 V
5.2 V

Figure 4.20: The STM images of the ABZZ-line for three biases of $[4.5, 4.8, 5.2]$ V at $Z = 2.5$ Å (left), and $Z = 4.361$ Å (right).

Indeed for 4.5 V, one sees a weak connection between the silica at the higher Z distance in the above set of images. The STS results for the ACh-line are presented in fig. 4.21.

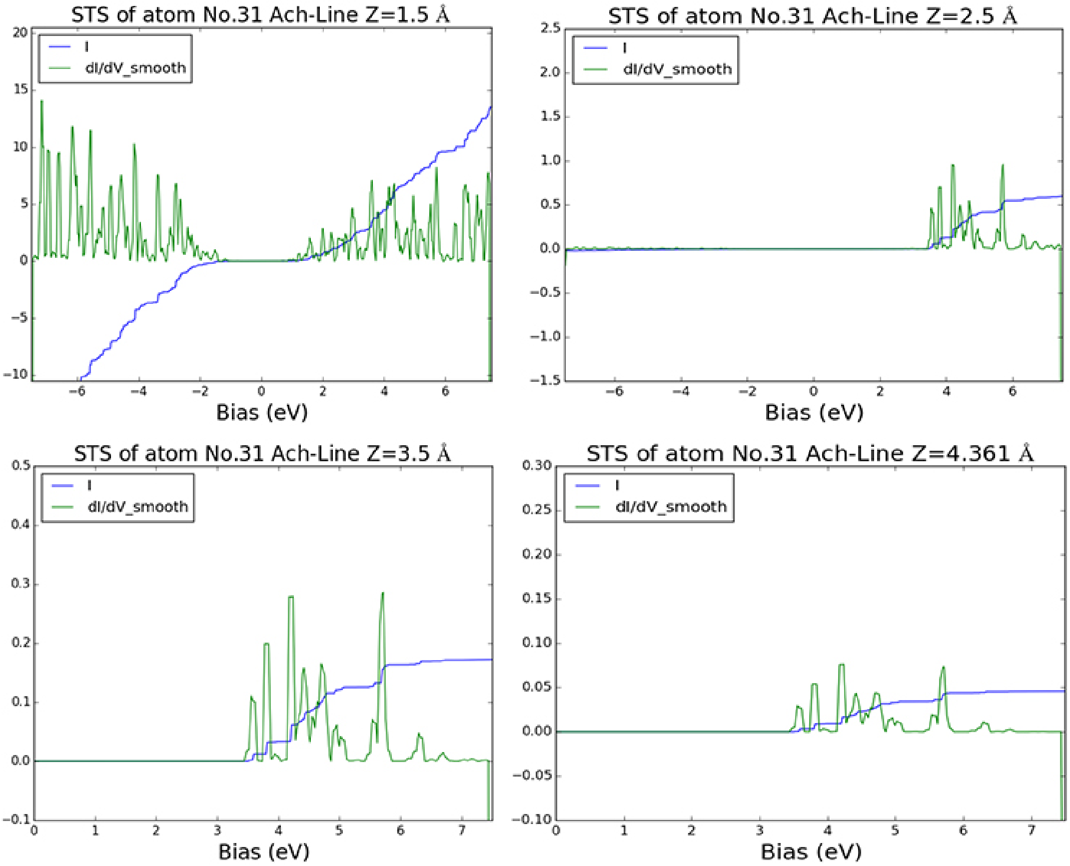
STS of atom No.31 Ach-Line Z=1.5 Å
STS of atom No.31 Ach-Line Z=2.5 Å
STS of atom No.31 Ach-Line Z=3.5 Å
STS of atom No.31 Ach-Line Z=4.361 Å

Figure 4.21: The STS of a central atom ACh-line at 4 differnet heights $Z = 1.5, 2.5, 3.5, 4.361$ Å.

A few LDOS peaks at larger heights of $Z \geq 2.5$ Å can be observed. Accordingly, the STM images in fig-4.22 are done at the peak biases.

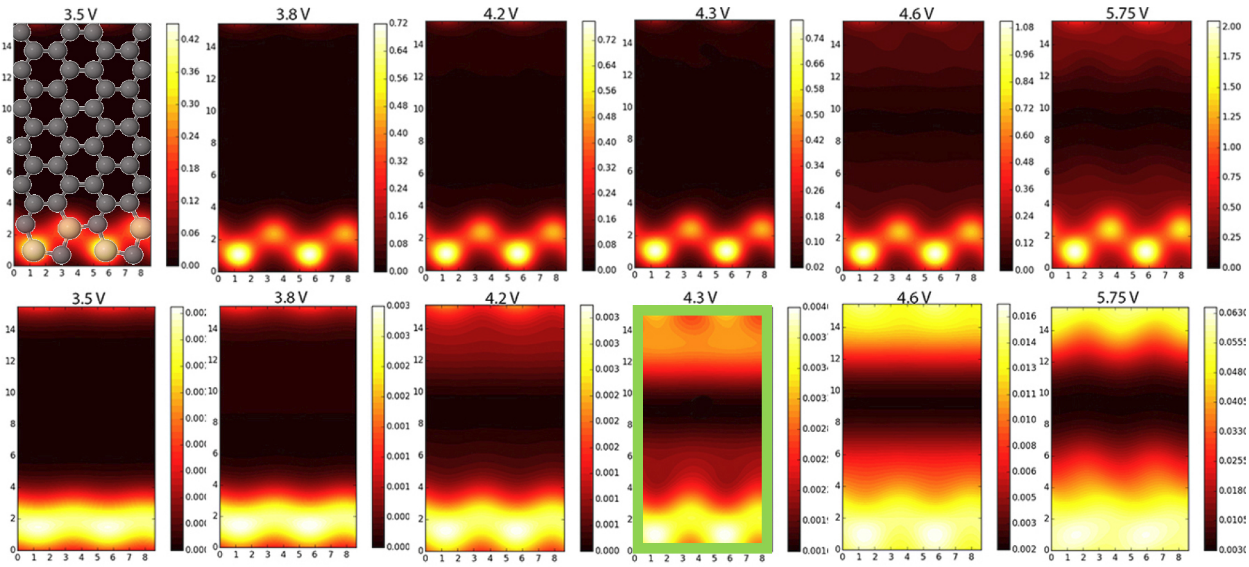

Figure 4.22: The STM images of the ACh-line for the biases of $(3.5, 3.8, 4.2, 4.3, 4.6, 5.75)$ V at $Z = 2.5$ Å (above), and $Z = 4.361$ Å (below), with the candidate image marked with a green frame.

As seen in the figures, there are additional states appearing as free standing states close to the Si-lines for 4.3 V bias at $Z = 4.361$ Å, which we look at in repeated fashin in fig. 4.23.

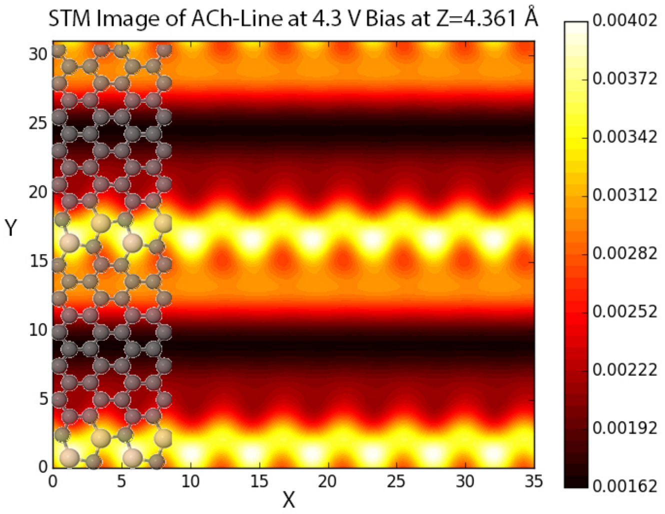

Figure 4.23: The repeated STM image of ACh-line at 4.3 V bias from the height of $Z = 4.361$ Å showing the confined states next to the armchair Si-lines (the Si-lines have the brightest color).

This kind of result is an example of significant potential for producing confined states, which then requires converging the unoccupied bands for more reliable STM images. And indeed this is what we have done, in order to have the results consolidated by converging the unoccupied bands amongst which these LDOS's appear.

Lastly for the closing of this section we look at the dashed versions of the hexagon, and the triangle, in order to analyse their potential. However, first we look at their total DOS's in fig. 4.24

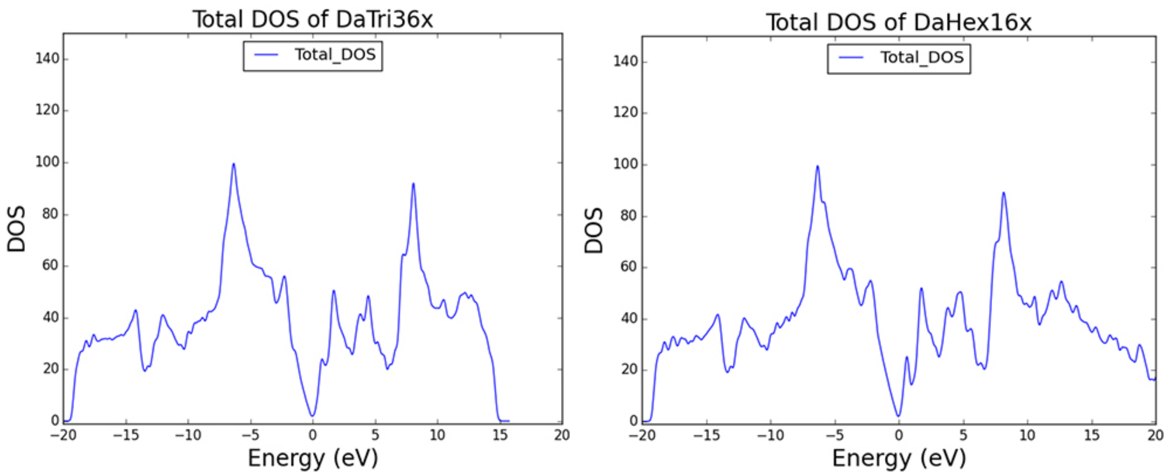

Figure 4.24: The total Kohn-Sham DOS's of dashed hexagon_16x (right), and the dashed triangle_36x (left).

Judging by the shape of the DOS curves, it seems that the unoccupied bands are more or less converged up to 5 eV (based on the definition of convergence for WF's, (e.g. log_{10} of error being -5.0 instead of -8.0)). Therefore it makes sense to examine the STM simulations according to the peak biases of STS spectra, to see to what states these unoccupied bands correspond to. Fig. 4.25 shows the STS spectra for 3 different atoms of the dashed hexagon, one at the border, one at the center, and one in between them.

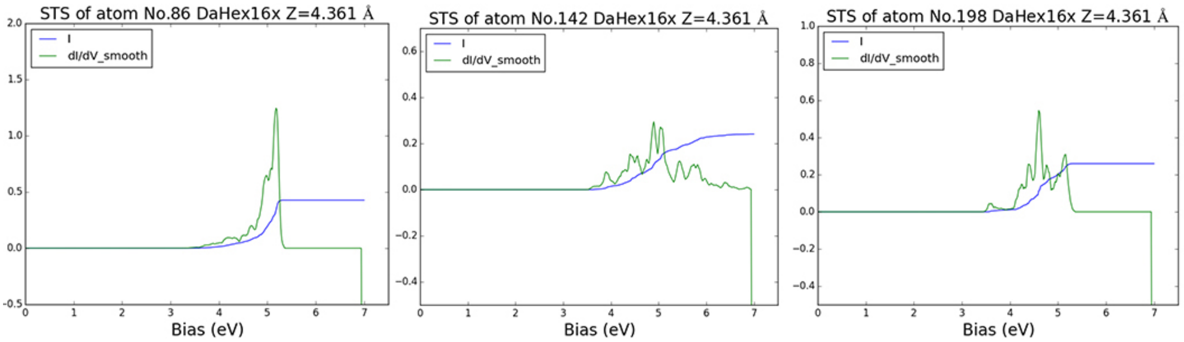

Figure 4.25: The STS of the border Si-atom (left), the central atom (center of the hexagon) (right), and the C-atom in between the previous two atoms (center) of the dashed hexagon_16x at $Z = 4.361$ Å.

From which the STM images of fig. 4.26 are made according to the peak biases.

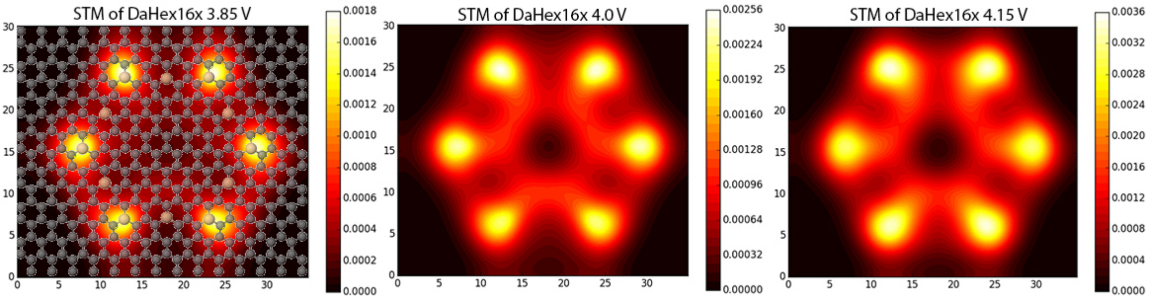

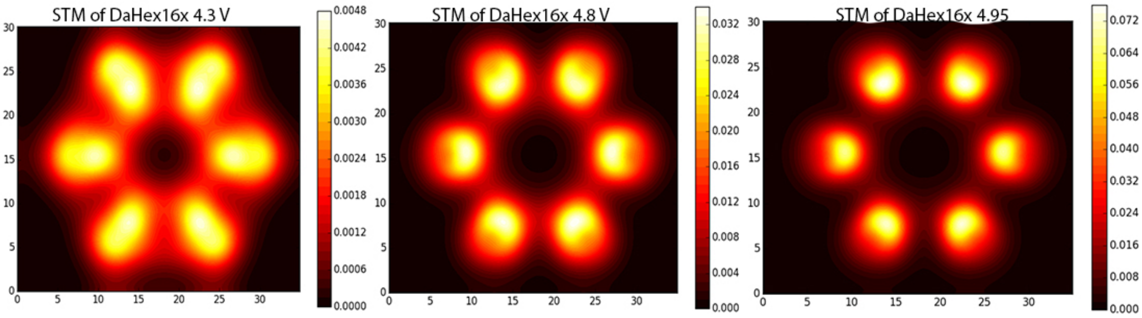

Figure 4.26: The STM images of the dashed Hexagon16x for the biases of $(3.85, 4.0, 4.15, 4.3, 4.8, 4.95)$ V at $Z = 4.361$ Å.

Analysing the STM/STS results, it seems that there are no new confined states are formed in the dashed hexagon.

In the following we look at the STS/STM of dashed Triangle36x starting with the STS in fig. 4.27, and the STM of peak biases up to 4.3 V in fig. 4.28:

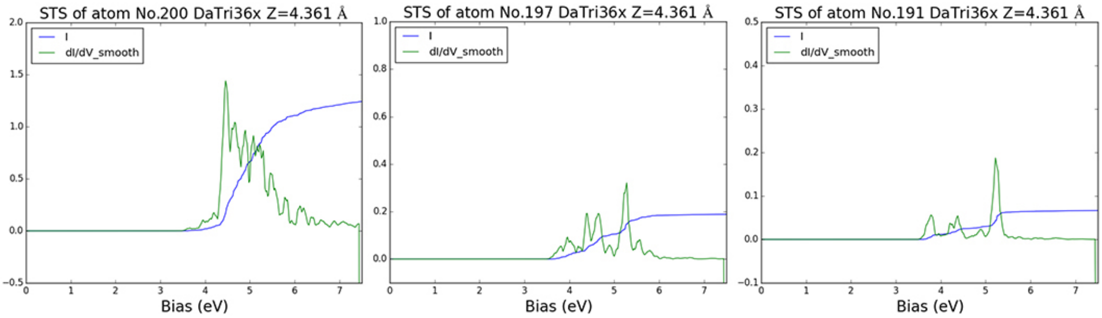

Figure 4.27: The STS of the border C-atom (left), the central atom (center of the triangle) (right), and the C-atom in between the previous two atoms (center) of the dashed Triangle36x at $Z = 4.361$ Å..

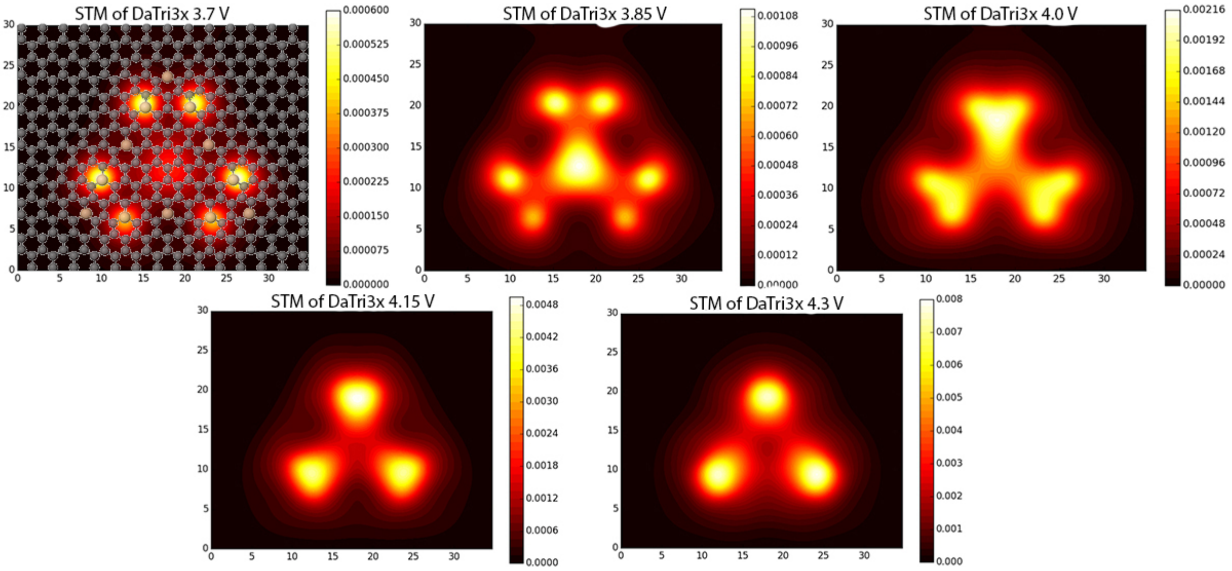

Figure 4.28: The STM images of dashed Hexagon16x for the biases of $(3.7, 3.85, 4.0, 4.15, 4.3)$ V at $Z = 4.361$ Å.

As it could be seen in the images of fig. 4.28 for 3.85 V bias we clearly see a new confined state in the form of a triangle, which also vaguely appears for bias ∼ 3.7 V. This confined state is relatively very reliable, since the the corresponding bias is relatively low, and would be more or less close to the convergence point. Therefore, contrary to the dashed hexagon, the dashed triangle has a clear potential for confining a surface state, even though we do not further examine this structure by converging the unoccupied bands.

4.2.2 STM/STS of Select Structures w/ Converged Unoccupied Bands

In this part we examine the quantum confinement of the surface states with structures, whose unoccupied energy bands have been converged, and which prior to convergence, showed clear potential for confining surface states. First we look at the atomic positions of each structure, on which a STS was done in fig. 4.29.

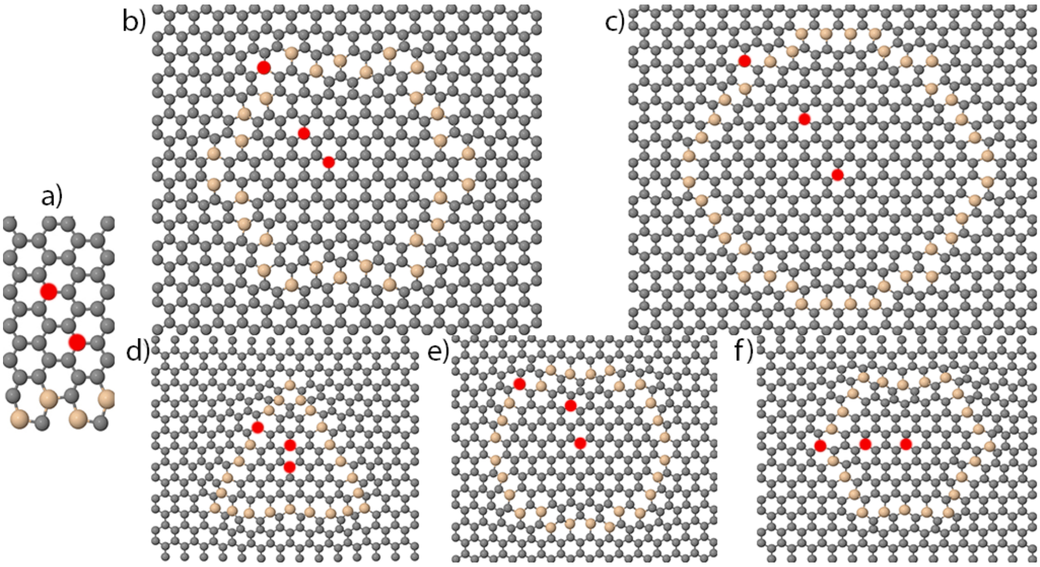

Figure 4.29: The atomic positions of a) ACh-line, b) ABZZ-Hexagon, c) XXL-Circle, d) Triangle36x, e) Circle4x, f) and Hexagon16x, for STS.

The shape and the biases of these confined states therefore can be trusted as far as the TH-STM model resembles the experimental STM imaging. We start by looking at the ACh-line (shown in fig. 4.29-a), this time with 192 converged bands out of 320 in total (the first 96 bands are occupied). Fig. 4.30 shows the total DOS of the ACh-line with 192 converged bands.

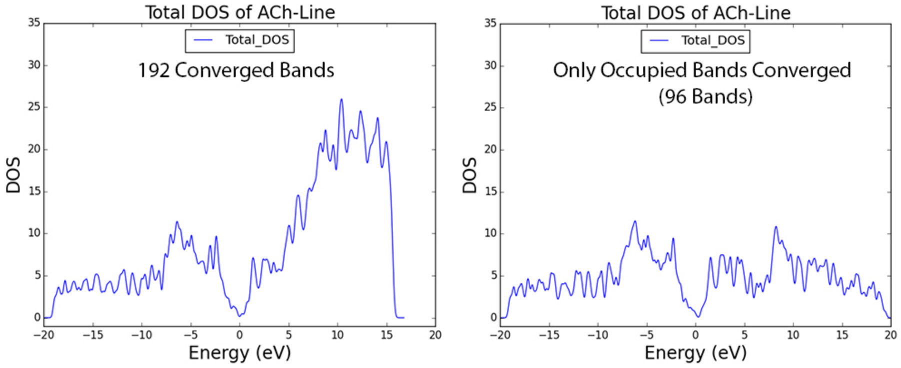

Figure 4.30: The total DOS of the ACh-line with 192 converged bands (left), compared to the ACh-line with only first 96 bands (the occupied bands) converged (right).

As the graphs show even bands at ≈ 4.0 eV are more or less converged in the right figure (based on the definition of convergence for WF's, (e.g. log_{10} of error being -7.0 instead of -8.0)). It is only the bands beyond 5.0 eV, which show a lot of difference in their DOS's. Now we look at the STS's of central and a mid-central C-atoms at two different height to check for any positive bias surface-states at the mentioned positions, in fig. 4.31. Additionally, we will be checking some negative biases as they appear in the lower-height STS's as well, however only for this structure.

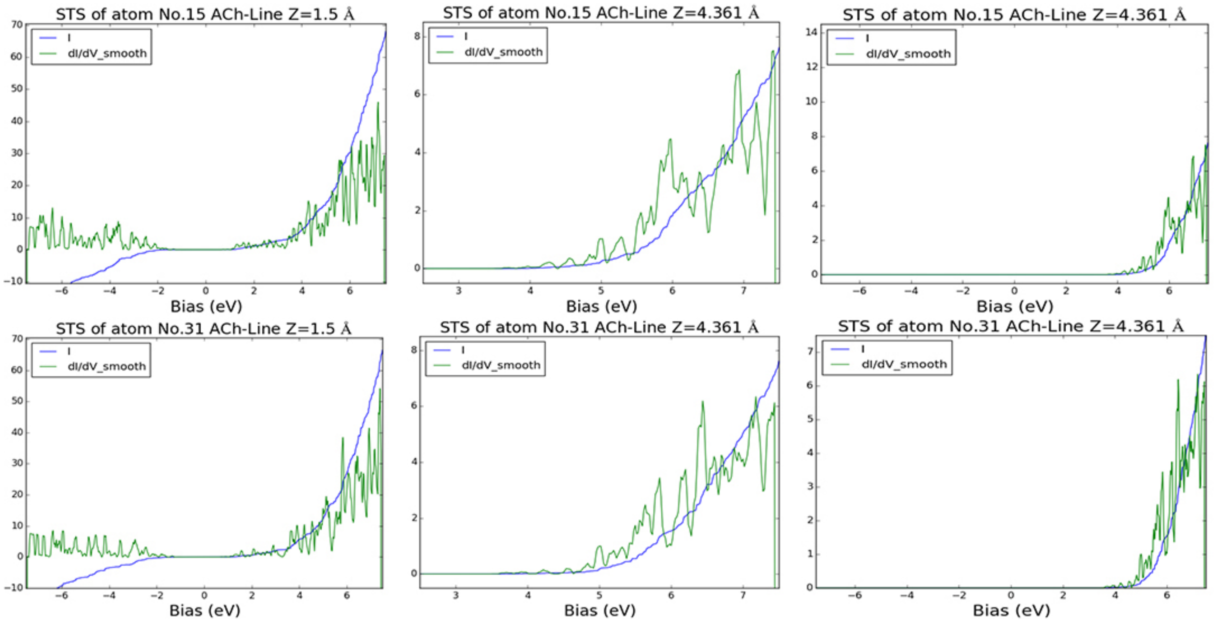

Figure 4.31: The STS of the ACh-line of the central (No.31, below row) and mid-central atom (No.15, above row) at two different heights $Z = 4.361$ Å, and $Z = 1.5$ Å, with the zoom in of the $Z = 4.361$ Å (the center figures).

Both the central atom, and the mid-central one show peaks for positive bias STS's, with high intensity, while the negative biases are only once again present for low heights. In fig. 4.34 we look at the STM images corresponding to the positive biases.

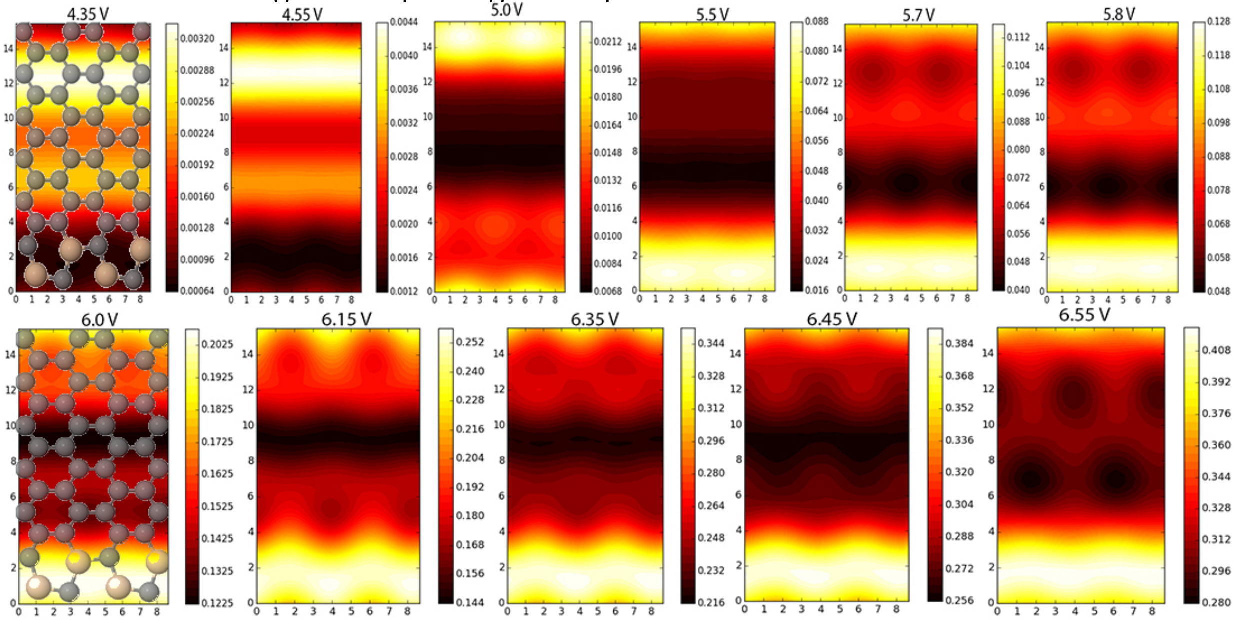

Figure 4.32: The STM images of ACh-line for the biases of $4.3 - 6.55$ V at $Z = 4.361$ Å.

Looking at the above snapshots, it is clear that the ACh-line indeed has a great potential for confining surface states, as the closer examination shows, that there is indeed 3 different confined surface-states present. (If we regard each bright line as peak and each dark line as trough) the three images below in fig. 4.33 show a double-peak mode (both being peaks), where the Si-lines are appearing as black for 4.55 V, another double-peak mode (one peak one trough), for 5.8 V, and finally a three peak mode (peak trough peak) between the bright Si-lines for 6.15 V.

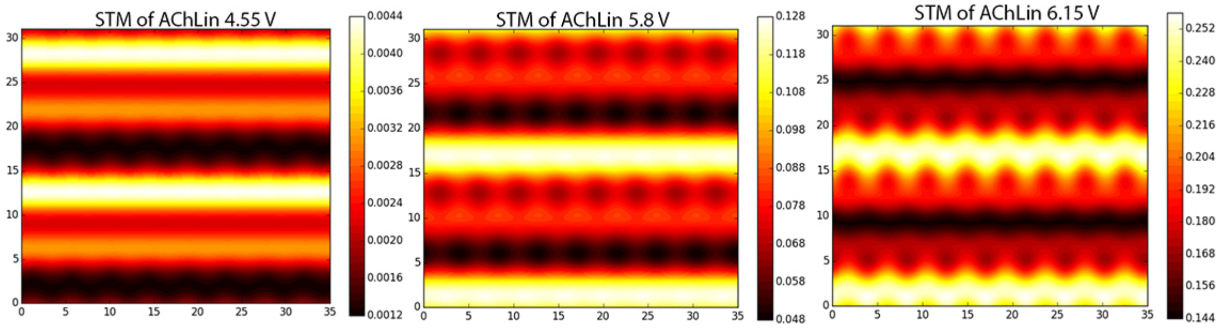

Figure 4.33: The repeated STM images of ACh-line showing three different confinement modes, two of which resemble the experimental STM images of confined states between two lines.

However, looking at the negative biases, even at 2.5 Å, there are no new confined states in fig. 4.34.

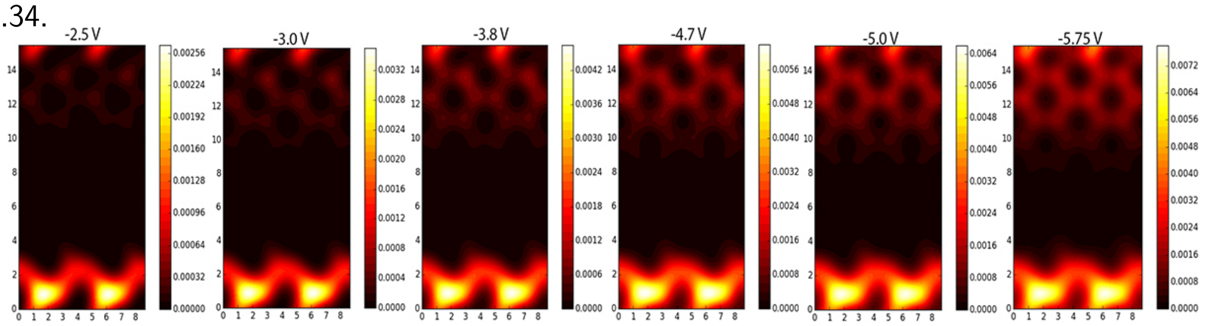

Figure 4.34: The STM images of ACh-line for biases of -2.5 → -5.75 V, taken at $Z = 2.5$ Å.

As expected negative biases STM images deliver no sign of confinement, which is consistent with the idea that the Si-impurity contributes to the positive states and LDOS of its neighbouring atom, which in turn may or may not become a confined surface state.

Next we look at three structures of the same class, namely the Hexagon16x, the Triangle36x, and the Circle4x (as shown in fig. 4.29), all of which have super-cells of 392 atoms, $\sim$ 786 occupied bands in total with very similar DOS's as shown in fig. 4.35.

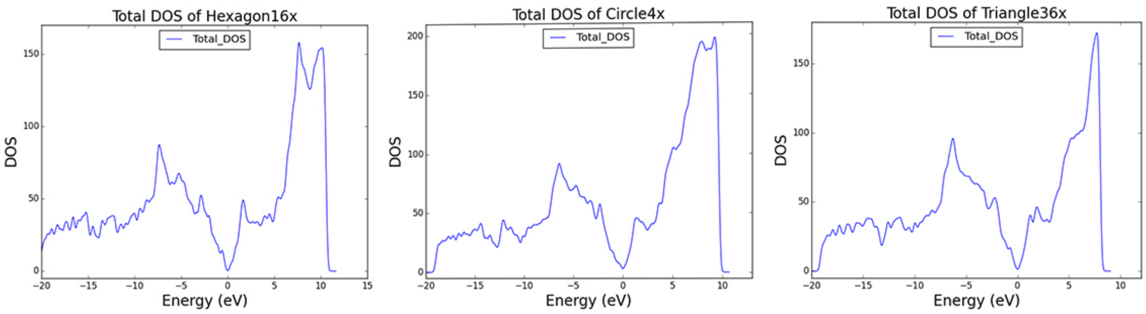

Figure 4.35: The DOS of the hexagon16x, triangle36x, and the circle4x, with 1400, 1350, and 1600 bands respectively converged.

We look at the STS's of the Hexagon16x on 3 different atoms from the highest Z-distance, similar in position to the dashed structures in the previous section, once in the full spectrum and once zoomed in as in fig. 4.31. Therefore, while we leave the negative biases aside altogether, we also note that the lower height STS's in the positive region only increase in intensity of the peaks with decreasing the z-distance (for example from 4.361 Å to 3.5 Å). The results are shown in fig. 4.36

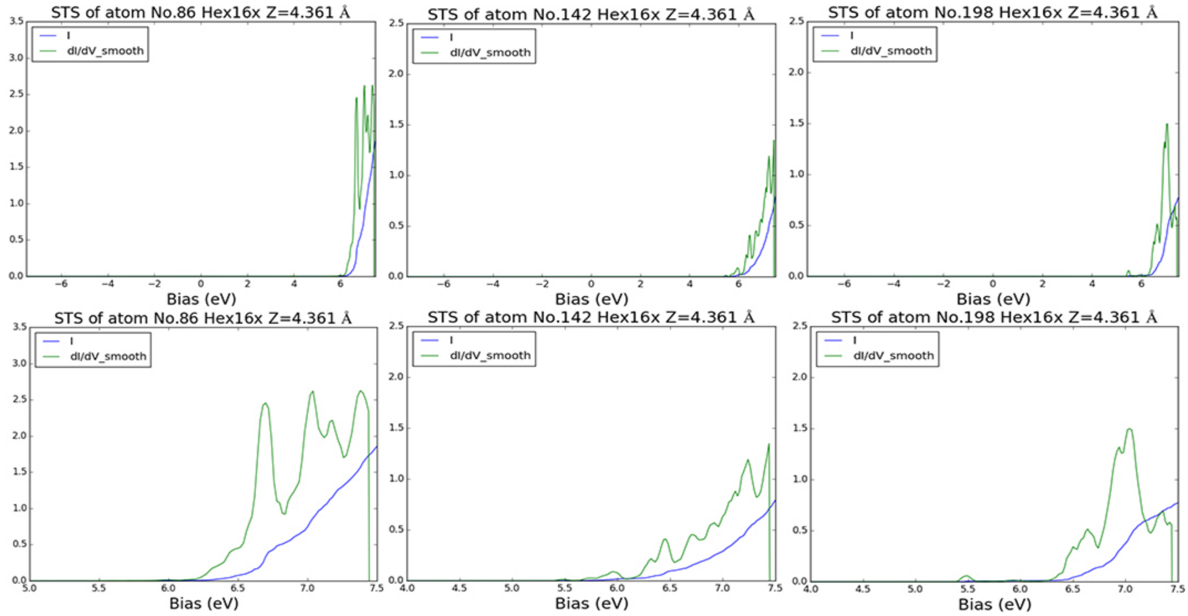

Figure 4.36: The STS of the 3 different atoms of the Hexagon16x, border Si-atom (left), the central C-atom (right) and the C-atom in between the previous 2 atoms (center), both in full spectrum (top), and the zoomed in spectrum (bottom).

The STS curves of the Hexagon16x indicate many modes, and indeed with high intensity both at the central atom and the mid-central atom. Therefore, we made a complete set of STM images according to the peaks of the C-atoms in the center and mid-way, not to miss any possible modes, as shown in fig. 4.37.

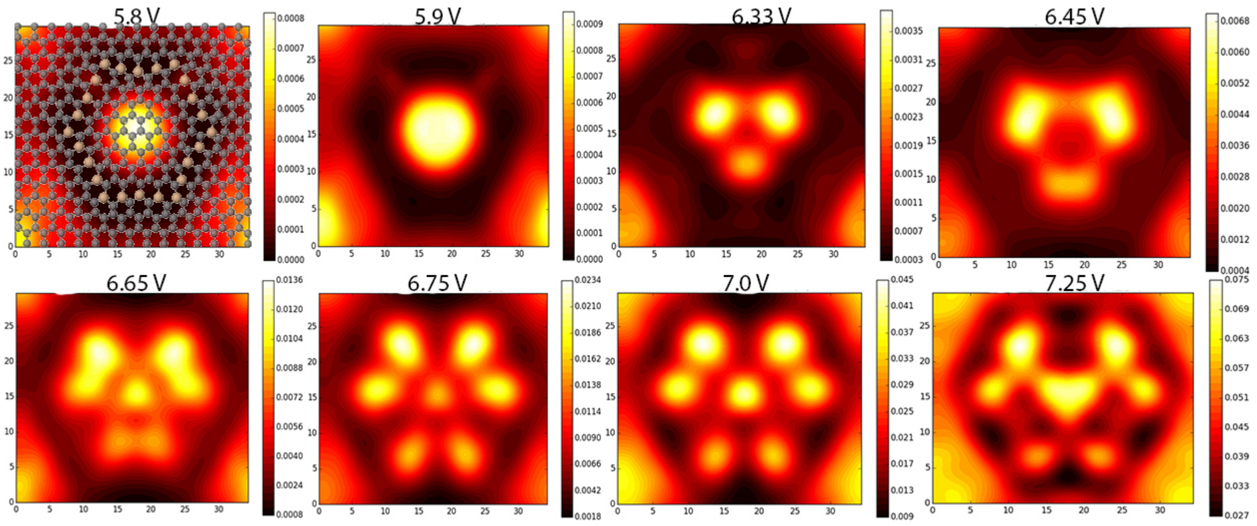

Figure 4.37: The STM images of the Hexagon16x at the mentioned biases showing the scattering and the multi-resonance process.

Based on the above set of images, there could at least four different modes be seen, as confined surface states. In the above row the Si-atoms appear black, and the side images come from the border graphene on the upper periodic image. In the bottom row the Si-atoms appear on the sides of the central confined mode, while the graphene that is attached to the Si-atoms outside the plateau appear dark. The interesting pattern that appears throughout, is that for the lower biases (5.8 V) a central confined mode appears, which then spreads into a triangle with increased biases, and then spreads over the Si-atoms, giving them intensity to appear in the image as the bias increases more, while simultaneously getting confined once again at the center, and then repeating the previous steps (as it turns into a triangle). In other words, this implies a dynamics of formation, that we can see a trace of in a set of images. This pattern looks similar to the multi-resonance occurring at the Dirac level for large potentials, in a 80-atoms corral STM experiment on the surface of a topological insulator as shown in fig. 1.7.

We continue by looking at the rest of the structures, expecting more or less the same behaviour that we just described for the hexagon. Fig. 4.38 shows the 3-atom STS of the Circle4x:

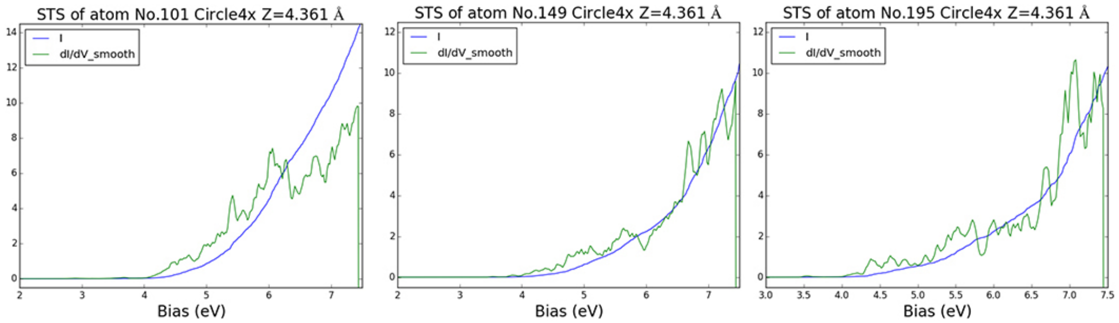

Figure 4.38: The STS spectra of the border Si, mid-central C, and the central C atoms in positive region at $Z = 4.361$ Å.

And fig. 4.39 the corresponding confined surface states, and their evolution with bias increase:

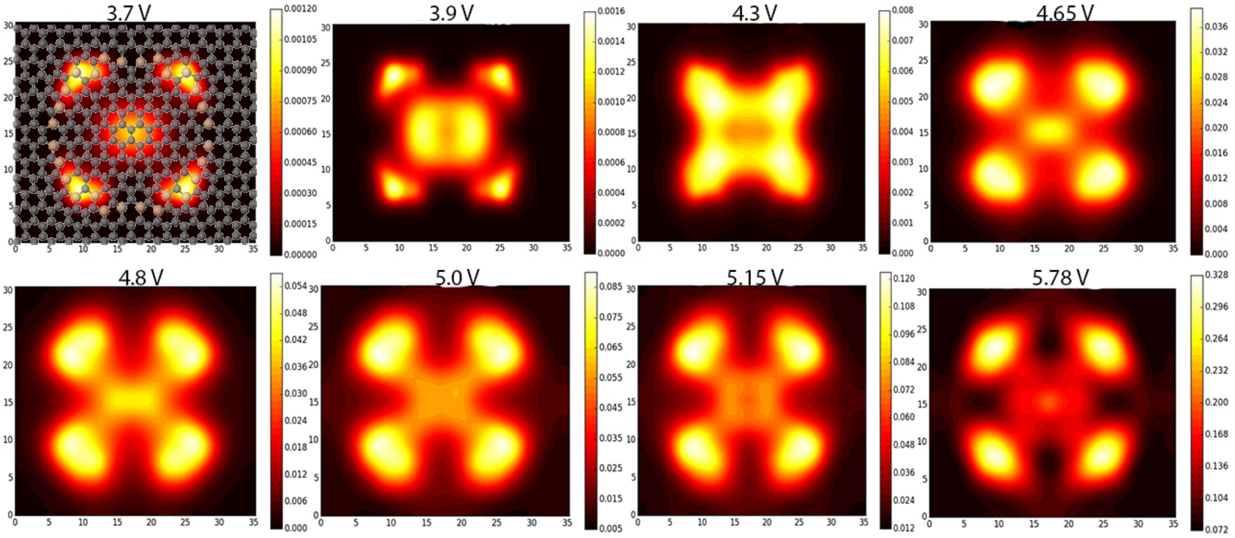

Figure 4.39: The STM images of the Cirle4x showing the similar multi-resonance process as in the Hexagon16x for increasing biases.

Once again looking at the image of 5.15 V biases the confined central mode is similar to that of 3.9 V biases, with only difference being the intensity of the Si-atoms LDOS, which resembles the multi-resonance scattering process as in the case of the hexagon.

Moving onto the Triangle36x, we notice the difference between the hexagon and the circle, namely that in hexagon initial confinement was without the presence of any Si-atoms. In fig. 4.40 we look at the 3 atoms STS of the triangle:

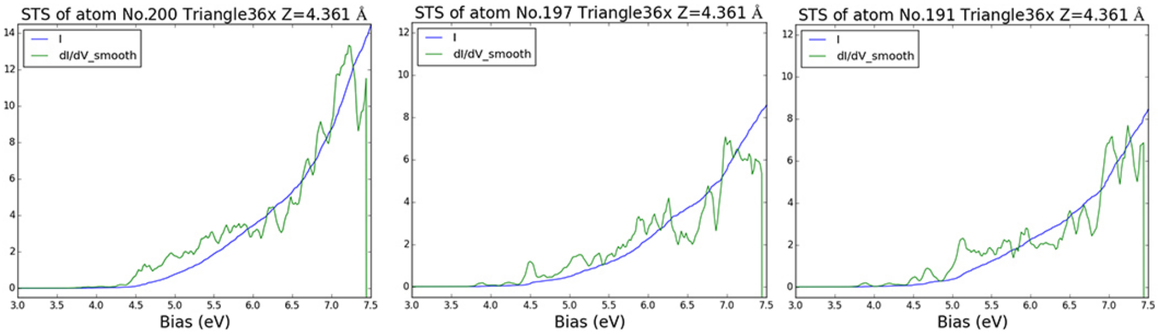

Figure 4.40: The zoomed-in 3-atom STS spectra of the Triangle36x at $Z = 4.361$ Å.

And accordingly in fig. 4.41 we have the STM images of the Triangle36x.

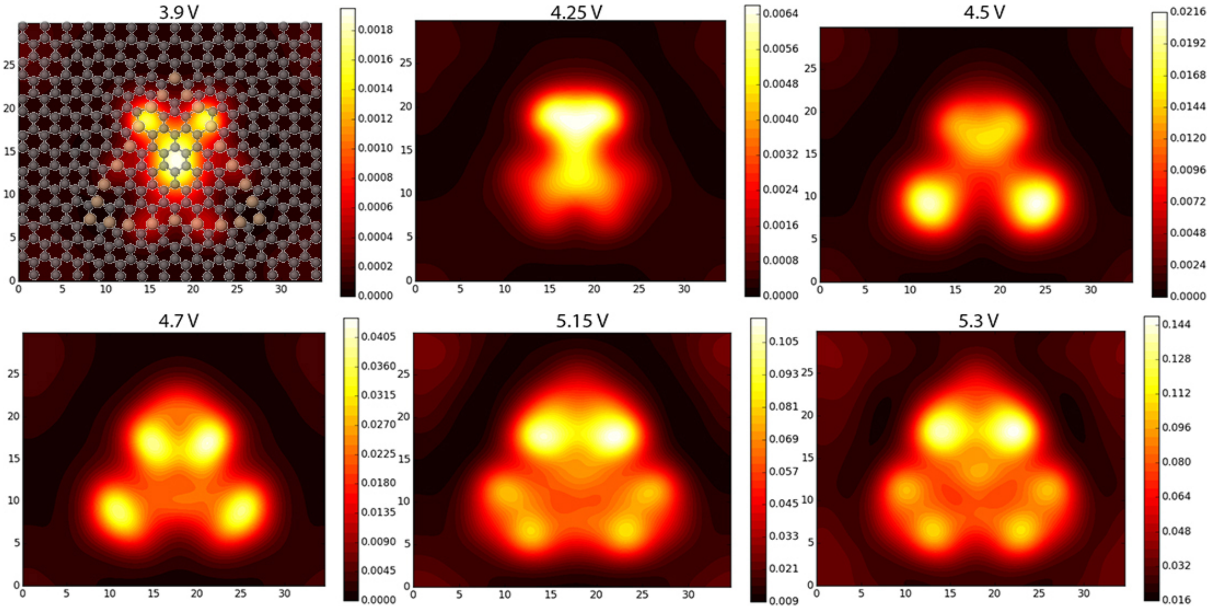

Figure 4.41: The STM images based on the STS peaks, of Triangle36x at $Z = 4.361$ Å.

Other than the low-bias central confined mode, there doesn't seem to be much intensification of that confinement with increasing bias however.

Having concluded this much about the confinement capabilities for our regular sized systems (392 atom cells), we also studied some large systems, The XXL-Circle and ABZZ-Hexagon (as shown in fig. 4.31), whose WF's we converged with many unoccupied bands beyond the Fermi level specifically for STM/STS simulations. Therefore we close the quantum confinements sections with the study of these structures. In fig. 4.42 we have the DOS's of the XXL-Circle with total of 2600 converged bands, and the ABZZ-Hexagon with 1700 total bands converged.

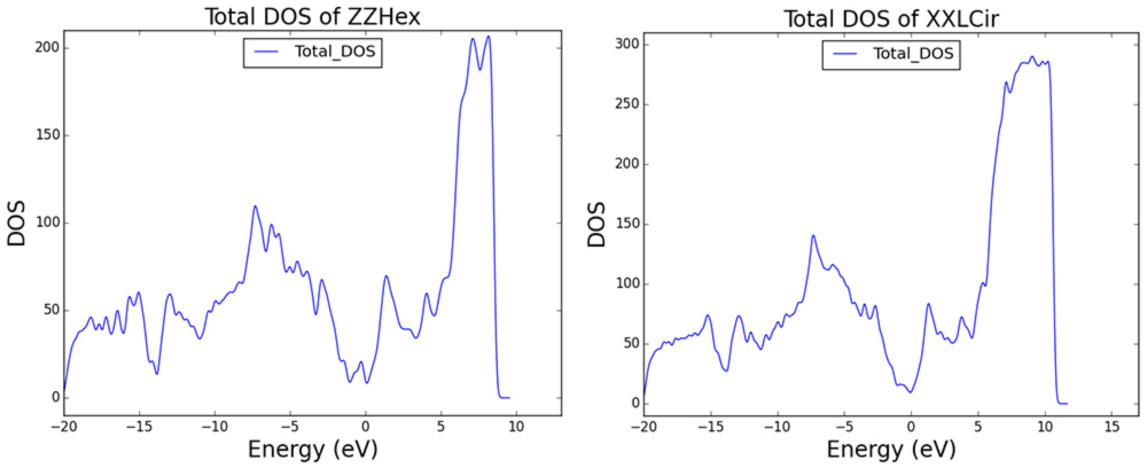

Figure 4.42: The DOS of the ABZZ-Hex with 1700 converged bands (left), and the XXL-Circle with 2600 converged bands (right).

The XXL-circle in its 648-atom cell has 1295, and the ABZZ-Hex, in its 512-cell atom, has 1024 occupied bands below the Fermi level. Fig. 4.43 and 4.44 are the 3-atom STS of the ABZZ-Hex similar to the normal structures, followed by the corresponding STM images:

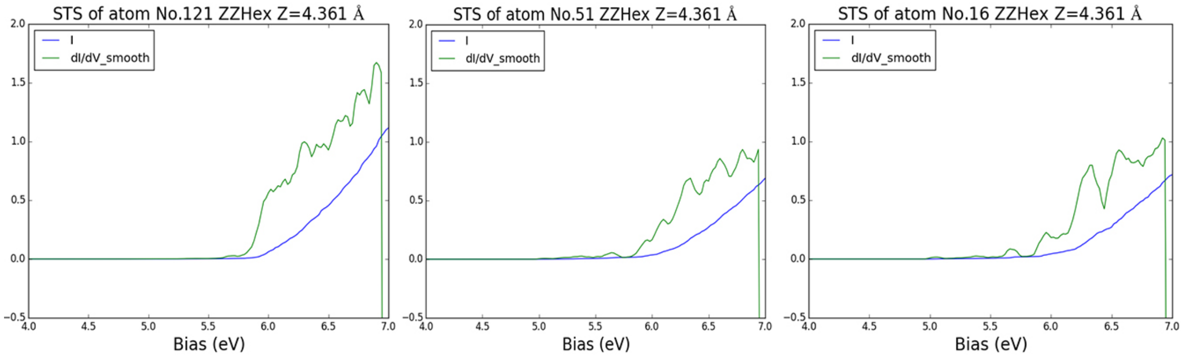

Figure 4.43: The zoomed-in 3-atom STS spectra of the ABZZ-Hex at $Z = 4.361$ Å..

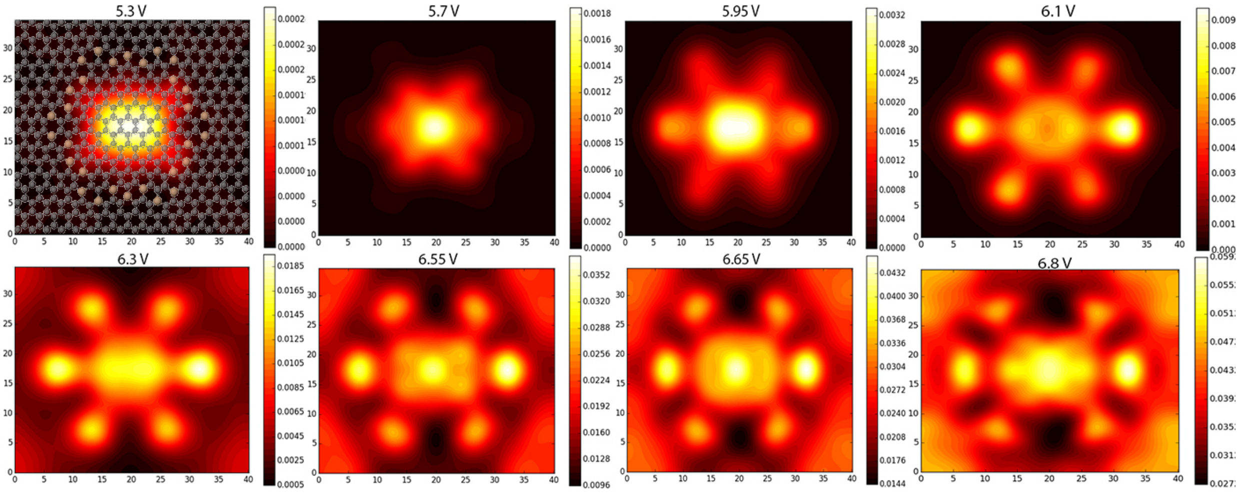

Figure 4.44: The STM images of ABZZ-Hex showing confined states, at $Z = 4.361$ Å, evolving with the increase of bias.

Similarly we have for the STS of the XXL-Circle in fig. 4.45.

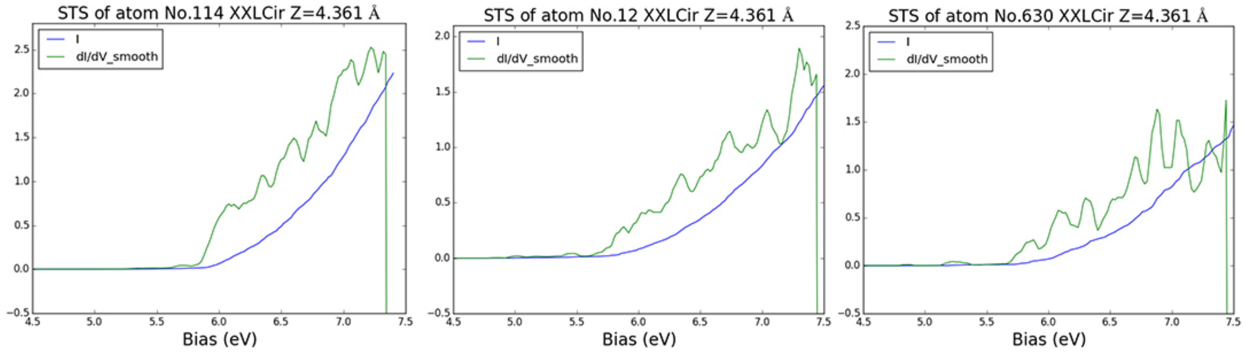

Figure 4.45: The zoomed-in 3-atom STS of the XXL-Circle at $Z = 4.361$ Å .

From which the STM images of fig. 4.46 have been produced.

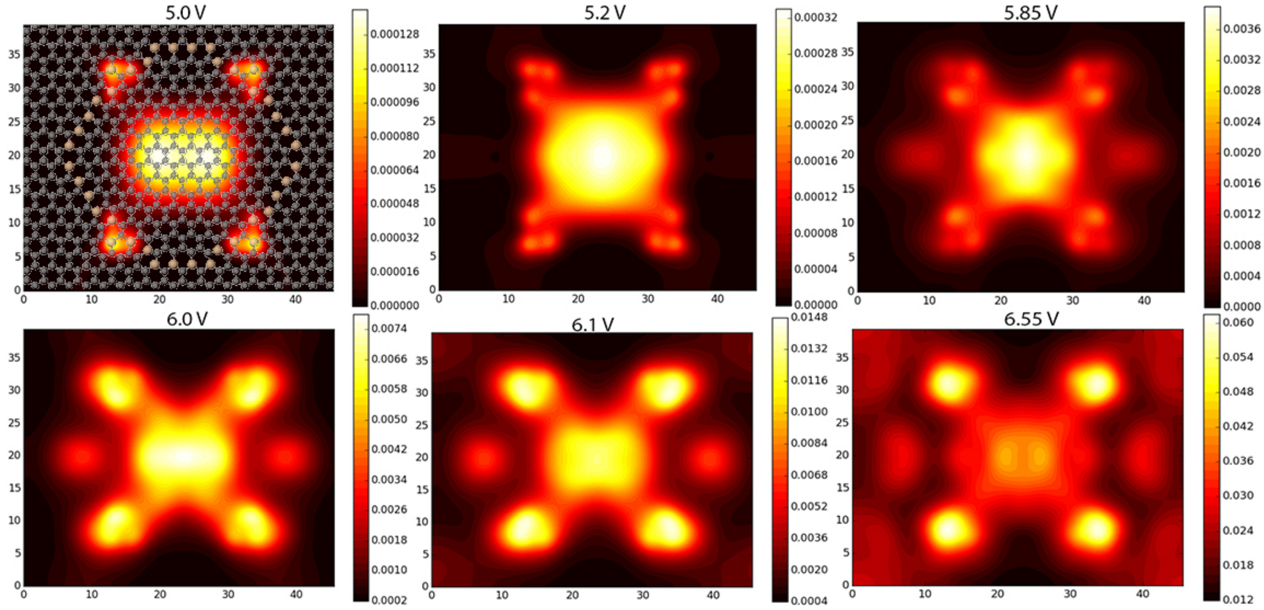

Figure 4.46: The STM images of the XXL-Circle for increasing biases showing the evolution of the confined state, at $Z = 4.361$ Å .

It is once again clear that the same pattern as in the hexagon is repeating itself in the large structures as well, only in a different shapes as in the hexagon. But one fact remains irrefutable, and that is that the capability of seeing confined surface states, and clear potential for producing quantum corrals given the possibility of having multi-scattering and interference using a STM tip. Clearly the patterns show that the confinement goes beyond a weak undetectable surface states, which may occur in the presence of any impurity on a conducting surface.

4.3 Linear Plasmonic Response

4.3.1 TDDFT Linear Dielectric Response & EELS

We start the simulations of the plasmonic response, with the calculation of the linear dielectric response of the periodic systems in TDDFT (RPA) such as 2D Si-C, for benchmarking and comparison purposes, from which also the plasmonic EELS spectrum of the systems could also be calculated as given by eq. **??**. This method calculates the frequency-dependent dielectric function of a periodic system with, and without local field corrections (LFC), in a given direction (which is defined by the geometry of the system as referred to in the figures). For 2D systems the EELS spectrum in the plasmonic region can then be calculated using the zero momentum vector $q = [0, 0, 0]$ from the dielectric function Re and Im parts. However, this calculation involves many parameters which can alter the results and with regard to which the results need to be converged. In fig. 4.47 we show the results of altering some of the parameters for the calculation of the EELS spectrum of pristine graphene in its 2-atom cell (with two different broadening parameters η in the upper and the lower curves).

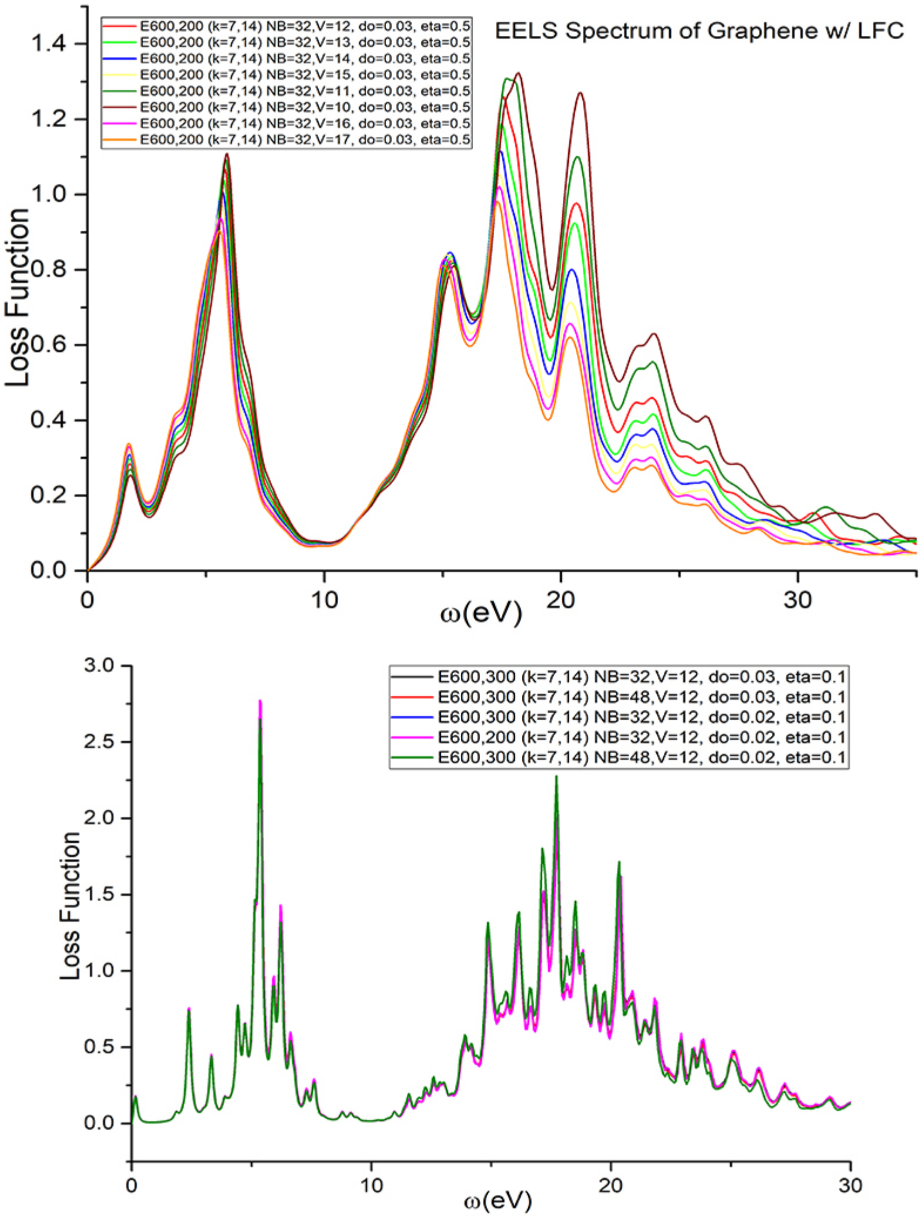

Figure 4.47: The EELS spectrum of graphene for the varying vacuum in the z-direction (above), and for the fixed vacuum of 12 Å (below), while changing other parameters ($\eta = 0.5$ above, $\eta = 0.1$ below).

About the set of parameters in the above calculations it should be said, that the first two are the E_{cut}'s for the ground-state (GS) wavefunction, and the LFC, the the k-point mesh initial and dense sampling 2D number ($k \times k \times 1$), the number of the converged bands (NB), the vacuum (V), the frequency increment (do=$\Delta\omega$) of the non-linear grid, and the broadening parameter (η).

As seen in fig. 4.47 for a 2D system the vacuum is one of the important parameters, as is the denseness of the k-point mesh and the number of the bands. However the bands and the k-point mesh can vary with the size of the 2D system. But the acceptable value for the vacuum in a 2D system seems to be $15 - 18$ Å. In the upper plot of fig. 4.47 we see that for $\mathrm{V} = 17$ Å, the spectrum almost overlaps with the previous one, therefore we used 18 Å of vacuum for the smaller (up to 10 atoms) systems in our calculations. However 15 Å is still an acceptable amount in the case of the heavy calculations, but for any value below 15 Å, the shift in the spectrum in 2D materials is visible. The parameters $do = \Delta\omega$, the frequency increment for the non-linear frequency-grid, and E_{cut} for the LFC, which is the smaller value in the diagrams of fig. 4.47 are two secondary parameters. These parameters, which add to the details of the spectrum, as opposed to being decisive about the correctness of the spectra, are chosen usually based on the necessity for details and the availability of computational resources. For larger systems high level of detail comes at very high computational cost, while for small systems its mostly necessary without being computationally expensive.

Therefore we start by presenting the dielectric function of graphene with and without LFC, and the corresponding EELS spectrum in fig. 4.48:

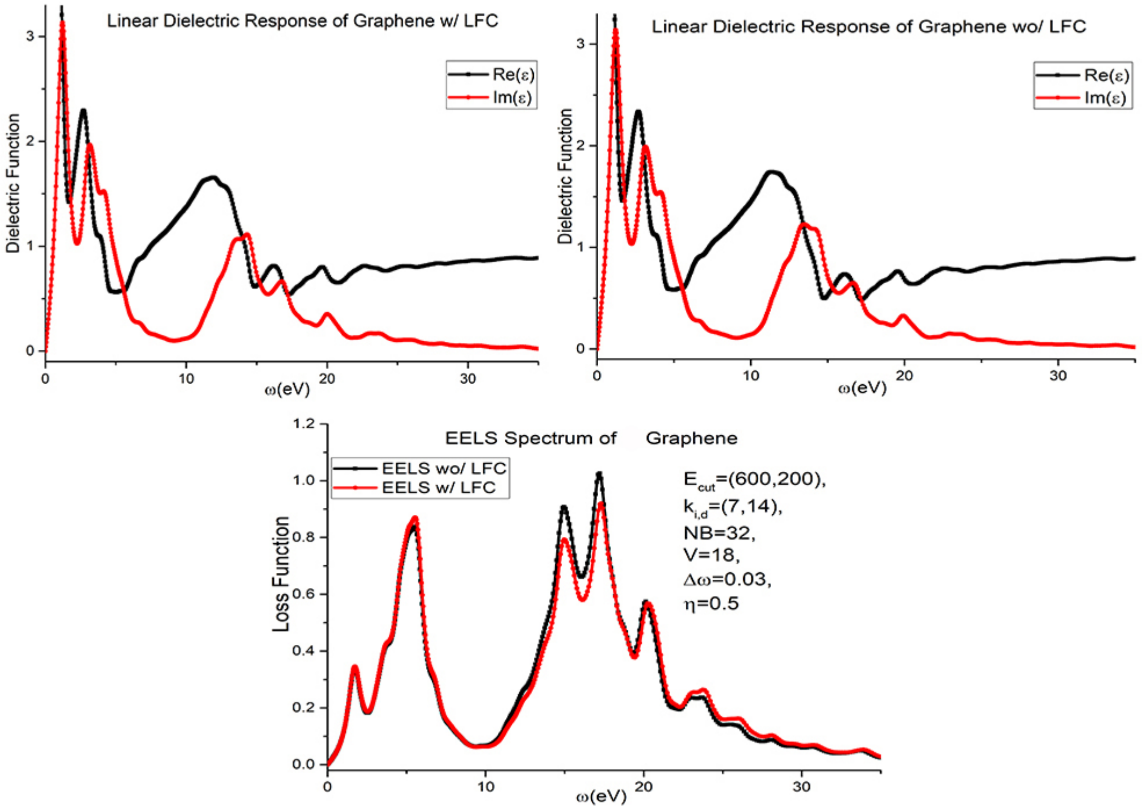

Figure 4.48: Above: The dielectric function of graphene with LFC (left), and within LFC. Below: The corresponding graphene EELS spectrum with and without LFC.

The calculation parameters are as follows: $E^{GS}_{cut} = 600$ eV for GS, and $E^{LFC}_{cut} = 200$ eV for LFC, 32 converged bands in total, k-point mesh of initial= $(7, 7, 1)$ and dense-sampling= $(14, 14, 1)$, $\mathrm{V} = 18$ Å, $\Delta\omega = 0.03$, $\eta = 0.5$. The dielectric functions are indeed very similar with or without the LFC, despite a large cut-off energy, and therefore the EELS spectra are close with and without LFC. In the following simulations we simply skip the dielectric function without LFC, mostly focus on comparing the EELS spectra. The dielectric function and the EELS of graphene in fig. 4.48 are all done in x-direction, and it is not expected that the y-direction spectra be any different. Therefore, next we move to another flat 2D structure, namely the 2D Si-C in fig. 4.49, whose y-direction spectra are also expected to remain the same as the x-direction spectra.

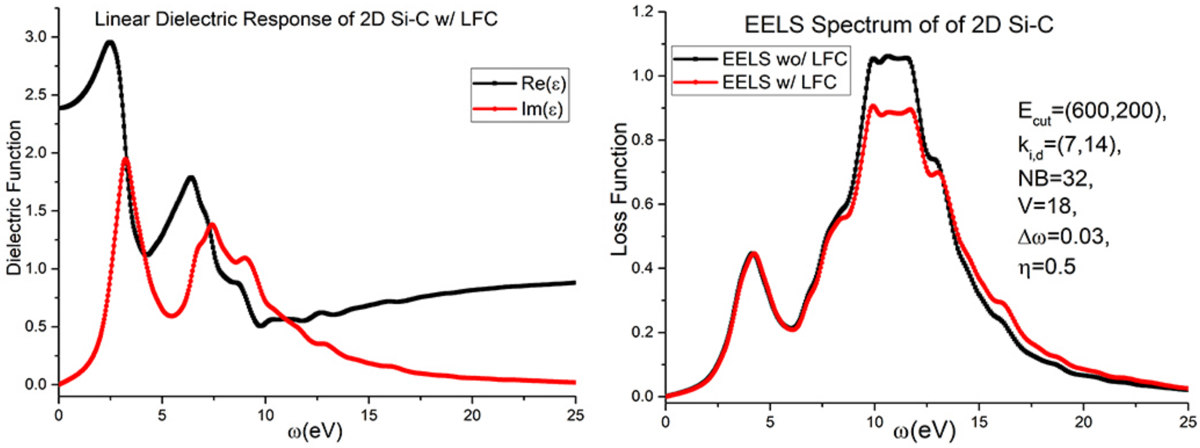

Figure 4.49: Above: The dielectric function of graphene with LFC (left), and without LFC. Below: The corresponding graphene EELS spectrum with and without LFC.

The simulation parameters are the same as in the graphene case. However, a significant change in the spectrum is observable, with a $6-7$ eV shift in the larger peak, and ~ 2 eV shift in the smaller peak. This structure, like the pristine graphene constitutes one end of the spectrum, meaning that any 2D combination of the Si-structures in graphene (as long as no two Si atoms bind together) is expected to have a plasmonic spectrum, that related to those of the pristine graphene, and/or the 2D Si-C. Furthermore, the 2D Si-C, similar to the pristine graphene, has the same spectrum in y-direction, as in the x-direction. With that we move to the next system, which is no longer as trivial as the 2-atom rhombus-cell systems like graphene or Si-C. This structure however, despite having an 8-atom armchair cell, is completely flat like the pristine graphene, and could be named as the ABZZ-line_2x, meaning that there are two ABZZ-lines in the super-cell which are closest to each other (with only two rows of graphene betweem them) as shown in fig. 4.50.

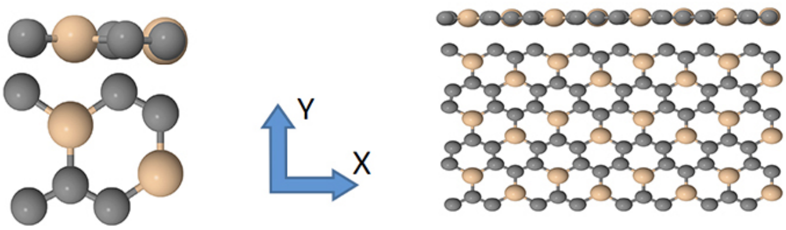

Figure 4.50: Left: The 8-atom armchair cell of ABZZ-line used is the dielectric response calculations. Right: The repeated image showing 4 ABZZ-lines with 2x separation between each.

Therefore we expect a spectrum close to that of the 2D Si-C in fig. 4.51:

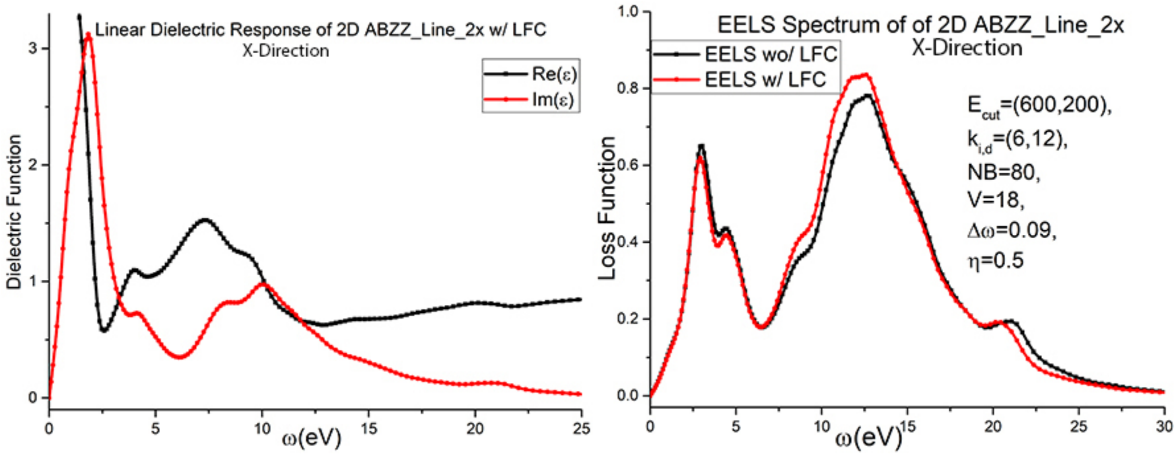

Figure 4.51: The Dielectric function (left) and the EELS spectrum (right) of ABZZ-Line_2x in x-direction.

Compared to the Si-C calculation's k-point mesh, the number of bands, and the $\Delta\omega$ hat to be accordingly adjusted (as seen on the figure), and as we can see in 4.51, despite similarities in the EELS spectrum, the dielectric functions are quite different. Furthermore, as expected, the y-direction spectrum is quite different, as seen in fig. 4.52.

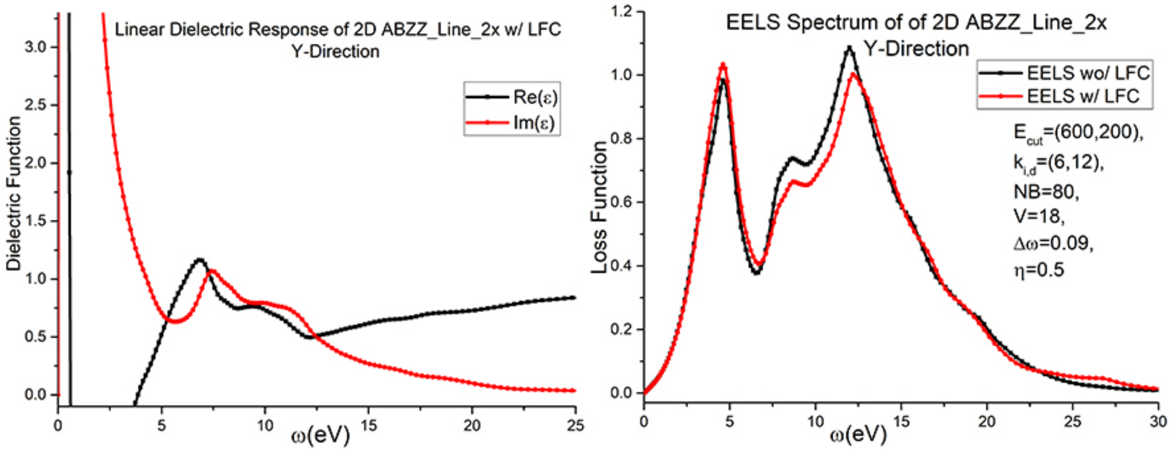

Figure 4.52: The Dielectric function (left) and the EELS spectrum (right) of ABZZ-Line_2x in y-direction.

Aside from the EELS spectrum the dielectric function is quite different with large zero-point asymptotes. This distinguished the 2x ABZZ-line from 2D Si-C in a clear manner, aside from emphasizing the importance of direction in heterogeneous 2D materials (2D materials with impurity or defect). We have 3 more structures to examine and for the ones that have different directional shapes, we look at their spectra in both directions. For the sake of comparison of the details we made the y-direction spectra with $\eta = 0.15$, which simply reveals more detail within the spectra. Therefore before we move to the next structure we look at the y-direction spectra of 2x ABZZ-line n fig. 4.53

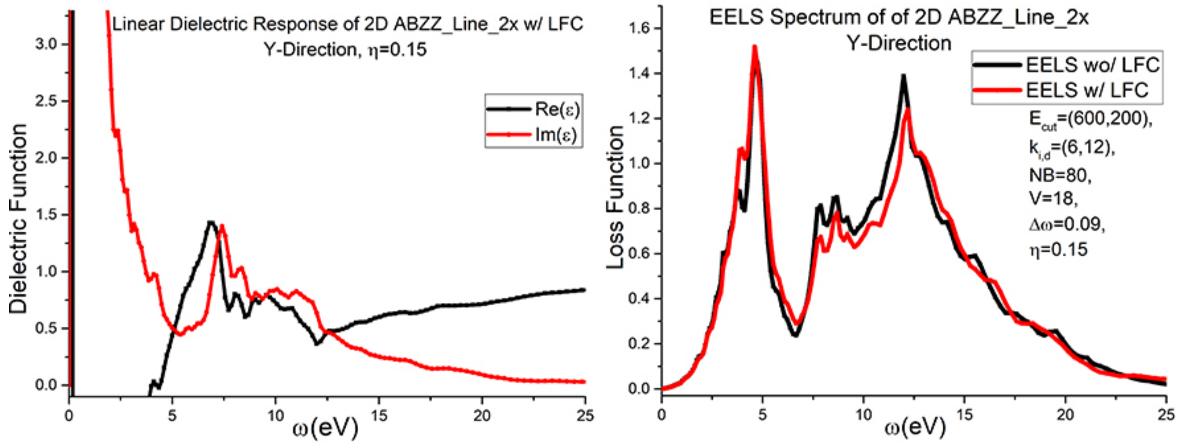

Figure 4.53: The Dielectric function (left) and the EELS spectrum (right) of ABZZ-Line_2x in y-direction, with $\eta = 0.15$.

Next we move to a larger system, a 24-atom rectangular cell with 2 Si-atoms, and 22 C-atoms in 2D periodic system. Repeated along the x-y direction many times, this structure would be the ACh-line in 6x super-cell, as depicted in fig. 4.2 right-side. This structure also has different spectra in the directions. In fig. 4.54, we look at the dielectric function and the EELS spectrum in x-direction:

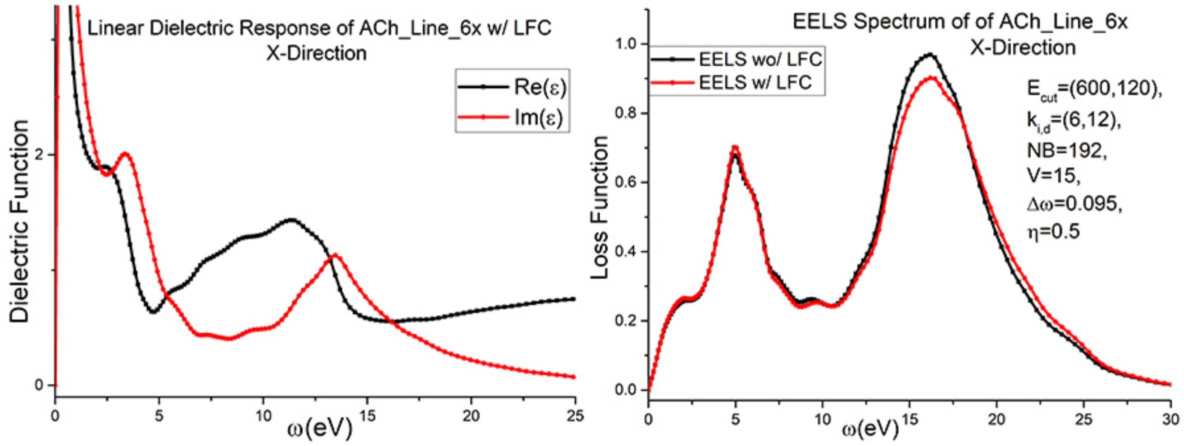

Figure 4.54: The Dielectric function (left) and the EELS spectrum (right) of ACh-Line_6x in x-direction, with $\eta = 0.5$.

For this simulation, the k-point mesh was adjusted to $k_{initial} = (6,4,1)$ and $k_{dense} = (12,6,1)$, due to the fact that system is far from being quadratic in x-y plane (cell-size of $[4.4 \times 15.63 \times 15.0]$ $\mathring{A}^3$). The vacuum was reduced to V=15 Å, and the number of bands increased to NB=192, and finally the combination of $E_{cut} = 120$ eV and $\Delta\omega = 0.095$ delivered an acceptably detailed results for this cell-size. As seen on fig. 4.54 the main peak $(\sigma + \pi)$ is exactly 15 eV, and smoother than for graphene, while the smaller peak (π) is very close to 5 eV with damped side-peak. Overall as expected the spectrum is closer to the pristine graphene as to that of the 2D Si-C. Next in fig. 4.55 we look at the y-direction spectra of the ACh-line_6x.

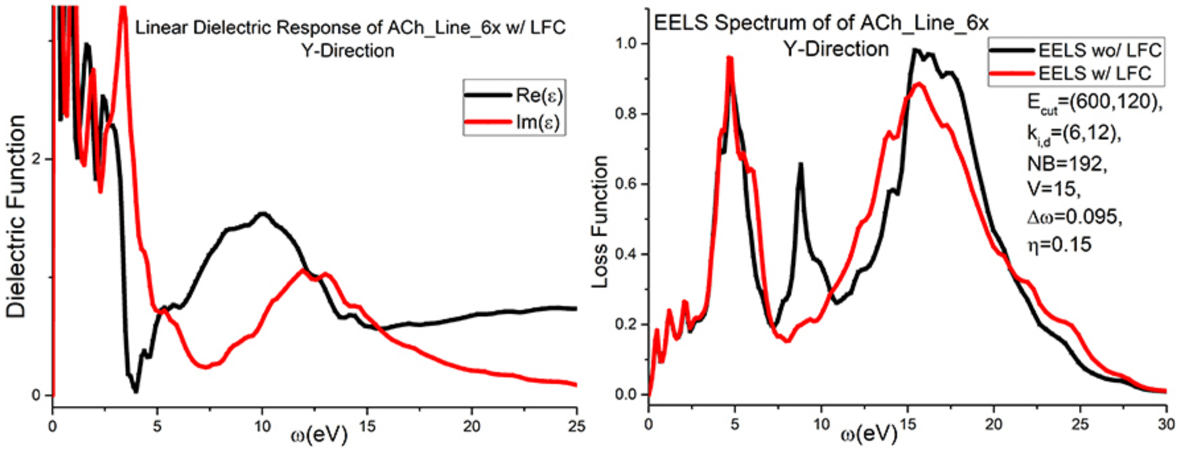

Figure 4.55: The Dielectric function (left) and the EELS spectrum (right) of ACh-Line_6x in y-direction, with $\eta = 0.5$.

Despite no parameter change from x- to y-direction calculations (other than the η), there seems to be some anomalistic behaviour in the dielectric function for this value of η at the low frequency region. However, notwithstanding the low frequency region there is clear difference between the spectra as the well the functions in x- and y- direction, especially the fact that for no LFC there is an additional peak at 8 eV in the EELS spectrum. It is worth mentioning that for $\eta = 0.25$ the oscillatory behaviour of the dielectric function in low frequency region is still there.

The next structure is the symmetric single trivalent silicon in a 4x cell, which has 31 C-atoms and one Si-atom (symmetric Dot-Si_4x) shown in fig. 3.16 right-side, in which one can see a super-cell of quadruple symmetric Dot-Si's in 6x cells (meaning instead of 4 there are 6 rows of graphene between the Si's along the line). This structure is therefore a periodic system of a symmetric Dot_Si in a 4x cell. Fig. 4.56 shows its dielectric function and the EELS spectrum.

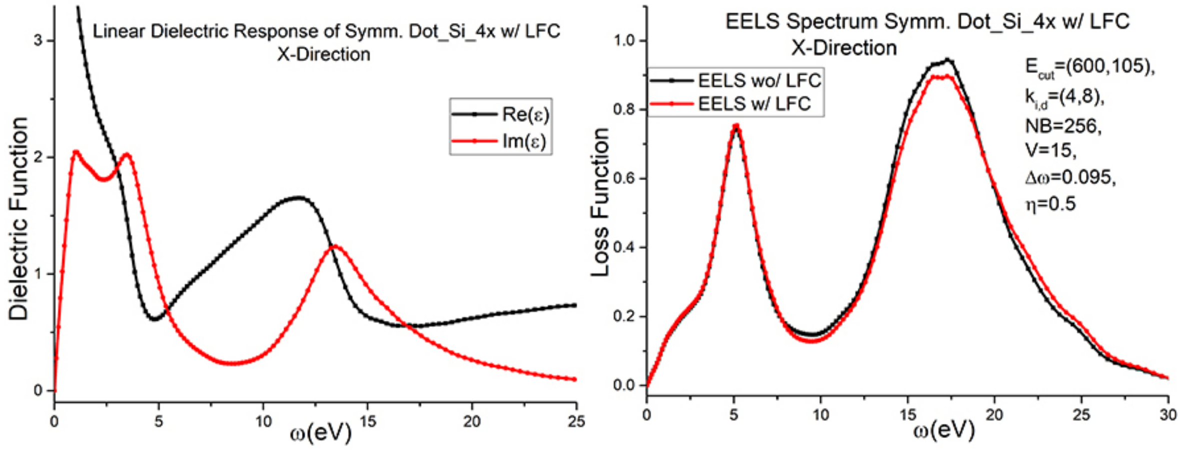

Figure 4.56: The Dielectric function (left) and the EELS spectrum (right) of symmetric Dot-Si_4x in x-direction, with $\eta = 0.5$.

The spectra in fig. 4.56 are calculated in x-direction, but indeed they are also the y-direction spectra due to the 2D symmetry and homogeneity of the system. Furthermore, since the cell is once again in x-y plane quadratic we have the k-points mesh of $k_{initial} = (4, 4, 1)$ and $k_{dense} = (8, 8, 1)$.

The number of converged bands were increased to NB=256, and the E_{cut} for LFC reduced to 105 eV. As for the spectra and the functions, we can see that the EELS spectrum is very close to that of ACh-line, but the main peak is at 17 eV this time instead of 15 eV. And there is slight difference in the shape and the position of the small peak. On the other hand the dielectric functions look relatively different for low frequencies and more similar for larger frequencies.

Finally we look at the dielectric function and the EELS spectrum of the dashed ZZ-line in symmetric configuration, in a 48-atom cell, 2 of which are Si-atoms, and 46 of which are C-atoms. The structure is the symmetric version of the one in the fig. 4.1 right-side, which is also half the size in terms of the number of the atoms in the simulation. Fig. 4.57 and fig. 4.58 show the X-Y spectra of the symmetric DaZZ-line_6x:.

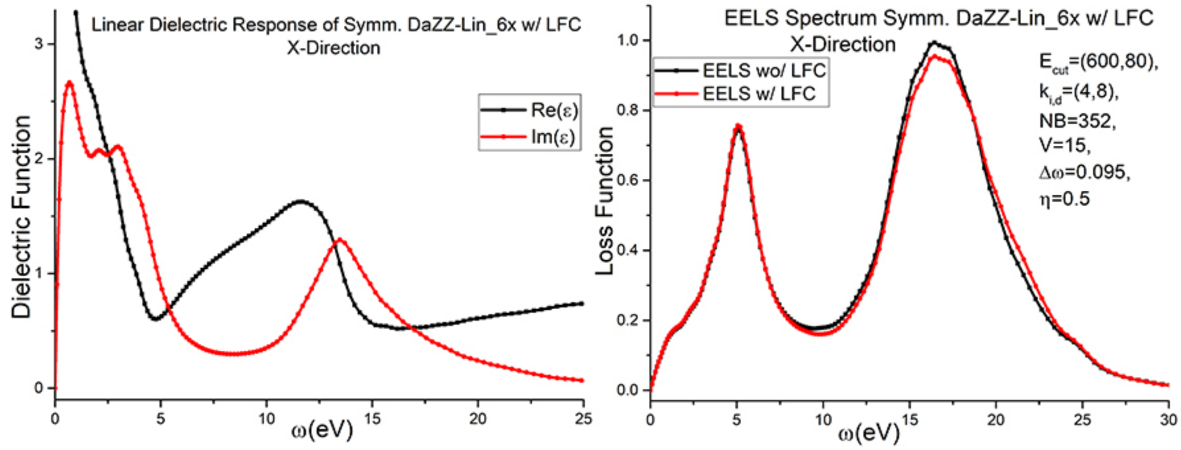

Figure 4.57: The Dielectric function (left) and the EELS spectrum (right) of symmetric DaZZ-line_6x in x-direction, with $\eta = 0.5$.

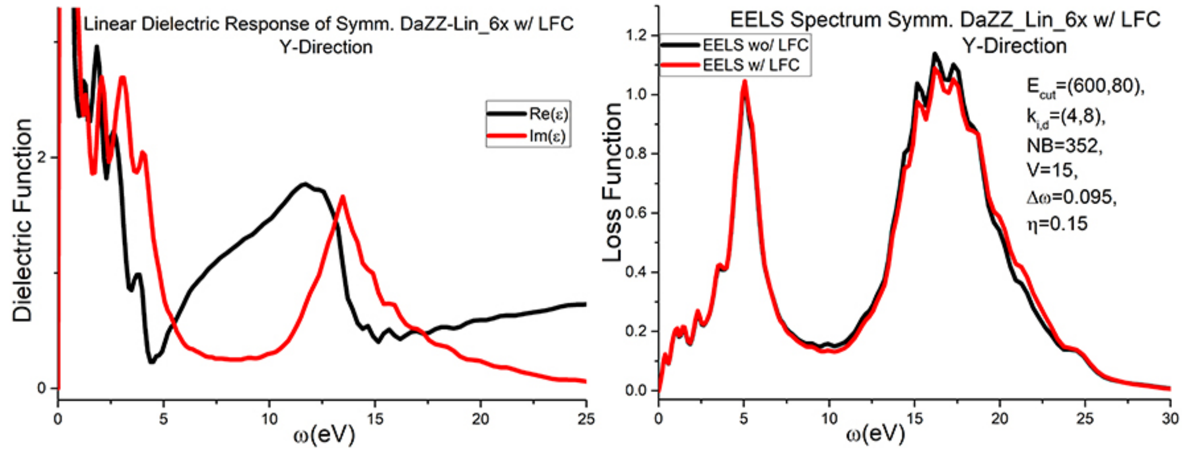

Figure 4.58: The Dielectric function (left) and the EELS spectrum (right) of symmetric DaZZ-line_6x in y-direction, with $\eta = 0.15$.

Once again we have parameter change in the calculations with the k-point mesh which is no longer uniform but reduced to $k_{initial} = (4, 3, 1)$ and $k_{dense} = (8, 6, 1)$, and the E_{cut} for the LFC at 80 eV, and the NB=352 converged bands. The x-direction EELS spectrum looks indeed very similar to the spectrum of the Dot_Si_4x, but the structures are also very similar. However, one can see the difference in details of the dielectric function (imaginary part), and the form of the main peaks in the EELS spectra. We will next look at the 3 similar x-direction EELS spectra in more detail to see the fine-differences. However the y-direction of the DaZZ-line doesn't reveal anything, as it is very similar to the x-direction functions with $\eta = 0.15$. In principle, up to a certain degree of detail, the spectra and the functions of the 3 previous figures simply mean that the DaZZ-line 6x is basically similar to the single trivalent silicon (Dot_Si_4x) in 4x cell.

Finally at the end, in fig. 4.59 we look at the EELS spectra of the ACh-line_6x, Dot_Si_4x, and Dazz-line_6x, with $\eta = 0.2$ to see the actual differences in the spectra.

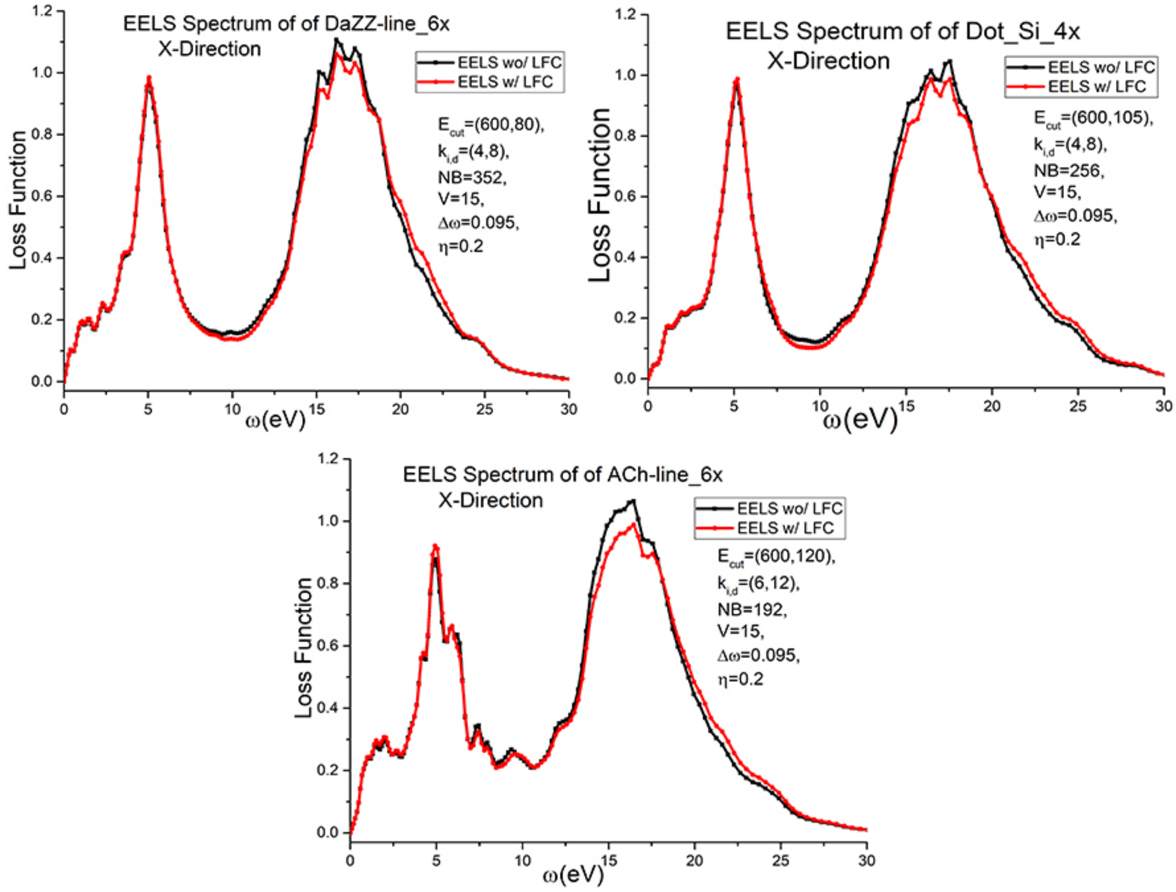

Figure 4.59: The EELS spectra of DaZZ-line_6x, Dot-Si_4x, and ACh-line_6x in x-direction, with $\eta = 0.2$.

As seen in fig. 4.59 the EELS spectra of the 4x Dot_Si and the 6x DaZZ-line are indeed slightly different, and the spectrum of the ACh-line_6x looks clearly different and distinguishable from the other two. Therefore, for this level of details one can even distinguish between such similar structures as DaZZ-line_6x and Dot_Si_4x.

4.3.2 FD LrTDDFT & Time-Propagation TDDFT, Induced Fields

In this section we look at the photoabsorption spectra (PAS) of some structures, many of which we already introduced in the previous section as periodic systems, whose spectra in this section are going to be measured as free standing molecules. The special property of the FD time-propagation of LrTDDFT is that they can only calculate the PAS of non-periodic systems with non-zero vacuum boundary conditions. Namely the systems are hexagonal flakes of graphene saturated with hydrogen, with a certain Si-pattern embedded onto them, in a simulation box with at least 8 Å vacuum in each direction. As in the case of linear response TDDFT, in time-propagation- and LrTDDFT a ground-state with enough converged unoccupied bands have to be first prepared, which then is either used for time-propagation or the construction of the omega matrix (in Casida's method eq. 2.149). In the case of time propagation for time step of 7 attoseconds, 5000 iterations are performed (total propagation time of 35 femtoseconds). Due to some problem in the code, we only used the Casida code for a couple of small flat 2D systems (graphene and Si-C in smaller molecule), but the time-propagation TDDFT, which scales very well also gathered the induced field and field enhancement data of the time-evolved systems for pre-chosen frequencies, the results which we present here together with the spectra.

At the beginning we describe two type of the molecules used in this set of calculations as an example, but the specific shape of the structures should also be obvious from their induced fields and the field enhancement visualizations. In fig. 4.60 we see the molecules used in LrTDDFT and time-propagation TDDFT calculations of graphene and Si-C:

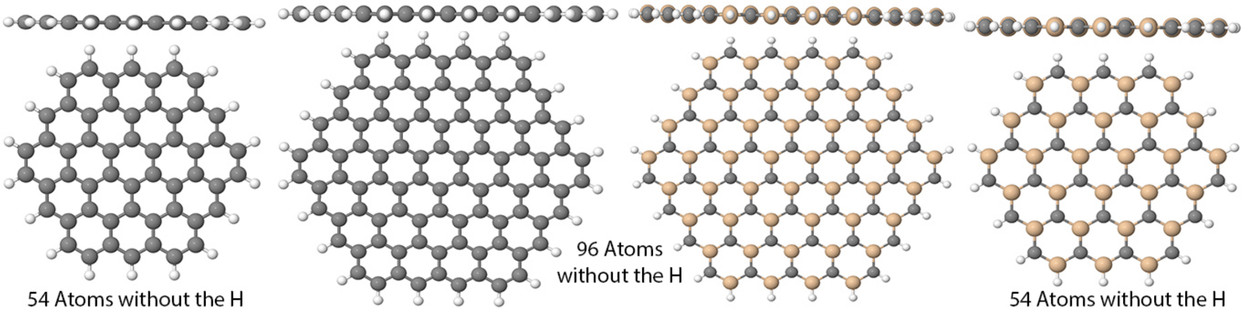

Figure 4.60: The geometrical shape of the saturated (with hydrogen) hexagonal graphene and Si-C flakes with 54 and 96 atoms (Si+C atoms without the H-atoms) used in respectively in LrTDDFT and time-propagation TDDFT.

With that we start looking at the PAS of graphene and 2D Si-C in fig. 4.61 and fig. 4.62 respectively.

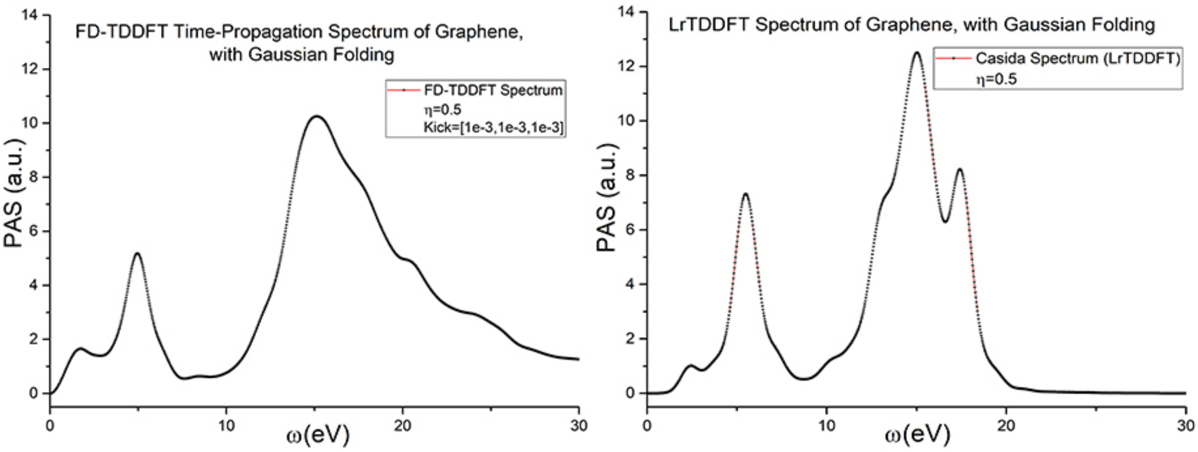

Figure 4.61: Left: FD-TDDFT time propagation PAS of 96-atom graphene-flake. Right: LrTDDFT (Casida) PAS of 54-atom graphene-flake.

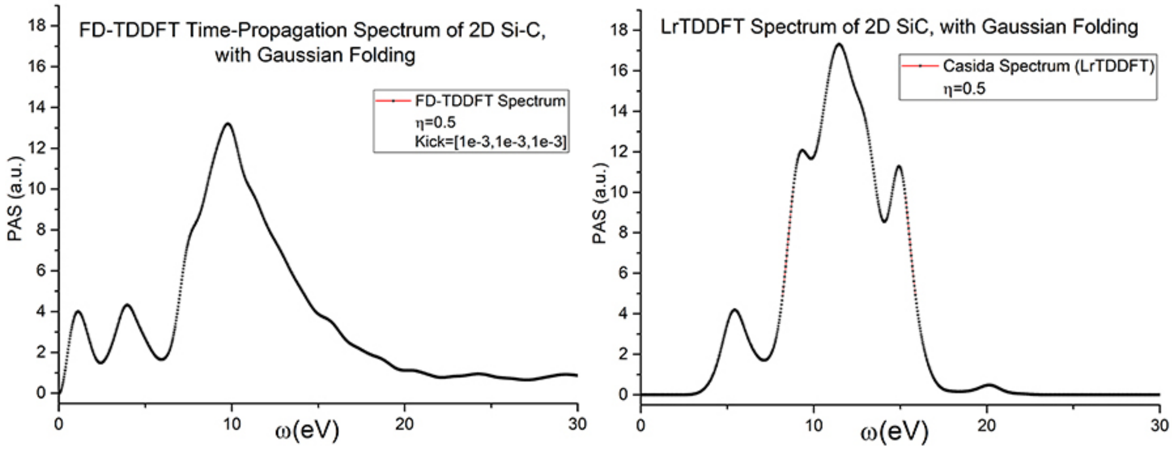

Figure 4.62: Left: FD-TDDFT time propagation PAS of 96-atom SiC-flake. Right: LrTDDFT (Casida) PAS of 54-atom SiC-flake.

The TDDFT code can capture, as mentioned, the induced charge density and the induced potential, and the electric field enhancement at given frequencies, which one can visualize in different dimensions. Here we look at the mentioned properties in z-direction and also in x-y plane for the 96-atom molecule. Fig. 4.63 shows the induced charge density and potential, plus the field enhancement of graphene in z-direction for the peak frequencies is the PAS.

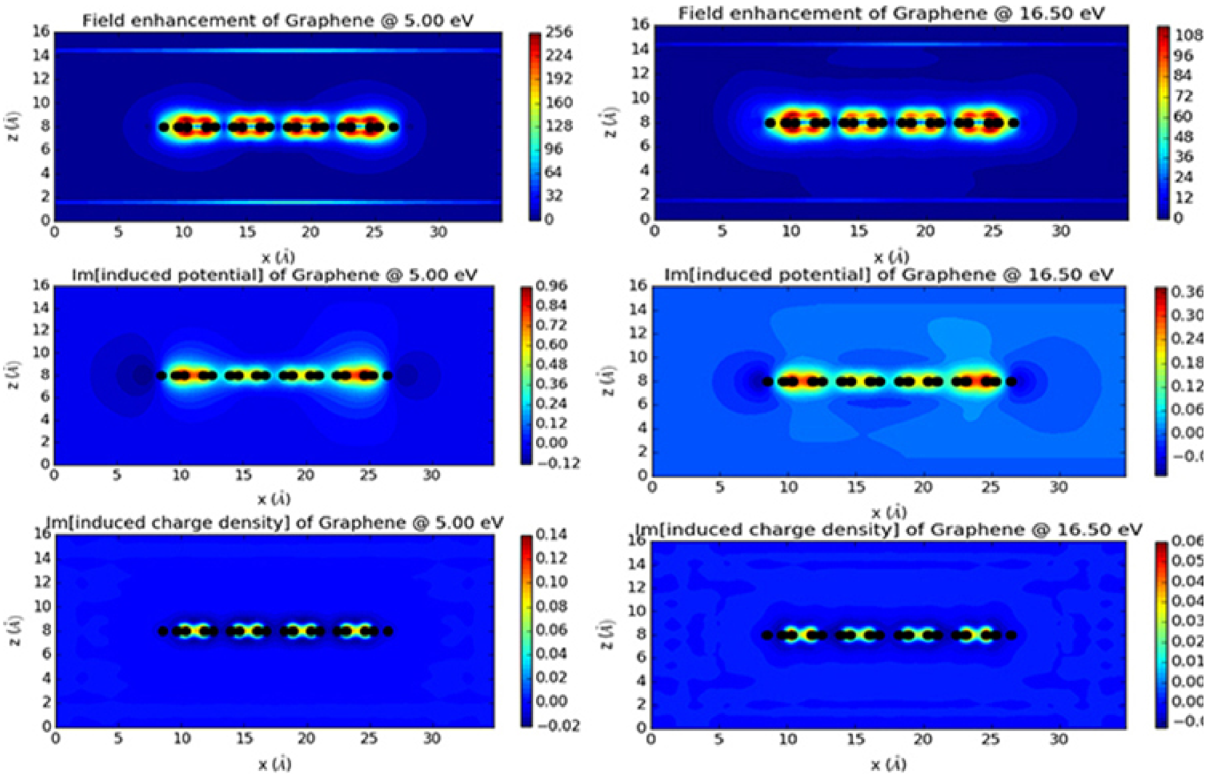

Figure 4.63: From top to bottom: Field enhancement, imaginary part of the induced potential, and imaginary part of the induced charge density, of graphene for two peak frequencies of the PAS (left and right) in z-direction.

Fig. 4.64 show the same mentioned properties in the x-y plane.

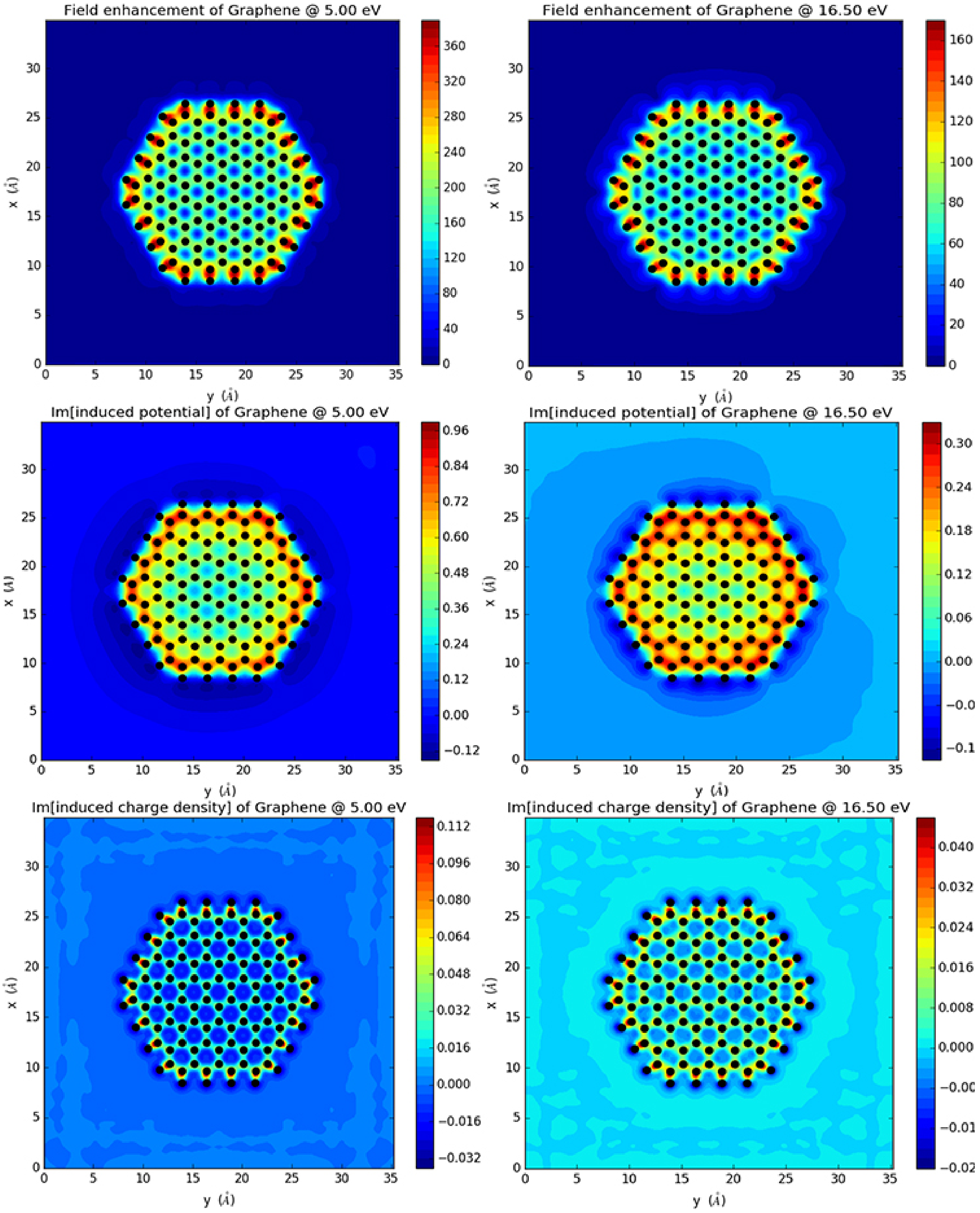

Figure 4.64: From top to bottom: Field enhancement, imaginary part of the induced potential, and imaginary part of the induced charge density, of graphene for two peak frequencies of the PAS (left and right) in x-y plane.

Similarly for 2D Si-C, we present in fig. 4.65 and 4.66.

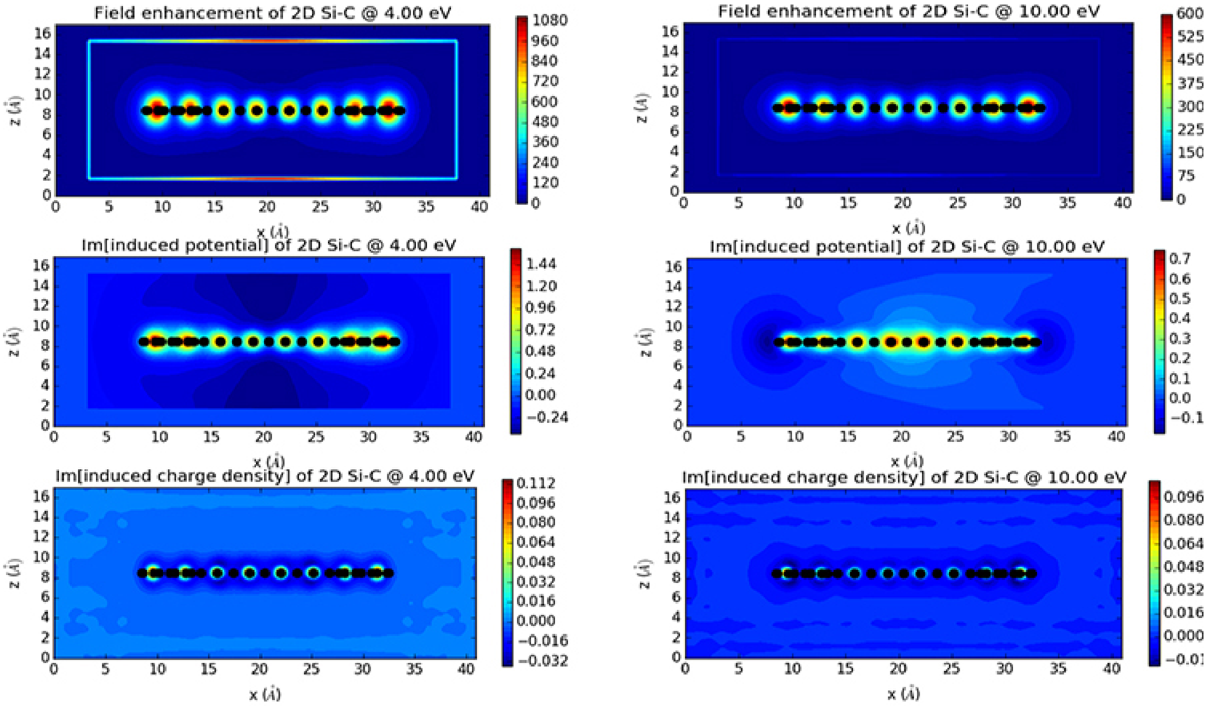

Figure 4.65: From top to bottom: Field enhancement, imaginary part of the induced potential, and imaginary part of the induced charge density, of 2D Si-C for two peak frequencies of the PAS (left and right) in z-direction.

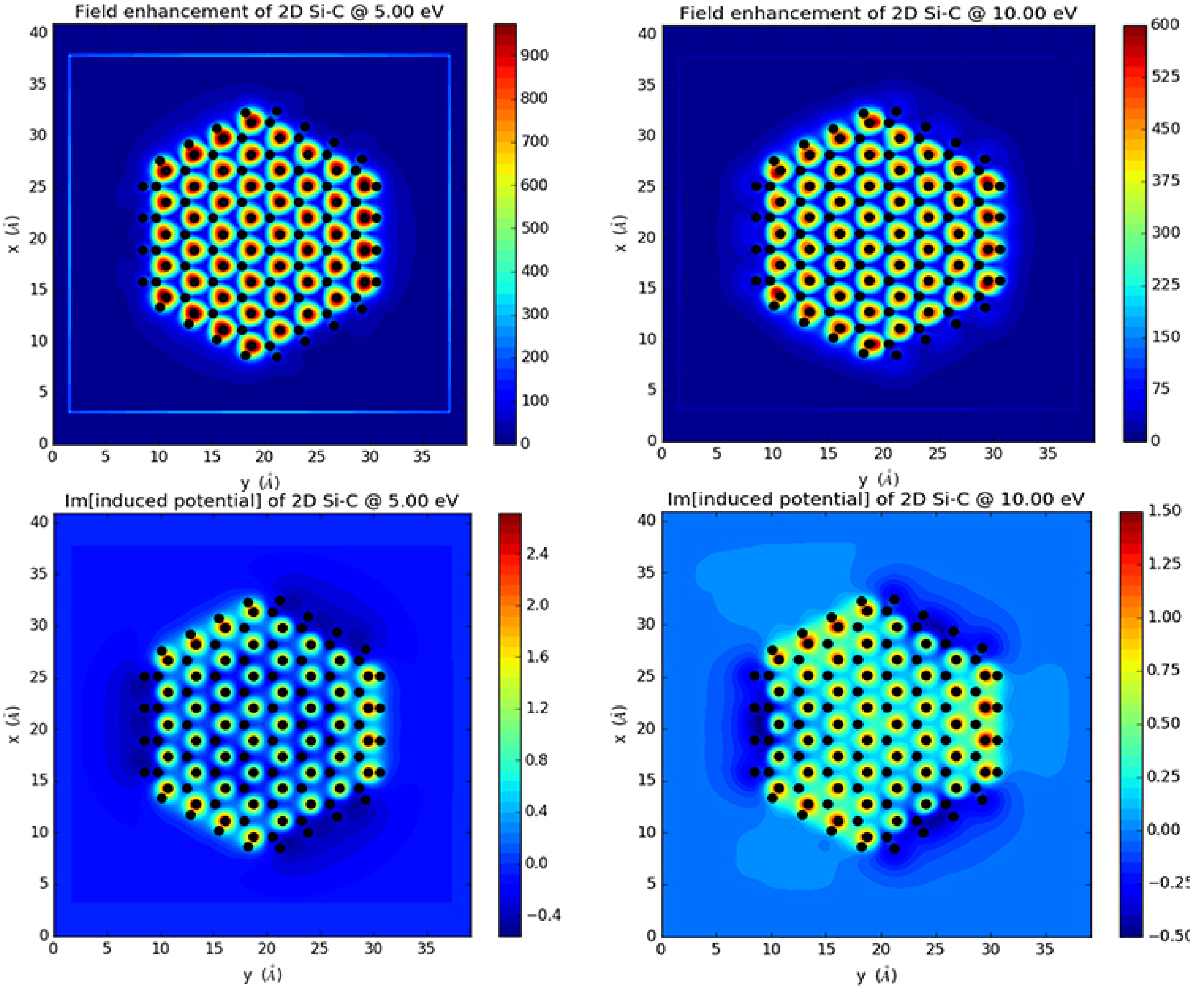

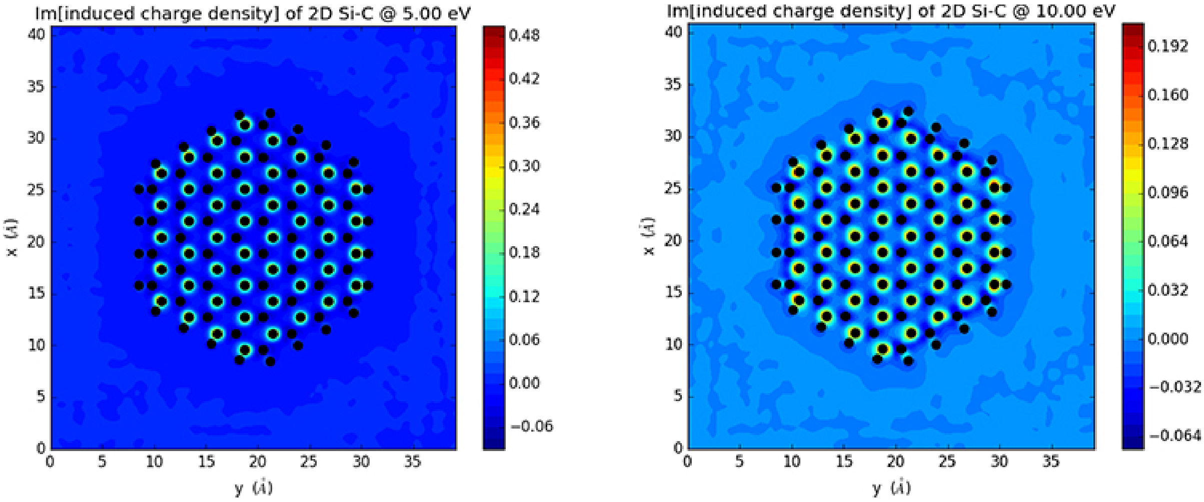

Figure 4.66: From top to bottom: Field enhancement, imaginary part of the induced potential, and imaginary part of the induced charge density, of Dot_Si for two peak frequencies of the PAS (left and right) in x-y plane.

One point should be made about the spectra in fig. 4.62 and 4.63, and that the Casida spectrum is based on the electron-hole excitations, and the PAS itself is the sum of all excitations in all directions. However the time-propagations TDDFT spectrum is based on the time-evolution of the dipole-moment in a given direction per given kick. Namely that above spectra is the PAS in x-direction resulting from a 3D perturbation of magnitude $[1e-3, 1e-3, 1e-3]$, and are supposed to be the same also in y-direction, however they are not perfectly so. Additionally regarding the induced fields, since the most effect of the Si-impurities on the fields of the graphene is in x-y plane, for the next structures we only present the x-y induced fields.

Next we look at the single trivalent silicon in graphene, Dot_Si, and the DaZZ-line, in a 96-atom flake, in time-propagation TDDFT. The shape of the structures will be observable from the induced fields visualizations, but to briefly describe it, it is indeed just the Dot_Si, and the DaZZ-line (fig. 3.11 and fig. 4.1 right-side) structures of the previous sections, with the difference, that the enclosing graphene is a saturated hexagonal graphene flake of fig. 4.60 left-side (Si-atom and the DaZZ-line in a central position as much as possible). Fig. 4.66 illustrates the PAS of these structures.

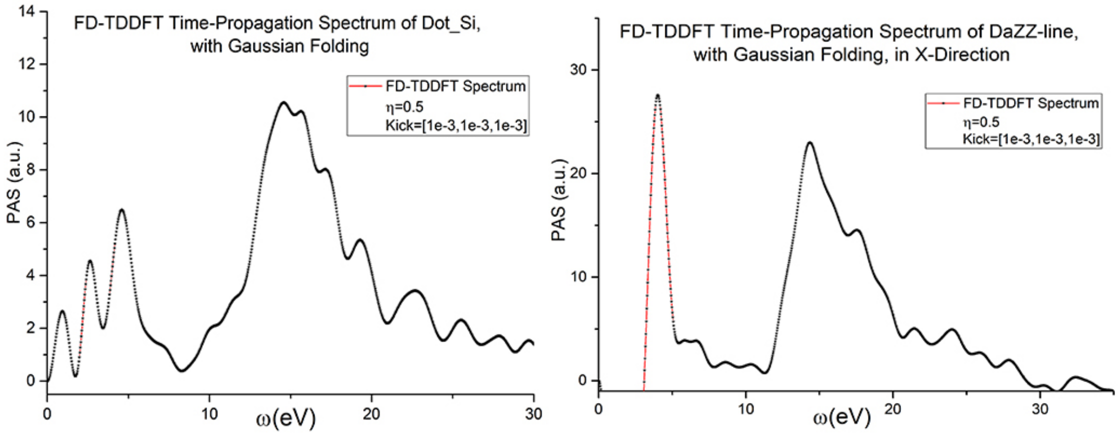

Figure 4.67: Left: FD-TDDFT time propagation PAS of 96-atom Dot_Si-flake. Right: FD-TDDFT time propagation PAS of 96-atom DaZZ-line-flake

It should be mentioned that the x-direction in the Dot_Si-flake is in agreement with the x-direction in the dielectric response calculations of the DaZZ-line_6x as shown in fig. 4.1, namely that the x-direction is along the DaZZ-line within the graphene flake. As for the spectra is it understandable, that the difference will be more visible as in the case of the dielectric response due to non-periodic boundary conditions. With that we move to the induced fields of the Dot_Si in fig. 4.68:

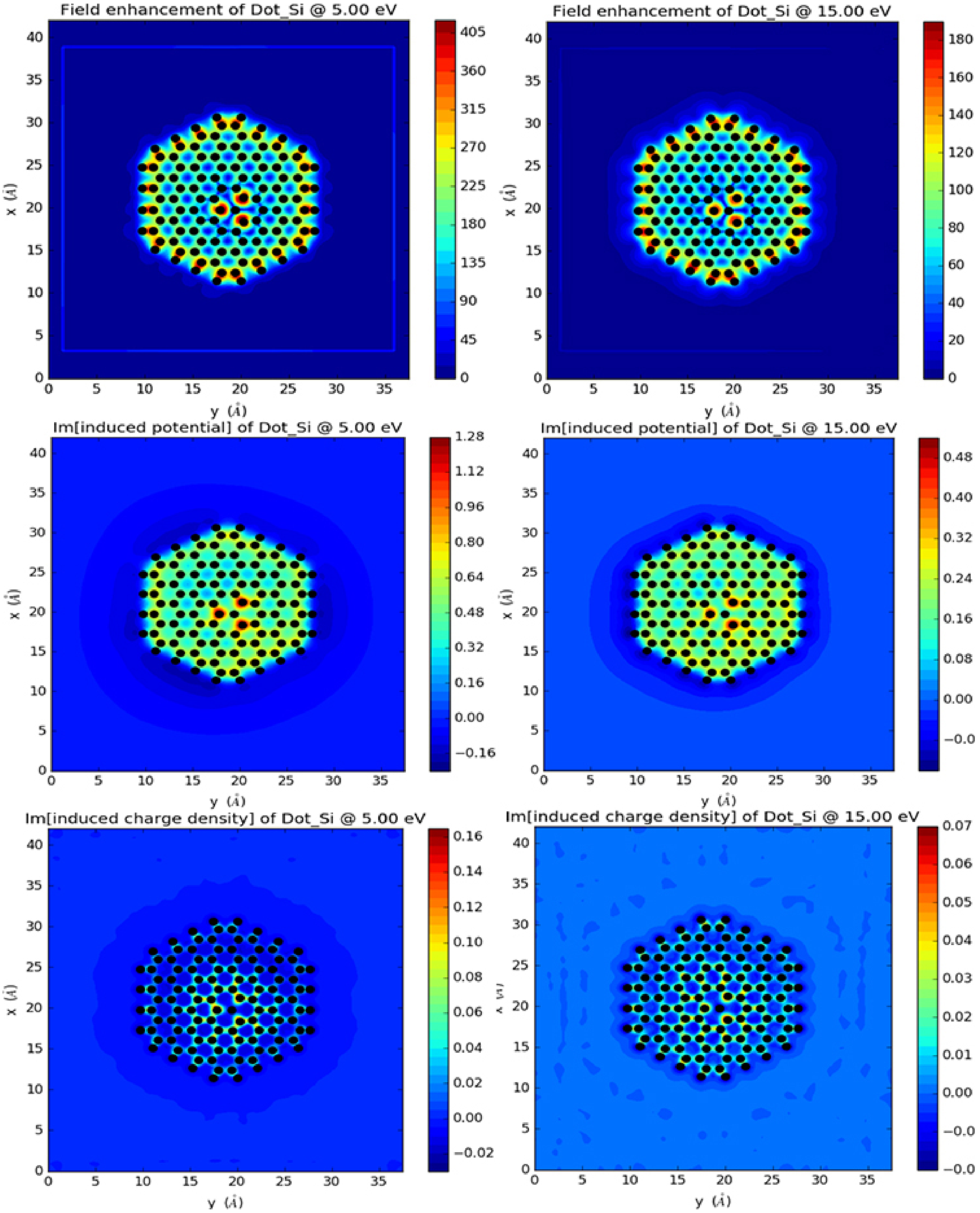

Figure 4.68: From top to bottom: Field enhancement, imaginary part of the induced potential, and imaginary part of the induced charge density, of 2D Si-C for two peak frequencies of the PAS (left and right) in x-y plane.

And the induced fields of the DaZZ-line in fig. 4.69:

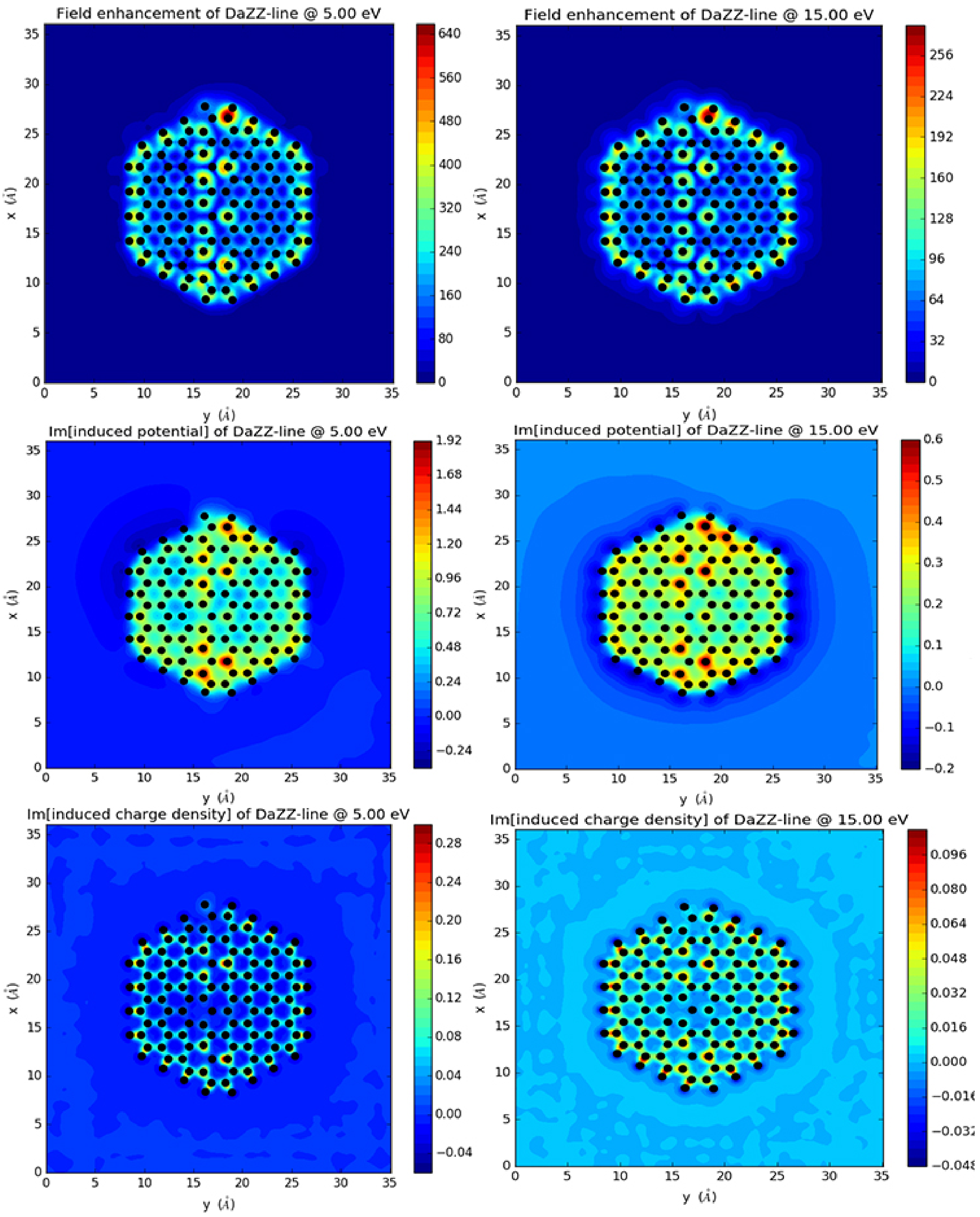
Field enhancement of DaZZ-line @ 5.00 eV

Field enhancement of DaZZ-line @ 15.00 eV

Im[induced potential] of DaZZ-line @ 5.00 eV

Im[induced potential] of DaZZ-line @ 15.00 eV

Im[induced charge density] of DaZZ-line @ 5.00 eV

Im[induced charge density] of DaZZ-line @ 15.00 eV

Figure 4.69: From top to bottom: Field enhancement, imaginary part of the induced potential, and imaginary part of the induced charge density, of DaZZ-line for two peak frequencies of the PAS (left and right) in x-y plane.

The induced fields of the Dot_Si indeed show in detail, the effect of embedding single trivalent silicon into the graphene lattice on the electronic properties of graphene. However the DaZZ-line goes a step further and illustrates the effect of multiple embeddings (impurity) on those properties. This effect is studied in this section, starting from the DaZZ-line structure, using the more reliable method of FD-TDDFT for small systems. But in the next section we expand our systems in order to see the collective effect of the Si-structures on the plasmonics (collective electronic oscillations) of graphene. Before moving to the next structure we take a quick look however, at the z-direction fields of the DaZZ-line in fig. 4.70, due to its corrugated shape in z-direction.

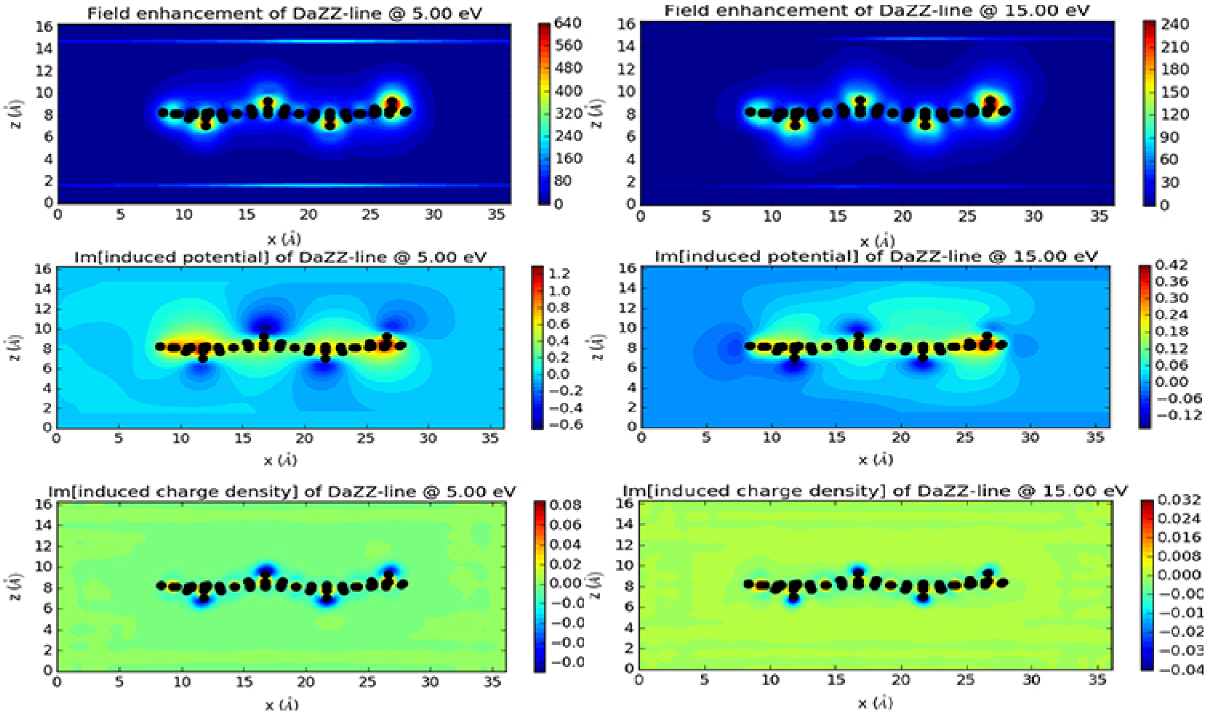

Figure 4.70: From top to bottom: Field enhancement, imaginary part of the induced potential, and imaginary part of the induced charge density, of DaZZ-line for two peak frequencies of the PAS (left and right) in z-direction.

Next we look at the spectra of the ABZZ-line, and the ACh-line in fig. 4.71.

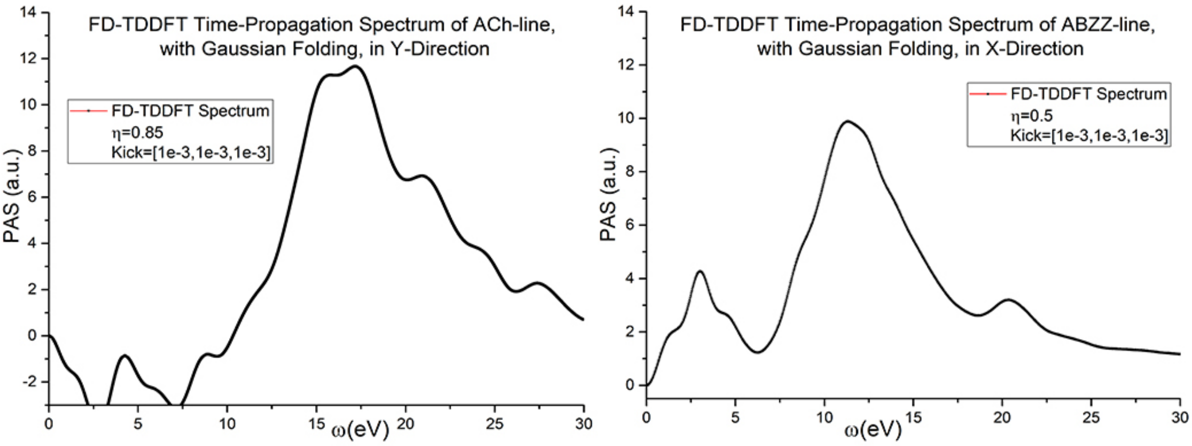

Figure 4.71: Left: FD-TDDFT time propagation PAS of 96-atom flake of ACh-line. Right: FD-TDDFT time propagation PAS of 96-atom flake of ABZZ-line

The PAS of the ABZZ-line is in full agreement with the EELS spectrum of the previous section. However the PAS of the ACh-line had to be refined with higher η value and taken n y-direction to resemble the EELS spectrum. Interestingly the EELS spectrum without LFC in y-direction had an unexpected peak at 8 eV (fig. 4.55 right-side). Here the same phenomenon happens except with the axes switched namely for the x-direction, even though the direction of the line in both simulations remain the same (x-direction goes along the line). Moving to the induced fields, fig. 4.72 shows the induced fields of the ABZZ-line in x-y plane.

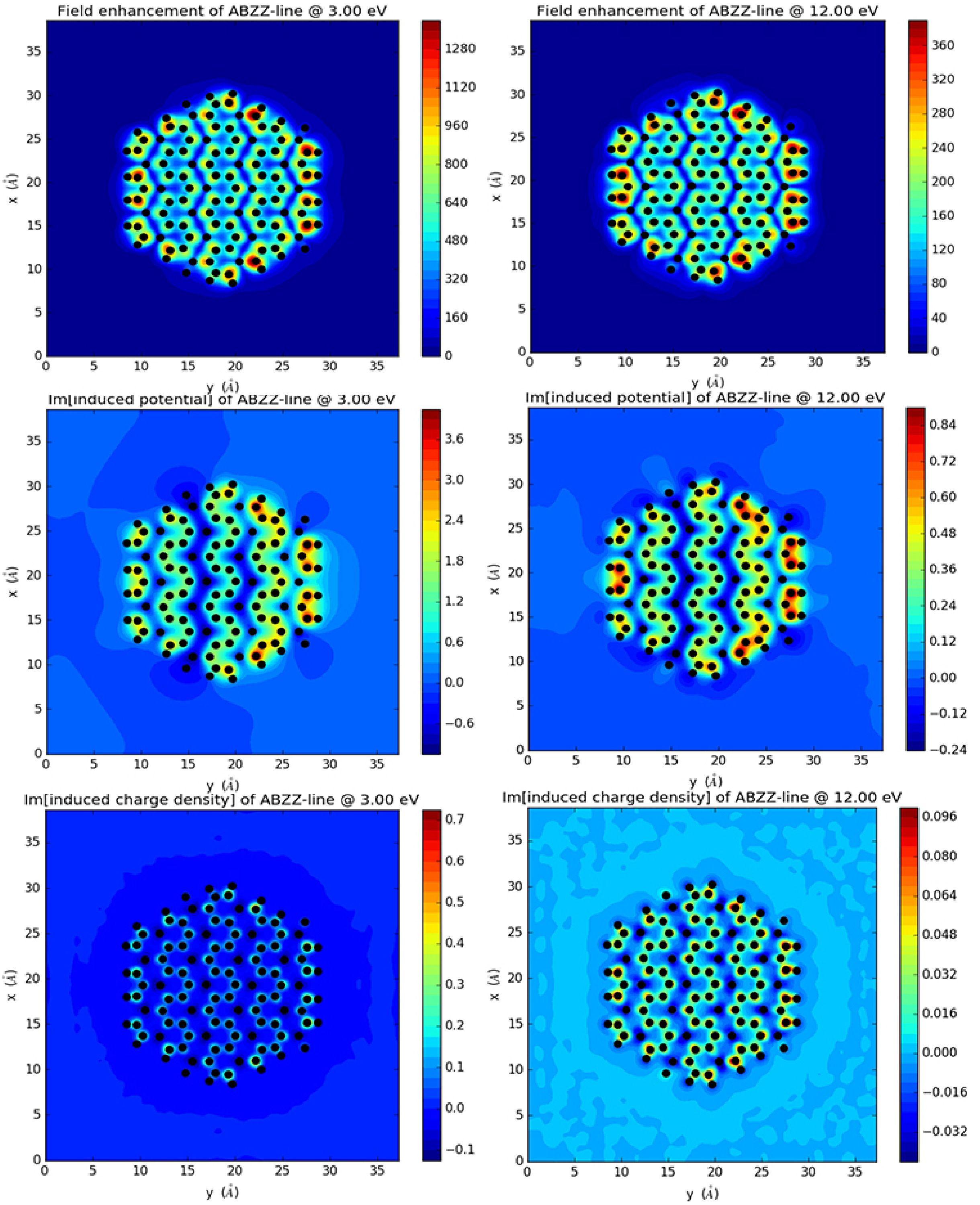

Figure 4.72: From top to bottom: Field enhancement, imaginary part of the induced potential, and imaginary part of the induced charge density, of ABZZ-line for two peak frequencies of the PAS (left and right) in x-y plane.

Fig. 4.73 illustrates those of the ACh-line in x-y plane:

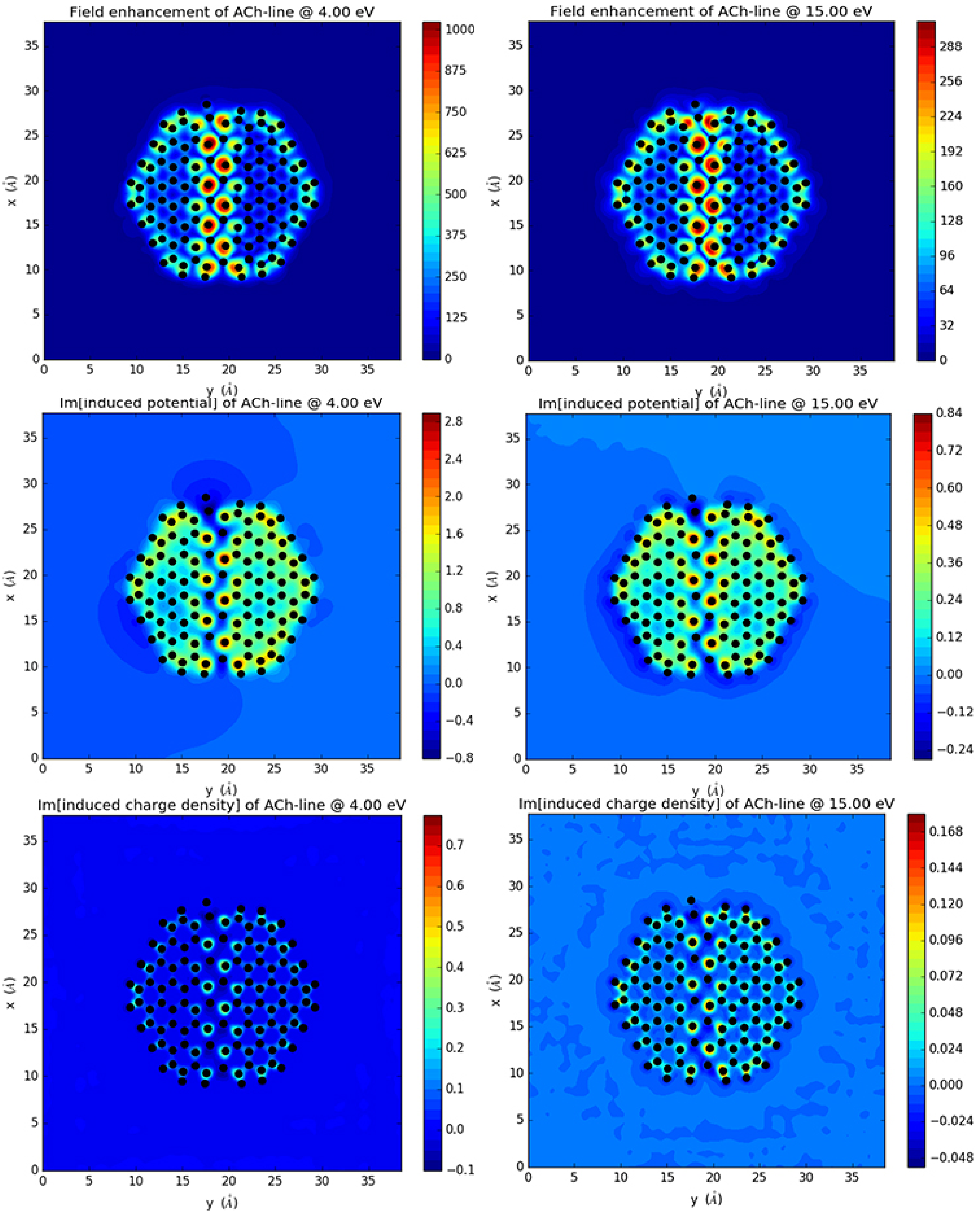

Figure 4.73: From top to bottom: Field enhancement, imaginary part of the induced potential, and imaginary part of the induced charge density, of ACh-line for two peak frequencies of the PAS (left and right) in x-y plane.

The last two set of images of fig. 4.72 and 4.73 illustrate very clearly the effect of a dense arrangement of Si on the surface fields of the graphene. Any dense line induces a positive charge density and positive potential around itself thereby deviding the graphene sheet into halves in terms of the electric potential and gathered charge density. This phenomenon has an implication for the surface plasmons of graphene, the effects of which we will see in the next section.

However before that we look at two last structures, which are embedded on a 154-atoms graphene flakes instead of 96-atoms. The smallest 1x-hexagon (fig. 4.4) and 4-symmetric Dot_Si_4x on the graphene sheet help us in the transition to LCAO-size systems (hundreds of atoms in the simulation). The 1x hexagon is also simulated in the LCAO in the exact same way, and 4Dot_Si_4x resembles the periodic boundary conditions of Dot_Si_4x much better that just one Si-atom in the graphene flake. First we look at the geometrical descriptions of these structures (fig 4.73).

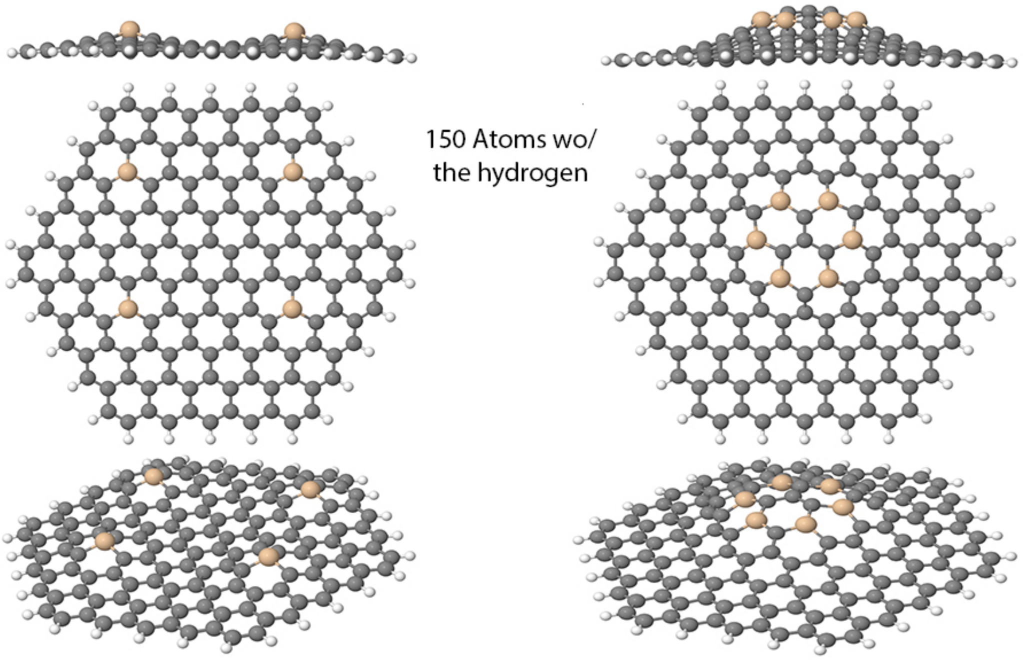

Figure 4.74: Left: Geometrical description of the 4Dot_Si_4x on a 150-atom saturated graphene flake. Right: Geometrical description of the 1x Hexagon on a 150-atom saturated graphene flake.

Fig. 4.73 shows the PAS of the 1x Hexagon and the 4Dot_Si_4x.

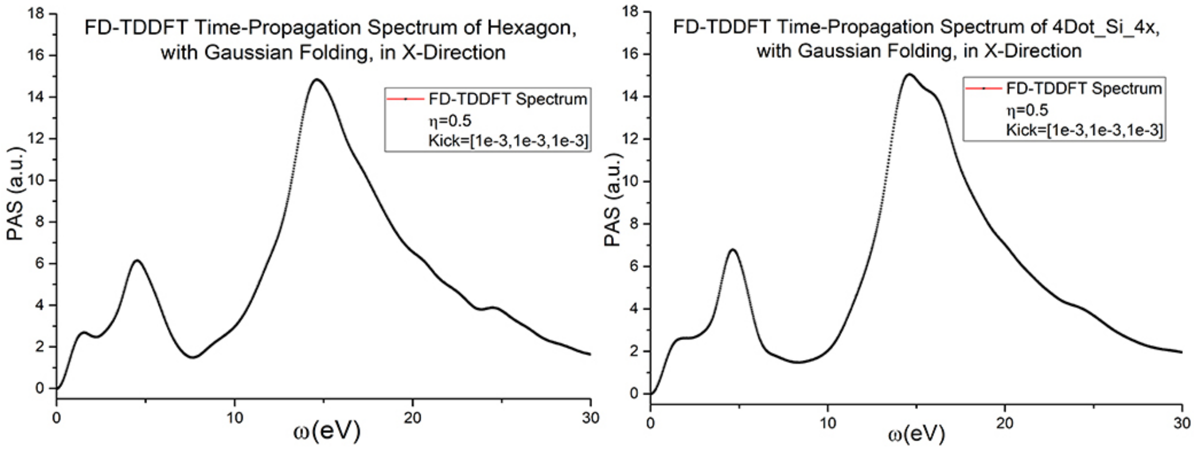

Figure 4.75: Left: FD-TDDFT time propagation PAS of 150-atom flake of 1x Hexagon. Right: FD-TDDFT time propagation PAS of 150-atom flake of 4Dot_Si_4x

We finally look at the induced fields of these structures once again in both dimensions z, and x-y. Fig. 4.76 shows the x-y plane fields of the 4Dot_Si_4x.

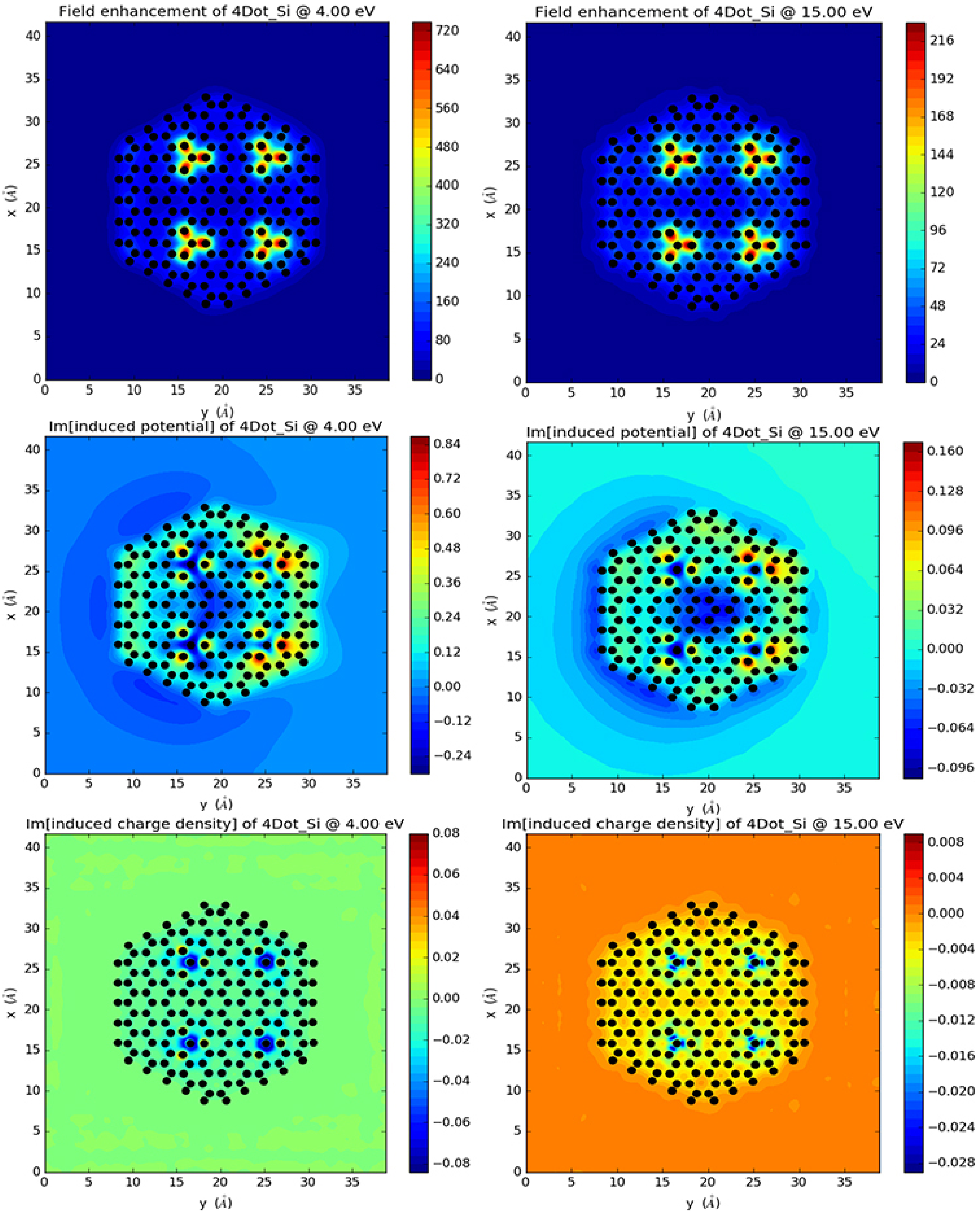

Figure 4.76: From top to bottom: Field enhancement, imaginary part of the induced potential, and imaginary part of the induced charge density, of 4Dot_Si_4x for two peak frequencies of the PAS (left and right) in x-y plane.

Fig. 4.77 shows the x-y plane fields of the 1x Hexagon:

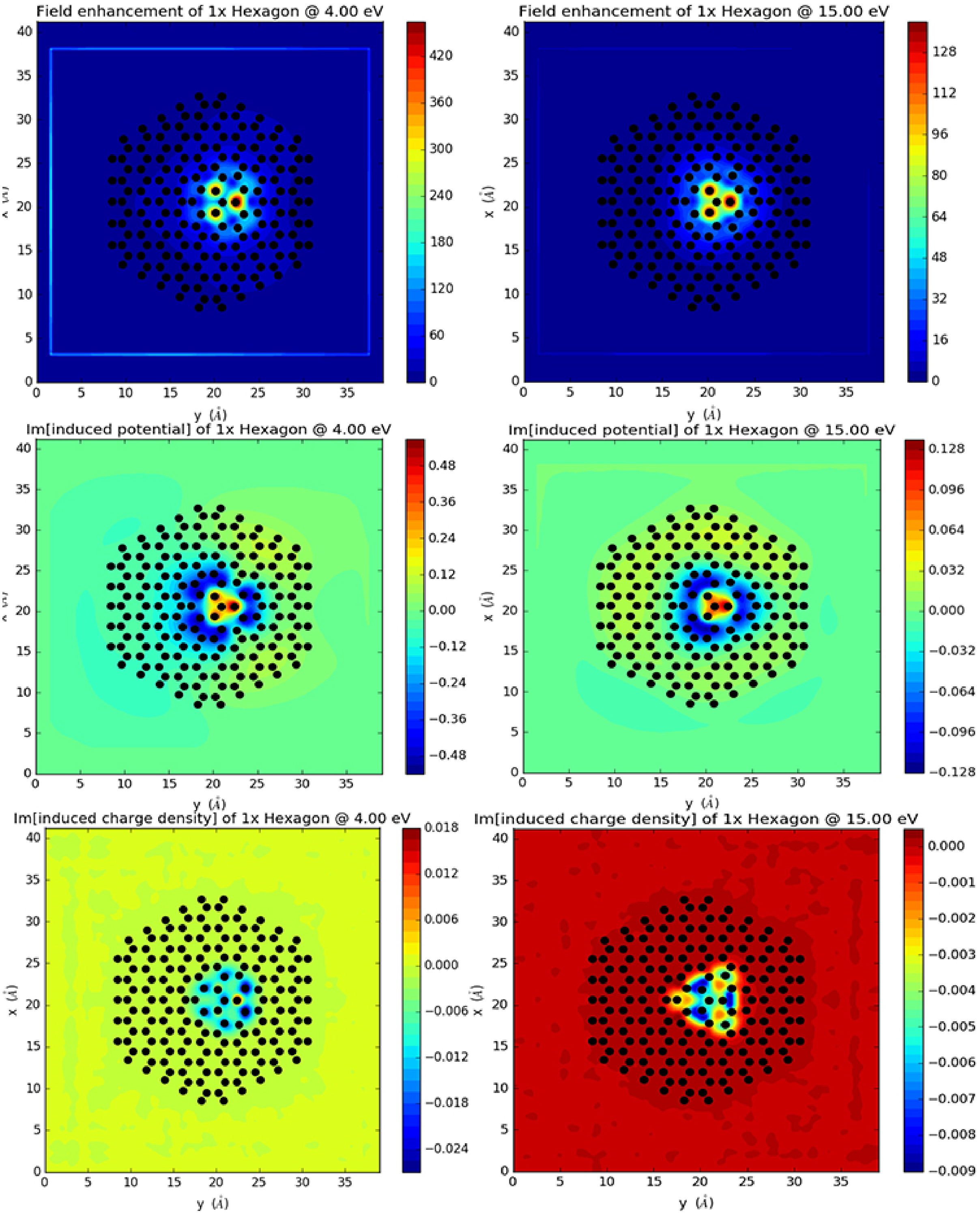

Figure 4.77: From top to bottom: Field enhancement, imaginary part of the induced potential, and imaginary part of the induced charge density, of 1x Hexagon for two peak frequencies of the PAS (left and right) in x-y plane.

Next we look at the z-direction fields of the 4Dot_Si_4x (fig. 4.78).

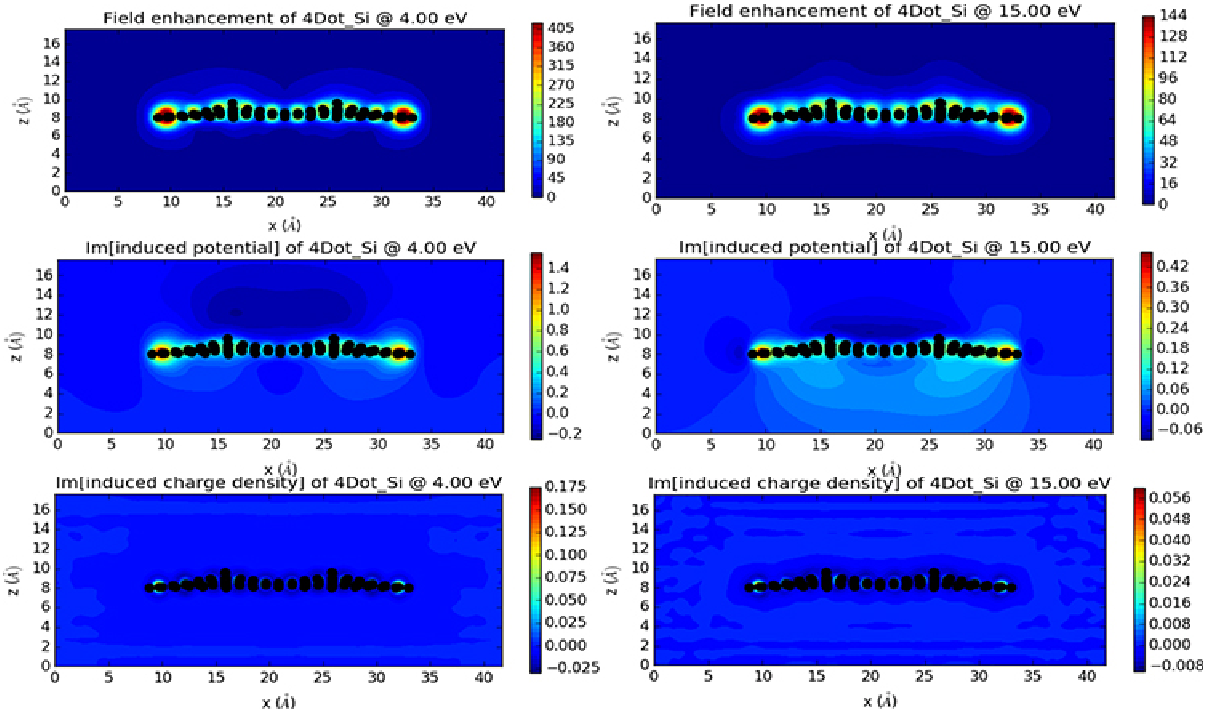

Figure 4.78: From top to bottom: Field enhancement, imaginary part of the induced potential, and imaginary part of the induced charge density, of 4Dot_Si_4x for two peak frequencies of the PAS (left and right) in z-direction.

And the z-direction fields of the 1x Hexagon in fig. 4.79:

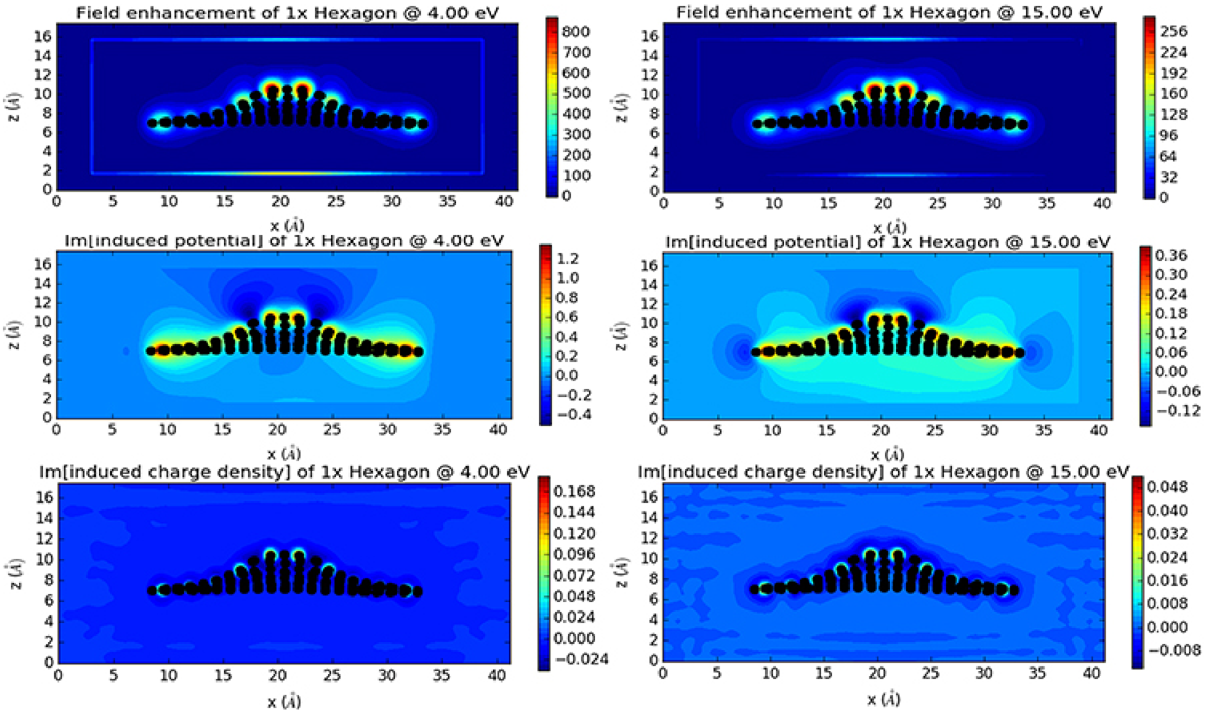

Figure 4.79: From top to bottom: Field enhancement, imaginary part of the induced potential, and imaginary part of the induced charge density, of 1x Hexagon for two peak frequencies of the PAS (left and right) in z-direction.

It is interesting to analyse the induced fields of the last two structures. It is clear, for the both structures, and that is the fact that the Si atoms around themselves tend to induce a positive potential, which then results in gathering of negative charge density. But when there are multiple Si-atoms around a particular area a negative potential is induced in the middle if the Si-atoms are not too close to each other, as in the case of the 4Dot_Si_4x, which compared to pristine graphene causes a negative charge density to accumulate inside the flake. However, it is expected if the Si atoms are densely wrapped around an area, the consequently induced potential is positive, resulting in trapped surface electronic states (instead of hole-states).

4.3.3 LCAO Time-Propagation TDDFT & LSPR's

In the last section of the result, we finally get to look at the PAS of the large systems which we have developed, namely the 16x Hexagon and 4x Circle, and so on. This section presents the result of PAS calculations in LCAO-mode, which together with the collection of the charge density, forms the study of the LSPR's of large molecules, namely once again some 600-atom graphene flakes (saturated with Hydrogen), or any systems embedded onto such pristine graphene flakes. The difference between surface plasmons (SP's) and LSPR's, which are localized, is explained in the theory section (fig. 2.3), but to present an example, fig. 4.80 shows the SP's compared to the LSPR's in 600-atom saturated (600 atoms without the Hydrogen) pristine graphene flakes.

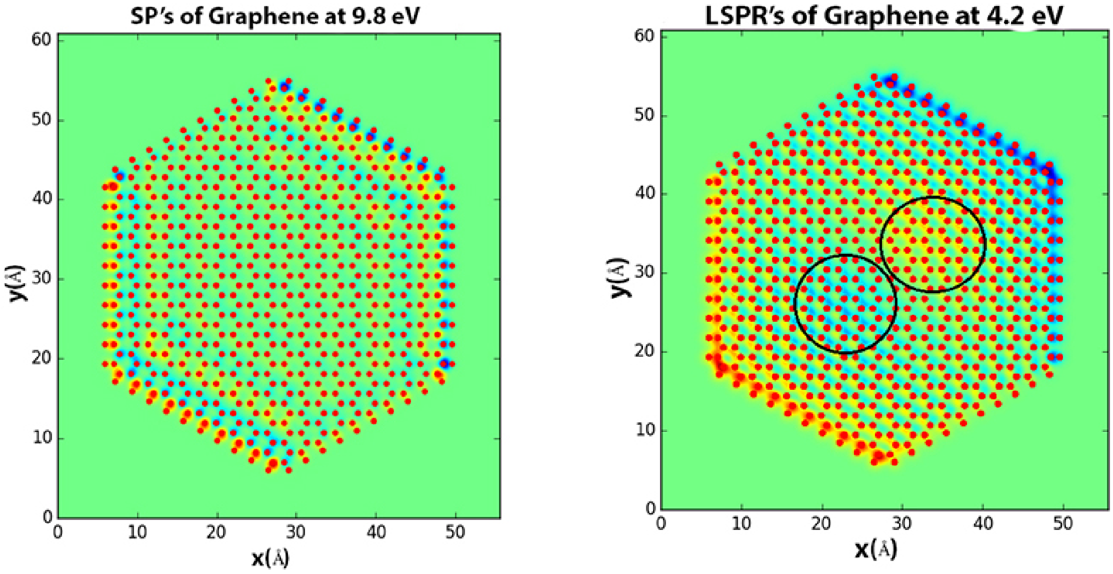

Figure 4.80: Left: The propagation of surface plasmons (SP's) of graphene at 9.8 in SZP-basis of LCAO. Right: The LSPR's of graphene at 4.2 eV in SZP-basis of LCAO.

In terms of the iterations and time propagation the parameters in this set of simulations are similart to the FD-TDDFT. However, as mentioned before, in any LCAO calculation the initial basis-set (SZ, SZP, DZ, etc.) are the most important parameter of simulations,especially for simulations of the electronic properties like the band gap, or PAS. Furthermore, the unoccupied bands in the LCAO-TDDFT time-propagation play no role, as there are no wavefunctions, or electron-hole basis excitations involved (not yet). It is mentioned in the GPAW documentations, that the basis-sets provided in the PAW-dataset, are not specifically tested for accuracy. Therefore, it is strongly suggested to benchmark the LCAO-bases against the FD-TDDFT. This however, requires careful and expert usage of advanced basis-generator program, doing a large statistical analysis of testing all the generated bases against FD-TDDFT, which would make up a masters-thesis on its own. Therefore, what we accomplish here should serve exclusively as initial benchmarking of the existing SZP-, and DZP-bases (in LDA and GLLB-SC functionals) against the previous smaller systems of last two sections. While, none of the spectra for the large systems (16x hexagons, etc) can be fully trusted, the LSPR's generated in these systems, as far as their geometries, shapes and intensities are concerned, can be trusted.

Therefore we start with a similar system to the previous ones, a 96-atom graphene flake, which we look at using SZP, and DZP bases in LDA, and GLLB-SC, and also it's fields in x-y plane and in z-direction. For small systems a large broadening $\eta = 0.5$ is usually more appropriate due to too much detail, however for the rest of the systems, which have 600+ atoms in them, we will switch to $\eta = 0.25$. Therefore fig. 4.81 show 3 PAS of the 96-atom graphene flake with $\eta = 0.5$.

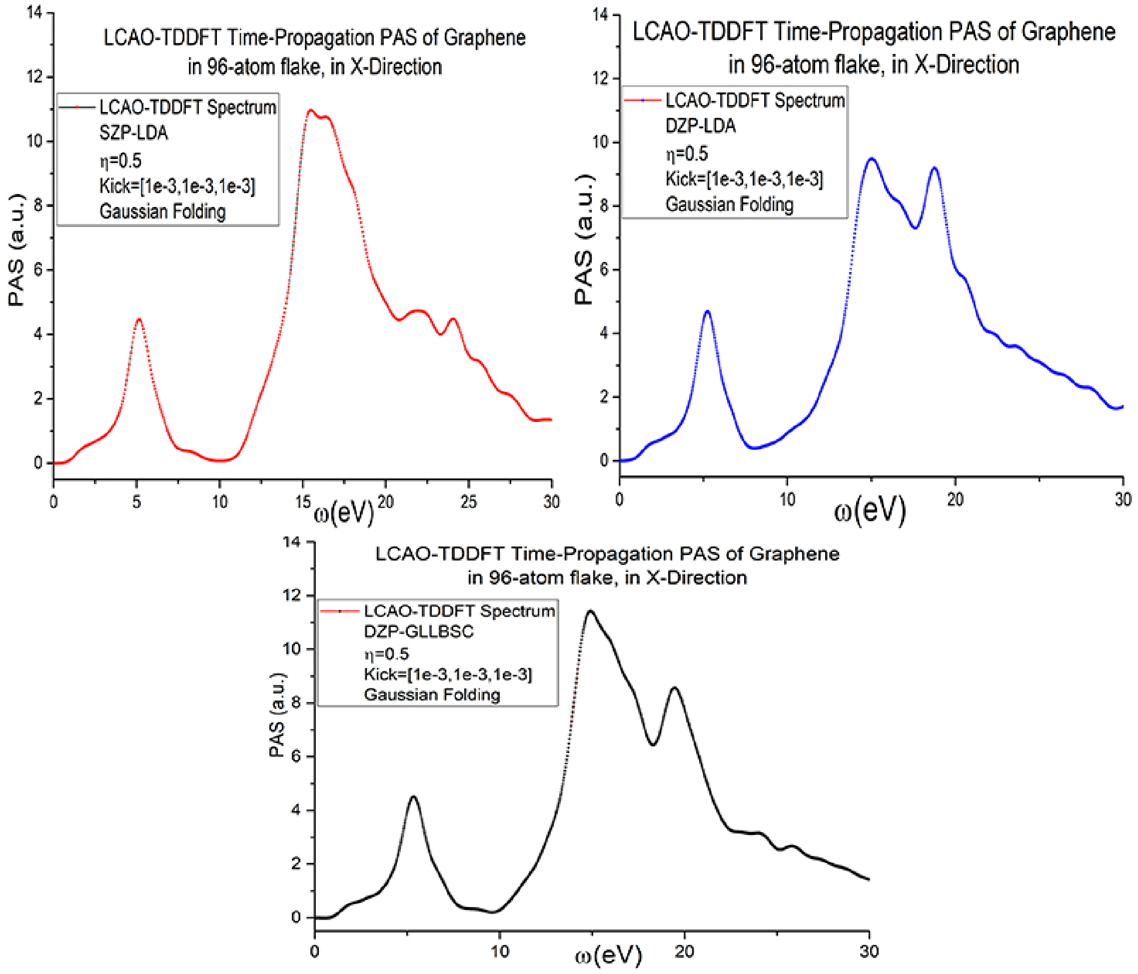

Figure 4.81: LCAO-TDDFT PAS of the 96-atom graphene flak in SZP-LDA basis (above left), in DZP-LDA basis (above right), and DZP-GLLBSC (below).

There is indeed a significant difference in the shape of the main-peak of the spectra, even when a DZP basis is chosen, which XC-functional the basis is based on also makes a significant difference, as seen in fig. 4.81. With that we move to the induced charge density of the graphene-flake in SZP-LDA, in fig. 4.82, from two different directions, to see what the systems size means for simulation of the LSPR's.

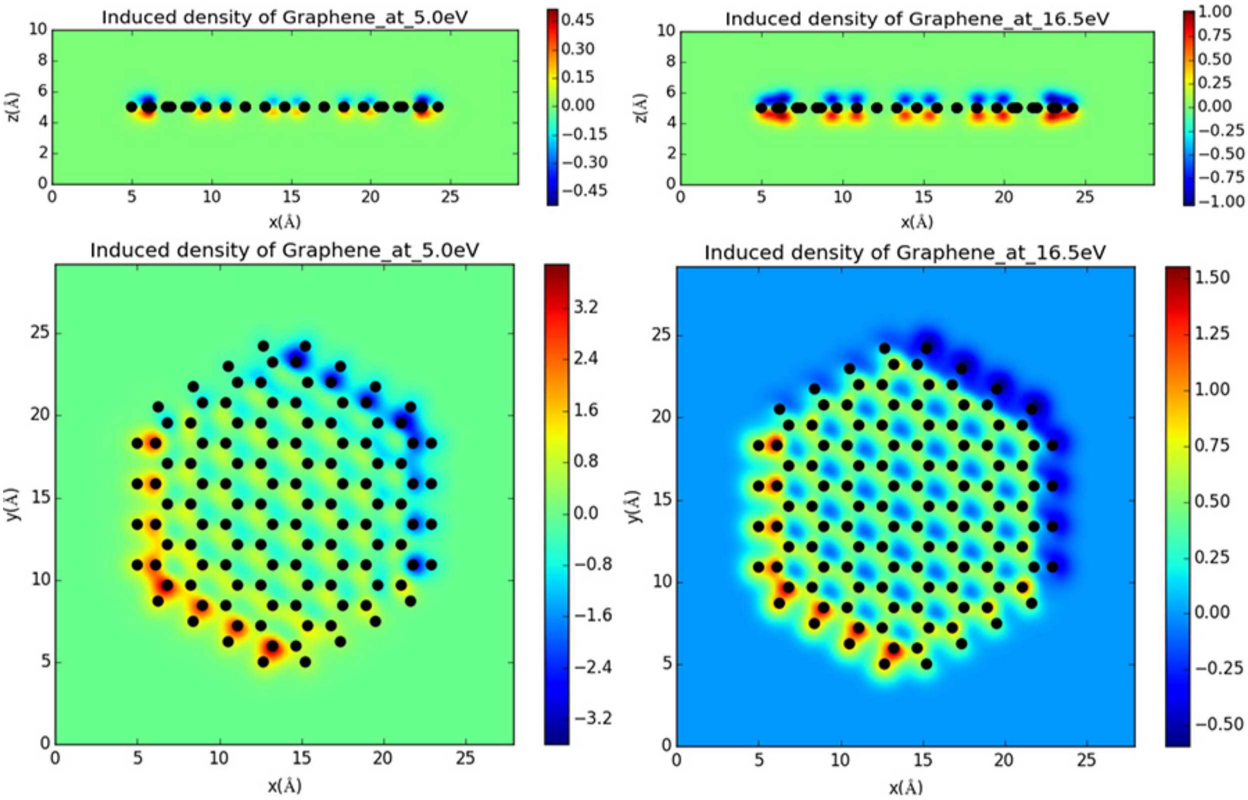

Figure 4.82: Induced charge densities of the 96-atom graphene flake, in SZP-LDA basis for $w \geq 5$, at resonance frequencies in z-direction (above set), and in x-y plane (below set).

The above induced fields, for a large enough width ($w \geq 5.0$, which is the width of the induced charge densities, set as a visualization parameter), look exactly like the induced charge density and the field enhancement of the 96-atom graphene flake in FD-TDDFT. Therefore, we realize that resonances of the induced charge density can only be interpreted as LSPR's for systems of large dimensions like the ones in fig. 4.80. Now SZP basis seems to generate the LSPR's with a weak intensity (note that while the width might change certain LSPR shapes altogether, in the case of low impurity it only increases the visibility of the effect of the impurity on the induced charge densities). Therefore, next in fig. 4.83, we look at the PAS, and the LSPR's in a 600-atom graphene flake using the DZP basis in fig. 4.84.

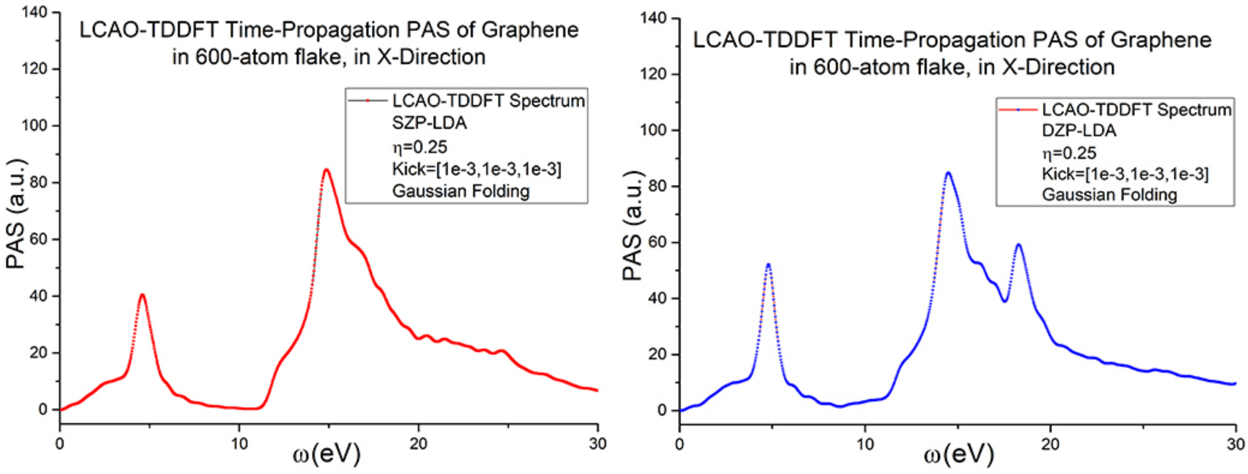

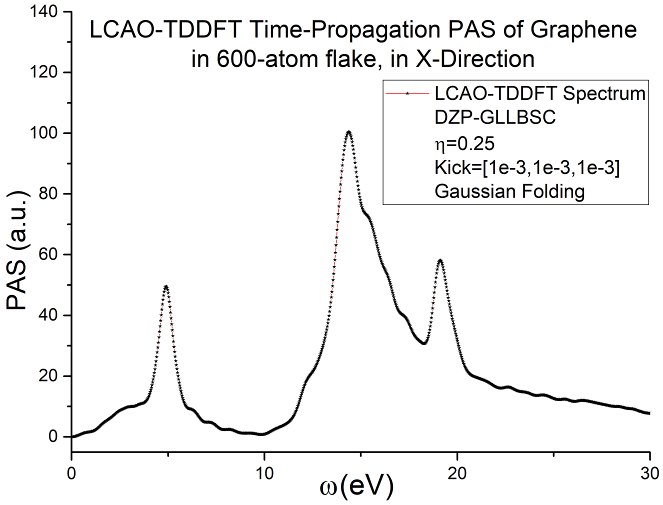

Figure 4.83: LCAO-TDDFT PAS of the 600-atom graphene flake in SZP-LDA basis (above left), in DZP-LDA basis (above right), and DZP-GLLBSC (below).

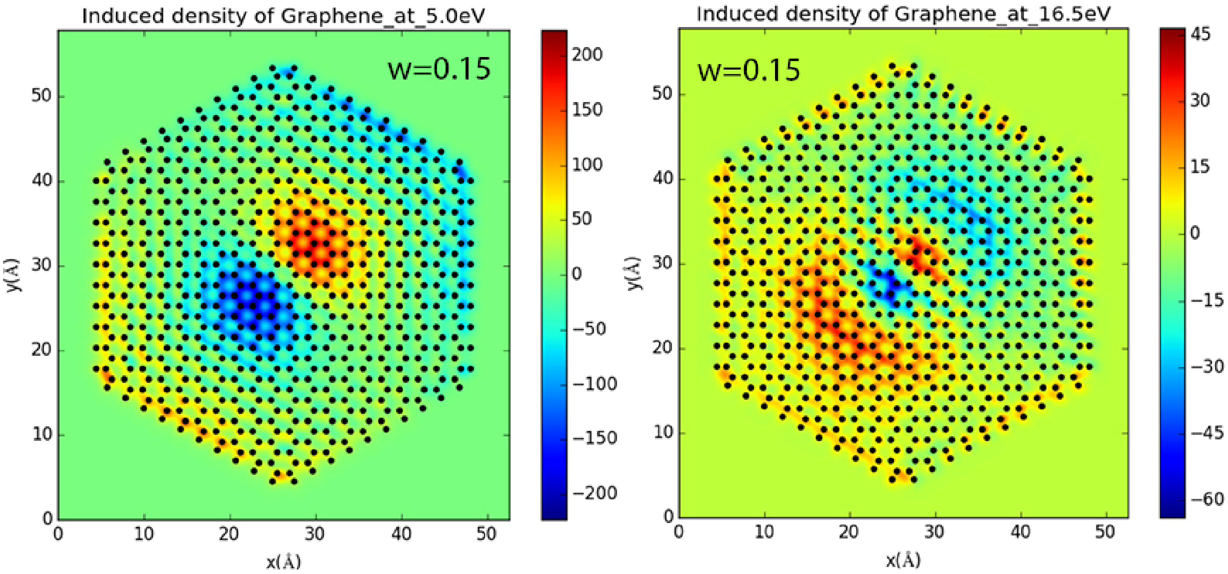

Figure 4.84: π LSPR at 5.0 eV (left), and the $\sigma + \pi$ LSPR at 16.5 eV (right), of graphene in 600-atom flake, in DZP-GLLBSC basis for $w = 0.15$.

In fig. 4.84 we clearly see the LSPR's, indeed localized at the center with negative and positive polarizations for the. Indeed for the smaller resonance frequency, which is due to the π band, we see a corresponding LSPR related to the bipolar shape of the π band. However, for the $\sigma + \pi$ LSPR, the σ LSPR is enclosed with two additional clouds of π band resonating at opposite polarities, interestingly. This is fully in agreement with the definition of the surface plasmonics of graphene, due to the fact that we see clearly, from the shape of LSPR's, that at $\sigma + \pi$ frequency we a LSPR that is made up of σ LSPR and an enclosing π LSPR. It would be interesting to see the effect of the Si-atom structures on this LSPR, which as we see tends to spread overall (or as one could say 600-atom sheet is too small for its size, as is the 96-atom for the σ LSPR). However, prior to that we look at one other homogeneous system, namely the 2D Si-C only in one size molecule, 600-atom saturated flake, and then look at it's LSPR's generated in DZP-GLLBSC. Fig. 4.85, and fig. 4.86, show the PAS, and the LSPR's (in DZP-GLLBSC) of the 2D Si-C.

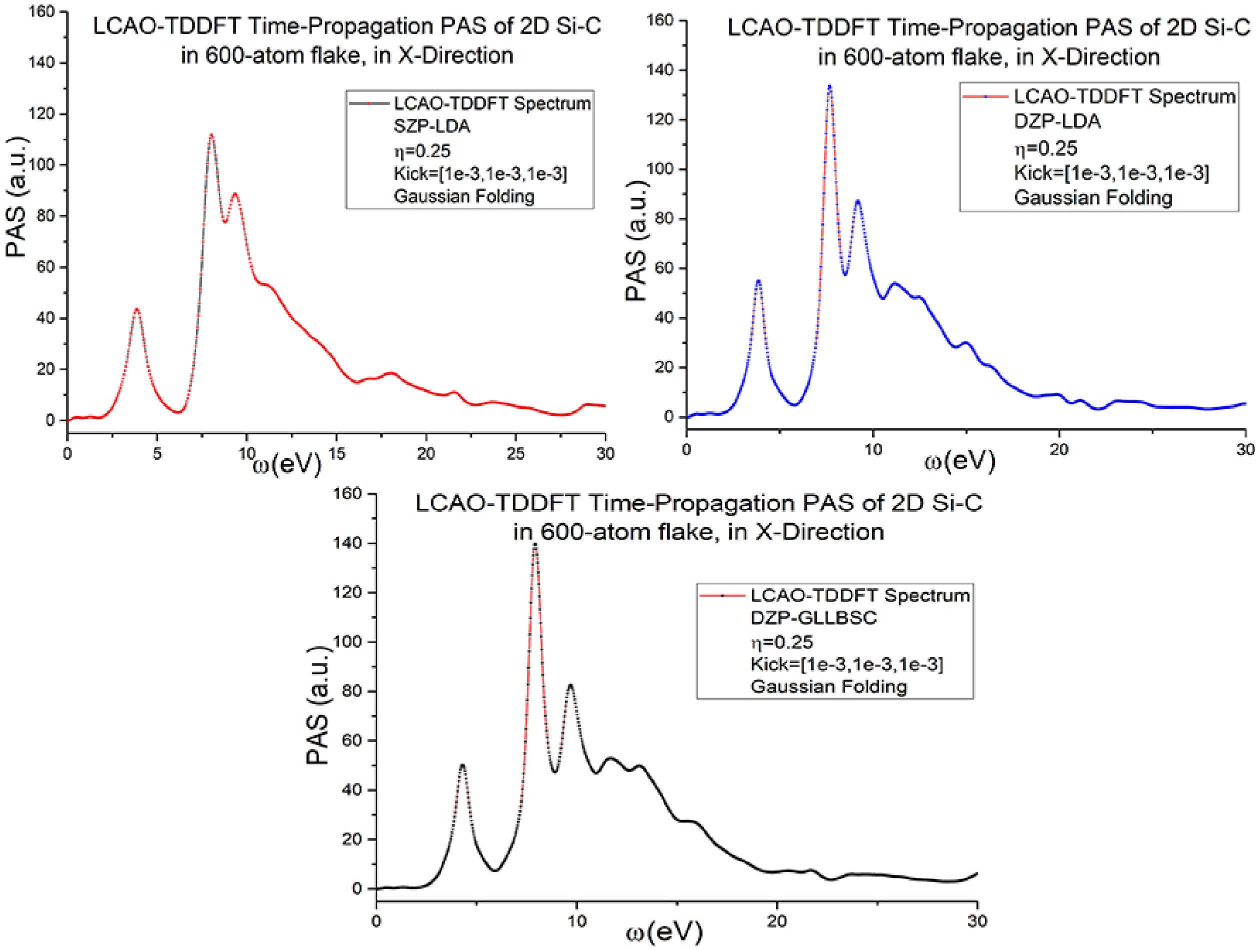

Figure 4.85: LCAO-TDDFT PAS of the 600-atom graphene flake in SZP-LDA basis (above left), in DZP-LDA basis (above right), and DZP-GLLBSC (below).

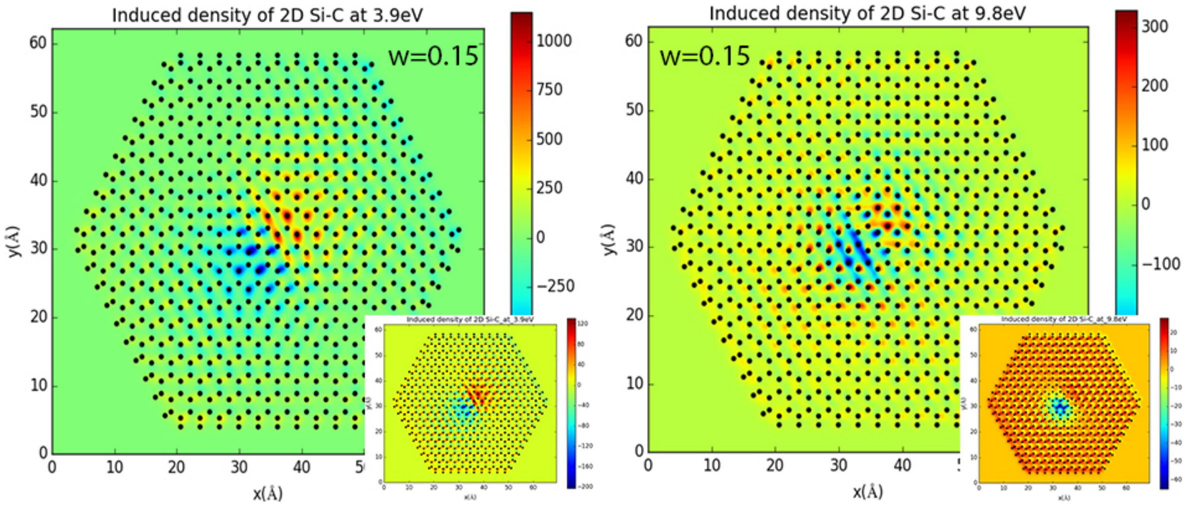

Figure 4.86: π LSPR at 3.9 eV (left), and the $\sigma + \pi$ LSPR at 9.8 eV (right), of 2D Si-C in 600-atom flake, in DZP-GLLBSC basis with $w = 0.15$ (and $w > 5.0$ for the smaller side figures).

We can see in fig. 4.86 the effect Si-doping (or impurity), which is on alternating lattice sites on the shape of the (π) LSPR at 3.9 eV, other than the fact that the resonance frequency is lowered by ≈ 1 eV. For the larger LSPR the negative part still is slightly affected by the position of the Si-atoms, and the positive part, despite being spread all over the sheet (more clear with larger width), still makes its appearance known adjacent to the blue charge densities, which shows that the positive $\sigma + \pi$ LSPR has not completely delocalized.

We move on next to the single trivalent silicon (Dot_Si) in two systems of different size with 216-, and 600-atom saturated flakes, and analyse their PAS and LSPR's if any. Fig. 4.87 shows the PAS of the 216-atom flake Dot_Si.

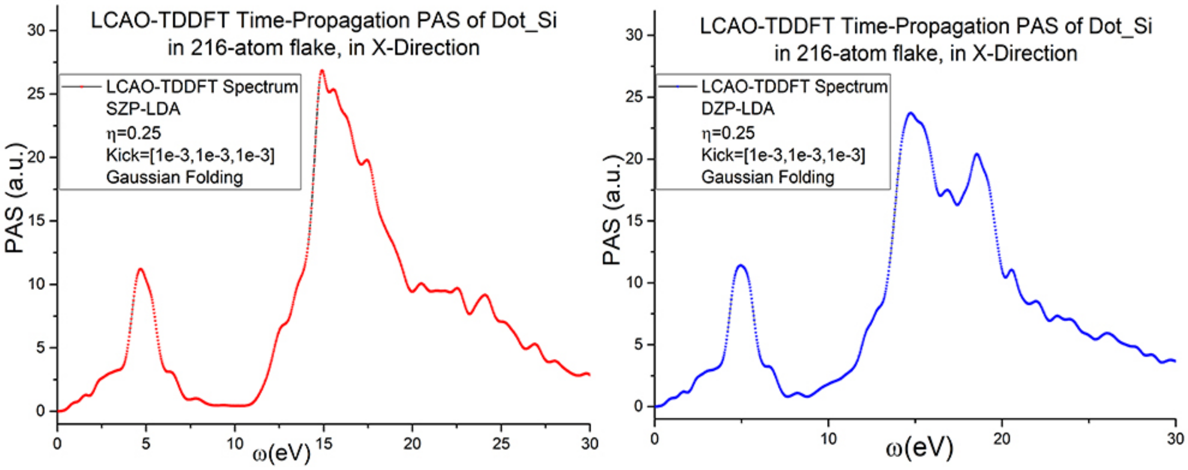

Figure 4.87: LCAO-TDDFT PAS of the 216-atom Dot_Si flake in SZP-LDA basis (left), in DZP-LDA basis (right)

Accordingly we have the LSPR's of the 216-atom flake in fig. 4.88.

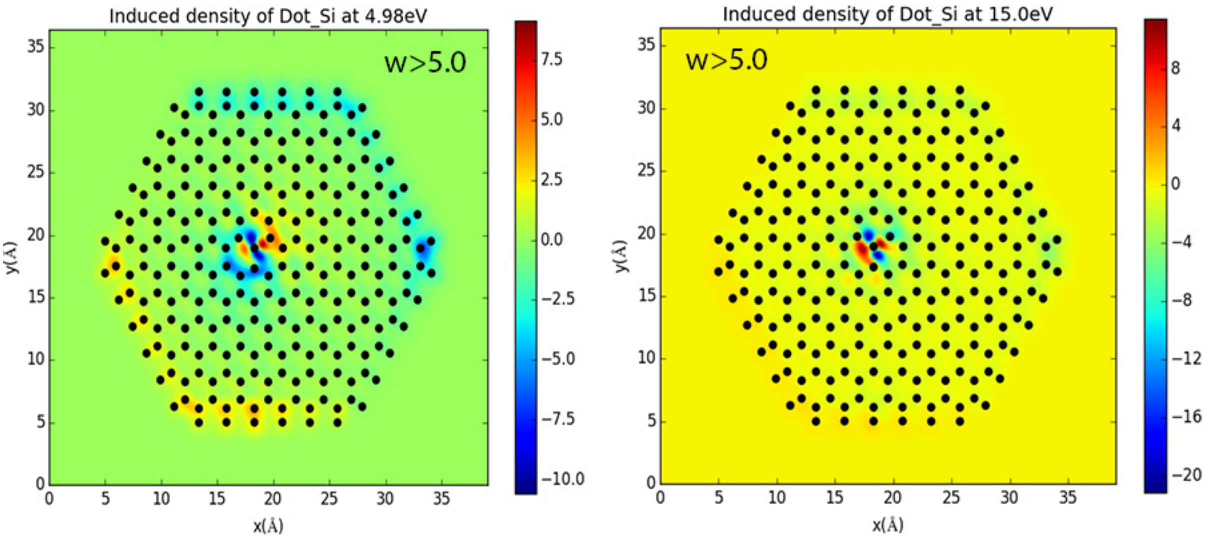

Figure 4.88: π LSPR at 4.98 eV (left), and the $\sigma + \pi$ LSPR at 15.0 eV (right), of 2D Si-C in 600-atom flake, in DZP-LDA basis with $w > 5.0$.

Looking at the PAS, the DZP-LDA, very well captures the wideness of the second peak centred at 15.0 eV, while the SZP basis produces a sharp peak at that frequency. From the simulations of the 4.3.1 we know that the peak at the 15.0 eV for the Dot_Si was not sharp and spread over a f eV's. As for the LSPR's for the lower frequency LSPR in fig. 4.88 left, one sees that the LSPR is much more compact and localized around the Si-atom in both polarities, while the graphene sheet is more or less neutral (other than the boundaries). But for the larger frequency LSPR, the positive charge seems to be more compact than the negative charge, and as a result we have cloud of negative charge density throughout the graphene flake (the green cloud overall, while yellow denotes neutral charge). Therefore, once again we can confirm that a Si-atom impurity induces a positive potential, and once spread (at higher resonance frequencies) this potential gathers (induces) negative charge density overall in graphene (compensated by the thick positive charge density close to the Si-atom, and the positive charge gathered at the boundaries). In the next structure this concept will become more clear.

Now we look at the same structure just in a larger graphene flake of 600-atom expecting more or less the same results, while we want to see what happens to the LSPR of a larger system (molecule) at the higher frequency. Fig. 4.88 and 4.89 show the PAS and the LSPR's of the system.

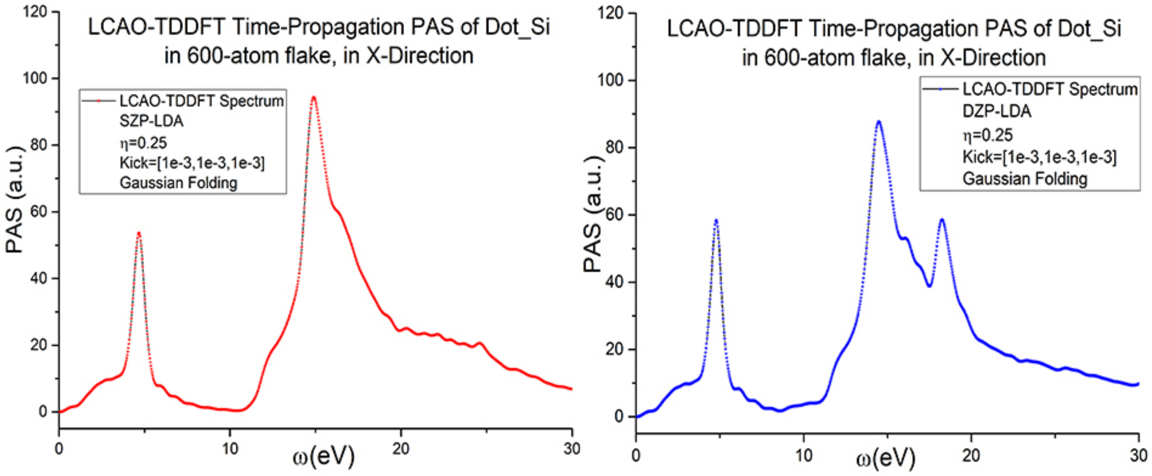

Figure 4.89: LCAO-TDDFT PAS of the 600-atom Dot_Si flake in SZP-LDA basis (left), in DZP-LDA basis (right).

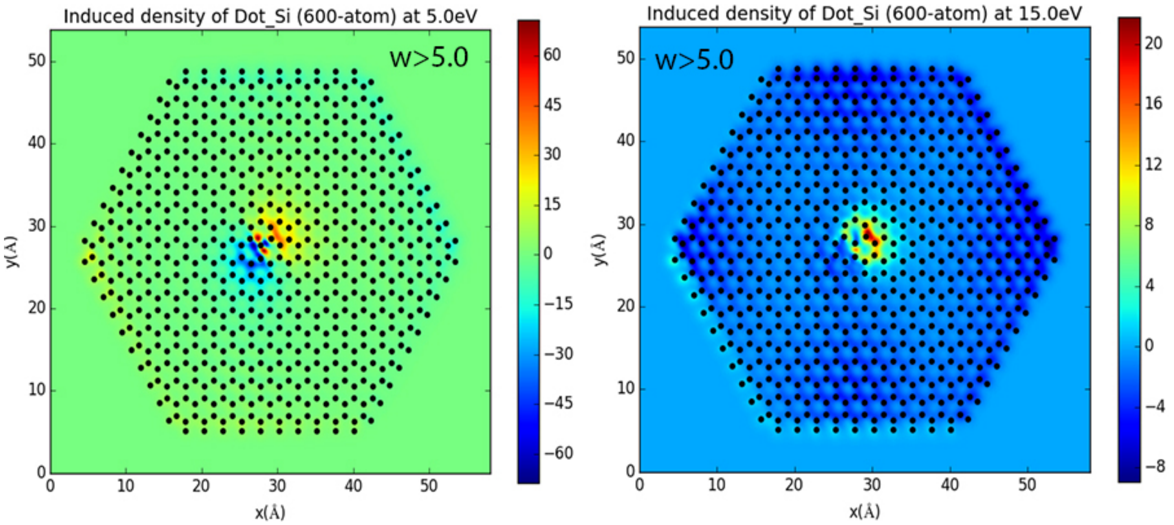

Figure 4.90: π LSPR at 5.0 eV (left), and the $\sigma + \pi$ LSPR at 15.0 eV (right), of 600-atom Dot_Si flake, in DZP-LDA basis with $w > 5.0$.

Aside from the PAS which have only been sharpened, the LSPR's are exactly as expected, even more clear. The namely the $\sigma + \pi$ LSPR confirms our analysis in the above paragraph about the smaller system. The fact is now clear, that a Si-atom impurity induces a negative charge density over the graphene sheet whole causing a positive charge and potential in its immediate vicinity, therefore changing the polarity of the charge density across the graphene sheet, compared to the case of pristine graphene as seen in fig. 4.82 right-side.

Next we look at two line structures, namely the 2x ABZZ-line, and the 6x ACh-line, as simulated in section 4.3.1. Once again to mention, one should note that the 2x and 6x indicated the number graphene rows between the lines. These structures are very appropriate for benchmarking purpose, as they could easily be simulated using periodic boundary conditions in a small cell. In fig. 4.91 and 4.92 we look at the PAS of these structures:

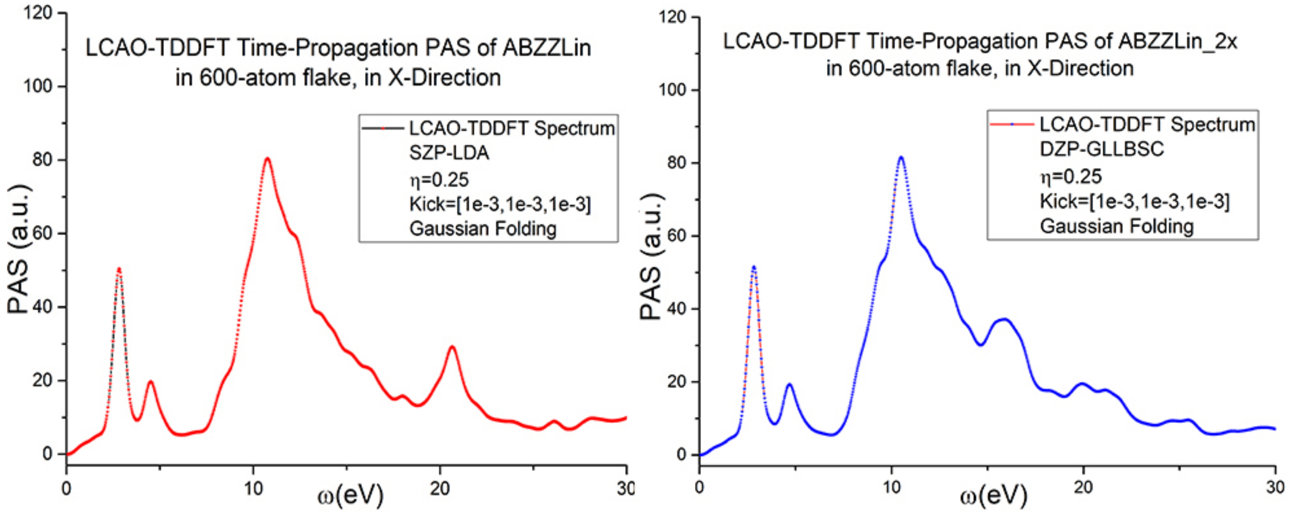

Figure 4.91: LCAO-TDDFT PAS of the 600-atom ABZZLin_2x flake in SZP-LDA basis (left), in DZP-LDA basis (right).

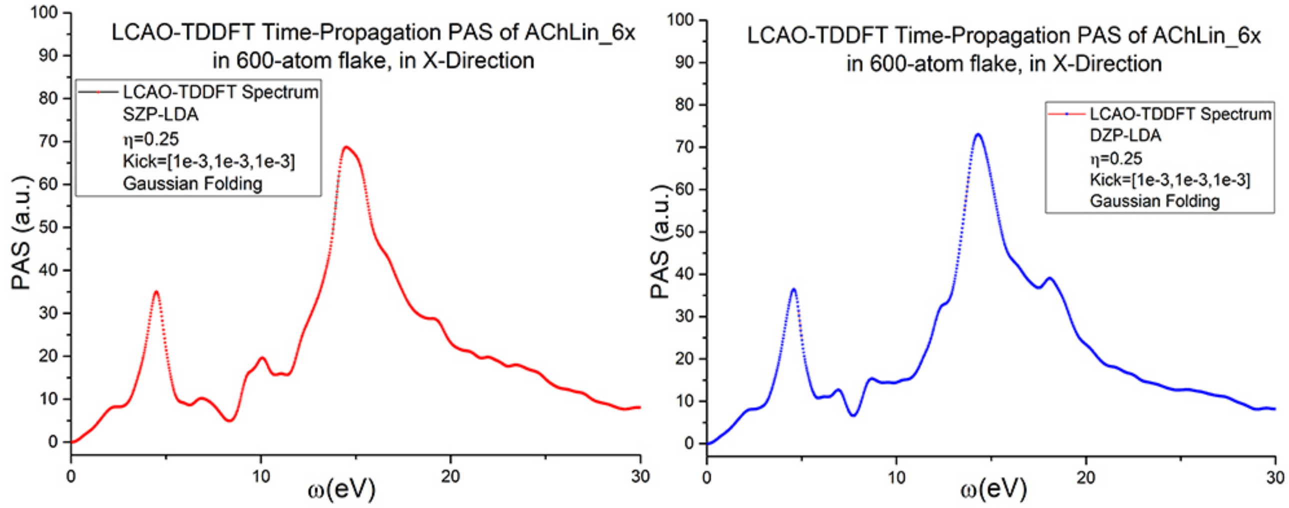

Figure 4.92: LCAO-TDDFT PAS of the 600-atom AChLin_6x flake in SZP-LDA basis (left), in DZP-LDA basis (right).

As expected the spectra look very different and acceptably similart to the spectra in section 4.3.1, namely that the peaks and the overall shape is in agreement, but there is still place for adjustment using both bases. It is interesting to observe that in the case of DZP-LDA, the wavefunction wouldn't converge for the given boundary condition corrections (momenta corrections, which we will talk about in the discussions). But switching to GLLB-SC in DZP basis, the wavefuction converged easily. This indicates the importance of the GLLB-SC functional for materials with semiconductor properties. In both cases however, the AChLin_6x, and the ABZZLin_2x, when we compared the spectra to those of section 4.3.1, DZP basis, due to it being bulkier at the $\sigma + \pi$ peak, seems more appropriate for benchmarking, even though it might have a sharp tip. If the entire peak is sharp however, like the SZP, there isn't much place for adjustment.

Next we look at the LSPR's for the peak frequencies in fig. 4.93 and 4.94.

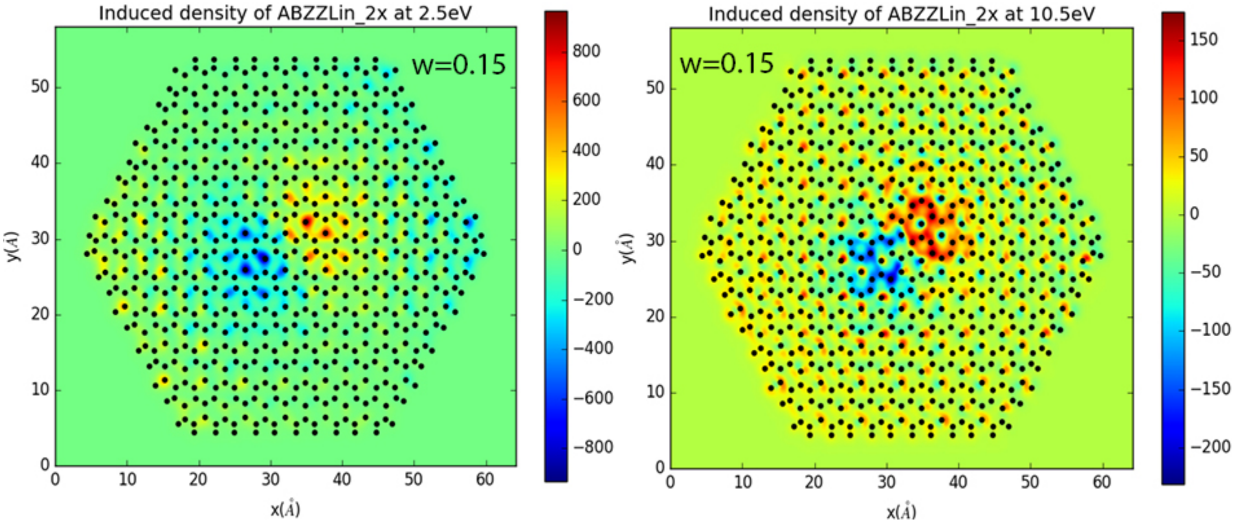

Figure 4.93: π LSPR at 2.5 eV (left), and the $\sigma + \pi$ LSPR at 10.5 eV (right), of 600-atom ABZZLin_2x flake, in DZP-LDA basis with $w = 0.15$.

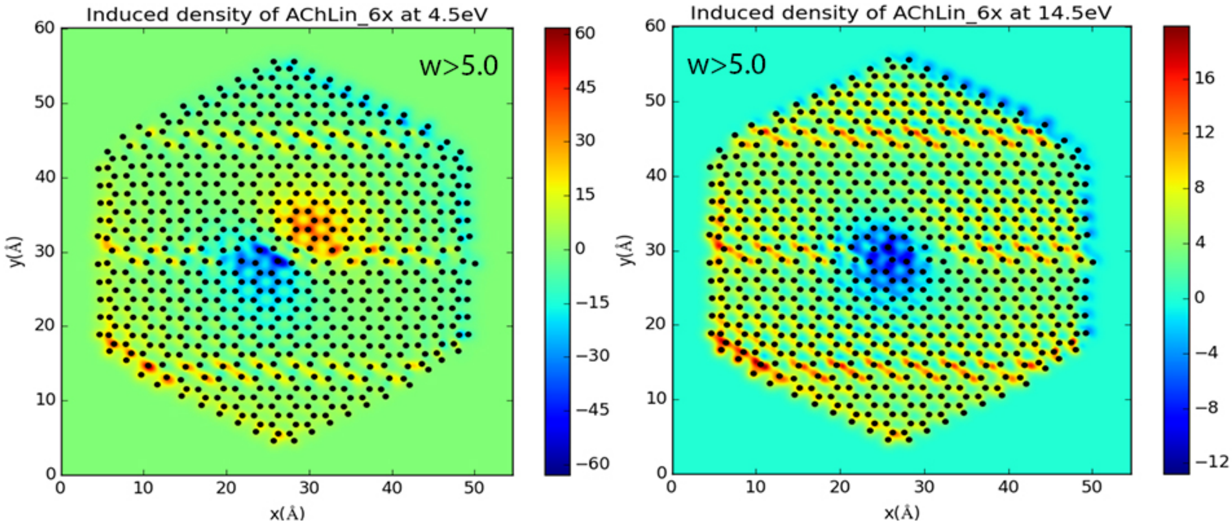

Figure 4.94: π LSPR at 4.5 eV (left), and the $\sigma + \pi$ LSPR at 14.5 eV (right), of 600-atom Dot_Si flake, in DZP-LDA basis with $w > 5.0$.

Another effect upon the LSPR's could be observed in the above figures. As for the ABZZLin_2x, the Si-atoms seem to delocalize the charge densities beyond a certain radius, which is case of the $\Sigma + \pi$ it looks very much like more charge concentration close to the center, and distributed charge everywhere else so that the original structure of the LSPR is lost. But in the case of

AChLin_6x, the Si-lines, which appear with positive charge around them, interestingly somehow separate the resonant charges for the lower frequency, while for the higher frequency the Si-lines cannot cut through the negative charge. Before we move on however, we look at the geometries of the lines within the flakes, and the PAS in y-direction. Fig. 4.95 shows the geometries of the ABZZLin_2x and AChLin_6x, in a 600-atom flake.

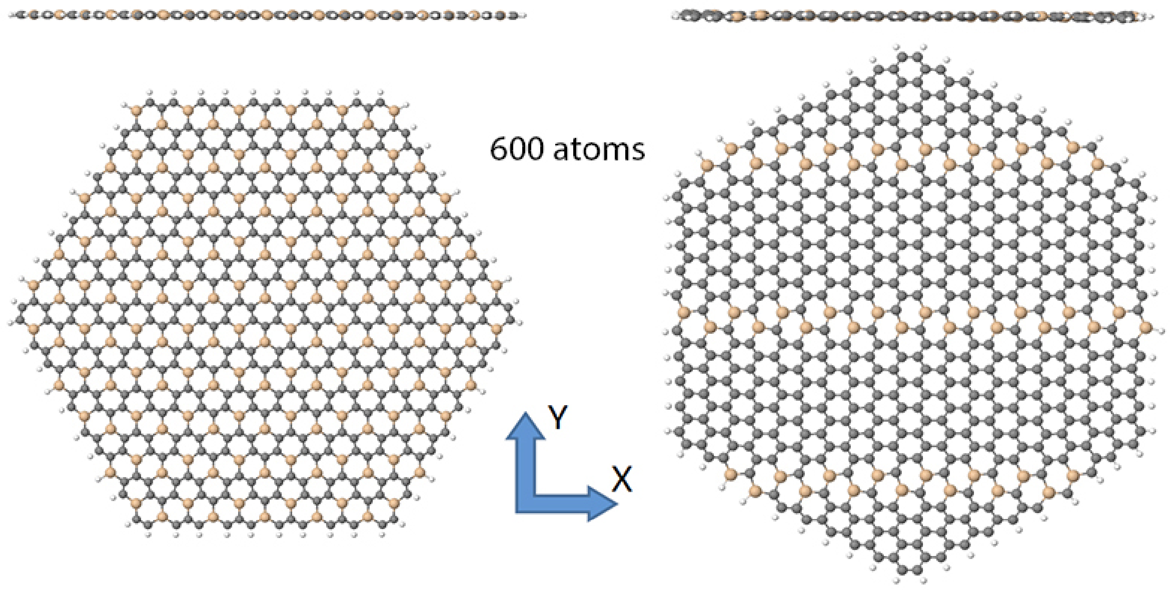

Figure 4.95: The geometries of the ABZZLin_2x (left) and AChLin_6x (right) in a 600-atom graphene flake.

Fig. 4.96, shows the PAS of these structures in y-direction:

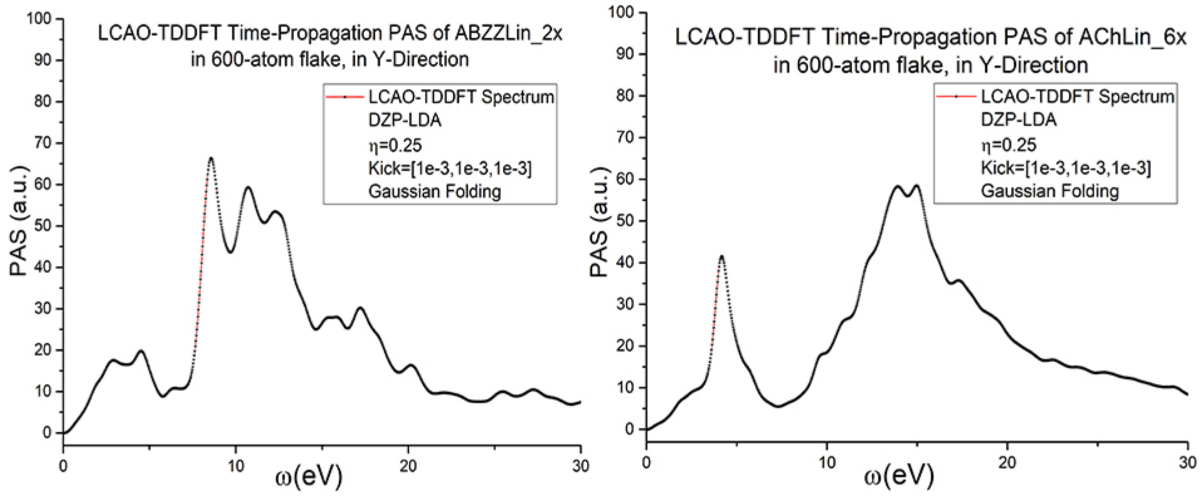

Figure 4.96: LCAO-TDDFT PAS in DZP-LDA basis of the 600-atom ABZZLin_2x flake (left), and 600-atom AChLin_6x flake (right) in y-direction.

Interestingly, the similarities in the y-direction spectra is very well observable compared to the dielectric response spectra in section 4.3.1. In the case of ABZZLin_2x, the behaviour of the larger peak leaning with an extra peak towards 8 eV, as seen is fig. 4.52 and 4.53, is clearly present, and for AChLin_6x the spectra are as similar as in the previous case of comparison, but once again there is a twitch at 8 eV in the x-direction in fig. 4.92.

Next we move on to a few structures, which we have not tried previously, due to their size, and with that we close this section. First it would be interesting to look at the small 1x circle, or dodecagon, in a 486-atom graphene flake (since it was smaller than other structures), and then look at a few larger structures like the 16x hexagon, and 36x triangle. Fig. 4.97 shows PAS of the dodecagon, and fig 4.98 the corresponding LSPR's on the plateau of the dodecagon for 2 different widths (w).

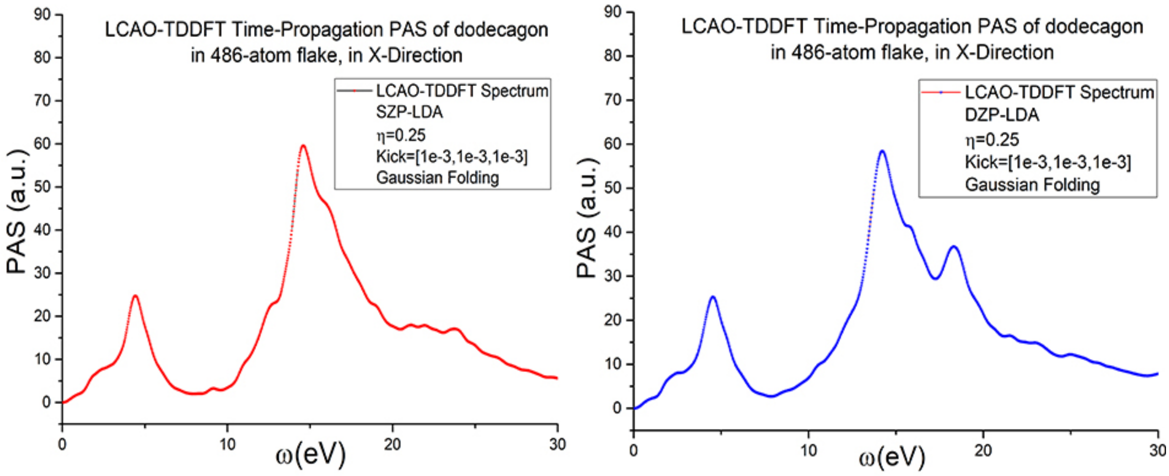

Figure 4.97: LCAO-TDDFT PAS of the 486-atom dodecagon flake in SZP-LDA basis (left), in DZP-LDA basis (right).

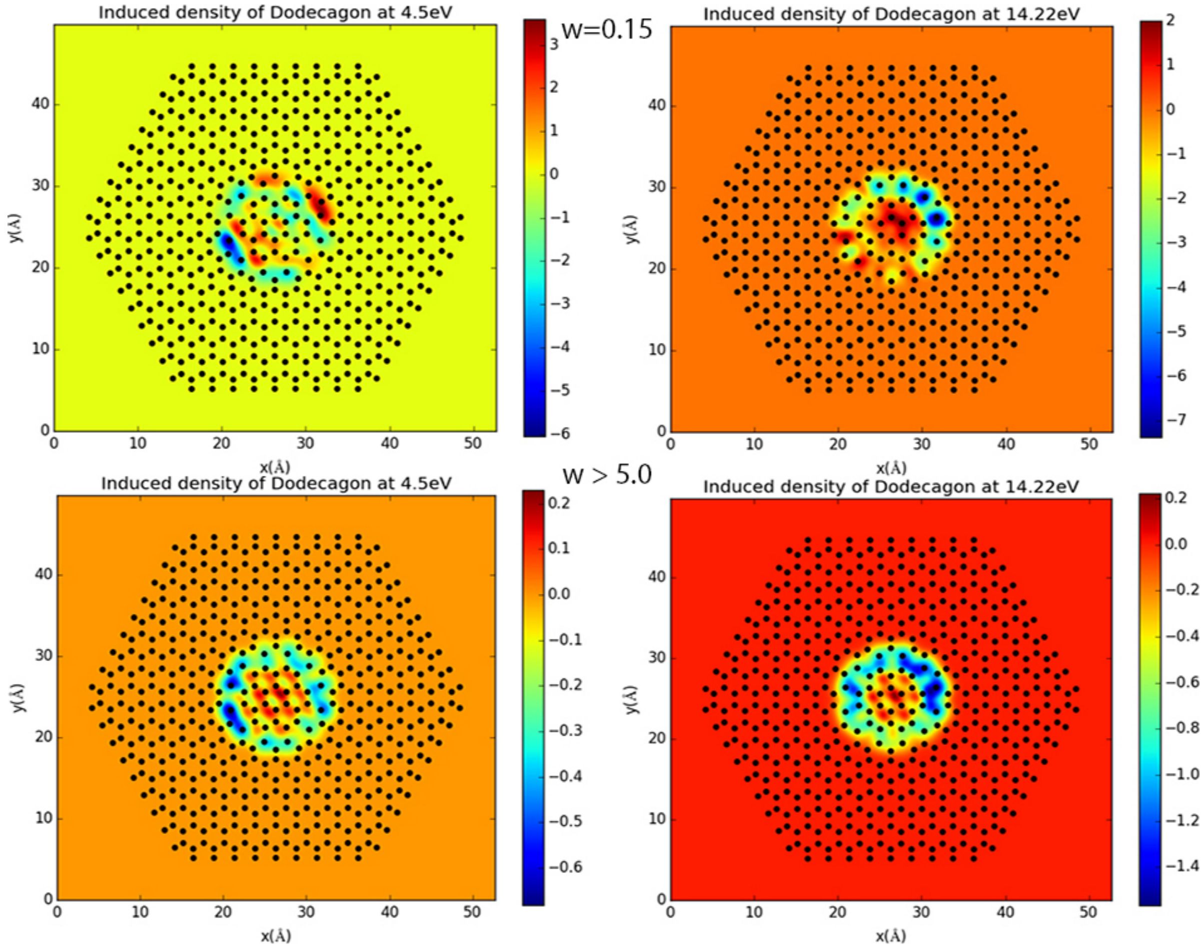

Figure 4.98: The LSPRS's of the dodecagon at peak frequencies and DZP-LDA basis for $w = 0.15$ (above set), and $w > 5.0$.

We can see for the small width that at larger resonance frequency, there seems to be a complete charge separation, with the Si-atoms acting as a wall of negative charge density causing the center of the dodecagon to glow red (positive), even though for the smaller frequency both charges seem to be present inside the circle. However, when we increase the width this confusion disappears, and wee that the scale is reduced in comparison, but the charge separation is consistent in both LSPR's.

With that we move to the Square8x, which is rather a particular structure in terms of the general lattice symmetry. This structure is on the 600-atom, and in fig. 4.99 we see the PAS of the Square8x.

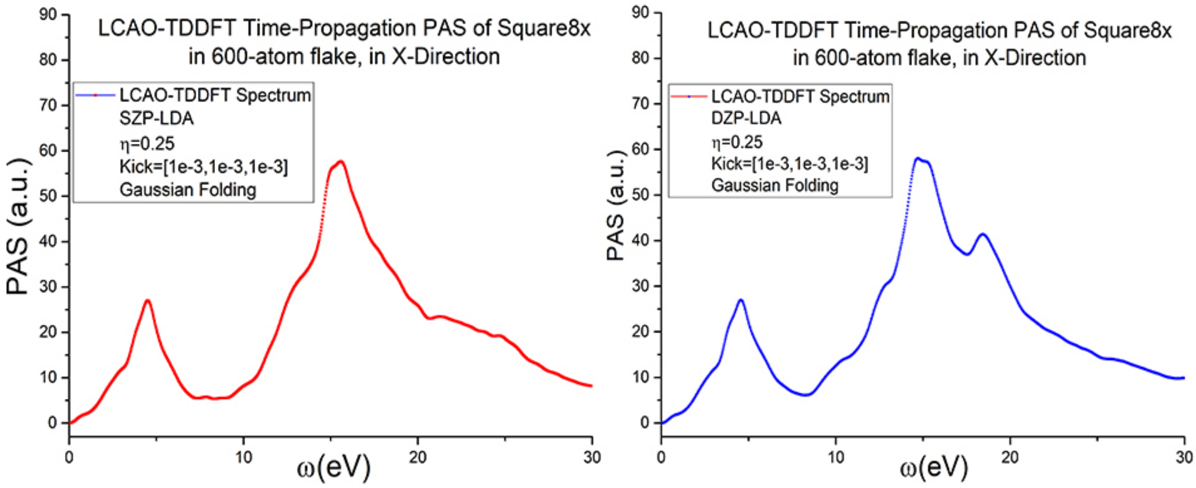

Figure 4.99: LCAO-TDDFT PAS of the 600-atom Square8x flake in SZP-LDA basis (left), in DZP-LDA basis (right).

Fig. 4.100 also shows the corresponding LSPR's for only one width.

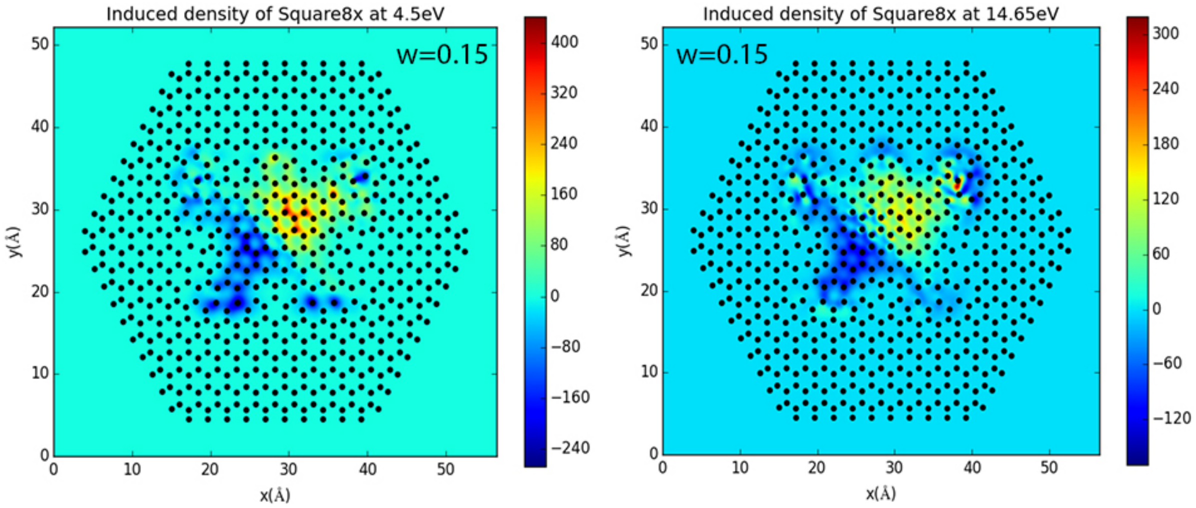

Figure 4.100: π LSPR at 4.5 eV (left), and the $\sigma + \pi$ LSPR at 14.65 eV (right), of 600-atom Square8x flake, in DZP-LDA basis with $w = 0.15$.

Here is a pattern that we observe in the shape of the LSPR's especially the larger one enclosing both negative and positive charge densities, and dividing them from the diagonal. This is very interesting indeed, as it seems that closed patterns indeed do change the shape of the LSPR into a desired form, and that in itself is a significant observation.

Following on that line we next look at the two structures, which are symmetric against the hexagonal lattice and are very important in terms of their shape, and aside from their calculated PAS using the existing bases, we study their effect on the graphene LSPR's. Fig. 4.101 and 4.102 show the PAS, and the corresponding LSPR's of the Hexagon16x.

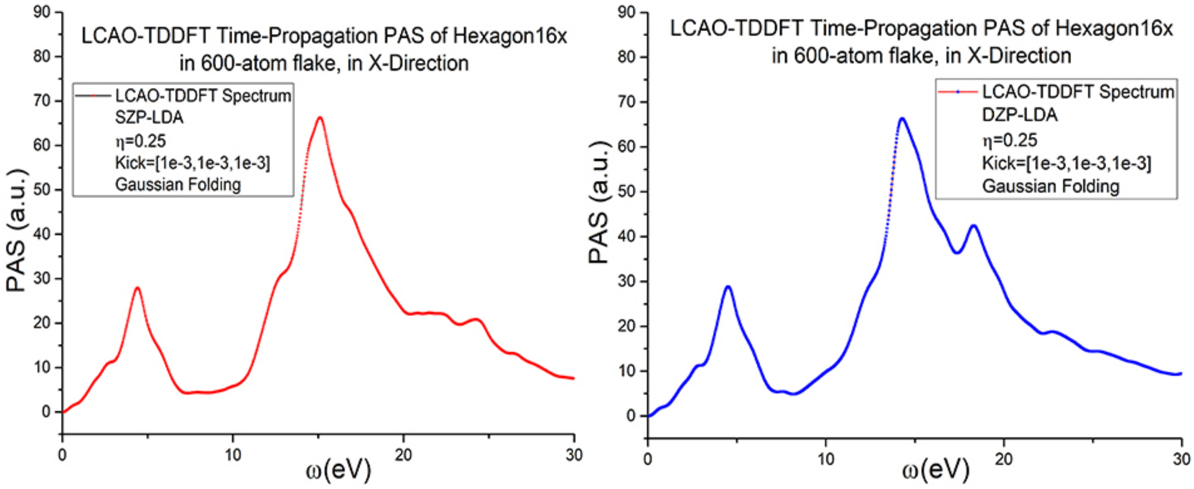

Figure 4.101: LCAO-TDDFT PAS of the 600-atom Hexagon16x flake in SZP-LDA basis (left), in DZP-LDA basis (right).

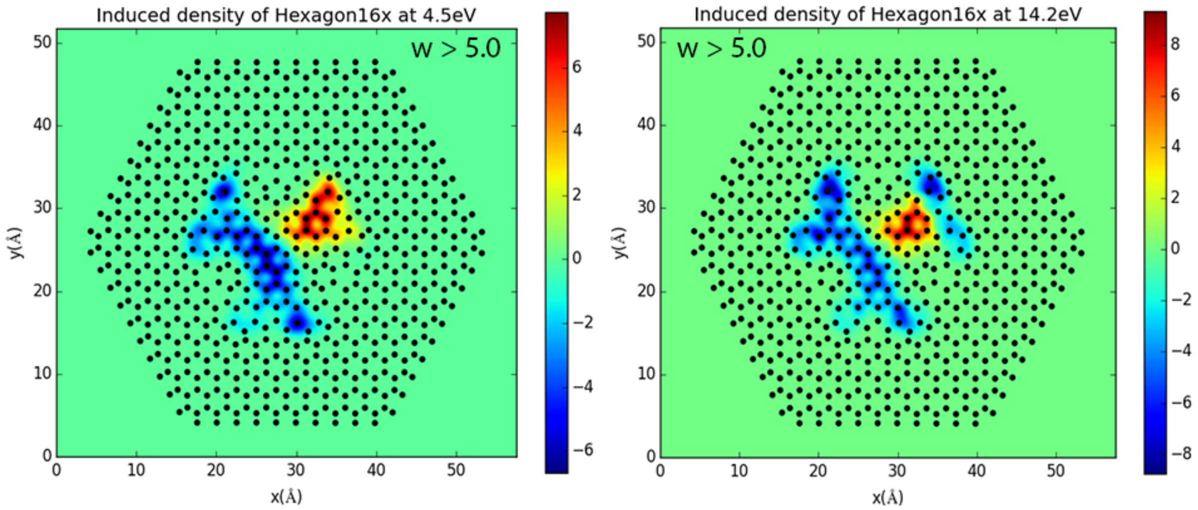

Figure 4.102: The LSPRS's of the Hexagon16x at peak frequencies and in DZP-LDA basis for $w > 5.0$.

Aside from the PAS, which is different from that of the Square8x, once again we see that the LSPR's have taken a funny shape resembling the elevated plateau of the Hexagon16x, while being separated in positive and negative from the diagonal. The figure however is limited to a certain height, which is being visualized at the time. The side-traces of the charges therefore would fill up the entire hexagon, making a unique shape based on the enclosure. This obviously brings geometrical control over the shape of LSPR's, which should be in turn very important for application in nano-electronics, and sensorics.

Finally we check the Trianlge36x, which is very similar to the hexagon in terms of crystallographic symmetry. Fig. 4.103 shows the PAS of the Triangle36x.

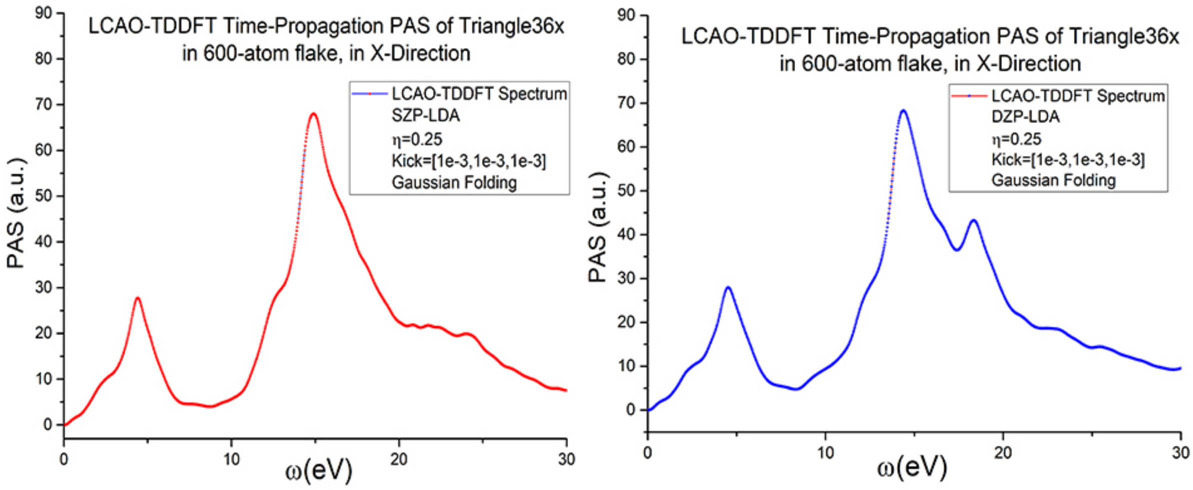

Figure 4.103: LCAO-TDDFT PAS of the 600-atom Triangle36x flake in SZP-LDA basis (left), in DZP-LDA basis (right).

Fig. 4.104 shows the LSPR's of the Triangle36x.

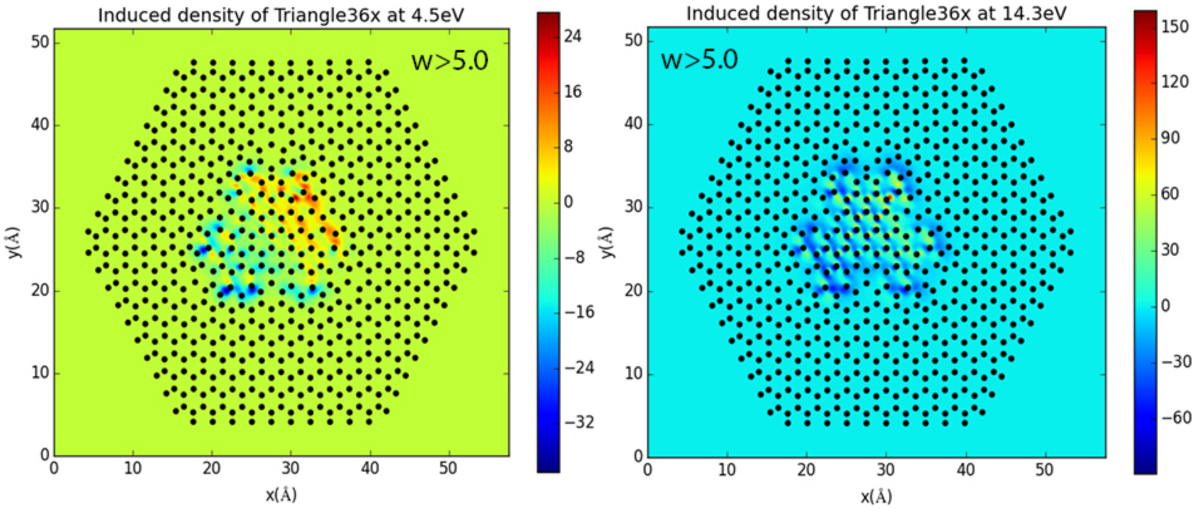

Figure 4.104: he LSPRS's of the Triangle36x at peak frequencies and in DZP-LDA basis for $w > 5.0$.

The PAS of the Triangle36x look very similar to that of the Hexagon, seeing from the above plots. There is only a small amount of detail in the difference between the two PAS, since for a 600-atom molecule, a rearrangement of the Si-atoms, which are the same in number (25 Si-atoms in both cases) can only cause so much of a difference. However, it is in the case of the geometry of their LSPR's that one can truly distinguish these structures. Therefore, even for a fully benchmark set, the structures that have the same number of impurity atoms, and close geometrical shapes, a very close PAS is to be expected. However these have to significantly differ from the pristine graphene, which unfortunately is not quite the case here, due to the aforementioned inaccuracies.

Chapter 5

Discussions & Conclusions

With regards to the relaxation of structures within the graphene lattice, a couple of points are noteworthy. The procedure how to come up with structures, and how to go about relaxing them is indeed a process, which requires some work regarding the methods of how to proceed. Indeed the role of analytical potentials have been crucial, as having the result of relaxation with analytical potential as the initial figure or condition for DFT relaxation is big jump and an advantage, if it does not lead to metastable higher energy configurations (as in the case of dense ZZ-line and it pseudo-flat variation). However, this probility is very small indeed, and in lieu of such small mistake-probabilities, it is definitely worth to start from analytical potentials, before embarking on *ab initio* methods for finding the relaxed form of a particular embedded pattern onto a 2D graphene sheet.

As for the DFT method of relaxing hundreds of atoms, once again it should be mentioned that, only real-space grid methods, with the domain-decomposition capability (which divides the grid points between the processors for parallel computing), are capable of handling this number of atoms. Normally DFT methods are said to be able to handle up to 300 atoms. However, in our case 400-atom structures have been easily dealt with, on our systems, a super-computer of some 2000 node, with each node (normal nodes) having $16x@\ 2.2\ GHz\ CPU,\ 64\ GB\ RAM$. Even a system of 650 atoms have been relaxed, though using more than a 1000 nodes for relaxation and FD-wavefunction convergence. Therefore, other mainstream DFT methods based on just plane-wave or PAW, or just LCAO (i.e. *Siesta*, which is based on Pseudo-potentials), without real-space grid PAW implementation and domain decomposition, will not be able to deal with this system-sizes. It is recommended however, for more efficiency and productivity a super-computer of hundreds of $128\text{-}GB\text{-}RAM$ nodes, as have been implemented elsewhere, which in the opinion of the author, combined with the GPAW-package, will be able to relax and converge WF's of structures of ~ 1000 atoms, breaking a record in DFT.

Regarding the STM results, there is potentially a lot to be said, since this stage of computer-based experiment is the very preliminary stage, which would pave the way for more complicated simulations and eventually actual STM experiments. However, as seen in the results and referring to the theoretical background, the ripple effect which was reported in the original quantum corral experiment in terms of bias, and position [7], is seen in a way in our simulation in terms of bias, as the sets of images for increasing bias shows the development of the confined state into a more complicated one which has wings and sides, all the way onto the Si-atom barriers. This is significant int that, it is a prelude to seeing ripple effects, once a more advanced STM formalism is applied (NEGF, Keldysh formalism). It has been shown experimentally that graphene is capable of guiding such standing wave ripples on its lattice in different situations.

In fig. 5.1 from [2], it is shown that under controlled doping conditions, where a p-n junction is created between the round area and the rest of the sheet, the ripples of standing wave of a quantum corral can be observed with a STM on the graphene lattice.

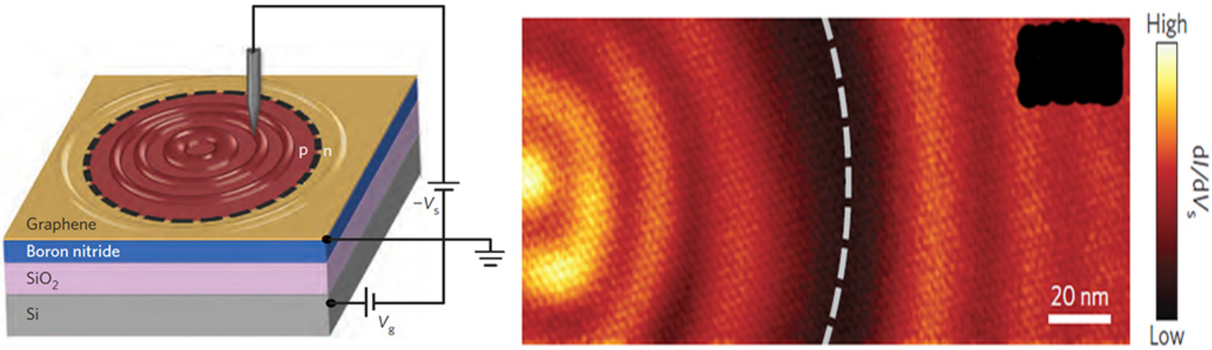

Figure 5.1: The STM experiment on a graphene p-n junctions on a set of substrates, showing the quantum corral ripples blocked by the junction border, and induced by the STM tip. From [2], reprinted with permission from Nature Publishing Group.

Equivalently fig. 5.2 from an article about tuning the plasmonics of gated graphene, illustrates the importance of the STM tip in inducing the surface electronic ripples initiated by infra-red light.

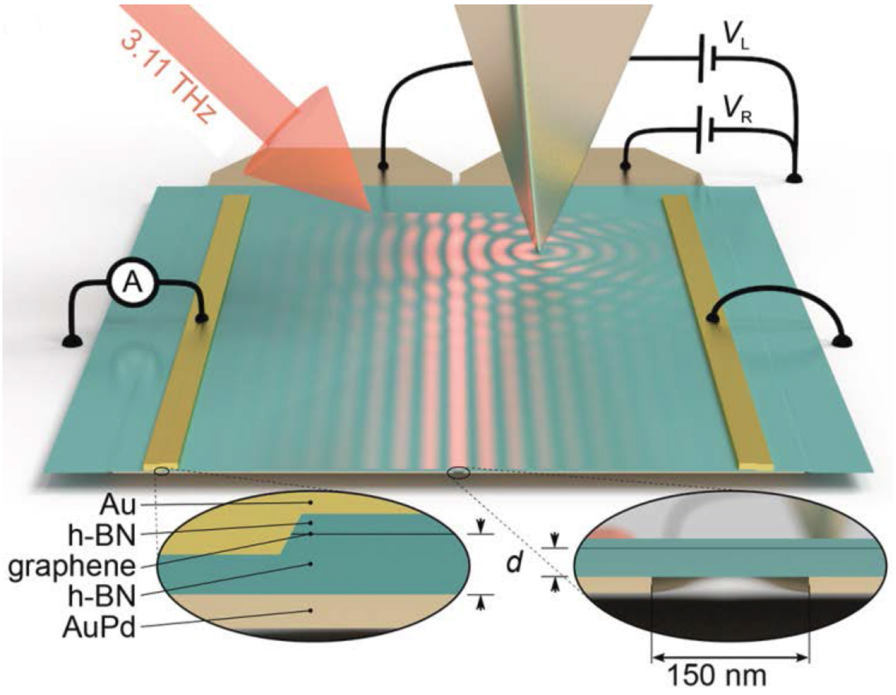

Figure 5.2: The effect of the STM tip on the surface electronic states (infra-red surface plasmons) of a gated graphene induced by 3.11 THz infra-red light. (note that the wavelneght of the ripples (150 nm) is related to the infra-red light frequency. For visible light this length would be ≈ 200 times smaller). From [59], reprinted with permission from AAAS.

And therefore, it is believed that also without explicit doping and creating p-n junctions, solely by embedding barriers at chosen lattice sites, it would be possible to scatter the surface states resulting from the interaction of the tip and the surface in a multi-scattering frame, reproducing the surface local ripples that we see in fig. 5.1, even in a much smaller scale (wavelength).

The main part of this thesis and the related project is the study of the effect of embedding controlled impurities, in the form of the geometrical shapes, on the plasmonics of graphene. And in this thesis we do the ground-laying work in this regard, which is also very much related to the STM simulations (as shown in fig. 5.2 the confined surface states might very well be produced by the equivalent wavelength surface plasmons), since experimentally they are just another electron microscopy technique for the study of surface electronics of graphene. However, as mentioned before, computer based simulations relay very much on the methods apply. Namely that even though there is one STM apparatus (same working principle), there is at least 3 different theoretical methods that describe the working-function of the STM. Therefore, extreme care has to be given as to which method is applied and in which context indeed (environmental parameters).

With regards to the calculation of the plasmonic response of materials, there are a few methods available. One would be the linear dielectric response, which itself has a variety of formulations, from which we have used the TDDFT method. This method can produce the low loss EELS, which would reveal information about the plasmonic excitations of materials, with periodic boundary conditions (namely crystal ans solids). The other methods are based on modern formulations of the DFT, namely time-dependence and time-propagation, which would deliver the PAS of materials. It so happens that the surface plasmons of graphene resonate in the visible light spectrum (refer to the plasmonic dispersion relation in section 1.2), and therefore it is expected that the PAS and the EELS of graphene have more or less the same form. In fig. 5.3 we see the comparison of EELS with LCAO-TDDFT for 2 systems.

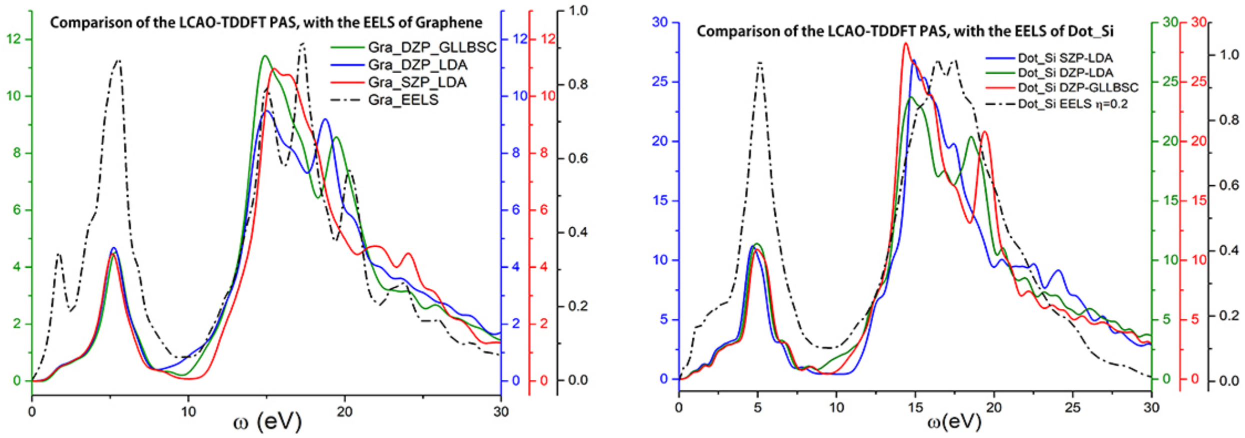

Figure 5.3: The comparison of the EELS with the LCAO-TDDFT time-propagation in different bases and XC-functionals for pristine graphene (left) and Dot_Si (right)

However, there are a few challenges to be overcome in order to obtain consistent results out of all the methods. First, as already mentioned the PAS calculation in TDDFT can only be done for a molecule without periodic boundary conditions. Therefore, a molecular representation of the extended periodic system has to be designed and its GS wavefunction converged. While in FD up to a 200 atoms this does not produce a challenge, in LCAO converging the GS density, can be very difficult. This is due to the fact that there are many parameters influencing the GS densities, whereas if there were wavefunctions these would easily be resolved. In FD the chosen basis makes absolutely no difference as the wavefunctions then replace the atomic orbitals an get expanded in a peridic way throughout the *Bravais* lattice, and also the wavefunctions easily obey the multipole corrected boundary conditions which is done by removing momenta up to level 9 ($s, p_x, p_y, p_z, d_{xx}, d_{xy}, d_{yy}, d_{yz}, d_{zz}$, this technique eliminates the effect of net charge, eliminating the so called cell-to-cell interaction due to the net charge [61]). However, converging the GS density in LCAO while applying the multipole corrections and choosing the right basis (SZ, SZP, DZP, etc) makes a big difference, as well as it may lead to convergence or non-convergence of the GS density at all.

In our LCAO-TDDFT simulations, we always applied at least L=4 multipole correction, and did at least two bases in a XC-functional (SZP and DZP in LDA) for minimal comparison. The GLLB-SC functional, which is very complicated functional, created for correcting the discontinuity in semiconductor band-gaps, would not converged in DZP for all the structures. For a few, for which it did, we also tried the DZP basis in GLLB-SC functional, without any adjustment. The results as they are presented in fig. 5.3 show a favorability towards DZP in GLLB-SC for this system sizes, when compared to the EELS spectra. Therefore, without any basis generation we can make the following statement regarding the bases and the XC-functions: And indeed the fact that, for our systems which include large semiconductor impurities the GLLB-SC functional, together with its DZP basis delivers more accurate results than any other basis/functional. Furthermore the existing bases are only good enough for systems of up to $\approx$ 200 atoms. For larger systems a custom basis must be generated and benchmarked against FD method, but once again they should be benchmarked in GLLB-SC functional. From our results we have the following common plot in fig. 5.4 to look at, which will show us a comparison of the larger 600-atom structures in DZP-LDA basis.

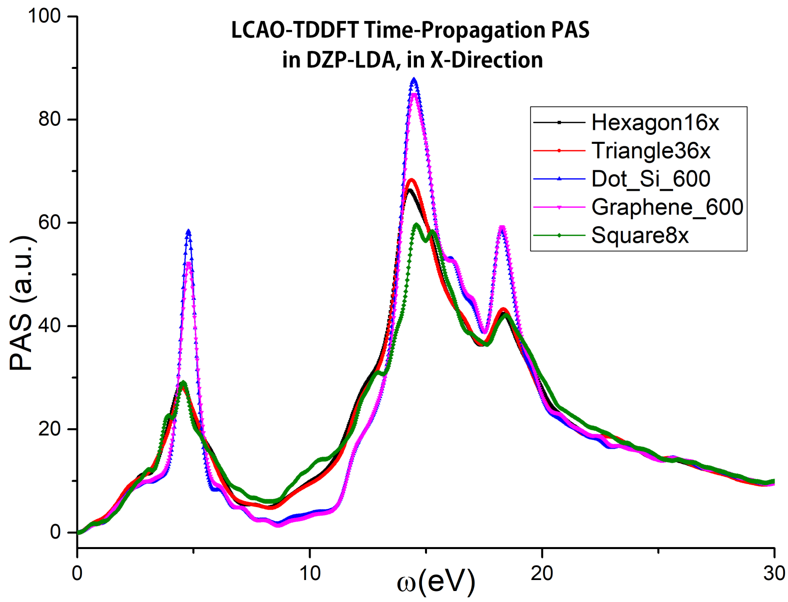

Figure 5.4: The comparison of the LCAO-TDDFT PAS of 4 different structures in 600-atom flake with the 600-atom pristine graphene flake, in DZP-LDA.

It is interesting looking at the peaks, which show that the closed structures, while having the peaks almost at the same place as graphene, they reduce the intensity, whereas the single silicon increases the intensity. The difference between the Square8x and Triangle36x/Hexagon16x, is also clear from the PAS.

Appendices

Appendix A

Optimization Algorithms

A.1 FIRE

Having described the theory behind the calculations of the forces and stress in DFT and classical potential codes, we should now describe some of the most important algorithms that do the energy minimization in both cases. One of the most efficient algorithms known is the *fast inertial relaxation engine* or FIRE. This algorithm scales very well compared to the other known gradients, some of which we will also describe. For the explanation of this algorithm the model of the blind skier is used in which, the skier looks for the fastest way down the range of the mountain, where the potential is the total energy which is supposed to be minimized $E_{tot}(x_1, ..., x_N)$. For this model the equation of motion is defined classically as:

$$\dot{\mathrm{v}}(t) = \mathbf{F}(t)/m - \gamma(t)|\mathrm{v}(t)|[\hat{\mathrm{v}}(t) - \hat{\mathbf{F}}(t)] \tag{A.1}$$

where the $\hat{\mathbf{F}}$ the force, v the velocity and $\gamma(t)$ the acceleration in the direction that is steeper than the current direction. As previously defined the forces are given by $\mathbf{F} = -\nabla E(x)$, and the power $P(t) = \mathbf{F}(t) \cdot \mathrm{v}(t)$ is positive. The trick in this scenario is that the ßkierßtops the motion when he is moving uphill, denoted by the fact that power would become negative.

The above equation as it has been shown brings the skier surprisingly fast to the desired destination, and so the aforementioned FIRE algorithm is the discretization of the above equation. For that numerical implementation in a MD-code which needs to use its integrator to check for the convergence, these two steps need to be taken into consideration: 1-Immediate stop upon the power becoming negative, 2-Mixing of the global velocity of all the atoms ($3N_{atom}$-velocities) with the Force vectors, $\mathbf{v} \to (1-\alpha)\mathbf{v} + \alpha\hat{\mathbf{F}}|\mathbf{v}|$, using the times step discretization of $\alpha = \gamma\Delta t$. Then algorithm has the following numerical steps, one MD steps and 5 force steps, given the initial guesses for $\Delta t, \quad \alpha_{start} \quad \mathbf{x}$, while $\mathbf{x} = 0$, [26]:
MD: calculate $\mathbf{x}, \mathbf{F} = -\nabla E(\mathbf{x})$ and $\mathbf{v}$ using the MD integrator; examine the convergences.
F1: calculate $P = \mathbf{F} \cdot \mathbf{v}$.
F2: set $\mathbf{v} \to (1-\alpha)\mathbf{v} + \alpha\hat{\mathbf{F}}|\mathbf{v}|$.
F3: if $P > 0$ and the number of the steps since P was negative was larger than N_{min}, increase the time step $\Delta t \to min(\Delta t f_{inc}, \Delta t_{max})$ and decrease $\alpha \to \alpha f_{\alpha}$.
F4: if $P \leq 0$, decrease the time step $\Delta t \to \Delta t f_{dec}$, freeze the system $\mathbf{v} \to 0$, and set α back to α_{start}.
F5: return to MD.

A thorough comparison of the speed and the effectiveness of this method with other methods will be given at the end of this section, after having described the other minimization algorithms.

A.2 Conjugate Gradient

One of the most popular algorithms, which is relatively an old one, but still quite in use and powerful is the method of Conjugate Gradient (CG), which like FIRE is a minimization algorithm. However, this algorithm has many aspects in comparison to FIRE which is used strictly for structural optimization. Conjugate gradient is mainly an algebraic algorithm for solving systems of linear or non-linear equations, which in the later case it is called the non-linear CG method. In particular, it can also be used for solving the eigenvalue problem. That is namely the most important difference between CG and other optimization methods such as FIRE, which can only be used for force minimization and structural optimization. For users of DFT codes, it is certainly known, that one of the methods for solving the Kohn-Sham eigenvalue equations, known with the technical term as the *eigensolver* is CG, in addition to other eigensolvers such as *Davidson* or RMM-DIIS (*residual minimization scheme, direct inversion in the iterative subspace*. Therefore the CG method is a multi-facet method in general, however here we want to look at the CG-algorithm for structural optimization and force/total-energy minimization.

As mentioned before CG is a minimzation method, namely a quadratic function, which may be viewed as a Newtonian function f which is twice differentiable, which has a Taylor expansion:

$$f_T(x) = f_T(x + \Delta x) \approx f'(x_n) + f(x_n)\Delta x + \frac{1}{2}f''(x_n)\Delta x^2 + O(\Delta x^3) + ... \tag{A.2}$$

which in the case of the *Newton-conjugate-gradient* method turns into:

$$f(x) \approx f(x_0) + \nabla f(x_0) \cdot (x - x_0) + \frac{1}{2}(x - x_0)^T \mathbf{H}(x_0)(x - x_0) \tag{A.3}$$

where $\mathbf{H}(x_0)$ is the Hessian matrix of the second derivatives. The minimum of the above quadratic equation, which is simultaneously its minimum, is found by solving $x_{opt} = x_0 - \mathbf{H}^{-1}\nabla f$, where the inverse of the Hessian matrix is calculated using the CG method, if the Hessian is positive definite. Furthermore, as instated in the code-description of ASE for example, due to the quadratic nature of the classical potentials, once the system is closed to the minimum it makes sense to use the CG method for finding the minimum of that quadratic equation as described below (as formulated by the Wikipedia article [67]):

A)-The object of minimization is a quadratic equation: $f(\mathbf{x}) = \frac{1}{2}\mathbf{x}^T\mathbf{A}\mathbf{x} - \mathbf{b}^T\mathbf{x} \qquad \mathbf{x} \in \mathbf{R}^n$
B)- The gradient of f is $\mathbf{A}\mathbf{x} - \mathbf{b}$, and the above equation suggests $\mathbf{p}_0$ is the negative of the gradient of f at $\mathbf{x} = \mathbf{x}_0$, therefore:
1- $\mathbf{r}_0 = \mathbf{b} - \mathbf{A}\mathbf{x}$, $\mathbf{p}_0 = \mathbf{r}_0$, $k = 0$,
2- Calculate $\alpha_k = \left[\mathbf{r}_k^T\mathbf{r}_k\right] / \left[\mathbf{p}_k^T\mathbf{A}\mathbf{p}_k\right]$,
3- Extract the result $\mathbf{x}_{k+1} = \mathbf{x}_k + \alpha_k\mathbf{p}_k$,
4- Checking the convergence: $\mathbf{r}_{k+1} = \mathbf{r}_k - \alpha_k\mathbf{A}\mathbf{p}_k$, if $\mathbf{r}_{k+1}$ is sufficiently small then exit loop,
5- Calculate $\beta_k = \left[\mathbf{r}_{k+1}^T\mathbf{r}_{k+1}\right] / \left[\mathbf{r}_k^T\mathbf{r}_k\right]$,
6- Calculate the next $\mathbf{p} = \mathbf{r}_{k+1} + \beta_k\mathbf{k}$,
7- And increase the index $k = k + 1$
.

The desired quantity that we are looking for is of course $\mathbf{x}_{k+1}$, however the loop includes more steps to make sure the desired convergence criterion is achieved.

A.3 BFGS

Another minimization algorithm, which is an approxiamtion of the Newton's method, is the *Broyden–Fletcher–Goldfarb–Shanno* method (BFGS). This is an iterative method, which tries to find the stationary point of a twice-differentiable function by finding the zero-gradient, and it also has a few modified versions as well, such as the limited-memory BFGS. The method falls into the category of *Quasi-Newton* methods, in which the Hessian does not need to be calculated, and is approximated using gradient evaluations. The quadratic function to be minimized remains as before similar to CG-method, $f(\mathbf{x}) = \frac{1}{2}\mathbf{x}^T\mathbf{A}\mathbf{x} - \mathbf{b}^T\mathbf{x} + \mathbf{c}$. This function is minimized in each iteration in the direction $\mathbf{p}_k$ by solving the following equation [**?**]: $B_k\mathbf{p}_k = -\nabla f(\mathbf{x}_x)$, where B_k is the approximation of the Hessian matrix, such that if inverted, it would be symmetric and possibly positive definite. and the quasi-Newton condition imposed on the B_k reads: $B_{k+1}(\mathbf{x}_{k+1} - \mathbf{x}_k) = \nabla f(\mathbf{x}_{k+1}) - \nabla f(\mathbf{x}_k)$.

Therefore, the the BFGS-algorithm in its original form, can be summerized as follows (as formulated by the Wikipedia article [66]):
1- Solve the equation $B_k\mathbf{p}_k = -\nabla f(\mathbf{x}_x)$ to obtain a direction $\mathbf{p}_k$.
2- Do a line search as follows:
    a)- Set $k = 0$, and take an initial guess $\mathbf{x}_0$
    b)- Calculate $\mathbf{p}_k$ such that it would get the initial guess closer to the desired minimum.
    c)- Choose a step-size to minimize $h(\alpha) = f(\mathbf{x}_k + \alpha\mathbf{p}_k)$, $\alpha \in \mathcal{R}^+$
    d)- Calculate the next $\mathbf{x}_{k+1} = \mathbf{x}_k + \alpha_k\mathbf{p}_k$, and set $k = k + 1$
    e)- Check the convergence, $\parallel \nabla f(\mathbf{x}_k) \parallel <$ tolerance.
3- Set $\mathbf{s}_k = \alpha_k\mathbf{p}_k$
4- $\mathbf{y}_k = \nabla f(\mathbf{x}_{k+1}) - \nabla f(\mathbf{x}_k)$
5- $B_{k+1} = B_k + \frac{\mathbf{y}_k\mathbf{y}_k^T}{\mathbf{y}_k^T\mathbf{s}_k} - \frac{B_k\mathbf{s}_k\mathbf{s}_k^T B_k}{\mathbf{s}_k^T B_k\mathbf{s}_k}$

The initial guess for $B = \mathcal{I}$, and the next step would be inverting this matrix for solving the equation in step 1. And finally the convergence can be checked by calculating the norm of the gradient $|\nabla f(\mathbf{x}_k)|$.

Appendix B

Scripts

B.1 GPAW-code Modifications

In this section we present a couple of modifications to the original GPAW code, for the simulations of the constant height topography STM, and STS dI/dV. We emphasis here that, there are no simulation scripts presented here as far as the input-parameter scripts for GPAW-simulations are concerned. The scripts here are engine modifications to the original GPAW code, which is an open-source software and editable with Python (where Python code is used), which then are called upon and utilized using the input-parameter GPAW-job scripts. The scripts use the features of already existing code for constant current STM simulation, epecially the syntax written for the calculations of the LDOS as a function of position and bias. The following code describe the STM function:

```
def scan2(self, bias, z, repeat=(1, 1)):
    """Constant height 2-d scan.

    Returns three 2-d arrays (x, y, I) containing x-coordinates,
    y-coordinates and currents.  These three arrays can be
    passed to matplotlibs contourf() function like this:

    >>> import matplotlib.pyplot as plt
    >>> plt.gca(aspect='equal')
    >>> plt.contourf(x, y, I)
    >>> plt.show()

    """

    self.calculate_ldos(bias)

    nz = self.atoms.calc.get_number_of_grid_points()[2]
    ldos = self.ldos.reshape((-1, nz))

    I = np.empty(ldos.shape[0])

    zp = z / self.cell[2, 2] * nz
    dz = zp - np.floor(zp)
    zp = int(zp) % nz
```

```
        for i, a in enumerate(ldos):
            I[i] = self.find_current(a, z)

        s0 = I.shape = self.ldos.shape[:2]
        I = np.tile(I, repeat)
        s = I.shape

        ij = np.indices(s, dtype=float).reshape((2, -1)).T
        x, y = np.dot(ij / s0, self.cell[:2, :2]).T.reshape((2,) + s)

        return x, y, I
```

And the following code describes the STS function:

```
    def sts(self, x, y, z, bias0, bias1, biasstep): #, width):
        """Calculates the dI/dV curve for position x, y at height z,
        for bias from bias0 to bias1 with step biasstep."""

        biases = np.arange(bias0, bias1+biasstep, biasstep)
        I = np.zeros(biases.shape)

        for b in np.arange(len(biases)):
            print b, biases[b]
            I[b] = self.pointcurrent(biases[b], x, y, z)



        dIdV = np.gradient(I,biasstep)

        return biases, I, dIdV
```

Glossary

GGA	Generalized Gradient Approximations
LDA	Local Densities Approximation
GLLBS-SC	Gauss-Lobatto-Legendre-Birkhoff Solids Corrected
GPAW	Grid-Based Projector Augmented Wave
DFT	Density Functional Theory
PAS	Photo-Absorption Spectrum/Spectra
VdW	Van der Waals
SWNT	Single Wall Nano-Tube
STM	Scanning Tunnelling Microscopy
STEM	Scanning Transmission Electron Microscopy
EELS	Electron Energy-Loss Spectroscopy
TDDFT	Time-Dependent Density Functional Theory
LFE	Local Field Effects
LFC	Local Field Corrections
MD	Molecular Dynamics
LAMMPS	Large-scale Molecular Massively Parallel Simulator
LDOS	Local Density of States
NEGF	Non-Equilibrium Green Function
DOS	Density of States
QED	Quantum Electrodynamics
MLG	Multi-Layer Graphene
BLG	Bilayer Graphene
SPE	Single Particle Excitations
RPA	Random Phase Approximations

SP	Surface Plasmons
TM/TE	Transverse Magnetic/Transverse Electric
QD	Quantum Dot
ZBL	Ziegler Biersack Littmark
EA	Erhard Albe
HK	Hohenberg-Kohn
PAW	projector Augmented Wave
LCAO	Linear Combination of Atomic Orbitals
FD	Finite Differences
XC	Exchange Correlation
LAPW	Linearised Augmented Plane-wave
LSDA	Local Spin Densities Approximations
SCF	Self Consistent Fields
PW	Plane-Wave
FFT	Fast Fourier Transform
AE/PS	All-Electron/Pseudo
SZP	Single-Zeta Polarized
DZP	Double-Zeta Polarized
PBE	Perdew, Burke and Ernzerhof
DFTB	Density Functional Tight Binding
VASP	Vienna Ab-Initio Simulation Package
HEG	Homogeneous Electron Gas
LUMO	Lowest Unoccupied Molecular Orbital
HOMO	Highest Occupied Molecular Orbital
TH	Tersoff Hamman
STS	Scanning Tunnelling Spectroscopy
DFPD	Density Functional Perturbation Theory
LrTDDFT	Linear Response TDDFT
ALDA	Adiabatic Local Densities Approximations
ABS	Absorption Spectrum

LDR	Linear Density Response
PBC	Periodic Boundary Condition
SPP	Surface Plasmon Polariton
LSP	Localized Surface Plamons
LSPR	Localized Surface Plasmonic Resonances
DDA	Discrete Dipole Approximations
FDTD	Finite Difference Time Domain
BASH	Bourne Again Shell
CG	Conjugate Gradient
ASE	Atomic Simulation Environment
BFGS	Broyden-Fletcher–Goldfarb-Shanno
FIRE	Fast Inertial Relaxation Engine
RMM-DIIS	Residual Minimization Scheme, Direct Inversion in the Iterative Subspace

Bibliography

[1] Castro Neto, A. H. et al. "The Electronic Properties Of Graphene." *Reviews Of Modern Physics*, vol 81, no. 1, 2009, pp. 109-162. *American Physical Society (APS)*, doi:10.1103/revmodphys.81.109.

[2] Lee, Juwon et al. "Imaging Electrostatically Confined Dirac Fermions In Graphene Quantum Dots." *Nature Physics*, vol 12, no. 11, 2016, pp. 1032-1036. *Springer Nature*, doi:10.1038/nphys3805.

[3] Castro, Eduardo V et al. "Electronic Properties Of A Biased Graphene Bilayer." *Journal Of Physics: Condensed Matter*, vol 22, no. 17, 2010, p. 175503. *IOP Publishing*, doi:10.1088/0953-8984/22/17/175503.

[4] Fuchs, Jean-Noel. *Dirac Fermions In Graphene And Analogues: Magnetic Field And Topological Properties*. Arxiv E-Prints, 2013, http://adsabs.harvard.edu/abs/2013arXiv1306.0380F.

[5] "Theory Of Scanning Tunneling Microscopy." Arxiv E-Prints, *45Th IFF Spring School*, 2014, pp. 7-17. http://adsabs.harvard.edu/abs/2014arXiv1404.0961L.

[6] Fiete, Gregory A., and Eric J. Heller. "Colloquium: Theory Of Quantum Corrals And Quantum Mirages." *Reviews Of Modern Physics*, vol 75, no. 3, 2003, pp. 933-948. *American Physical Society (APS)*, doi:10.1103/revmodphys.75.933.

[7] Amusia, Miron et al. "Handbook Of Theoretical Atomic Physics." 2012, *Springer Berlin Heidelberg*, doi:10.1007/978-3-642-24752-1.

[8] Maier, Stefan A. *Plasmonics*. New York, NY, Springer, 2007,.

[9] Grigorenko, A. N. et al. "Graphene Plasmonics." *Nature Photonics*, vol 6, no. 11, 2012, pp. 749-758. *Springer Nature*, doi:10.1038/nphoton.2012.262.

[10] Luo, Xiaoguang et al. "Plasmons In Graphene: Recent Progress And Applications." *Materials Science And Engineering: R: Reports*, vol 74, no. 11, 2013, pp. 351-376. *Elsevier BV*, doi:10.1016/j.mser.2013.09.001.

[11] Jablan, Marinko et al. "Plasmons In Graphene: Fundamental Properties And Potential Applications." *Proceedings Of The IEEE*, vol 101, no. 7, 2013, pp. 1689-1704. *Institute Of Electrical And Electronics Engineers (IEEE)*, doi:10.1109/jproc.2013.2260115.

[12] Takagahara, Toshihide, and Kyozaburo Takeda. "Theory Of The Quantum Confinement Effect On Excitons In Quantum Dots Of Indirect-Gap Materials." *Physical Review B*, vol 46, no. 23, 1992, pp. 15578-15581. *American Physical Society (APS)*, doi:10.1103/physrevb.46.15578.

[13] Martin, Richard M. *Electronic Structure. Cambridge*, Cambridge University Press, 2013,.

[14] Crommie, M.F. et al. "Quantum Corrals." *Physica D: Nonlinear Phenomena*, vol 83, no. 1-3, 1995, pp. 98-108. *Elsevier BV*, doi:10.1016/0167-2789(94)00254-n.

[15] Fu, Zhen-Guo et al. "Quantum Corrals And Quantum Mirages On The Surface Of A Topological Insulator." *Physical Review B*, vol 84, no. 23, 2011, *American Physical Society (APS)*, doi:10.1103/physrevb.84.235438.

[16] Crampin, S. "Electron States In Quantum Corrals." *Philosophical Transactions Of The Royal Society A: Mathematical, Physical And Engineering Sciences*, vol 362, no. 1819, 2004, pp. 1149-1161. *The Royal Society*, doi:10.1098/rsta.2004.1368.

[17] Rossi, Tuomas P. et al. "Nanoplasmonics Simulations At The Basis Set Limit Through Completeness-Optimized, Local Numerical Basis Sets." *The Journal Of Chemical Physics*, vol 142, no. 9, 2015, p. 094114. *AIP Publishing*, doi:10.1063/1.4913739.

[18] Kuisma, M. et al. "Localized Surface Plasmon Resonance In Silver Nanoparticles: Atomistic First-Principles Time-Dependent Density-Functional Theory Calculations." *Physical Review B*, vol 91, no. 11, 2015, *American Physical Society (APS)*, doi:10.1103/physrevb.91.115431.

[19] Das Sarma, S. et al. "Electronic Transport In Two-Dimensional Graphene." *Reviews Of Modern Physics*, vol 83, no. 2, 2011, pp. 407-470. *American Physical Society (APS)*, doi:10.1103/revmodphys.83.407.

[20] Hwang, E. H., and S. Das Sarma. "Dielectric Function, Screening, And Plasmons In Two-Dimensional Graphene." *Physical Review B*, vol 75, no. 20, 2007, *American Physical Society (APS)*, doi:10.1103/physrevb.75.205418.

[21] Lin, I-Tan et al. "Terahertz Optoelectronic Property Of Graphene: Substrate-Induced Effects On Plasmonic Characteristics." *Applied Sciences*, vol 4, no. 1, 2014, pp. 28-41. *MDPI AG*, doi:10.3390/app4010028.

[22] Mishchenko, E. G. "Minimal Conductivity In Graphene: Interaction Corrections And Ultraviolet Anomaly." *EPL (Europhysics Letters)*, vol 83, no. 1, 2008, p. 17005. *IOP Publishing*, doi:10.1209/0295-5075/83/17005.

[23] Gangadharaiah, S. et al. "Charge Response Function And A Novel Plasmon Mode In Graphene." *Physical Review Letters*, vol 100, no. 16, 2008, *American Physical Society (APS)*, doi:10.1103/physrevlett.100.166802.

[24] Hartmann, R. R. et al. "Smooth Electron Waveguides In Graphene." *Physical Review B*, vol 81, no. 24, 2010, *American Physical Society (APS)*, doi:10.1103/physrevb.81.245431.

[25] Huang, Zhongkai et al. "Quantum Confinement In Graphene Quantum Dots." *Physica Status Solidi (RRL) - Rapid Research Letters*, vol 8, no. 5, 2014, pp. 436-440. *Wiley-Blackwell*, doi:10.1002/pssr.201409064.

[26] Bitzek, Erik et al. "Structural Relaxation Made Simple." *Physical Review Letters*, vol 97, no. 17, 2006, *American Physical Society (APS)*, doi:10.1103/physrevlett.97.170201.

[27] Thompson, Aidan P. et al. "General Formulation Of Pressure And Stress Tensor For Arbitrary Many-Body Interaction Potentials Under Periodic Boundary Conditions." *The Journal Of Chemical Physics*, vol 131, no. 15, 2009, p. 154107. *AIP Publishing*, doi:10.1063/1.3245303.

[28] Maranganti, R., and P. Sharma. "Revisiting Quantum Notions Of Stress." *Proceedings Of The Royal Society A: Mathematical, Physical And Engineering Sciences*, vol 466, no. 2119, 2010, pp. 2097-2116. *The Royal Society*, doi:10.1098/rspa.2009.0636.

[29] Fyta, Maria. "Classical Potentials And Force Fields." 2017

[30] Hafner, J. "FOUNDATIONS OF DENSITY-FUNCTIONAL THEORY." 2013,.

[31] Eidel, Bernhard et al. "Energy-Minimization In Atomic-To-Continuum Scale-Bridging Methods." *PAMM*, vol 11, no. 1, 2011, pp. 509-510. *Wiley-Blackwell*, doi:10.1002/pamm.201110246.

[32] Navon, I. M., and David M. Legler. "Conjugate-Gradient Methods For Large-Scale Minimization In Meteorology." *Monthly Weather Review*, vol 115, no. 8, 1987, pp. 1479-1502. *American Meteorological Society*, doi:10.1175/1520-0493(1987)115¡1479:cgmfls¿2.0.co;2.

[33] Hestenes, M.R., and E. Stiefel. "Methods Of Conjugate Gradients For Solving Linear Systems." *Journal Of Research Of The National Bureau Of Standards*, vol 49, no. 6, 1952, p. 409. *National Institute Of Standards And Technology (NIST)*, doi:10.6028/jres.049.044.

[34] Erhart, Paul, and Karsten Albe. "Analytical Potential For Atomistic Simulations Of Silicon, Carbon, And Silicon Carbide." *Physical Review B*, vol 71, no. 3, 2005, *American Physical Society (APS)*, doi:10.1103/physrevb.71.035211.

[35] Tersoff, J. "New Empirical Approach For The Structure And Energy Of Covalent Systems." *Physical Review B*, vol 37, no. 12, 1988, pp. 6991-7000. *American Physical Society (APS)*, doi:10.1103/physrevb.37.6991.

[36] Brenner, Donald W. "Empirical Potential For Hydrocarbons For Use In Simulating The Chemical Vapor Deposition Of Diamond Films." *Physical Review B*, vol 42, no. 15, 1990, pp. 9458-9471. *American Physical Society (APS)*, doi:10.1103/physrevb.42.9458.

[37] Soler, José M et al. "The SIESTA Method Forab Initioorder-Nmaterials Simulation." *Journal Of Physics: Condensed Matter*, vol 14, no. 11, 2002, pp. 2745-2779. *IOP Publishing*, doi:10.1088/0953-8984/14/11/302.

[38] Mortensen, J. J. et al. "Real-Space Grid Implementation Of The Projector Augmented Wave Method." *Physical Review B*, vol 71, no. 3, 2005, *American Physical Society (APS)*, doi:10.1103/physrevb.71.035109.

[39] Mi, Wenhui et al. "ATLAS: A Real-Space Finite-Difference Implementation Of Orbital-Free Density Functional Theory." *Computer Physics Communications*, vol 200, 2016, pp. 87-95. *Elsevier BV*, doi:10.1016/j.cpc.2015.11.004.

[40] Enkovaara, J et al. "Electronic Structure Calculations With GPAW: A Real-Space Implementation Of The Projector Augmented-Wave Method." *Journal Of Physics: Condensed Matter*, vol 22, no. 25, 2010, p. 253202. *IOP Publishing*, doi:10.1088/0953-8984/22/25/253202.

[41] Larsen, A. H. et al. "Localized Atomic Basis Set In The Projector Augmented Wave Method." *Physical Review B*, vol 80, no. 19, 2009, *American Physical Society (APS)*, doi:10.1103/physrevb.80.195112.

[42] Blanco, Jose Manuel et al. "STM-Theory: Image Potential, Chemistry And Surface Relaxation." *Progress In Surface Science*, vol 81, no. 10-12, 2006, pp. 403-443. *Elsevier BV*, doi:10.1016/j.progsurf.2006.07.004.

[43] Kuisma, M. et al. "Kohn-Sham Potential With Discontinuity For Band Gap Materials." *Physical Review B*, vol 82, no. 11, 2010, *American Physical Society (APS)*, doi:10.1103/physrevb.82.115106.

[44] Gritsenko, Oleg V. et al. "Molecular Exchange-Correlation Kohn–Sham Potential And Energy Density From Ab Initio First- And Second-Order Density Matrices: Examples For XH (X=Li, B, F)." *The Journal Of Chemical Physics*, vol 104, no. 21, 1996, pp. 8535-8545. *AIP Publishing*, doi:10.1063/1.471602.

[45] Mayer, Kathryn M., and Jason H. Hafner. "Localized Surface Plasmon Resonance Sensors." *Chemical Reviews*, vol 111, no. 6, 2011, pp. 3828-3857. *American Chemical Society (ACS)*, doi:10.1021/cr100313v.

[46] Tersoff, J., and D. R. Hamann. "Theory Of The Scanning Tunneling Microscope." *Physical Review B*, vol 31, no. 2, 1985, pp. 805-813. *American Physical Society (APS)*, doi:10.1103/physrevb.31.805.

[47] Tersoff, J., and D. R. Hamann. "Theory And Application For The Scanning Tunneling Microscope." *Physical Review Letters*, vol 50, no. 25, 1983, pp. 1998-2001. *American Physical Society (APS)*, doi:10.1103/physrevlett.50.1998.

[48] Yan, Jun et al. "Linear Density Response Function In The Projector Augmented Wave Method: Applications To Solids, Surfaces, And Interfaces." *Physical Review B*, vol 83, no. 24, 2011, *American Physical Society (APS)*, doi:10.1103/physrevb.83.245122.

[49] Walter, Michael et al. "Time-Dependent Density-Functional Theory In The Projector Augmented-Wave Method." *The Journal Of Chemical Physics*, vol 128, no. 24, 2008, p. 244101. *AIP Publishing*, doi:10.1063/1.2943138.

[50] Casida, M.E., and M. Huix-Rotllant. "Progress In Time-Dependent Density-Functional Theory." *Annual Review Of Physical Chemistry*, vol 63, no. 1, 2012, pp. 287-323. *Annual Reviews*, doi:10.1146/annurev-physchem-032511-143803.

[51] Marques, Miguel A. L. *Fundamentals Of Time-Dependent Density Functional Theory*. Berlin, Springer-Verlag, 2012,.

[52] van Gisbergen, S.J.A. et al. "Implementation Of Time-Dependent Density Functional Response Equations." *Computer Physics Communications*, vol 118, no. 2-3, 1999, pp. 119-138. *Elsevier BV*, doi:10.1016/s0010-4655(99)00187-3.

[53] Lu, Deyu. "Evaluation Of Model Exchange-Correlation Kernels In The Adiabatic Connection Fluctuation-Dissipation Theorem For Inhomogeneous Systems." *The Journal Of Chemical Physics*, vol 140, no. 18, 2014, pp. 18A520. *AIP Publishing*, doi:10.1063/1.4867538.

[54] Furche, Filipp. "On The Density Matrix Based Approach To Time-Dependent Density Functional Response Theory." *The Journal Of Chemical Physics*, vol 114, no. 14, 2001, pp. 5982-5992. *AIP Publishing*, doi:10.1063/1.1353585.

[55] Liu, Chao et al. "Theoretical Assessment Of Localized Surface Plasmon Resonance Properties Of Au-Interlayer-Ag Multilayered Nanoshells." *Plasmonics*, vol 11, no. 6, 2016, pp. 1589-1595. *Springer Nature*, doi:10.1007/s11468-016-0214-5.

[56] Pereira, Vitor M. et al. "Coulomb Impurity Problem In Graphene." *Physical Review Letters*, vol 99, no. 16, 2007, *American Physical Society (APS)*, doi:10.1103/physrevlett.99.166802.

[57] Andrei, Eva Y et al. "Electronic Properties Of Graphene: A Perspective From Scanning Tunneling Microscopy And Magnetotransport." *Reports On Progress In Physics*, vol 75, no. 5, 2012, p. 056501. *IOP Publishing*, doi:10.1088/0034-4885/75/5/056501.

[58] Jablan, Marinko et al. "Plasmonics In Graphene At Infrared Frequencies." *Physical Review B*, vol 80, no. 24, 2009, *American Physical Society (APS)*, doi:10.1103/physrevb.80.245435.

[59] Lundeberg, Mark B. et al. "Tuning Quantum Nonlocal Effects In Graphene Plasmonics." *Science*, vol 357, no. 6347, 2017, pp. 187-191. *American Association For The Advancement Of Science (AAAS)*, doi:10.1126/science.aan2735.

[60] Castro, A et al. "Solution Of Poisson's Equation For Finite Systems Using Plane-Wave Methods." *Canadian Journal Of Physics*, vol 81, no. 10, 2003, pp. 1151-1164. *Canadian Science Publishing*, doi:10.1139/p03-078.

[61] Takagahara, Toshihide, and Kyozaburo Takeda. "Theory Of The Quantum Confinement Effect On Excitons In Quantum Dots Of Indirect-Gap Materials." *Physical Review B*, vol 46, no. 23, 1992, pp. 15578-15581. *American Physical Society (APS)*, doi:10.1103/physrevb.46.15578.

[62] Hjorth Larsen, Ask et al. "The Atomic Simulation Environment—A Python Library For Working With Atoms." *Journal Of Physics: Condensed Matter*, vol 29, no. 27, 2017, p. 273002. *IOP Publishing*, doi:10.1088/1361-648x/aa680e.

[63] Bahn, S.R., and K.W. Jacobsen. "An Object-Oriented Scripting Interface To A Legacy Electronic Structure Code." *Computing In Science & Engineering*, vol 4, no. 3, 2002, pp. 56-66. *Institute Of Electrical And Electronics Engineers (IEEE)*, doi:10.1109/5992.998641.

[64] Plimpton, Steve. "Fast Parallel Algorithms For Short-Range Molecular Dynamics." *Journal Of Computational Physics*, vol 117, no. 1, 1995, pp. 1-19. *Elsevier BV*, doi:10.1006/jcph.1995.1039.

[65] Mikhailov, S. A., and K. Ziegler. "New Electromagnetic Mode In Graphene." *Physical Review Letters*, vol 99, no. 1, 2007, *American Physical Society (APS)*, doi:10.1103/physrevlett.99.016803.

[66] "Broyden–Fletcher–Goldfarb–Shanno Algorithm." *En.Wikipedia.Org*, 2017, https://en.wikipedia.org/wiki/Broyden%E2%80%93Fletcher%E2%80%93Goldfarb %E2%80%93Shanno

[67] "Conjugate Gradient Method." *En.Wikipedia.Org*, 2017, https://en.wikipedia.org/wiki/Conjugate_gradient_method.

[68] Koole, Rolf et al. "Size Effects On Semiconductor Nanoparticles." *Nanoparticles*, 2014, pp. 13-51. *Springer Berlin Heidelberg*, doi:10.1007/978-3-662-44823-6_2.

List of Publications

(a) D. Nosraty Alamdary, J. Kotakoski & T. Susi, *Structure and energetics of embedded Si structures in graphene*, Submitted for publication (2017). ArXiv: 1704.08019

(b)

(c)